IRRADIATION DAMAGE IN NEUTRON-IRRADIATED FE-CR MODEL ALLOYS

BY

WEI-YING CHEN

DISSERTATION

Submitted in partial fulfillment of the requirements
for the degree of Doctor of Philosophy in Nuclear Engineering
in the Graduate College of the
University of Illinois at Urbana-Champaign, 2014

Urbana, Illinois

Doctoral Committee:

Professor James F. Stubbins, Chair
Professor Brent J. Heuser
Professor Rizwan Uddin
Professor Ian M. Robertson

ABSTRACT

Ferritic-martensitic (F-M) steels are considered as lead candidate structural materials for Generation IV fission reactors and future fusion reactors. Compared to austenitic stainless steels, these steels have superior properties in thermal conductivities and thermal expansion coefficients. In addition, they have better resistance to swelling, helium embrittlement and irradiation creep at elevated temperature (T/T_m >0.4). However, F-M steels exhibit low-temperature irradiation-induced embrittlement that leads to a substantial decrease in toughness at lower irradiation temperature (T <500°C) even at very low doses. The underlying microstructral mechanisms and their dependence on the irradiation temperatures and chromium contents are not well understood.

Body-centered cubic iron (Fe) and iron-chromium (Fe-Cr) (Cr = 10-16 at%) are used as model to study the irradiation-induced microstructural evolution and their relationship to mechanical properties. The irradiation effects as a function of Cr contents and irradiation temperatures were systematically investigated. Through using model materials, the effects of other substitutional alloying elements (e.g. nickel, tungsten and manganese), interstitial impurities (e.g. carbon and nitrogen) and secondary phases (e.g. carbides, nitrides and G-phase precipitates) commonly seen in commercial F-M steels can be reduced.

Neutron irradiations were carried out at Advanced Test Reactor with target doses of 0.01, 0.1 and 1 dpa and target irradiation temperatures of 300 and 450°C. Following irradiations, the resulting microstructure were investigated with transmission electron microscopy (TEM), atom probe tomography (APT) and electron backscatter diffraction (EBSD). TEM was used to observe the crystallographic defect structures caused by irradiation damage, including dislocation loops and voids. APT was used to study the precipitation of Cr-rich α' phase under irradiation-enhanced diffusion process. EBSD is used to examine the grain

size distribution and possible grain growth. The corresponding mechanical properties were evaluated with the hardness measurements. Both Vicker hardness test (microhardness) and high-load nanoindentation were used.

The results of mechanical properties and microstructures were compared and related through Orowan model. In general, the increase in hardness in irradiated specimens can be attributed primarily to the formation of dislocation loops and α' precipitates. The dislocation loops appeared to results hardening at the lowest dose of 0.01 dpa. The addition of Cr in Fe greatly reduced the mobility of interstitials and small $\frac{a}{2}\langle 111\rangle$ dislocation loops, leading to smaller loop size and more uniform distribution. The Cr effect on loop density is not clear in this study.

Increasing irradiation temperature increased the mobility of point defects and small $\frac{a}{2}\langle 111\rangle$ dislocation loops, resulting in larger loop size and lower loop density. In Fe, $\frac{a}{2}\langle 111\rangle$ loops were sufficiently mobile at 300°C, leading to a dislocation decoration structure. Irradiation at 450°C predominantly produced immobile a$\langle 100\rangle$ dislocation loops in Fe, leading to a relatively uniform loop distribution. The addition of Cr caused a retention of $\frac{a}{2}\langle 111\rangle$ loops in Fe-Cr irradiated at 450°C. The enhanced mobility of $\frac{a}{2}\langle 111\rangle$ loops at higher temperature is related to the formation of some dislocation decoration in Fe-Cr.

α' precipitate effects on hardening in Fe-Cr appeared at higher dose of 1 dpa. The precipitate density is higher with increasing Cr contents and decreasing irradiation temperatures. On contract, the size of α' precipitates was relatively invariant as $\sim$2 nm (radii) to irradiation conditions. α' precipitates were identified to be the major reason that resulted in higher hardening in Fe-Cr with higher Cr contents at 1 dpa.

Voids formation was observed in Fe irradiated at both 300 and 450°C to 1 dpa. The void size is larger in 450°C than in 300°C specimen. No voids formation was evidently observed in Fe-Cr. No grain growth can be detected in Fe irradiated at 450°C.

ACKNOWLEDGMENTS

I would like to thank my advisor, Prof. James F. Stubbins, for his advice, support and guidance. Since my graduate study, I benefited from his vision in science, and the opportunity and freedom he has given me to explore and pursue my scientific interests.

This research involves the characterization of radioactive materials. Efforts from many people have been made in order to make it possible and successful. Firstly, I would like to thank my research group from Idaho National Laboratory, including Dr. Jian Gan, Dr. Maria A. Okuniewski and Dr. Yaqiao Wu. Dr. Gan has been overseen specimen preparations and transmission electron microscopies. He has also provided insightful advice since the inception of this work. Dr. Okuniewski has worked with me about the hardness measurements and has given me many useful suggestions. Dr. Wu has been performing the atom probe tomography relevant to this work and has been training me how to analyze atom probe tomography data.

I would like to thank Dr. Stuart A. Maloy from Los Alamos National Laborotory for his helpful discussions. He has also provided us single crystal Fe-Cr alloys for use in the irradiation experiments.

This work won't be possible without many other scientists and staffs at ATR NSUF in National Idaho Laboratory, including Mary Catherine Thelen, Dr. Brandon D. Miller, Jeff B Benson, Dr. James I. cole and Collin J. Knight. Particularly, I greatly appreciate Collin for his timely and coordinated management to keep the project moving forward. Special thanks to Dr. Miller for his help in specimen preparations.

Most of the experiments were conducted in Microscopy and Characterization Suite in the Center of Advanced Energy Studies in Idaho Falls. I would like to thank Joanna Taylor, Jatu Burns, Bryan Forsmann and Kristi Moser-Mclntire for running such a great laboratory.

Special thanks to Jatu for her training me to use FIB for preparing APT samples and for her help in EBSD.

Some characterizations, including TEM and microhardness tests, were performed in the LAMDA facility in Oak Ridge National Laboratory. I would like to thank Dr. Kieth J. Leonard and Dr. Lizhen Tan for their time facilitating the experiments.

I am thankful that I can discuss my works with many scientists and get invaluable suggestions and thoughts from them. Dr. Marquis A. Kirk from Argonne National Laboratory is gratefully acknowledged for his insightful discussions. His knowledge in irradiation damage in Fe and Fe-Cr systems and transmission electron microscopy help greatly understand my microscopy results. I would like to thank Dr. Xianming Bai and Dr. Yongfeng Zhang from Idaho National Laboratory, Dr. Zhongwen Yao from Queen's University and Dr. Bai Cui from University of Illinois for their useful discussions.

I wish to express my thank to Dr. Meimei Li and Dr. Krishnamurti Natesan from Argonne National Laboratory who allowed me to join the EPRI project as an internship student where I learned a great deal of irradiation damage in engineering materials. I particularly thank Dr. Li for her guidance and advice in irradiation experiments, TEM analysis and the vision in scientific research.

This study was supported by ATR NSUF under identification number 08-092 and by NEUP under grant number 485363-973000-191100. Both funding are titled 'Irradiation Performance of Fe-Cr Base Alloys'.

Thank you to Yinbin Miao, Aaron Oaks, Carolyn Tomchik, Kun Mo, Xiang Liu and Kuan-Che Lan in my research group in University of Illinois for your support. I enjoy the moments in your company. Special thank to Yinbin, who has accompanied me in many experiments and actually acquired some data himself for me. I would like to thank Carolyn for initiating this project. I would also like to thank Di Yun, who graduated from our group a few years ago, for his useful discussions in research.

I would like to thank my committee members, Prof. Brent J. Heuser, Prof. Rizwan Uddin and Prof. Ian M. Robertson for their time, support and reviewing my thesis.

Thank you to Gail Krueger, Idell Dollison and Becky Meline in the Department of Nuclear, Plasma and Radiological Engineering in University of Illinois for their warm help in many

ways.

Finally, I deeply appreciate my family and my wife's family for their support and encouragement during my graduate career. I particularly thank my wife's parents for their time and efforts taking care of my son and daughter, Chao-Yi and Zi-Ciao, so I had time for writing thesis. And lastly, but most importantly, thank you to my wife Bei for her love, sacrifice and endless support during this period.

TABLE OF CONTENTS

CHAPTER 1

INTRODUCTION

1.1 Development of Ferritic-Martensitic Steels for Use in the Advanced Fission and Fusion Nuclear Reactors

International cooperation has proposed several next-generation (Generation IV) nuclear reactor concepts to produce safe, reliable, economically-competitive and proliferation-resistant energy [1]. The current generation of light-water reactors (LWRs) operate at a temperature of ∼288° and pressure of ∼7 MPa for boiling-water reactor and ∼15 MPa for pressurized-water reactors [2]. The Gen IV reactor concepts often require demanding operation conditions such as elevated temperatures, extended neutron exposures and corrosive environments. Figure 1.1 shows the operating temperature and dose exposure for the structural materials of current and future nuclear reactors.

Ferritic-Martensitic steels, i.e. Fe based alloys with body-centered-cubic (bcc) and body-centered-tetragonal (bct) structure, are considered as lead candidate material for in-core (cladding, duck and wrapper) and out-of-core (pressure vessel, piping etc.) applications in Gen-IV reactors [1]. For Fusion reactors, it has been considered for the first wall and blanket structures [4]. Following the development history reviewed by Klueh and Nelson [5], ferritic-martensitic steels were firstly appealed in the fast reactor program to replace the austenitic in-core structure (cladding wrappers and duckts) due to their higher thermal conductivities and lower thermal expansion coefficients [4]. In addition, they have superior resistance to swelling [6][7], helium embrittlement [8][9], and irradiation creep at elevated temperature (T/T_m>0.4) [10].

In despite of its many advantages, ferritic-martensitic steels exhibit low-temperature irradiation-induced embrittlement that leads to a substantial increase in the ductile-to-brittle

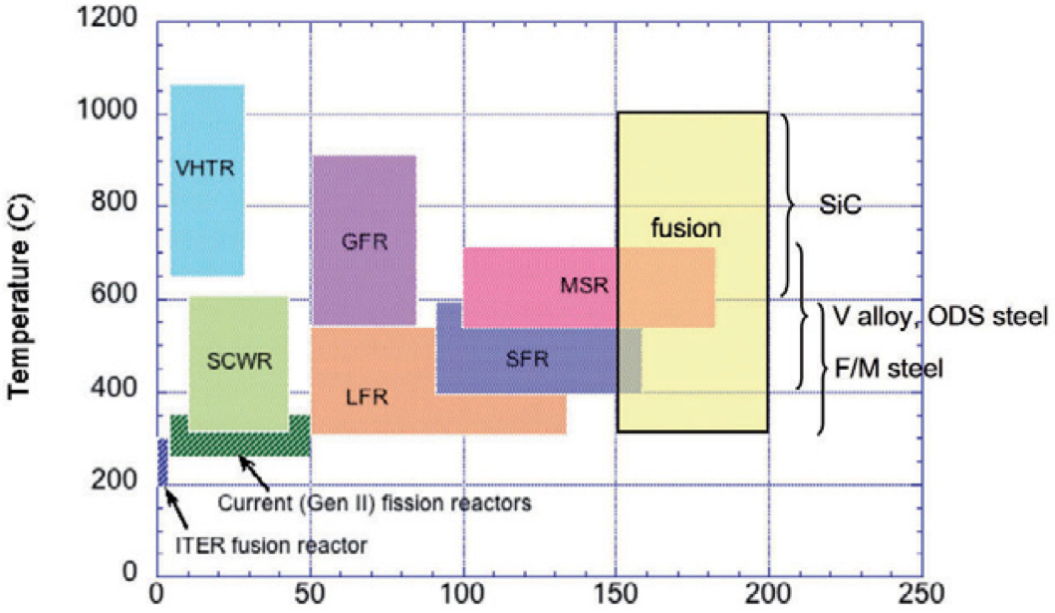

Figure 1.1: The operating temperatures and displacement damage dose regimes for structural materials in current (Generation II) and proposed future (Generation IV) fission and fusion energy systems. VHTR: Very High Temperature Reactor; SCWR: Super Critical Water Reactor; LFR: Lead Fast Reactor; GFR: Gas Fast Reactor; SFR: Sodium Fast Reactor; MSR: Molten Salt Reactor. [3]

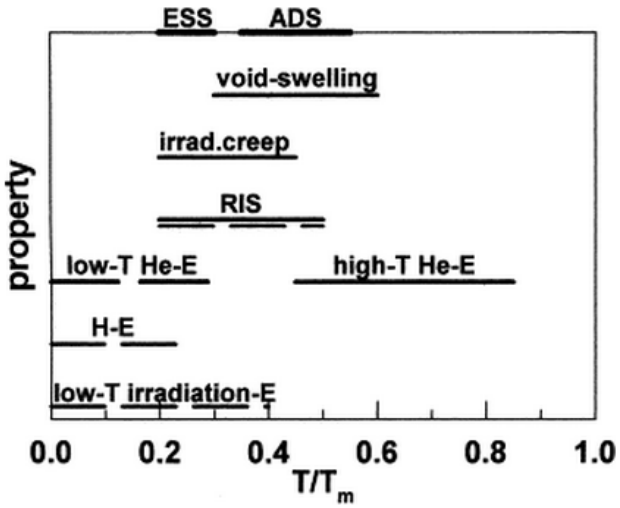

Figure 1.2: Schematic view of the ranges of homologous temperatures for austenitic (solid) and martensitic (dashed) steels to be affected greatly by irradiation damage in the perspective of the degradation of physical and mechanical properties. E represents embrittlement. RIS represents radiation induced segregation. The top ESS and ADS represent the operation regime for European Spallation Source and the Accelerator Driven Systems respectively [11]

transition temperature (ΔDBTT) at lower irradiation temperatures (T $<$ 500°C) even at very low doses, as shown in Figure 1.3 . In addition to the irradiation temperature, the Cr content in ferritic-martensitic steels also strongly influences the irradiation-induced ΔDBTT. Figure 1.4 shows the dependence of ΔDBTT on the Cr concentration. A minimum ΔDBTT was observed approximately at 9%Cr. Because of this Cr concentration dependence of the mechanical property, the development of ferritic-martensitic steels for use in advanced nuclear reactors has focused on 7-12%Cr steels including several commercial and experimental ferritic-martensitic steels such as HT9, F82H and EUROFER.

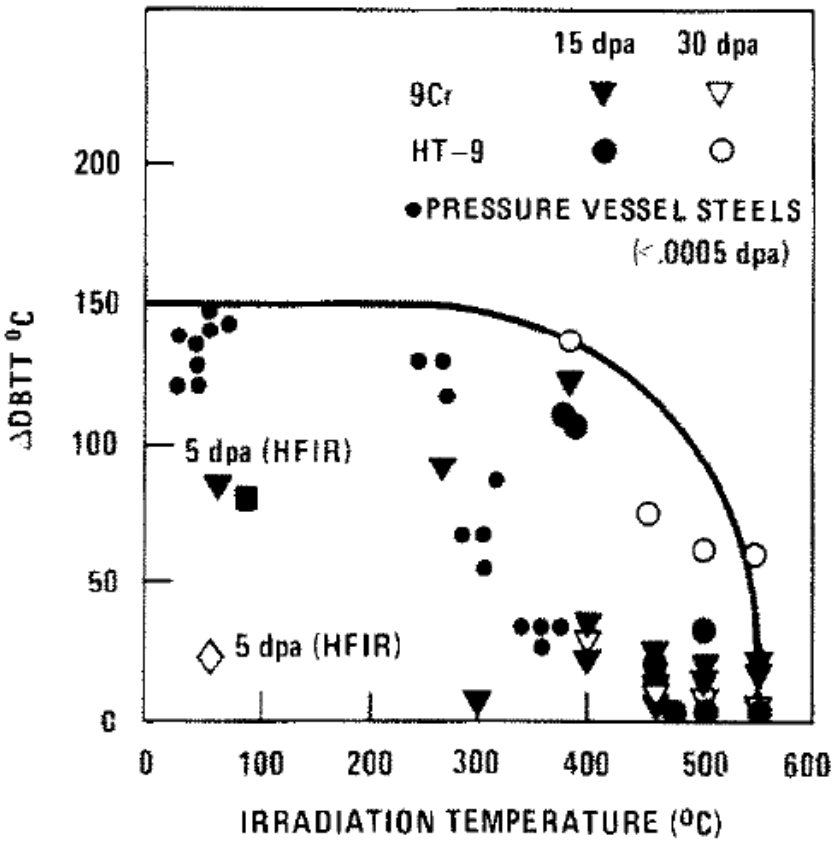

Figure 1.3: The increases in ductile-to-brittle transition temperature as a function of irradiation temperatures for 9Cr (Fe-9Cr-1MoVNb), HT9 (Fe-12Cr-1MoWV) and several pressure vessel steels [12]

In US, Sandvik HT9 (see Table 1.1 for nominal composition for all steels discussed in this chapter) has been extensively investigated during the project of Clinch River Breeder Reactor (CRBR) in 1970s. Therefore, HT9 was the reasonable first choice of structural

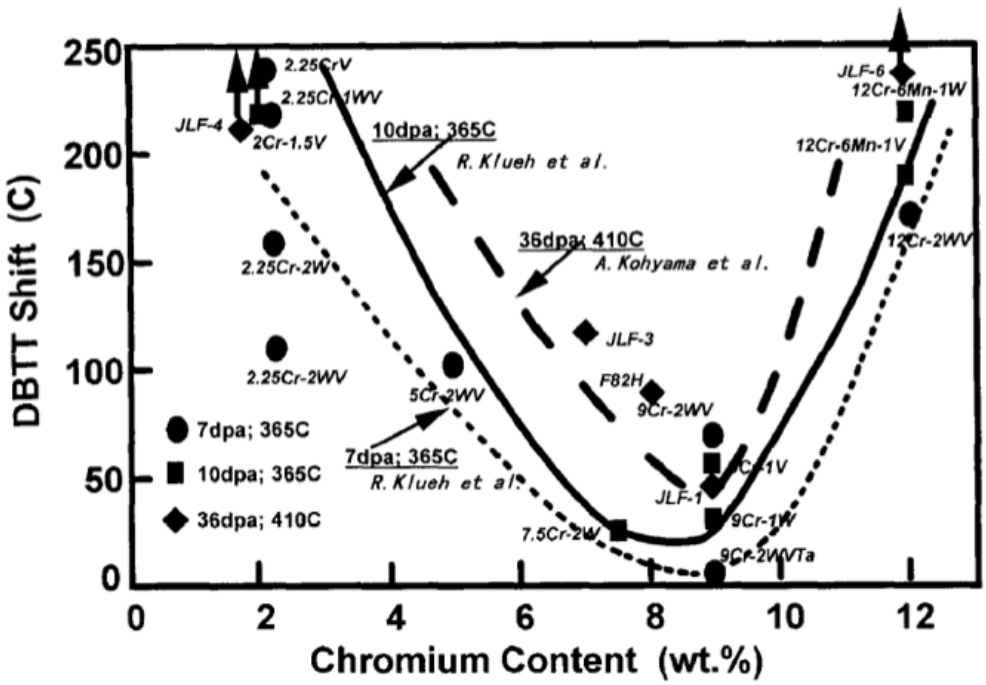

Figure 1.4: Dependence of DBTT on Chromium content of the alloy [13]

material in Gen-IV reactors. However, since the 1970s, the 9-12%Cr elevated-temperature steels have been introduced and exhibit much superior creep property compared to HT9 . These steels such as modified 9Cr-1Mo (T91) and NF616 (T92) can potentially outperform HT9 for the in-core applications in Gen-IV reactors [5].

For the US Fusion Materials Program, HT9 was the first structural material to be considered as the first wall and blanket [4]. Since mid-1980, in order to improve the safety of hands-on maintenance and operation of fusion reactors, the concept of 'low activation' or 'reduced activation' steels was introduced to the international fusion program to develop materials that would not activate or would decay quickly [14][15]. Steels of 7-9%Cr with the minimized alloying elements Mo, Nb, Ni, Cu and N were chosen for further investigation. These steels include F82H (Japan), EUROFER (Europe) and ORNL 9Cr-2WVTa (US). Lower Cr contents of 7-9% were favored over 12% in the fusion program due to the feasibility of diminishing δ-phase formation without increasing carbon and manganese content for austenite stabilization [5].

Although ferritic-martensitic steels, as a category, are already regarded as lead candidate

structural materials in both advanced fission and fusion reactor concepts, different reactor concepts need to optimize the steels (composition, fabrication process etc.) according to their specific operation window (i.e. temperature, dose exposure, corrosion etc.). For irradiation properties, neutron experiments are necessary for design guidance and for code qualification. Because these experiments are very expensive, an effort has been spent to study the irradiation response in Fe-Cr model alloys, instead of actual ferritic-martensitic steels with the aim to develop the knowledge base for irradiation-induced changes in microstructure and mechanical property. The result can be used to narrow down the parameter spectrum necessary for neutron experiments on the actual ferritic-martensitic steels, and to develop the multi-scale modeling capability [16]. In the following chapters, studies on irradiated Fe-Cr model alloys are reviewed for mechanical property (Chapter 1.2) and microstructure (Chapter 1.3).

Table 1.1: The elemental compositions (wt%) of commercial and experimental steels [5]

Steel	C	Si	Mn	Cr	Ni	Mo	W	V	Nb	B	N	Other
A533 Grade B[1]	0.25	0.2	1.30			0.60	0.50					
A508 Class 2[1]	0.25	0.30	0.75	0.30	0.75	0.60						
Mod 9Cr-1Mo (T91)	0.10	0.40	0.40	9.0	0.10	1.0		0.20	0.08		0.05	
12Cr-1MoWV (HT9)	0.20	0.40	0.60	12.0	0.50	1.0	0.50	0.25				
NF616 (T92)	0.07	0.06	0.45	9.0	0.25	0.50	1.8	0.20	0.05	0.004	0.06	
F82H	0.10	0.20	0.50	8.0				2.0	0.2		0.03	0.04Ta
EUROFER	0.11	0.05	0.50	8.5			1.0	0.25			0.025	0.08Ta
ORNL 9Cr-2WVTa	0.10	0.30	0.40	9.0			2.0	.025			0.025	0.07Ta

[1] Pressure vessel of current LWR (Gen-II))

Table 1.2: List of literature reviewed regarding the tensile properties in neutron-irradiated Fe and Fe-Cr model alloys

Cr (wt.%)	T_{irr} (°C)	Dose (dpa)	T_{test} (°C)	Ref.
Pure Fe	47	0.0075, 0.075, 0.375	47	Singh et al.(1999)[17]
Pure Fe	250	0.075, 0.225	250	Singh et al. (1999)[17]
Pure Fe	70	10^{-4},10^{-3}, 0.01, 0.79	RT	Eldrup et al. (2002)[18]
Pure Fe	300	0.026, 0.1, 0.19	RT	Verheyen et al. (2006)[19]
0, 1, 5, 10, 15	200	0.02	350-556	Suganuma et al. (1982)[20]
0, 0.1, 0.4, 2	400	0.15	RT	Okada et al. (1994)[21]
0, 0.1, 0.4, 2	425	100	RT	Okada et al. (1994)[21]
0,2,6,12,18	400	5.5-7.1	RT	Porollo et al. (1998)[22]
0, 2.5, 4, 9, 12	300	0.06, 0.6, 1.5	-160∼300	Matijasevic & Almazouzi(2008) [23]

1.2 The Irradiation-Induced Degradation in Mechanical Properties of Fe and Fe-Cr Model Alloys

The studies since 1990s on the tensile properties of irradiated Fe and Fe-Cr model alloys are summarized in Table 1.2 where T_{irr} is the irradiation temperature and T_{test} is the temperature at which the tensile tests were performed. As shown in Figure 1.5, the unirradiated pure Fe exhibited a stress-strain curve of typical bcc metal showing a initial yield drop, then Lüders band formation and finally work hardening. Irradiation at low temperature around RT causes an increase in the upper yield stress and the yield drop, and a decrease in total elongation [17][18]. In addition, the ability of work hardening was lost after irradiation.

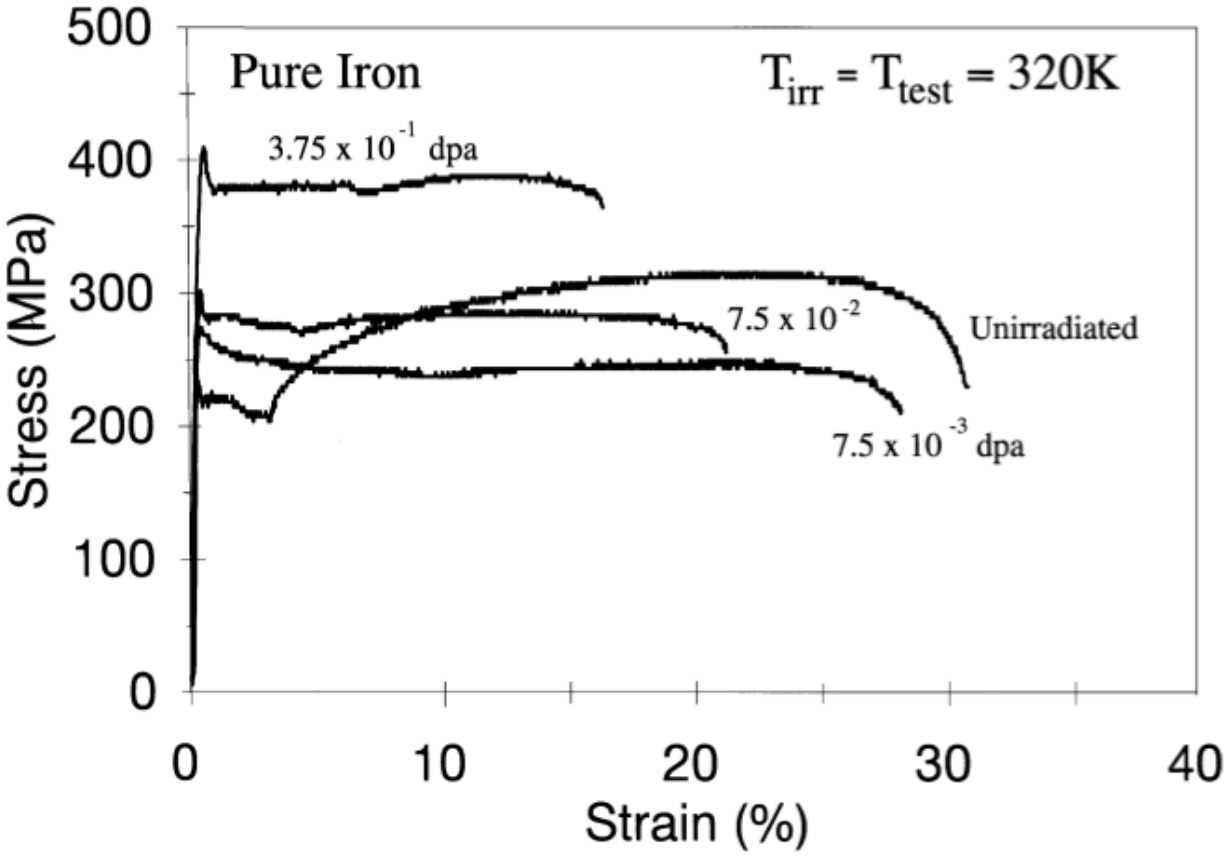

Figure 1.5: Stress-strain curve of the unirradiated and the irradiated Fe. The irradiation and tensile test temperatures were both 47° [17]

Compared to lower-temperature irradiation, higher-temperature irradiation resulted in less hardening in Fe. Figure 1.6 shows the hardening in Fe as a function of irradiation dose for

irradiation temperatures near RT and at 300°C. Up to 1 dpa, no indication of saturation in hardening was observed for near room temperature irradiation. However, some saturation for 300°C irradiation appeared in between 0.19 and 0.81 dpa. The effect of irradiation temperature on the hardening in Fe is demonstrated in Figure 1.7 where hardening data for Fe irradiated to a dose near 1 dpa for several irradiation temperatures were collected. Irradiation hardening is apparently negatively dependent on the irradiation temperature.

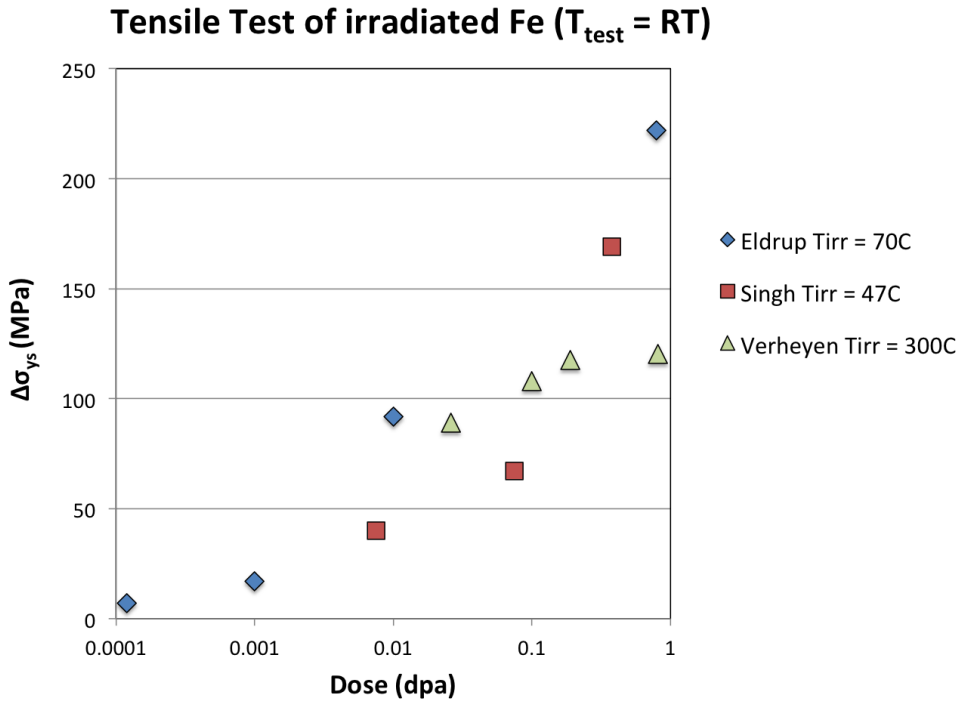

Figure 1.6: Yield strength increment as a function of irradiation dose for several irradiation temperatures. Data collected from [18][17][19][22][21].

Tensile test at higher temperature resulted in a shape change of the strain-stress curve. Figure 1.8 is the stress-strain curves of 250°C tensile tests on the unirradiated and irradiated (T_{irr} = 250°C) Fe. The unirradiated Fe exhibited lower yield strength and enhanced strain hardening, compared to lower-temperature tensile tests. Besides, there was no yield drop and Lüders strain, indicating that dislocations can escape the C and N solute atmosphere (Cottrell Theory) without much resistance at this temperature. With irradiation at 250°C, yield strength increased. In addition, a finite Lüders strain appeared again for the 0.225 dpa specimen. The reappearance of the sharp yield point and Lüders band implies that another

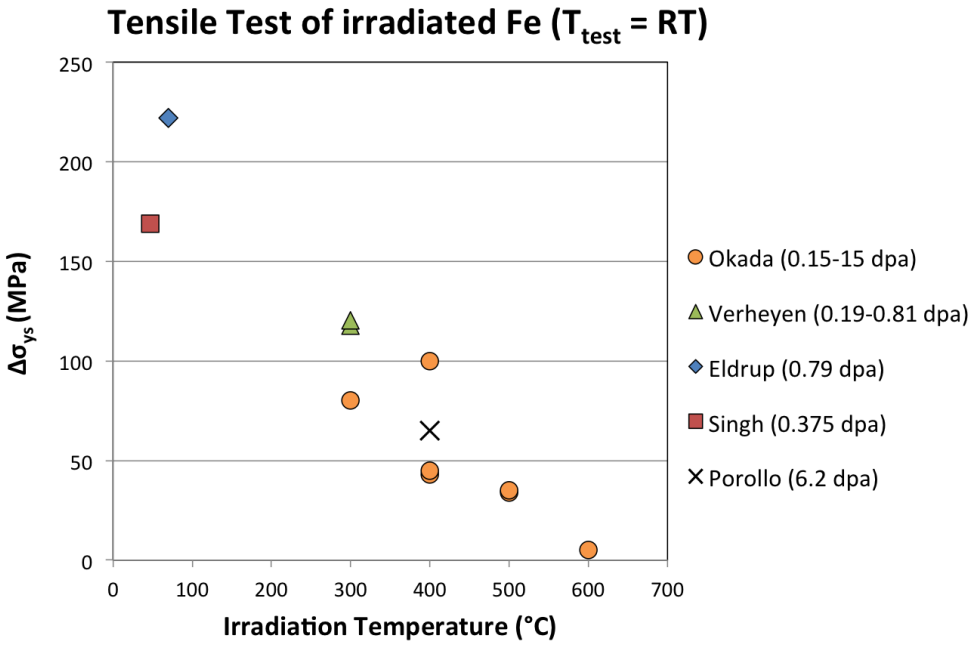

Figure 1.7: Yield strength increment as a function of irradiation temperature for a irradiation dose near 1 dpa. [18][17][19][22][24].

resistant atmosphere formed after irradiation, which are likely dislocation loops.

In Fe-Cr model alloy, the addition of Cr in Fe hardens the alloy through solution hardening. As shown in Figure The yield stress and ultimate tensile stress increases linearly with increasing Cr concentration, while the ductility decreases with increasing Cr concentration [23]. In addition, the yield drop and Lüders band gradually disappear with increasing Cr concentration.

Concerning the effect of Cr on the irradiation-hardening, it has been well established that Fe-Cr alloys harden more than Fe under the same irradiation condition [21][20][22]. Figure 1.10 shows a collection of available data in the literature about the increase in yield stress as a function of Cr concentration in irradiated Fe-Cr alloys. Earlier studies shows a monotonic increase in yield stress with increasing Cr content [22][20]. However, recent study of Matijasevic and Almazouzi [23] shows that there is subtle dependence, the so-called 'snaky' dependence, of irradiation-hardening on the Cr content. As summarized in [25], the qualitative trend is that the hardening plateaus up to 2%Cr [21], decreases with increasing Cr content until around 9% [23], and increases again with Cr content [21]. As

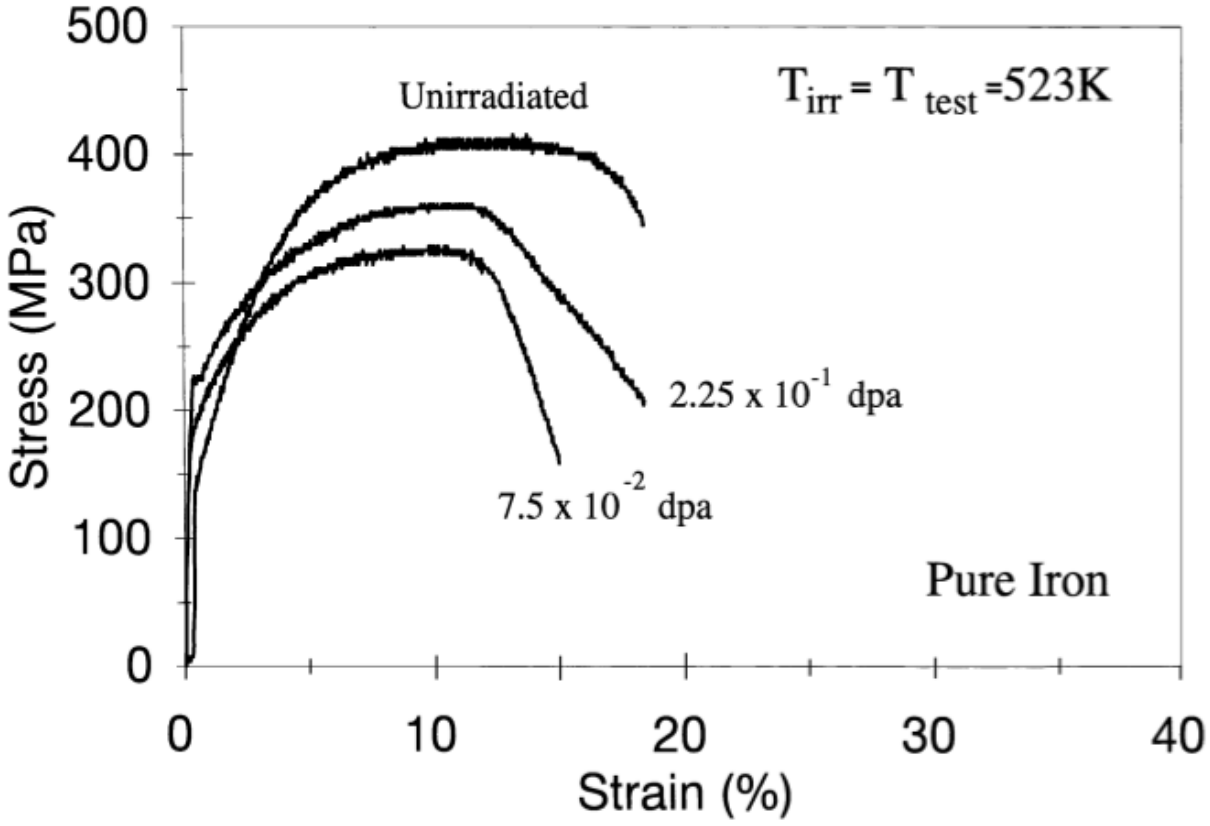

Figure 1.8: Stress-strain curve of the unirradiated and the irradiated Fe. The irradiation and tensile test temperatures were both 250° [17]

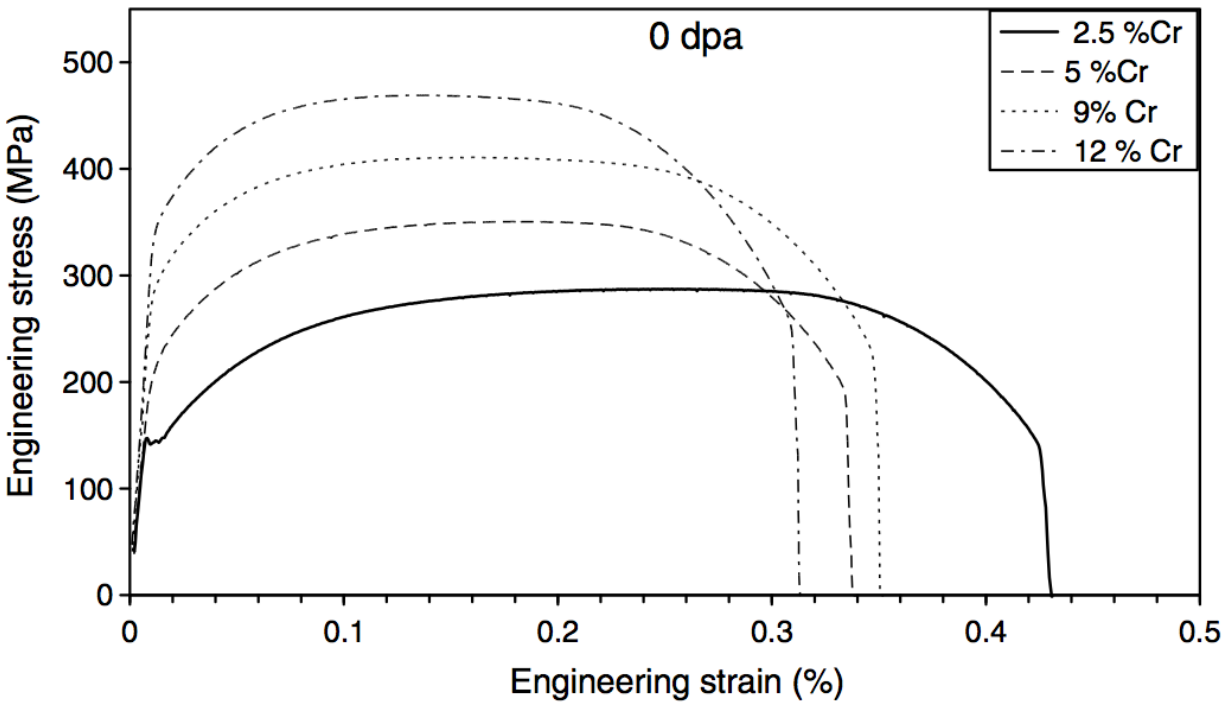

Figure 1.9: Stress-strain curve at RT of unirradiated model Fe-Cr alloys [23]

this 'snaky' dependence is consistent with the observation in the ferritic-martensitic steels (both have a minimum around 9%Cr) as shown earlier in Figure 1.4, this Cr dependence of the irradiation-induced hardening is the current prevailing opinion.

1.3 The Irradiation-Induced Microstructural Modification in Fe and Fe-Cr Model Alloys: Dependence on Irradiation Temperature and Cr Concentration

1.3.1 Dislocation loop

Neutron irradiation causes point defects, that migrate, and annihilate or cluster. Dislocation loops are one of the major cluster form contributing to the irradiation-hardening because of their ability to hinder the gliding of dislocations during deformation [25]. Table 1.3 shows a list of selected works of microstructural characterization on dislocation structure in Fe and Fe-Cr alloys irradiated with neutrons. The works on Fe will be discussed firstly then followed

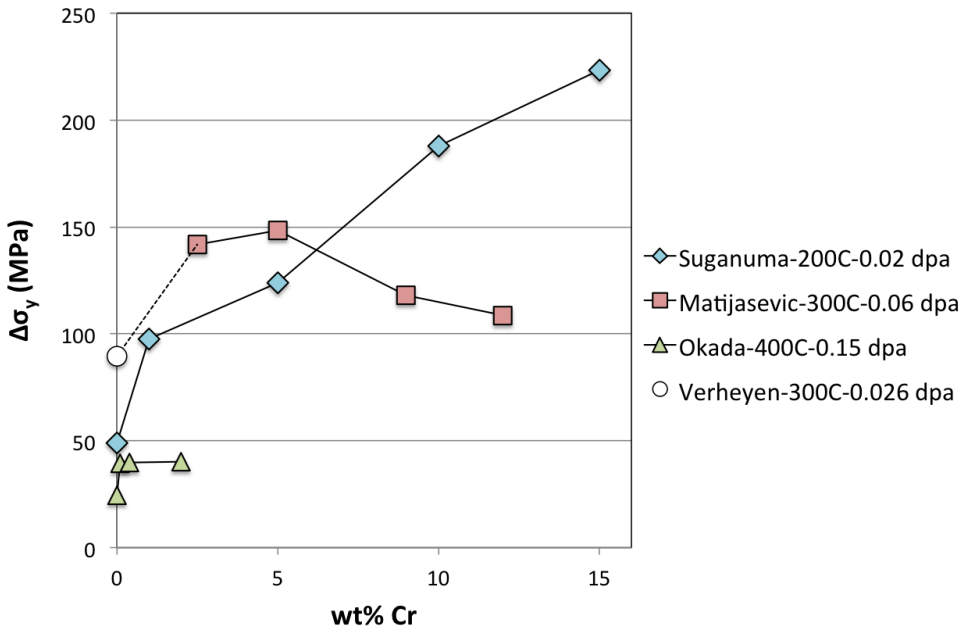

(a) Low dose $\ll$ 1 dpa

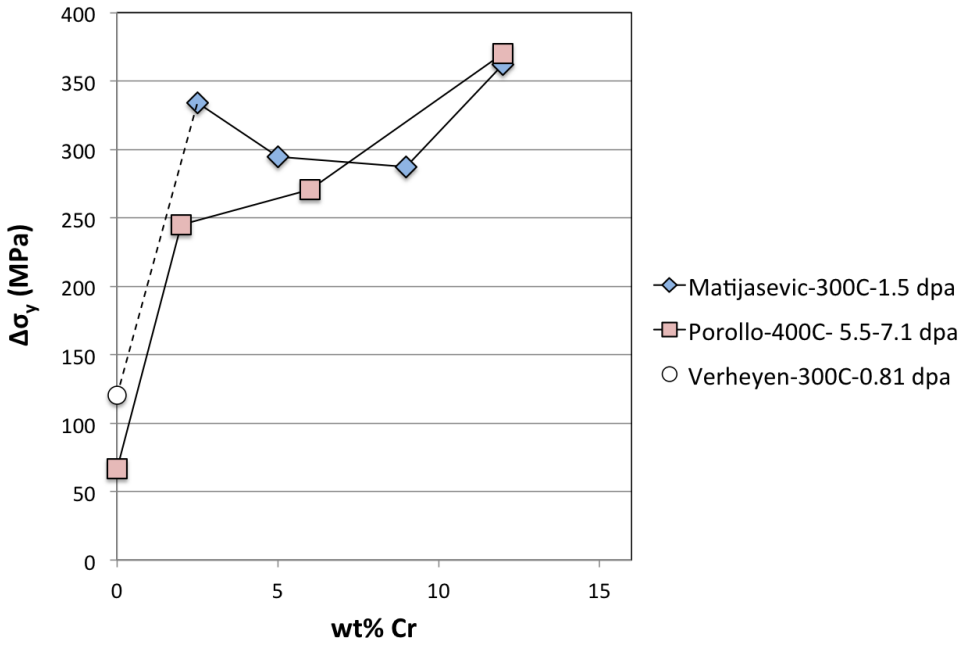

(b) High dose >1 dpa

Figure 1.10: Irradiation-induced hardening in Fe-Cr model alloys as a function of Cr concentration. The dose rate in all cases is comparable as $\sim 10^{-7}$ dpa/s. The figure is a reproduction from [25].

by Fe-Cr alloys.

Table 1.3: List of selected literatures about the characterization of dislocation loops in neutron-irradiated Fe and Fe-Cr model alloys

Cr (wt.%)	T_{irr} (°C)	Dose (dpa)	Loop Burgers vector	Ref.
Pure Fe	60	0.00071, 0.0014, 0.36	a/2⟨111⟩	Eyre & Bartlett (1965)[26]
Pure Fe	30-90	0.0029, 0.014, 0.29	a/2⟨111⟩	Bryner (1966)[27]
Pure Fe	182-740	0.51-0.98	a⟨100⟩ [1]	Horton et al. (1982)[28]
Pure Fe	80	0.0014-0.17	a/2⟨111⟩ & a⟨100⟩[2]	Robertson et al. (1982)[29]
Pure Fe	200-600	0.14-14	a⟨100⟩	Okada et al. (1991)[24]
Pure Fe	47	0.0075, 0.075, 0.375	n.d.	Singh et al.(1999)[17]
Pure Fe	280	0.06	80% a⟨100⟩ & 20% a/2⟨111⟩	Nicol et al. (2001) [30]
Pure Fe	70	10^{-4},10^{-3}, 0.01, 0.79	a/2⟨111⟩	Zinkle & Singh (2006)[31]
Pure Fe	300	0.026, 0.051, 0.1, 0.19	86% a⟨100⟩ & 10%$\frac{a}{2}$⟨111⟩	Hernández-Mayoral & Gómez-Briceño (2010) [32]
3, 6, 9, 12, 15, 18	400-450	∼ 60	a/2⟨111⟩ & a⟨100⟩[3]	Gelles (1982)[33]
0, 0.1, 0.4, 2	400	0.15	n.d.	Okada et al. (1994)[21]
3, 6, 9, 12, 15, 18	425	140	a⟨100⟩ & few a/2⟨111⟩[3]	Katoh et al. (1995) [34]
0, 2, 6, 12, 18	400	5.5-7.1	a/2⟨111⟩ & a⟨100⟩[4]	Porollo et al. (1998)[22]
0, 2, 6, 12, 18	400	∼ 26	a⟨100⟩	Konobeev et al. (2006) [35]
0, 2.5, 4, 9, 12	300	0.06, 0.6, 1.5	a/2⟨111⟩ & a⟨100⟩[5]	Matijasevic & Almazouzi(2008) [23]
0, 15	300	0.2	(Fe) 99% a⟨100⟩ & 1% a/2⟨111⟩	Matijasevic et al. (2009)[36]

n.d. not determined

[1] Burgers vector not determined for $T_{irr} \leq 253$°C. For T_{irr} = 275-300°C, some loops were determined as a⟨100⟩.

[2] Mixed but more a/2⟨111⟩ than a⟨100⟩ in overall

[3] Dislocation networks of both a/2⟨111⟩ and a⟨100⟩ exist besides loops.

[4] For Low Cr% a⟨100⟩ loops are predominant. Appearance of a/2⟨111⟩ loops increase with Cr%.

[5] Both types were observed, but the ratio was not determined.

Review of Fe

Since the pioneering work of Eyre in 1962 [37], irradiation damage in Fe has attracted research interests for more than 50 years. One of the most significant anomalies is the observation of two types of irradiation-induced interstitial dislocation loops in Fe, which exhibit Burgers vector $\mathbf{b} = a\langle 100\rangle$ or $\frac{a}{2}\langle 111\rangle$. In contrast, only $\frac{a}{2}\langle 111\rangle$ loops were exclusively observed in other irradiated bcc metals such as Mo, V, W [38][39]. The self-energy argument using isotropic elasticity indicates that $\frac{a}{2}\langle 111\rangle$ loops are energetically favored [40], therefore the origin of $a\langle 100\rangle$ loops in irradiated Fe has remained a mystery.

In despite of the continuing theoretical investigation on how $a\langle 100\rangle$ loops could have ever formed (e.g. Some of recent papers [41][42][43]), the temperature dependence of the ratio between the two Burgers vectors has been well established experimentally; higher ratio of $a\langle 100\rangle$ loops were observed at elevated irradiation temperatures. As shown in Table 1.3, for irradiations near room temperature $\frac{a}{2}\langle 111\rangle$ loops were found exclusive in [26][27][31], and predominantly in [29]. For irradiation temperature of 280°C and above, $a\langle 100\rangle$ loops become predominant [28][24][30][36]. Systematic investigations of irradiation-temperature effect on the relative occurrence between $a\langle 100\rangle$ and $\frac{a}{2}\langle 111\rangle$ loops were also confirmed by using *in-situ* heavy ion irradiations in Fe [44][45]. Figure 1.11 shows the relative fraction of interstitials in $a\langle 100\rangle$ and $\frac{a}{2}\langle 111\rangle$ loops as a function of irradiation temperature, obtained from *in-situ* TEM observations of heavy ion irradiation by Yao et al [44]. It demonstrates the increasing stability of $a\langle 100\rangle$ with increasing irradiation temperature. Although the ion irradiation results in [44] are qualitatively consistent with the neutron irradiation results, it should be noted that $a\langle 100\rangle$ loops do not become predominant until 450°C for ion irradiation while $a\langle 100\rangle$ loops are already predominant loops at 300°C for neutron irradiation. This is in agreement with that the irradiation temperature for ion irradiations need to be increased in order to match the resulting microstructure produced by neutrons [46].

The mobility of $a\langle 100\rangle$ and $a/2\langle 111\rangle$ loops are different. *In-situ* electron and heavy ion irradiations show that $a/2\langle 111\rangle$ loops are highly mobile while $a\langle 100\rangle$ loops are almost immobile [47][48]. The distinction of the mobility of the two loop types at small size would cause unique microstructural evolution and the corresponding mechanical properties. As proposed

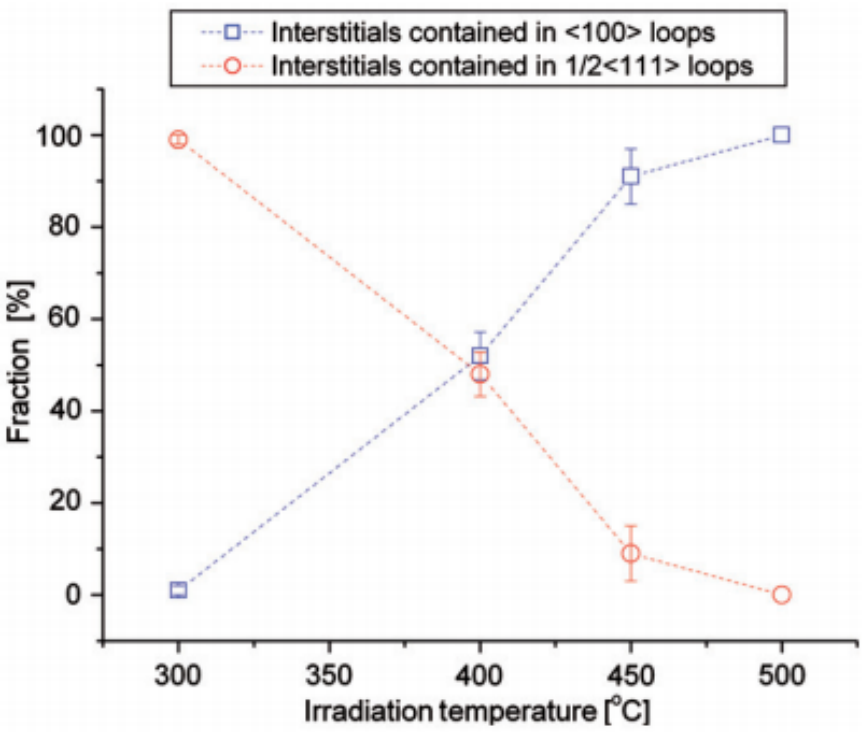

Figure 1.11: Relative fraction of interstitials in 1/2<111> and <100> dislocation loops as a function of irradiation temperatures [44]

by Xu et al. [43], a/2⟨111⟩ loops can easily migrate, and be absorbed by, permanent sinks such as dislocations and grain boundaries. As a result, they are not likely to accumulate to high density. On the other hand, a⟨100⟩ loops are immobile, and they would accumulate as stationary sinks if they form.

In addition to the Burgers vector of dislocation loops, irradiation temperature also affects the evolution and morphology of dislocation loops in irradiated Fe. The microstructure in neutron-irradiated Fe as a function of irradiation temperature can be described as follows. Irradiation at low temperature, as low as near room temperature, produced mostly highly-mobile $\frac{a}{2}\langle 111\rangle$ loops that can easily interact with nearby objects that exhibit a strain-field as they travel. Zinkle and Singh found the rafting of $\frac{a}{2}\langle 111\rangle$ loops primarily on $\{111\}$ planes and secondarily on $\{110\}$ and few on $\{100\}$ [31]. Robertson et al. observed dislocation decoration of loops with mixed Burgers vectors [29]. However, when a considerable amount of interstitial impurities (e.g. C and N) are present in Fe, the distribution of dislocation loops would become more uniform due to the high affinity of impurities to point defects and defect clusters. The phenomenon of rafting or dislocation decoration would diminish when irradiating Fe of lower purity [29][26][36].

When increasing the irradiation temperature to about 300°C, an inhomogeneous distribution of dislocation loops was still observed in some studies. Horton et al. observed dislocation decoration and equiaxed clusters of loops at T_{irr} = 182-253°C and 275-300°C, respectively [28]. Okada et al. observed higher loop density in the vicinity of grain boundaries [24]. Figure shows the TEM micrographs the raft, clusters of loops, dislocation decoration and grain boundary that has been mentioned above. Similar to RT irradiations, some study reported uniformly distributed dislocation loops [36][30], which is likely due to their impurity contents and the predominant a⟨100⟩ loops (instead of a/2⟨111⟩). Finally, for higher irradiation temperature above 400°C, a uniform distribution of immobile a⟨100⟩ loops were unambiguously observed in neutron-irradiated Fe [28][24][35][22]. For ion irradiation, rafts of dislocation loops were observed by Hernández-Mayoral et al. [49] using self-ion irradiation in Fe at RT and 300°. The decoration of dislocations in Fe have been observed by Robertson in 3.5 MeV proton irradiation [50], but have not been reported with heavy ion irradiations to the best of author's knowledge.

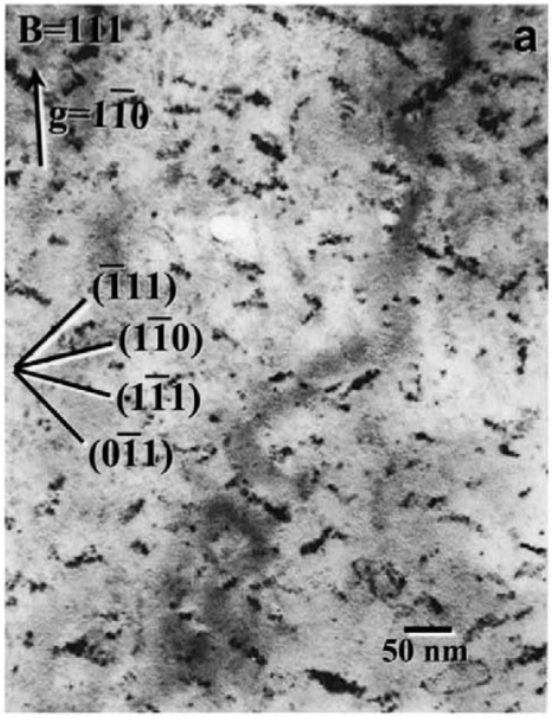

(a) Loop raft [31]

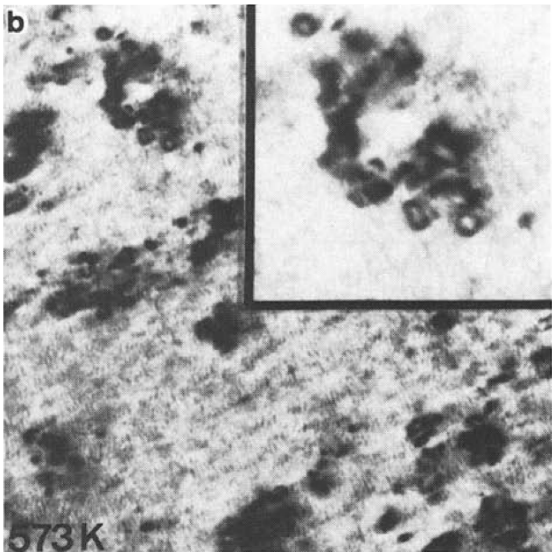

(b) Clusters of loops [28]

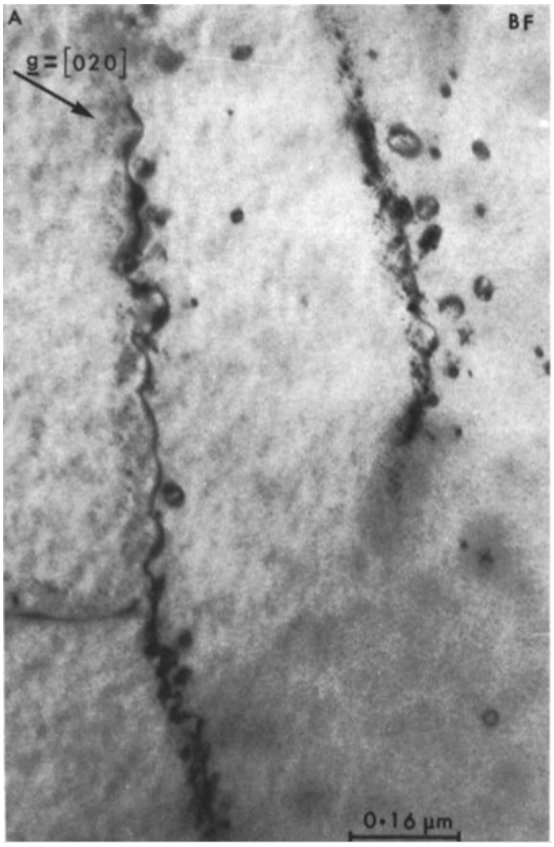

(c) Dilsocation decoration [29]

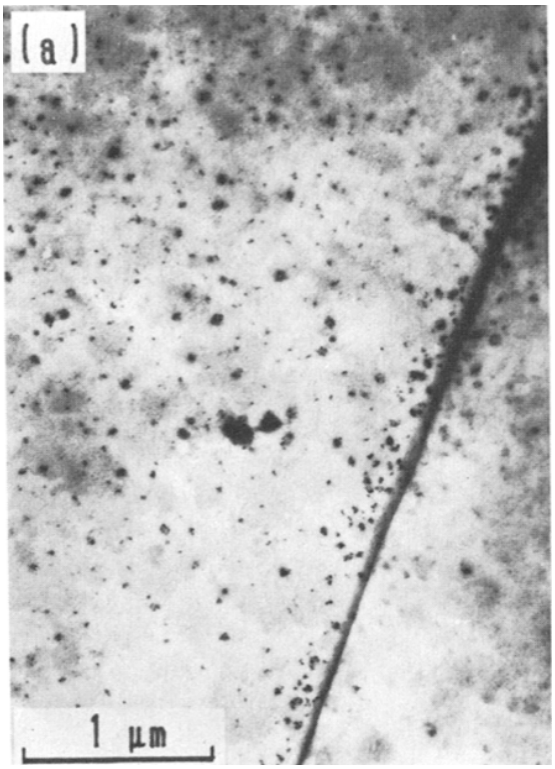

(d) Grain boundary decoration [24]

Figure 1.12: Inhomogeneous distribution of dislocation loops in neutron-irradiated Fe

Review of Fe-Cr

The Cr as a substitutional element in Fe-Cr alloy has a strong affinity to self-interstitial clusters, especially a/2⟨111⟩ loops, which would reduce the mobility of loops when they are associated [36]. *In-situ* TEM experiments employing high-voltage electron and heavy ion irradiation in Fe-Cr alloys have shown that the mobility of small a/2⟨111⟩ interstitial loops were significantly reduced in Fe-Cr alloy comparing to pure Fe [48][51][52]. Arakawa et al. further shows that this trapping effect of Cr on small loops is more pronounced at elevated temperature when Cr atoms segregate to the dislocation loops [51].

Regarding the Cr effect on the type of loops, neutron and ion irradiation shows that the addition of Cr increases the proportion of $\frac{a}{2}\langle 111\rangle$ compared to a⟨100⟩ loops [22][33][48]. However, a recent ion irradiation performed at RT [53] shows that the addition of Cr increased the fraction of a⟨100⟩ loops. Considering all these observations, the effect of Cr on the loop type should be to equalize the proportion of a⟨100⟩ and a/2⟨111⟩ loops, rather than to increase only one type of them. In general, the dependence of the their proportion as a function of Cr concentration has not be been fully established most likely due to the small size of the loops and the magnetic nature of the specimens that makes clear determination of their Burgers vector difficult [36].

The effect of Cr on the evolution (i.e. the size and density) of the irradiation-induced dislocation loops in Fe-Cr is not straightforward. Figure 1.13 summarizes the literature data about the density and size of dislocation loops as a function of the Cr concentration in Fe-Cr model alloys irradiated with neutrons. It should be noted that these TEM measurements are restricted by the TEM resolution of around 1 nm. Defect clusters with size smaller than the resolution limit were not detected and not measured. That is, the densities and sizes were underestimated and overestimated, respectively. Because of the variation in irradiation temperature and irradiation dose between individual studies, it is not easy to make direct comparison and to deduce a correlation.

As shown in Figure 1.13(a), a dramatic drop in mean loop size with increasing Cr content was unambiguously observed for 0-2%Cr [22][35][21]. Beyond 2%Cr, this dependence is much weaker. Porollo et al. [22] shows that the loop size does not depend on the Cr contents when

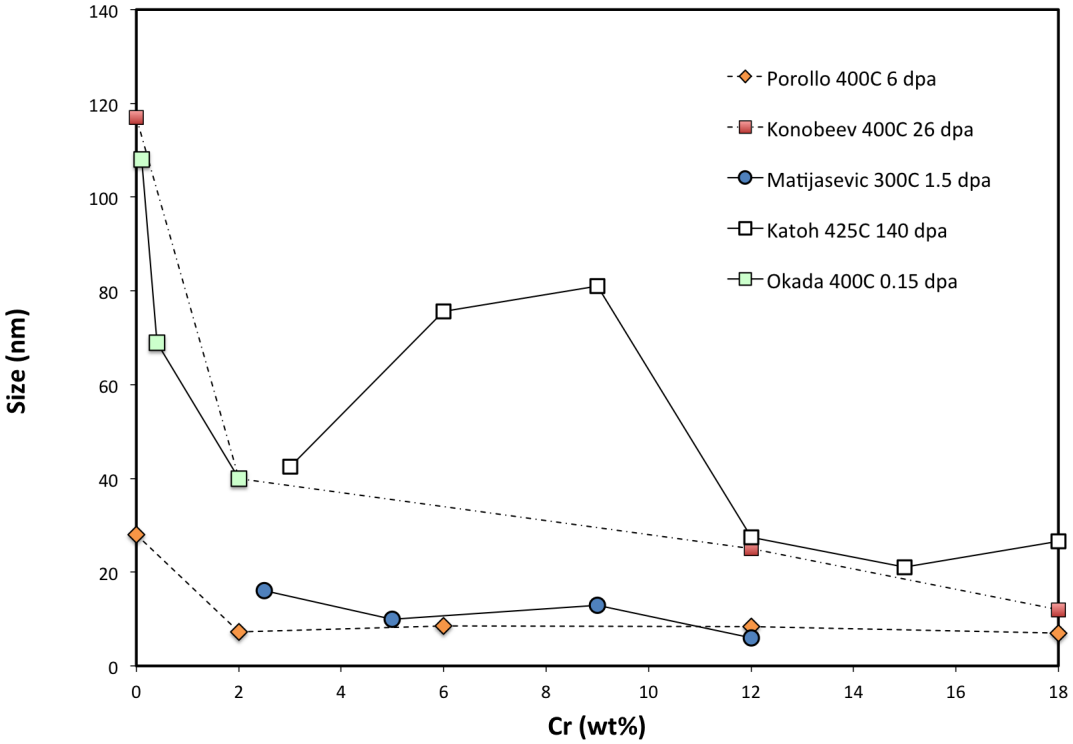

(a) Loop size vs. Cr content

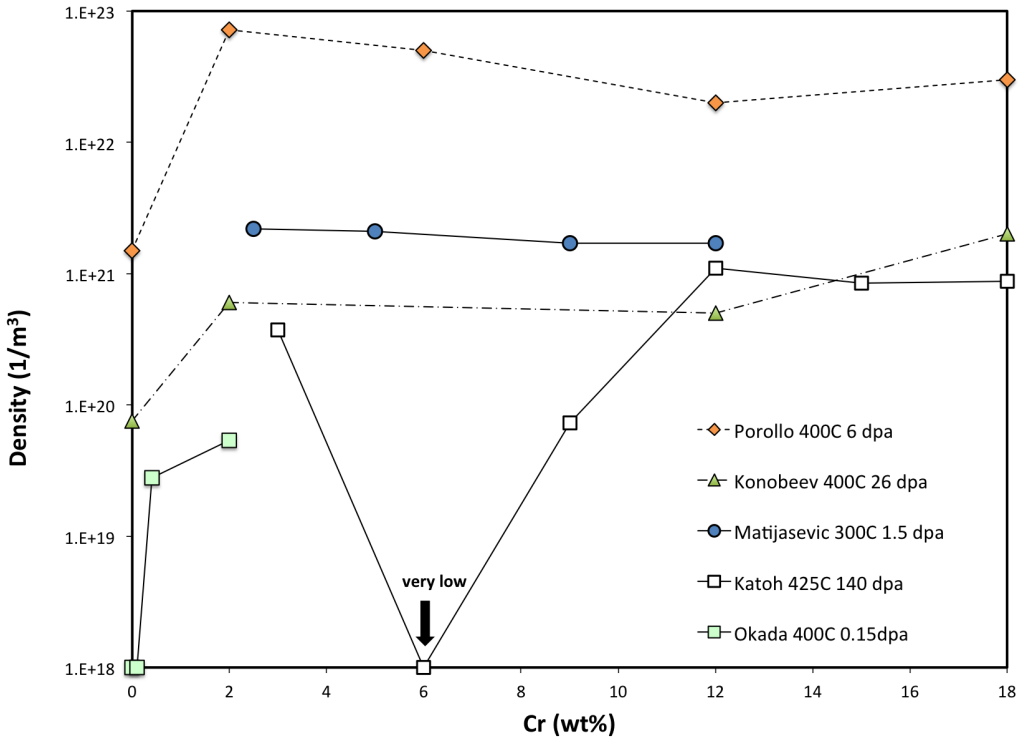

(b) Loop density vs. Cr content

Figure 1.13: A summary of the mean loop size and density as a function of the Cr content in Fe-Cr model alloys irradiated with neutrons. Data collected from literatures shown in Table 1.3

Cr contents is more than 2%. Other studies [23][35] indicate that the loop size continues to decrease with increasing Cr contents. A high dose (140 dpa) study by Katoh et al. [34] shows, however, that the loop size is strongly dependent on Cr concentration and a local maximum was observed for 9%Cr. Although the lower-dose studies of 1.5 dpa [23] and 6 dpa [22] also show a local maximum around 9%Cr, the magnitude of size variation in these studies is too small (<3 nm) to be an evident early stage of the local maximum of loop size.

Figure 1.13(b) is the corresponding loop density measurement as a function of Cr contents in irradiated Fe-Cr model alloys. Similar to the loop size, the loop density increases significantly with increasing Cr concentration from 0 to about 2% [21][22][23]. Beyond that, the loop density remains fairly constant with Cr content[35], except for the work of Katoh et al. [34] where a significcant drop in loop density at 6%Cr was observed.

The addition of Cr and interstial impurities such as C and N increases the threshold dose to form visible dislocation loops in TEM [48][29][36]. This might be due to the smaller loop size with increasing Cr. In addition, enhanced recombination due to suppressed mobility of interstitial loops by Cr or C and N atoms was suggested to attribute to this delay [36][54].

Finally, dislocation decoration, as was discussed earlier in the Fe section, was also observed in Fe-Cr alloys. Matijasevic et al. [23] found dislocation decoration in all of the irradiated Fe-Cr alloys (2.5-12%Cr). In addition, they observed that high Cr alloys contain more loops located at the dislocation lines than the low Cr alloys.

1.3.2 α' Precipitate

Under service conditions in next-generation nuclear reactors, ferritic alloys are unstable or metastable against phase separations. The σ phase is one of the hazardous phases that causes embrittlement and alter the corrosion resistance of ferritic alloys. However, the σ phase precipitates typically between 600 °C and 1000 °C and its production below this temperature is very sluggish [55][56].

The Cr-enriched α' phase is another important phase affecting the mechanical properties in ferritic alloys. The α' phase shares the same bcc lattice with the original δ ferrite and its counter-part α phase with a slight misfit in lattice constant (0.2886 nm for α and 0.2885 nm

for α') and a higher chromium concentration. Bonny et al. [57] proposed an Fe-Cr phase diagram (shown in Figure 1.14) according to reported radioactive experiments, indicating a solubility limit at about 9% Cr in the temperatures between 300 K and 700 K at the Fe-rich side. Bonny et al. assumed that the irradiation accelerated the precipitation process, but not induced it. This assumption was criticized by Xiong et al. [58] who stated that the phase diagram in [57] only presents the steady state under irradiation, and not the true equilibrium state. Nevertheless, this phase diagram is currently the most updated one, and it is useful since this study is also about irradiation experiments.

In addition, at this temperature range, the Fe-Cr alloy has been shown to undergo a transition of short range order (SRO) at about 10% Cr, which is also close to the phase boundary at 9% Cr in Figure 1.14 [59]. Using neutron scattering, Figure 1.15 demonstrates that Cr atoms are short-range-ordered and are intending to repel each other when Cr $<$ 10%. On the other hand, when Cr $>$ 10%, Cr atoms attract each other and tend to cluster. At 10%, Cr distribution in Fe is absolutely random. The explanation of this inversion of the sign of SRO was given recently by DFT calculations. Several DFT studies showed that the mixing enthalpy of random or quasi-random Fe-Cr alloys exhibit a critical Cr concentration that change signs above and below it, which provides the observation of the inversion of SRO a interpretation based on electron band and magnetic property [60][61][62].

There are two mechanisms to precipitate α' phase. One is nucleation-and-growth, and the other is spinodal decomposition. Depending on the chromium concentration, the α' phase would precipitate preferably through one mechanism over the other. When chromium concentration is less than about 30% [63], there is an energy barrier to overcome for phase transformation, and therefore it will undergo the nucleation-and-growth process. When chromium concentration is more than about 30%, the phase separation will occur through spinodal decomposition. Different from the nucleation-and-growth process, spinodal decomposition does not have thermodynamic barriers, leading to a quite distinguished morphology often called the mottled structure or the moderated structure.

Despite of the importance of spinodal decomposition on the mechanical property degradation in ferritic alloys, the chromium concentration of materials involved in this study is less 20% and only nucleation-and-growth process is expected. Therefore, spinodal decomposition

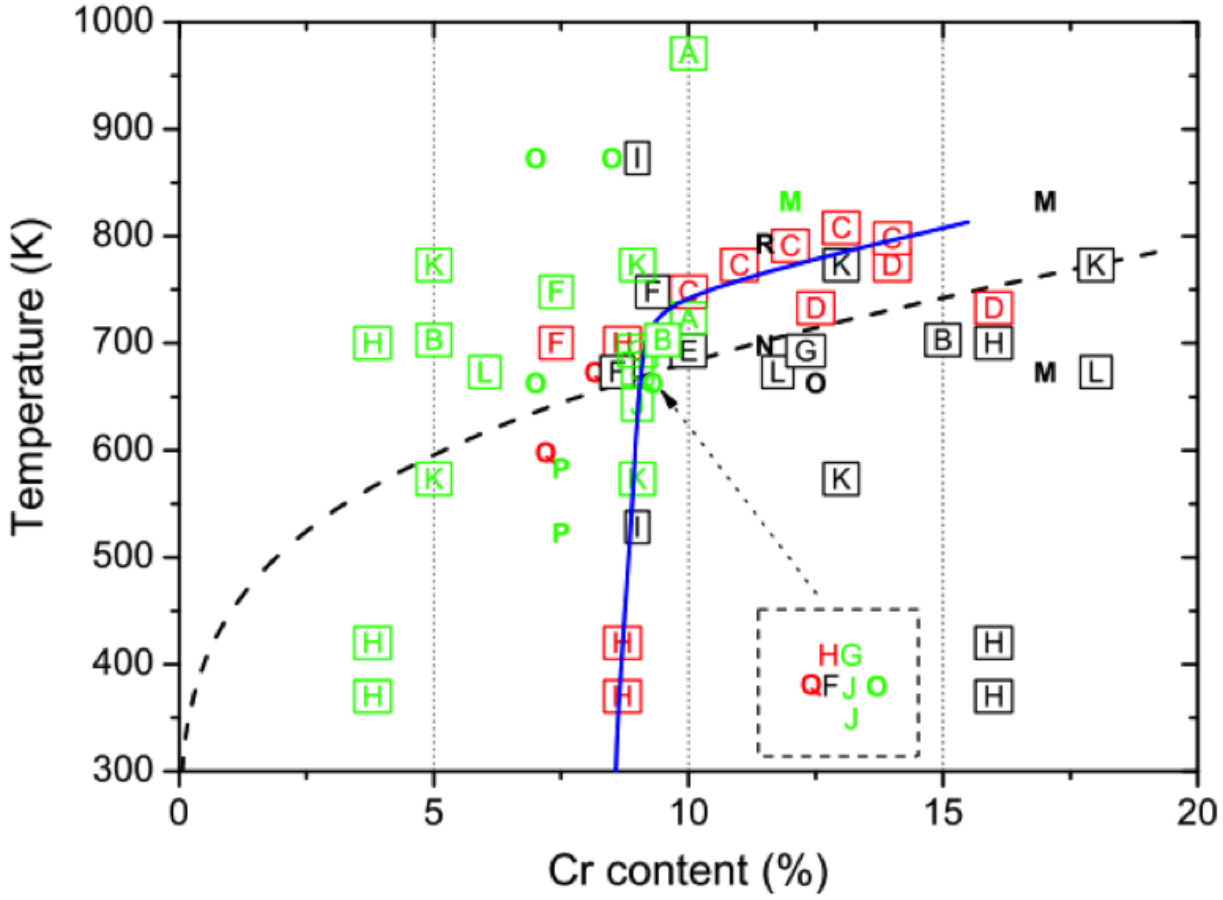

Figure 1.14: The Fe-rich portion of the Fe-Cr binary phase diagram. The dashed line is the phase boundary of the conventional Fe-Cr phase diagram. The blue line is the updated phase boundary deduced from modern experimental data. The data points are indicated with colors and letters. The green indicates Cr ordering. The black indicates precipitation. The red indicate phase boundary. The letters is to indicate the original source of the data. See ref. [57] for details.

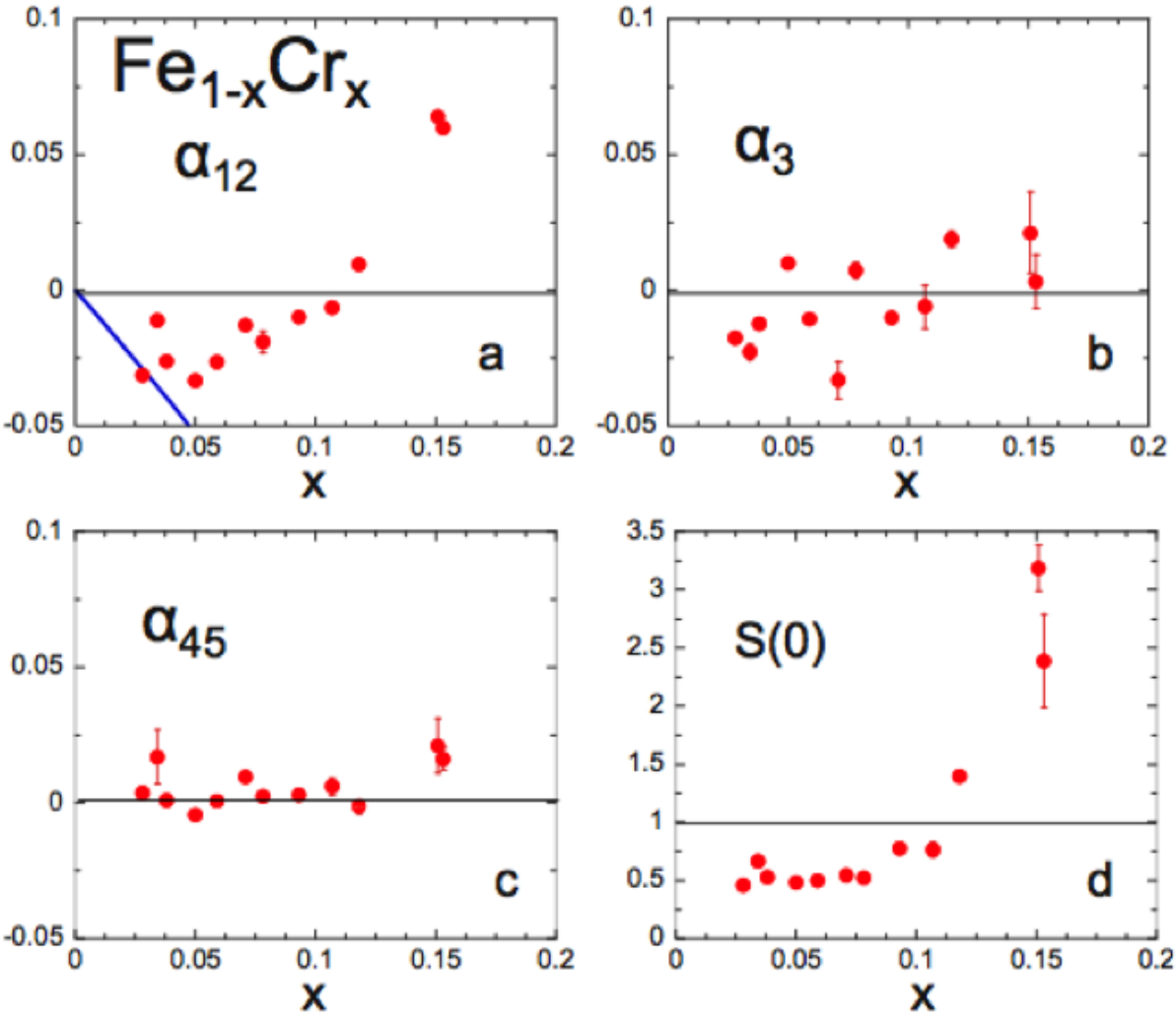

Figure 1.15: The SRO parameters α_i (vertical axis) as a function of concentration x (horizontal axis) in the bcc $Fe_{1-x}Cr_x$ alloys. (a) Average parameter for the first two neighbor shells; the thick blue line is the curve corresponding to maximal repulsion between Cr atoms; (b) third shell; (c) 4-5 shells; (d) calculated value of the short range ordered function at k = 0 [59]

will not be a major focus in this study.

The α' phase precipitation in ferritic alloys as a result of aging has been extensively studied in the duplex stainless steels (austenite and ferrite) due to their wide applications in the coolant piping in nuclear reactors [64][65][66][67]. Besides, the aging effects in Fe-Cr model alloys have also been investigated as the surrogates for the more complicated ferritic alloys [68][69]. Most of the studies exclusively focus on the aging effects in between 300 °C and 500 °C because little irradiation dose in the coolant system would be anticipated.

Atom Probe Examination on α' phase precipitation

Because of the little misfit in lattice constant between α and α' phases and the tiny mass difference between iron(56) and chromium(52), it has been proven difficult to study this phenomenon with a conventional TEM or an analytical TEM [68]. Instead, atom probe have been shown to be the best tool for this field.

Two types of α' phase morphologies were being observed after long-term aging: interconnected percolated network and isolated islands. The interconnected network morphology has been observed in several aging experiments by Miller et al. at 500 °C for 500 hours in Fe-24%, 32% and 45%Cr bcc models alloys [56][69][70], where the 45% Cr case is shown in Figure 1.16 and 1.17. On the other hand, the isolated island morphology was found in Fe-17 and 19%Cr alloys for similar aging conditions [56][70], where the field ion image of this kind of morphology is shown in Figure 1.18.

Because the interconnected percolated structures were thought to be resistant to coarsening and spheroidization (due to the observations that the interconnected structure is stable even after long-term heat treatment at 470 °C for 10800 hours [56].), Miller et al. believed that the different volume fractions of the α' phases for Fe-Cr alloys with different chromium contents caused the distinct morphologies being observed [56].

However, a recent atom probe study showed that the coarsening and the spheroidization of the α' phase did occur in the ferritic part of a duplex stainless steel with a chromium content of about 20% under similar aging conditions (as shown in Figure 1.19 [64]). This observation obviously contradicts the observations and arguments by Miller et al., therefore

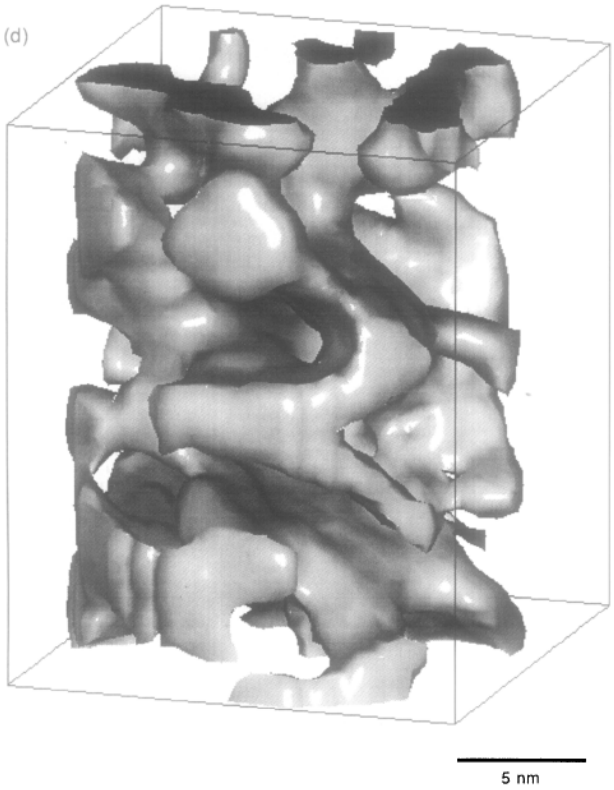

Figure 1.16: The 40%Cr lsosurface reconstructions from PoSAP analyses showing the Cr-enriched regions of a Fe-45%Cr alloy aged at 500 °C for 500 hours [69]

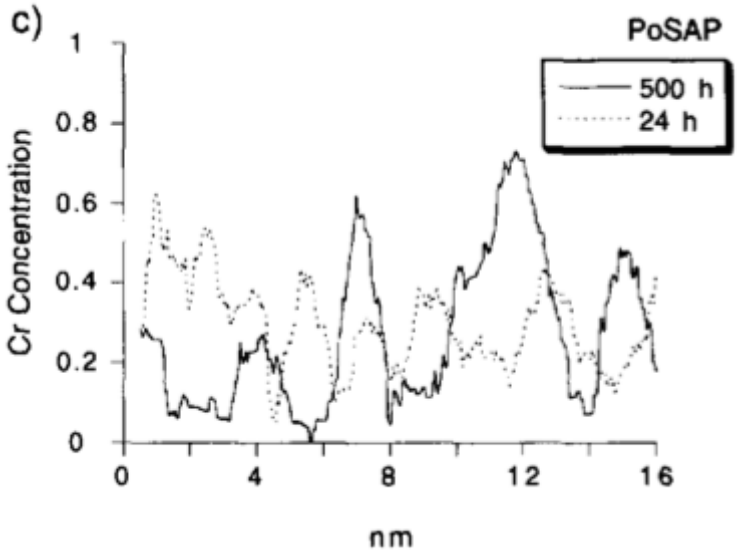

Figure 1.17: Composition profiles for two Fe-45%Cr alloys thermally aged for 24 and 500 h [69]

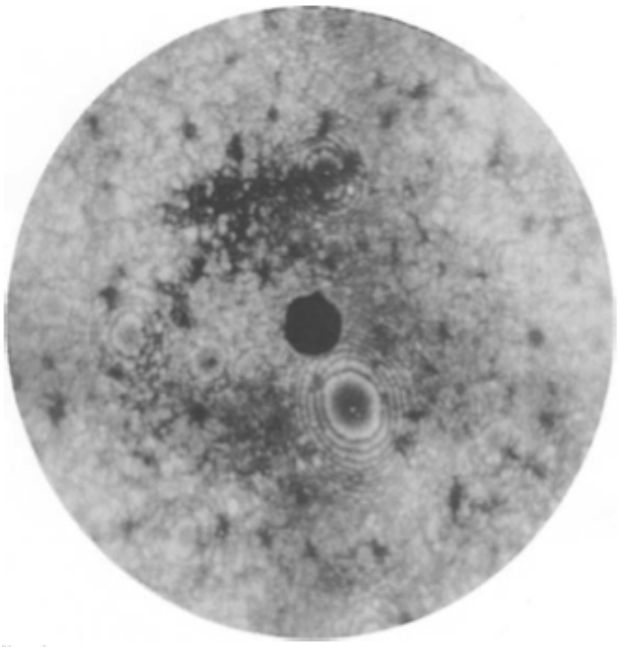

Figure 1.18: The field ion image of Fe-19%Cr alloy aged at 500 °C for 500 hours, demonstrating the isolated island structures of the darker imaging α' phase [56]

a further investigation would be required.

Neutron-Irradiation-Enhanced α' phase precipitation

The irradiation-enhanced α' phase precipitation (spinodal decomposition type) was examined by Miller et al. by comparing neutron-irradiated Fe-32%Cr model alloys at 290 °C to a dose of 0.03 dpa with another Fe-32%Cr specimen aged at 290 °C for the same duration [56]. As shown in Figure 1.20(a) and in Figure 1.20(b), the isolated islands of α' phase evidently appear in the specimen with neutron irradiation. However, no phase segregation could be found in the one without being irradiated (aged only).

Because the average size of α' islands in the neutron-irradiated Fe-32%Cr at 290 °C is about three to four times larger than Fe-19%Cr aged at 500 °C, it indicates that the radiation has significantly increased the diffusivity possibly as a result of the availability of extra vacancies caused by cascades [56]. In spite of the plausible correlation between the cascades and the α' islands, Miller et al. intended not to link one α' islands with a single cascade directly based on the discrepancy in the observed number densities of the two.

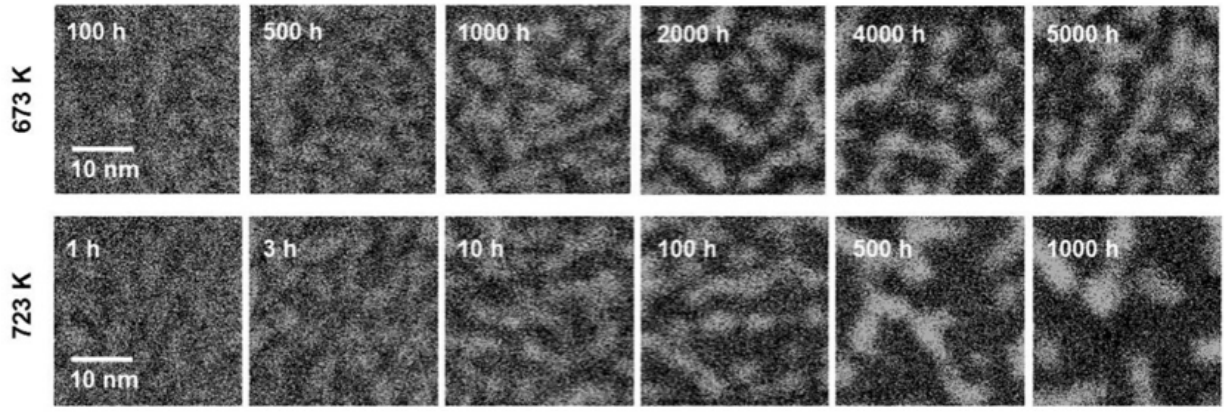

Figure 1.19: Chromium maps in the ferrite phase in as-quenched and aged duplex stainless steel. Each bright dot represent a single chromium atom. The thickness of the maps normal to the paper is 5 nm [64].

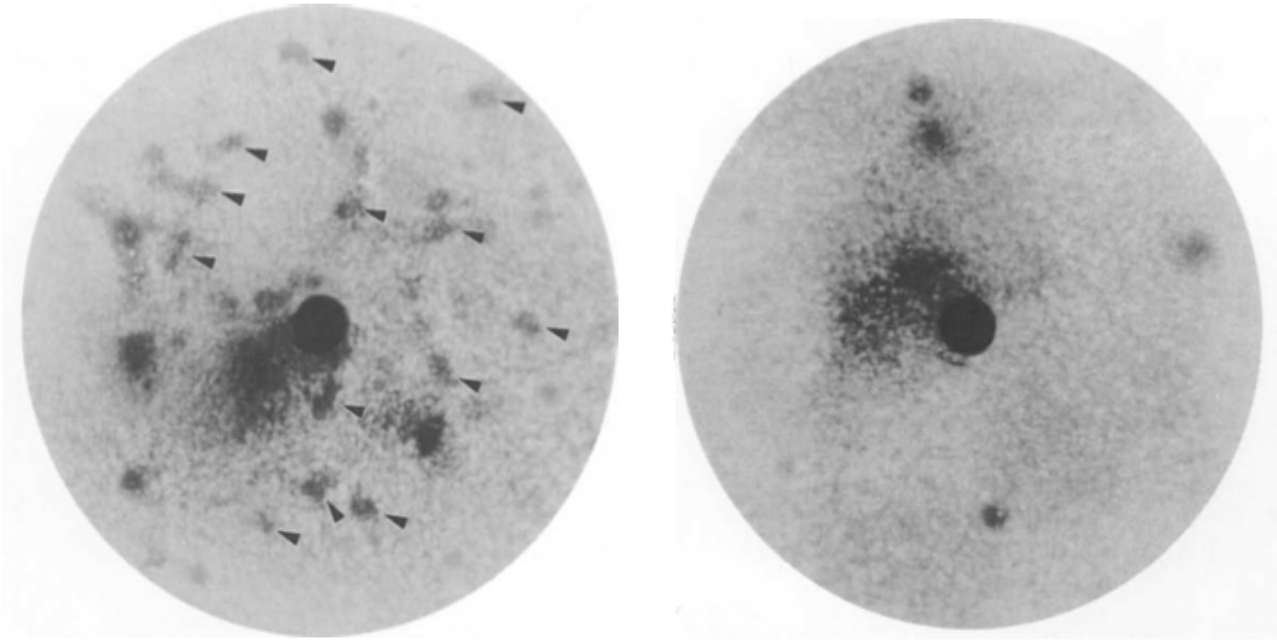

(a) With neutron irradiation

(b) Without neutron irradiation

Figure 1.20: Field evaporation micrograph of the microstructure of the Fe-32%Cr model alloys (a) being neutron-irradiated at 290 °C and (b) being thermally aged for 2150 hours at the same temperature. [56].

1.3.3 Void

The superior swelling resistance to irradiation is one of the advantages of the ferritic-martensitic steels over the austenitic steels. The swelling results from the formation of voids, the three-dimensional agglomeration of vacancies. Garner et al. [71] showed that ferritic-martensitic steels have a much longer transient regimes prior the beginning of the steady-state swelling than the austenitic steels. Also, the steady-state swelling rate is smaller ($\sim$0.2%/dpa) for ferritic-martensitic steels than for austenitic steels ($\sim$1%/dpa).

The irradiation-induced swelling in Fe-Cr model alloys is strongly affected by the Cr concentration, irradiation temperature. Figure 1.21 shows the void formation in Fe and Fe-12Cr model alloys irradiated with neutron at 400°C to about 6 dpa. The voids formation was significantly suppressed in Fe-12Cr comparing to Fe. However, the dependence of void swelling on the Cr content in Fe-Cr alloys is not simply monotonic, and not entirely consistent between studies. Little and Stow [72] showed that the first 1%Cr addition in Fe significantly suppressed the swelling after neutron irradiation to 30 dpa, as shown in Figure 1.22(a). Porollo et al. [22] and Konobeev et al. [35] studied Fe and Fe-Cr up to 18%Cr irradiated with neutron at 400° to $\sim$6 dpa and $\sim$26 dpa, and showed that the formation of voids were mainly suppressed by the presence of Cr, as shown in Figure 1.22(c). The swelling is about one order of magnitude less in in Fe-Cr than in Fe [16].

Other data [71][33][34], however, showed that shortly after about 3%Cr, the swelling increases with increasing Cr until a local maximum around 10%Cr as shown in Figure 1.22(b). This phenomenon of local maximum swelling is more pronounced at very high doses of 140 [34] and 200 dpa [73]. Garner et al. [71] suggested that the Cr affects the duration of incubation that is shortest at about 10%Cr. The formation of α' was thought to be associated with the second reduction in swelling in higher Cr [74].

In addition to Cr concentration, swelling is also dependent on the irradiation temperature; irradiation-induced swelling in Fe and Fe-Cr alloys peaks at $\sim$400°C [28][75][72]. Figure 1.22(d) shows the irradiation temperature dependence of the void swelling in Fe at $\sim$1 dpa. Similar observation of maximum swelling at temperature in between 400°C to 450°C can be found in Little and Stow [72].The decline of swelling beyond $\sim$500°C is due to the onset

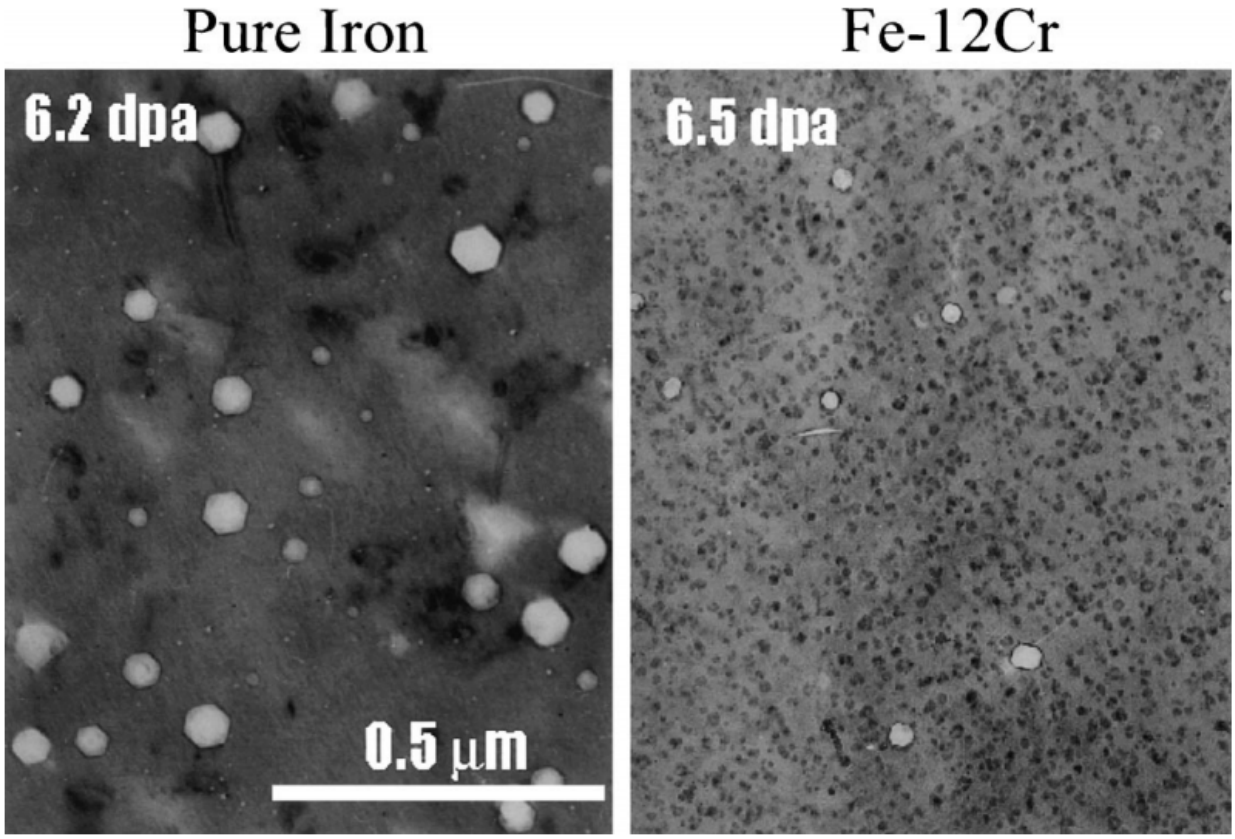

Figure 1.21: Microstructure of Fe and Fe12Cr model alloy irradiated at 400 $\sim$ to 6 dpa. The bright faceted contrasts are bubbles. The smaller dark contrasts in Fe-12Cr were suggested to be α' precipitates [22]

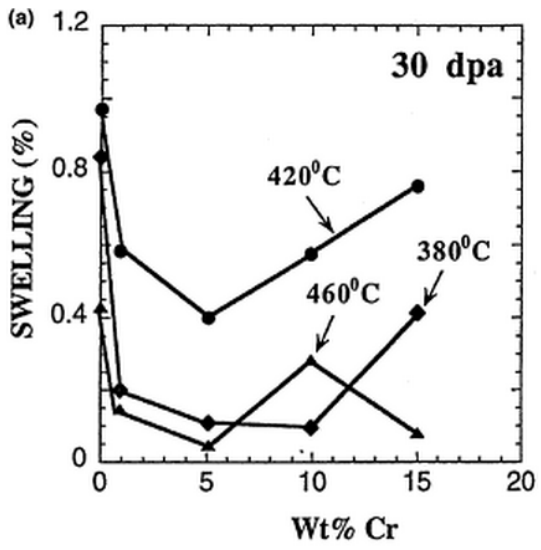

(a) Cr effects on swelling in Fe showing the suppression of swelling after the first addition of 1-5%Cr [72]

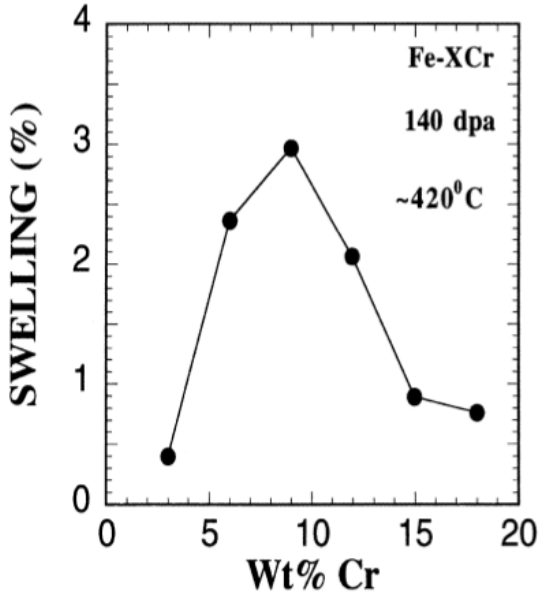

(b) Cr effects on swelling in Fe showing the swelling peaks at ∼10%Cr [72]

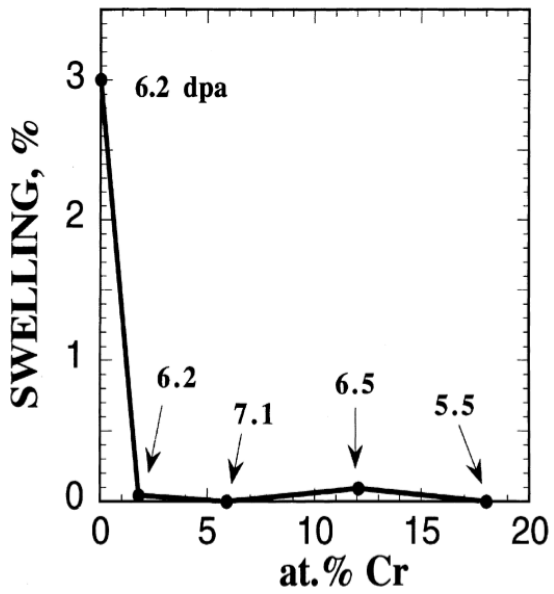

(c) Cr effects on swelling in Fe showing the universal swelling suppression with Cr addition [22]

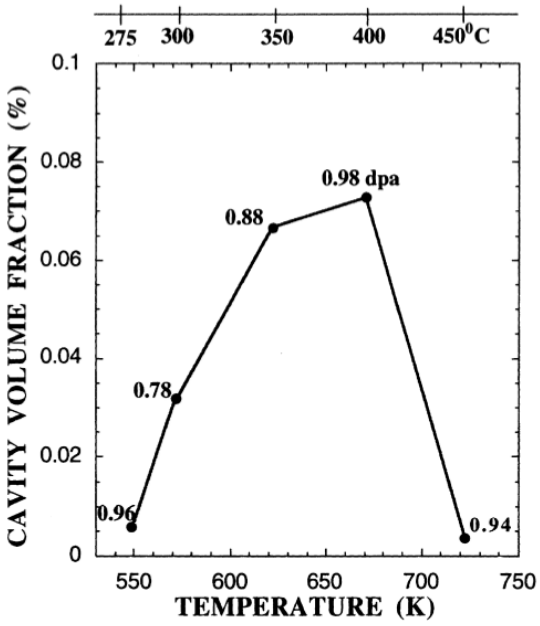

(d) Temperature dependence of swelling in Fe [75]

Figure 1.22: The effect of Cr concentration on the irradiation-induced swelling in ferritic Fe-Cr alloys irradiated by neutron to doses of (a)30 dpa (b) 140 dpa and (c) $\sim$ 1 dpa at various temperatures [71]. The sub-figure (d) shows the irradiation temperature effects.

of voids dissociation (Stage IV) [76]. Garner et al. [71] suggests that there is possibly dependence of the duration of the transient regime on the irradiation temperature.

1.4 Motivation and Objectives

Ferritic-martensitic steels are long recognized to exhibit superior resistance to radiation effect, such as swelling and damage accumulation, especially compared to the austenitic steels, Fe based alloys with a face-centered-cubic (fcc) structure [77][78][71]. For these reasons, ferritic-martensitic steels are lead candidate for the structural materials of core-internals in Gen-IV nuclear reactors and several core components of fusion reactor designs. However, long-term neutron exposure will unavoidably degrade their properties and reduce their capabilities to hold applied loads. Therefore, a precise knowledge about their response to neutron irradiation is required to guide the reactor design. In addition, the composition should be optimized to achieve most desirable performance.

Although, the research in radiation damage in ferritic-martensitic steels has spanned more than half an century, the knowledge of their radiation property is still far from complete. The complication is most likely due to their highly non-monotonic behavior under irradiation (both microstructure and mechanical property) as a function of Cr contents. For instance, one of the peculiarity is the inversion of short-range order at about 10%Cr in Fe-Cr. Its origin can be explained with DFT calculations, however how to correlate the irradiation-induced DBTT shift (ex. Figure 1.4) with SRO in terms of the microstructure has not been established, although being speculated about by almost every paper coming across this issue.

The formation of α' phase is long known to be one of the major contributor to the irradiation-induced hardening in high Cr Fe-Cr alloys. However, it is not until recently that the atom probe tomography became widely available to provide quantitative and relevant measurements on the irradiation-enhanced α' phase formation in irradiated Fe-Cr alloys. It is therefore beneficial to take this advantage of this advance in microscopy capability to provide new information that could not be acquired before.

The objective of this study is to use bcc Fe-Cr model alloys as the surrogates to investigate the radiation damage in ferritic-martensitic steels by conducting a coordinated set of

experiments with post-irradiation examination and analysis that provide significant insight into the irradiation performance of ferritic-martensitic steels for advanced nuclear reactor applications. In addition, this study aims to provide useful data for the use in the benchmark of atomic-level modeling.

This study fully characterizes the qualitative and quantitative evolution of the damage microstructures in Fe-Cr model alloys as a function of irradiation doses, chromium levels and irradiation temperatures. The mechanical properties are evaluated and correlated to the corresponding microstructure.

CHAPTER 2

EXPERIMENTAL THEORY AND TECHNIQUES

This work involves irradiation experiments and post-irradiation examinations using microscopy and specialized testing techniques. This chapter describes the specimen specification (Chapter 2.1), irradiation experiments (Chapter 2.2), transmission electron microscopy (TEM) and TEM data analysis techniques (Chapter 2.3), atom probe tomography (APT) introduction and APT data analysis techniques (Chapter 2.4), and the introduction of hardness measurement (Chapter 2.5).

2.1 Sample Description

Fe polycrystals, Fe-10Cr polycrystals and Fe-Cr single crystals were irradiated and characterized in this study. Their chemical composition, initial dislocation density (before irradiation) and grain size are summarized in Table 2.1 and Table 2.2.

Fe polycrystalline specimens were provided by Goodfellow Corporation as a bar of 10 mm diameter and 25 mm length. As shown in Figure 2.1, the grain size is small (2.7 μm in average). The initial dislocation density of the Fe specimens were estimated by measuring the Fe specimens irradiated at 300°C to 0.01 dpa. The obtained density is $1.4\times10^{14}\frac{1}{m^2}$ (Chapter 3.1.4), which is significantly higher than the Fe-Cr model alloys. Although the unirradiated Fe specimens was not measured, their dislocation density should be close to this value because of the low dose (0.01 dpa) and low irradiation temperature (300°C). Even if a certain degree of irradiation-annealing had indeed occurred, this value would then represent the lower limit of the dislocation density in the unirradiated Fe.

The Fe-10Cr poly-crystals was manufactured by Carpenter. The Cr concentration is 9.65 at% so Fe-10Cr is named. No noticeable deviation on chemical composition between irradi-

Table 2.1: The elemental compositions (at%), initial dislocation density before irradiation and grain size of the Fe and Fe-Cr model alloys

	Fe polycrystals	Fe-10Cr polycrystals	Fe-Cr single-crystals
Element	Goodfellow[1]	Carpenter[2]	APT[3]
Cr	<0.000002	9.65	10-16 [4]
C		0.023	<0.09
Mn	0.00001	<0.01	<0.02
Si	<0.00001	<0.02	
P		<0.009	
S			
Ni	<0.000005		
Mo		<0.006	
Cu	<0.000005	<0.009	
Co			
Al	<0.000005	<0.021	
N		0.006	<0.04
V			<0.02
Ag	<0.000005		
Ca	<0.00008		
Mg	0.000002		
Fe	bal.	bal.	bal.
Dislocation Density $\left(\frac{1}{m^2}\right)$	$\sim 1.1\times10^{14}$	1.3×10^{13}	3.5×10^{12}
Grain size (μm)	2.7	181	-

[1] Goodfellow - analysis was conducted by the manufacturing company.
[2] Carpenter - analysis was conducted by the manufacturing company.
[3] APT - analysis was conducted by APT in CAES facility
[4] Cr concentration varies from specimen to specimen. See Table 2.2 .

Table 2.2: Chromium concentration in Fe-Cr single crystalline specimens (at%)

Irradiation Condition	Cr content (APT[1])
No irradiation (archive)	13.67
300°C-0.01dpa	13.95
300°C-0.1dpa	10.02
300°C-1dpa	16.03
450°C-0.01dpa	14.14
450°C-0.1dpa	14.18
450°C-1dpa	12.93

[1] APT - analysis was conducted by APT in CAES facility

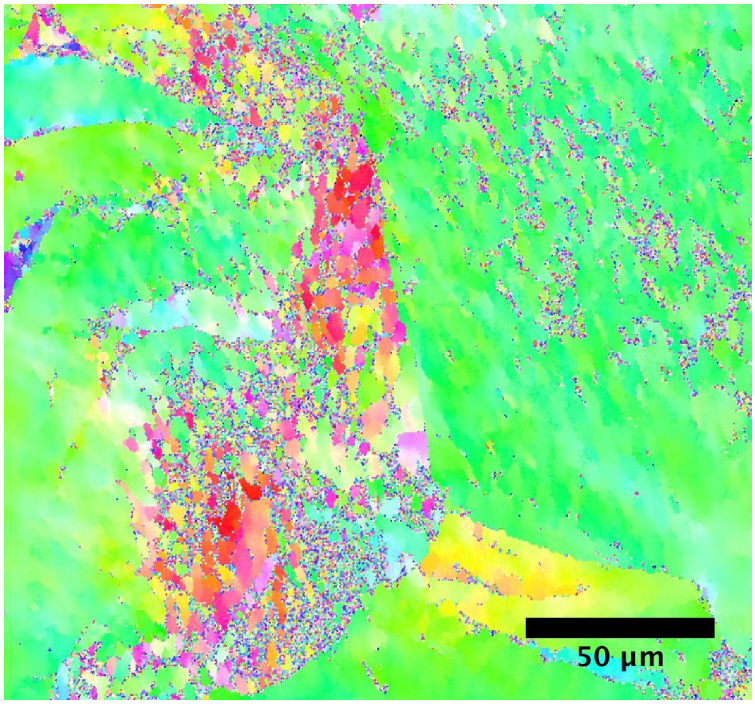

Figure 2.1: The EBSD image of an un-irradiated Fe.

ated Fe-10Cr specimens was observed. Figure 2.2 shows the EBSD image of the un-irradiated Fe-10Cr specimen. The average grain size estimated with EBSD is 181 μm. The dislocation density in un-irradiated Fe-10Cr measured with TEM is 1.6×10^{23} $\frac{1}{m^2}$.

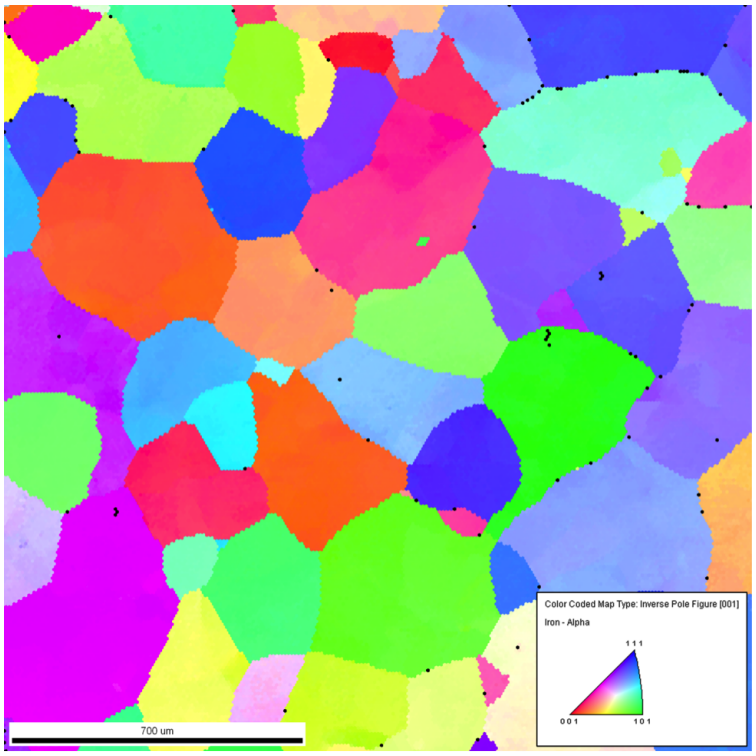

Figure 2.2: The EBSD image of an un-irradiated Fe-10Cr at the lower right shows the color maps of the grain orientations.

The single-crystal Fe-Cr specimens were provided by Los Alamos National Laboratory and were fabricated using the Czochralski growth. Although the nominal Cr concentration is 14 at%, during the growth process, Cr was lost through evaporation, resulting in a crystal with decreasing Cr concentration along its length. The specimens were taken from cross-sectional slices of the original bar material (Figure 2.3.) and, therefore, had different Cr concentrations. The Cr concentration was, however, homogeneous inside individual specimens. Table 2.2 summarizes the Cr contents measured with atom probe and the corresponding irradiation conditions of all of Fe-Cr single crystal specimens. The dislocation density in the un-irradiated Fe-Cr single crystal specimen is 3.2×10^{12} $\frac{1}{m^2}$, which is the lowest among the three specimen categories.

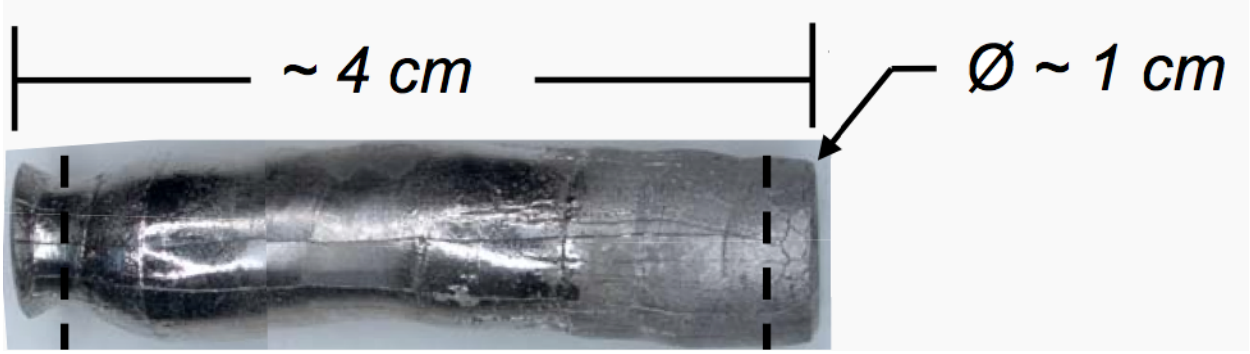

Figure 2.3: As-received Fe-Cr single crystal bar. *Picture courtesy to Stuart Maloy and Andy Nelson.*

2.2 Reactor Irradiations

In this section, some aspects of the irradiation experiments are described. The specimens to be irradiated were prepared in University of Illinois with the rest of the specimens of the ATR-NSUF-University of Illinois Project [79]. Then, the specimens were encapsulated in Idaho National Laboratory. Two types of capsules were used. The 1 dpa specimens were encapsulated in 2.0 inch capsules in the form of a drop-in containment vessel suitable for A-11 position of the Advanced Test Reactor (ATR). The 0.1 dpa and 0.01 dpa specimens were encapsulated in capsules fabricated in the form of drop-in with spacers to position the specimen capsule in the center of the standard Ti test capsules for B-7 position of ATR (rabbit system). The A-11 position require capsules to stay in reactor during the entire cycle, so it is used for high dose irradiation. On the other hand, B-7 position could be inserted and withdrawn during the cycle, and it could be used for low dose irradiation. Figure 2.4 is the schismatic diagram of the reactor core structure of ATR showing the A and B positions.

The irradiation in ATR began in the summer of 2009. Target irradiation dose was achieved by loading specimen capsules in desired axial location of the reactor for desired period of time. The design (location and duration) was based on the neutronic and thermal-hydraulic calculations. The irradiation temperature was controlled by adjusting the He/Ar mixture of the capsule. SiC temperature rod and melt wire was implemented in the capsules to provide actual irradiation temperature information. Unfortunately, these information was not available before the completion of this dissertation. Table 2.3 summarized the irradiation

parameters.

Table 2.3: Parameters of the irradiation conditions in ATR

Target Dose (dpa) [1]	1	0.1	0.01
Reactor Location	A-11	B-7	B-7
Duration in Reactor	1 cycle $\sim$ 49 days	$\sim$ 10 day	$\sim$ 1 days
Location from the Core Midplane	35 cm	0	0
Fast Neutron Flux ($\frac{n}{cm^2 \cdot s}$) (E>1 MeV)	1.7×10^{14}	8.1×10^{13}	8.1×10^{13}
Thermal Neutron Flux ($\frac{n}{cm^2 \cdot s}$)	2.3×10^{14}	n/a	n/a
%He / %Ar	85/15 (T_{irr} = 300°C)	n/a	n/a
	50/50 (T_{irr} = 450°C)	n/a	n/a

[1] Dose in dpa was estimated using conversion of 7×10^{20} $\frac{n}{cm^2}$ per dpa in stainless steel

2.3 Transmission Electron Microscopy (TEM)

Transmission electron microscopy (TEM) was used to characterize the irradiation-induced dislocation loops and voids. The resolution limit of TEM prevents it from resolving defect clusters of a size less than 0.5 nm [31]. Therefore, other characterization technique such as positron annihilation spectroscopy (PAS), small-angle neutron scattering (SANS) or X-ray diffuse scattering is used to study these very small defect clusters. However, the use of those techniques is beyond the scope of this study. Only defect clusters with a size larger than TEM resolving power are characterized. Besides, Energy-dispersive X-ray spectroscopy (EDS) equipped in a TEM was used, in addition to the atom probe, to verify the chemical composition of the specimens.

Chapter 2.3.1 describes the procedure of the TEM specimen preparation. Chapter 2.3.2 describes the basic operation of a TEM and the imaging techniques used to resolve defect clusters. In order to acquire the density of defect clusters, it is necessary to estimate the

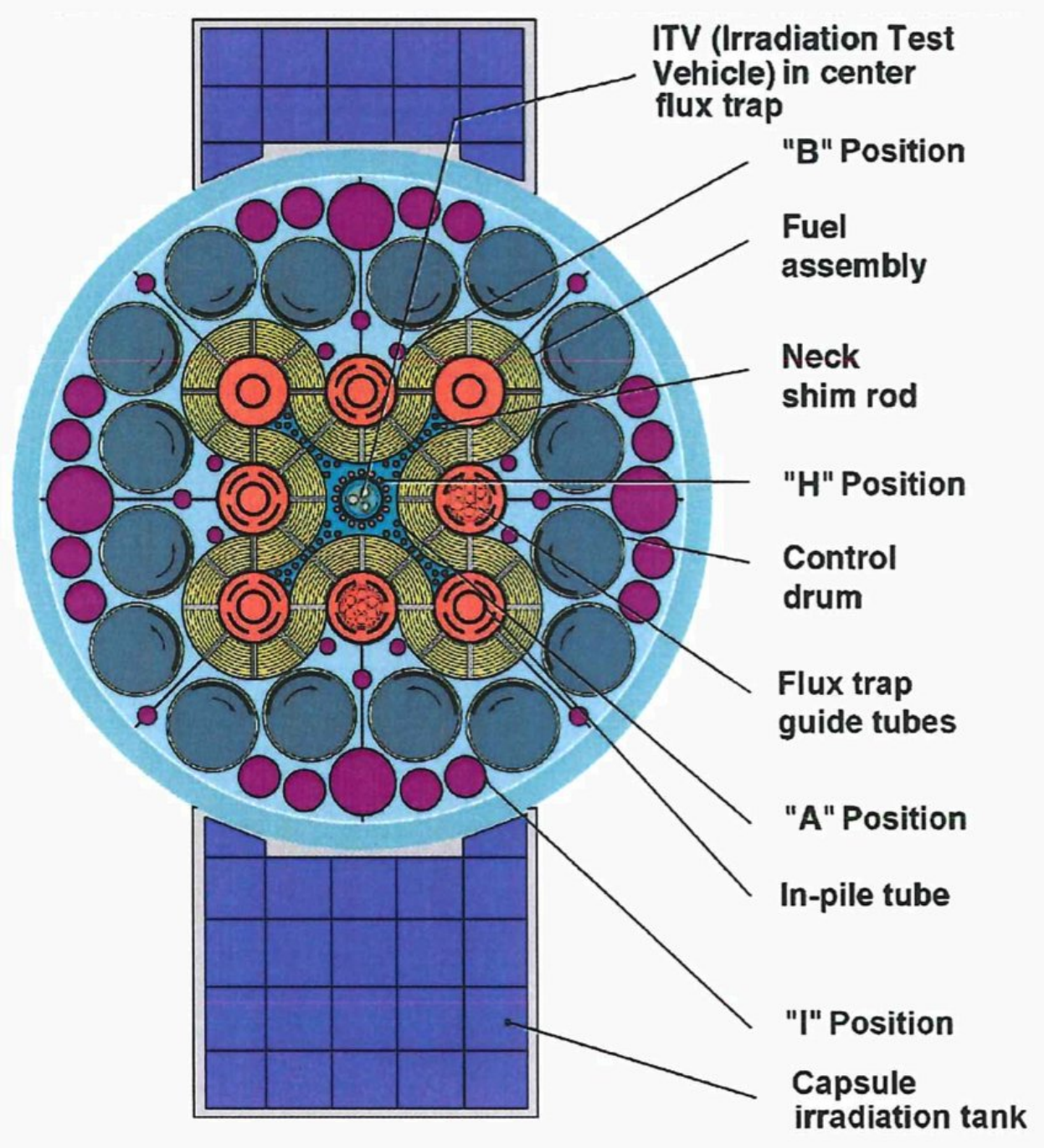

Figure 2.4: A schematic diagram of the core structure of the Advanced Test Reactor

thickness of the TEM foil being examined. Chapter Chapter 2.3.3 describes the methodology used to obtain the density of line dislocations and defect clusters.

2.3.1 TEM specimen preparation

TEM requires electron transparent specimens with a typical thickness around 100 nm, depending on the electron accelerating voltage and the specimens. Higher accelerating voltage and lower element mass number (of the specimen) increase the foil thickness for electron transparency. There are several techniques to prepare TEM specimens, including ion milling (ion milling machine and focused ion beam) and jet-polishing. The disadvantage of ion milling specimens for TEM is the radiation damage produced during the process. The artifact produced by the FIB is discussed in Chapter 3.1.6 with an TEM example shown in Figure 3.15. Especially when the irradiation dose is low, the size of the defect clusters induced by the neutron and by the ions might be indiscernible. In order to avoid possible confusion, jet-polishing (electro-polishing) is used to prepare the TEM specimens in this study. The principle of jet-polishing is to achieve a applied voltage at which "the current due to anodic dissolution of the specimen creates a polished surface rather than etching or pitting [80]". Jet-polishing can only be utilized for electrically-conductive specimens like metals and alloys.

2.3 diameter mm discs were punched from the large 9 mm disc and mechanically thinned with 2400 grit SiC paper down to around 80 μm in the Electron Microscopy Laboratory (EML) at INL. 2.3 mm instead of the standard 3 mm was used in order to reduce the magnetic nature of the specimens. Following mechanical polishing, TEM discs were jet-polished with a SouthBay Model 550 Single jet-polishing unit (performed jet-polishing from both sides) with electrolyte of 5% perchloric acid ($HClO_4$) in 95% methanol (CH_3OH) at -30 to -40°C. The polishing time required to perforation was around 1 min. Jet-polishing was performed in EML at INL and in the LAMBDA (Low Activation Material Design and Analysis) lab at ORNL.

In the very early stage of this study, sulfuric acid were used instead of perchloric acid as the electrolyte. The success rate and the quality was poor. Only two Fe-Cr single crystal

specimens (Fe-14Cr irradiated at 450°C to 0.01 and 0.1 dpa) were prepared with reasonable quality with sulfuric electrolyte. The rest of specimens were all prepared with perchloric electrolyte.

Ideally, specimens should be introduced into a TEM directly after they are jet-polished. However, due to the rad nature of the specimens, it is not practical to do so. Multiple specimens were polished in one session, and then were stored until a TEM was available. In average, the specimens were examined one week after they were polished. The jet-polished specimens were stored in a vacuum desiccator (0.1 mTorr), methanol or dehydrated ethanol before being introduced into a TEM in order to minimize oxidation. We found that storing specimens in methanol or dehydrated ethanol is more effective than in a 0.1 mTorr vacuum desiccator. This is especially important for Fe specimens as it is notoriously vulnerable to oxidation. For Fe-Cr alloys, they were more resistant to oxidation. Their quality and the success rate were in general better than the Fe specimens.

2.3.2 Basics of TEM and imaging conditions

A basic TEM consists of electron source, an assembly of magnetic lenses and the imaging device all arranged in a vertical column vacuumed to a pressure of about 10^{-7} or less. A coherent electron beam generated at the electron source is accelerated by the applied voltage and is constrained and aligned by the magnetic field while it travels through the column. Normal accelerating voltage is 200 kV and 300 kV. Higher voltage of 300 kV gives higher electron penetration and better resolution. However, the downside is the higher possibility of electrons displacing atoms and causing radiation damage. As shown in Figure 2.5, assuming a displacement energy E_d of 40 eV, the displacement threshold energy E_{th} is 640 keV, which is well above the 300 keV. In addition, the threshold for Frenkel pair production in Fe was reported to be 330 kV by Maury et al. [81], which is still above the 300 kV although the margin reduced. In this study, no observable radiation damages (production of visible loops and voids) were induced by 300 keV electrons during TEM examinations.

The electron beam passes through, interacting with the specimen thin foil as it transmits and forming images as it is focused onto a fluorescent screen or a charged-coupled device

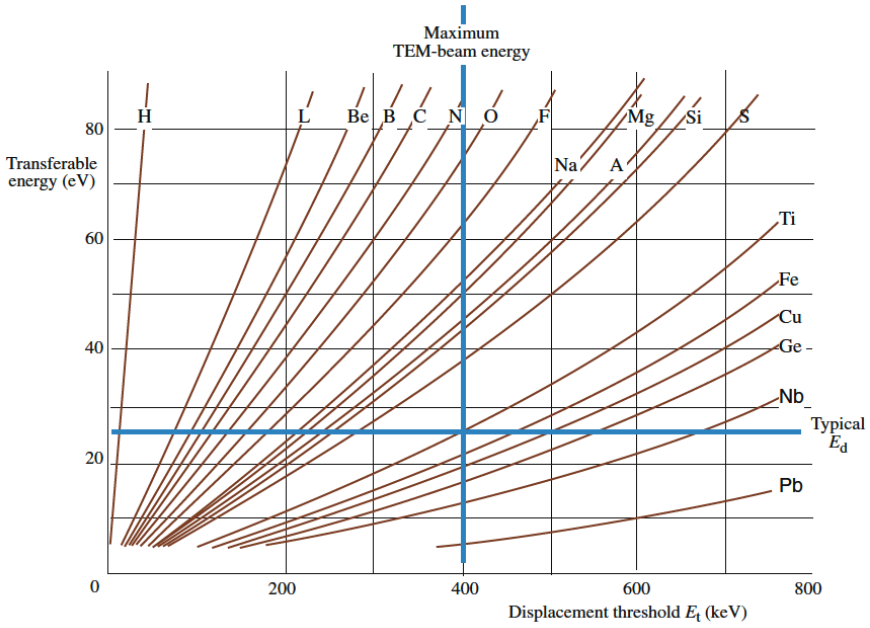

Figure 2.5: The maximum transferable energy for various elements as a function of the displacement-threshold energy. A maximum intermediate-voltage electrn microscope (IVEM) beam energy 400 keV and a typical displacement energy E_d = 25 eV were indicated in the diagram. [80]

(CCD) camera. A typical modern TEM provide a magnification up to several 10^6 times.

The TEM imaging conditions were mostly g=110 (g, 4.3g) dark field (DF) and kinematical bright field (BF). Such a dark-field condition gives s_g ∼0.1 nm^{-1}, which is less than the definition $|s_g| \geq 0.2$ nm^{-1} for weak-beam dark field (WBDF) condition. Although it is close to WBDF and is larger than the so-clled semiweak-beam condition s_g ∼0.06 nm^{-1} [82], it is not true weak-beam condition by definition. Nevertheless, the dark field imaging condition used in this study was found capable of properly showing small defects.

Additional images were taken using g = 200 when g·b analysis was conducted. If possible, specimens were examined in the TEM at around {100}, because the habit plane of resolved dislocation loops can be determined according to their inclination plane in this orientation. A magnification of 30,000x - 60,000x were used to image dislocation loops. When extended defect structure (ex. dislocation network) formed, a lower magnification to ∼10,000x was employed.

The voids were imaged with under- and over-focused imaging conditions. This technique

reveals the features of low electron density (voids or bubbles) by showing their Fresnel fringes that become visible with under- and over-focused conditions. When the distance between the exit surface of the specimen foil to the focal plane, ζ, is negative, the small voids and bubbles appear as a white central region surrounded by a dark ring. While ζ is positive, they appear as a dark central region surrounded by a white ring. When $\zeta = 0$, there is no contrast. In this study, voids were observed at a magnification of 60,000x-100,000x.

2.3.3 Quantitative measurements of line dislocation, dislocation loops and voids

To characterize and compare radiation damage in various materials and irradiation conditions, it is important to measure the size and density of the dislocation loops, voids and line dislocations in each specimen.

To get the density of defect clusters or line dislocations, it is necessary to determine the foil thickness where the density measurements were taken. Several techniques were employed including thickness fringe, electron energy loss spectroscopy (EELS), convergent beam electron diffraction (CBED) and Contamination-deposition method.

The thickness fringe, also called thickness contour, is the intensity oscillation between direct beam I_0 and diffracted beam I_g. The foil thickness is then determined by counting the number of thickness fringe from the edge. Each fringe (a pair of black and white band) represents a constant increment of thickness t, provided no foil bending occurs and the many-beam effect is negligible.

The thickness increment t can be calculated through

$$t = (s_{eff})^{-1} = \left(\sqrt{s^2 + \frac{1}{\xi_g^2}} \right)^{-1} \tag{2.1}$$

$$s = \frac{1}{2}(n-1)|g|^2\lambda \tag{2.2}$$

$$|g| = \frac{1}{d_{hkl}} \tag{2.3}$$

where ξ_g is the extinction distance for diffraction **g**. λ is the electron wavelength. n is the position where the Ewald sphere cut through the **g**-systematic row. The calculated t and relevant parameters for various diffraction conditions used in this study are shown in Table 2.4.

Table 2.4: Parameters for Calculating the Thickness Using Thickness Contour Method [83]

Condition	g = 110 (g,4.3g)	g = 110 (g,4.3g)	g = 200 (g,3g)	g = 200 (g,3g)
Electron Voltage (kV)	200	300	200	300
λ (nm)	0.00251	0.00197	0.00251	0.00197
d_{hkl} (nm)	0.2015	0.2015	0.1425	0.1425
n	4.3	4.3	3	3
ξ_g (nm)	34.2	38.2	50.1	55.93
s (nm^{-1})	0.102	0.080	0.124	0.097
t(nm)	**9.42**	**11.87**	**7.98**	**10.14**

The thickness contour method was the primarily method used in this study. However, it became unfeasible for some occasions. For example, it was difficult to count the thickness fringes when working on a grain not located at the perforation edge in a polycrystalline specimen.

One of the technique used to get around this difficulty is the CBED method. Convergent electron beams were used to form diffraction patterns under two-beam condition. The number of the Kossel-Möllenstedt (K-M) fringes was counted to deduce the foil thickness of the location at which the diffraction was taken. The number of the K-M fringes increase with increasing thickness. Detailed procedure of CBED method can be found in textbook

by Williams and Carter [80].

Contamination-deposition method was also used on the occasion when thickness contour method was not applicable. Electron beam was focused to a spot at the location where thickness information was required. After a few minutes, the illuminated area (by focused electron beam) would be deposited with contamination on the top and the bottom surface of the thin foil. After the contamination formed, the specimen was tilted and the tilting angle θ was recorded. The foil thickness t_{foil}, approximately the distance between the two contamination piles, can be deduced from

$$t_{foil} = \frac{d}{\sin\theta} \tag{2.4}$$

where d is the separation distance between the projections of the two contamination piles after tilting. Figure 2.6 shows the schematic diagram of this method. This method is applicable only when a certain degree of contamination exists in vacuum, and contamination pile could be formed on thin foil under electron illumination in a reasonable period of time.

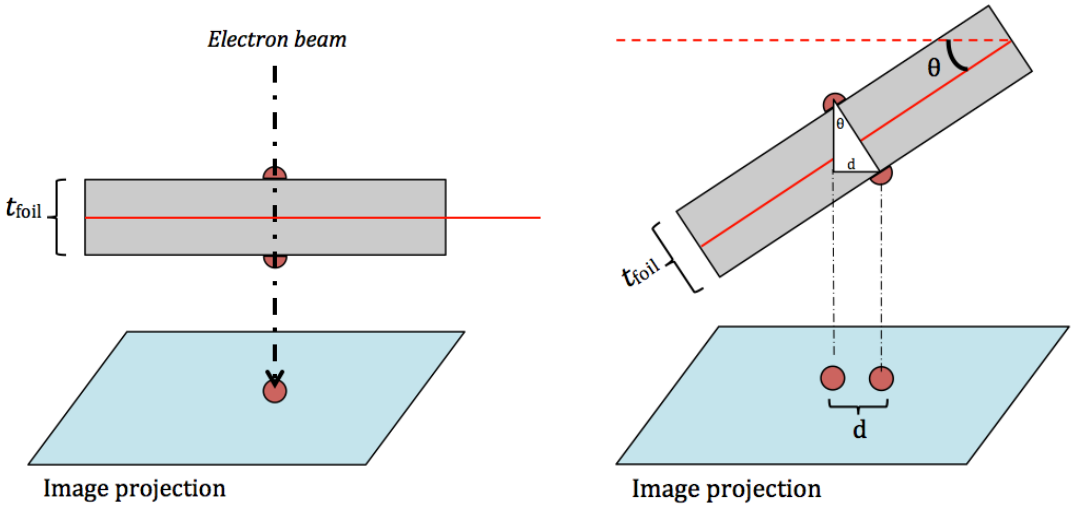

(a) Before tiltingl (b) After tilting

Figure 2.6: Schematic diagram showing contamination method to determine foil thickness

However, the above techniques would fail when the foil thickness become too large. The contrast of the thickness fringe and CBED fringe would fade away with increasing foil thickness due to the absorption. This becomes a problem when examination on relatively thick

region is necessary.

EELS is the methods employed for this occasion. It has been applied for the 1 dpa 450°C Fe-10Cr poly-crystal and Fe13Cr single-crystal specimens where dislocation networks in the thick region were required to be characterized. EELS deduces the foil thickness from the spectrum of elecron energy loss. The electrons lose their energy by inelastic scattering as they travel through the thin foil. The thicker the foil, the amount of the electrons experiencing no energy loss before they exit the thin film would decrease, while the amount of electrons losing some energies will increase. Detailed introduction of using EELS to determine the foil thickness can also be found in the textbook by Williams and Carter [80]. The equations used to calculate foil thickness using EELS are shown as follows:

$$t = \lambda ln\left(\frac{I_t}{I_o}\right) \tag{2.5}$$

$$\lambda = \frac{106F\left(E_o/E_m\right)}{ln\left(2\beta E_o/E_m\right)} \tag{2.6}$$

$$E_m = 7.6Z^{0.36} \tag{2.7}$$

$$F = \frac{1 + E_o/1022}{\left(1 + E_o/511\right)^2} \tag{2.8}$$

Where I_0 is the zero loop peak (ZLP) count, I_t is the total count, λ is the average mean free path for low energy loss, E_0 is the incident electron energy in keV, E_m is average energy loss in eV for material of average atomic number Z and F is the relativistic correction term. The β is the collection semi angle in mrad, here 14.06.

With the foil thickness measured, the volume density of dislocation loops and voids were obtained by dividing their areal density on the micrograph by the estimated foil thickness. The density of line dislocations ρ was estimated through the formula [84]

$$\rho = \left(\frac{4}{\pi}\right)\frac{R_p}{At} \tag{2.9}$$

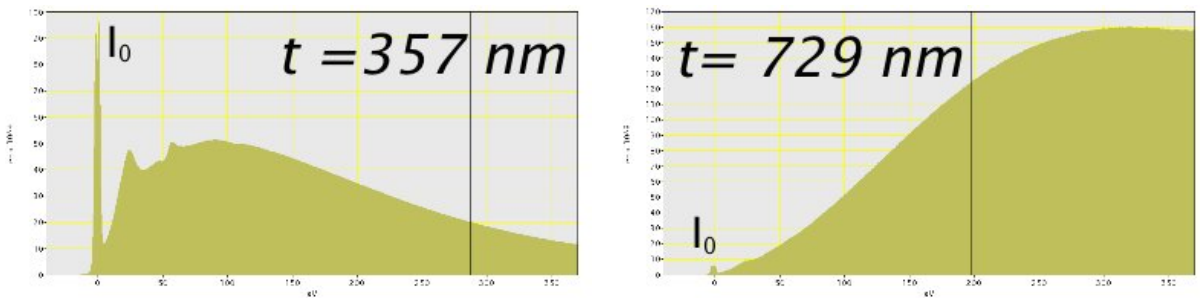

(a) Thinner Region (b) Thicker Region

Figure 2.7: Energy loss spectrum used to calculate the foil thickness. The specimens used here is Fe-10Cr poly-crystal specimen irradiated at 450°C to 1 dpa.

where R_p is the total projected length of line dislocations, A is the area of the measured micrograph and t is the estimated foil thickness. When the density of line dislocations is high, an alternative method was employed by measuring the number of total intersections N to random lines drawn on the micrograph of a the total length L [85]

$$\rho = \frac{2N}{Lt} \tag{2.10}$$

Given enough intersections (about 50), there is no significant difference between the two methods [86].

2.4 Atom Probe Tomography (APT)

The APT was used to study the α' precipitation in the irradiated Fe-Cr model alloys. The procedure of specimen preparation and data collection was described in Chapter 2.4.1. Three analysis techniques were performed: isoconcentration surface, frequency distribution analysis and proximity histogram [87][88][89][90]. The fundamentals of these techniques are described individually in the following Chapters 2.4.2, 2.4.3 and 2.4.4.

2.4.1 Specimen preparation and data collection

After irradiation, the specimens were mechanically polished and then electro-polished to achieve mirror-like surface condition in MFC at INL. This is to avoid surface roughness and contamination to affect the APT and, especially, nanoindentation. Polished specimens were then shipped to the Center for Advanced Energy Studies (CAES) and were mounted on SEM pin stubs with super glue with the shinning side facing upward.

5-6 APT needle specimens were lifted-out from each bulk specimen, and were mounted to the silicon with focused ion beam (FIB). The circular end form of the needle were produced by align the needle axis parallel and centered to the column of the ion beam. The needle specimen was then rastered across the end of the specimen in a circular annular patter, as shown in Figure . The ion energy and the size of the annular aperture decreased step-by-step until desirable needle size has been achieved (roughly 0.200 μm $\times$ 0.2 μm $\times$ 3 μm). The stepwise parameters of the ion energy and the size of annular aperture were shown in Table 2.5. Detailed description of the APT needle preparation using FIB can be found in the book by M.K. Miller [89].

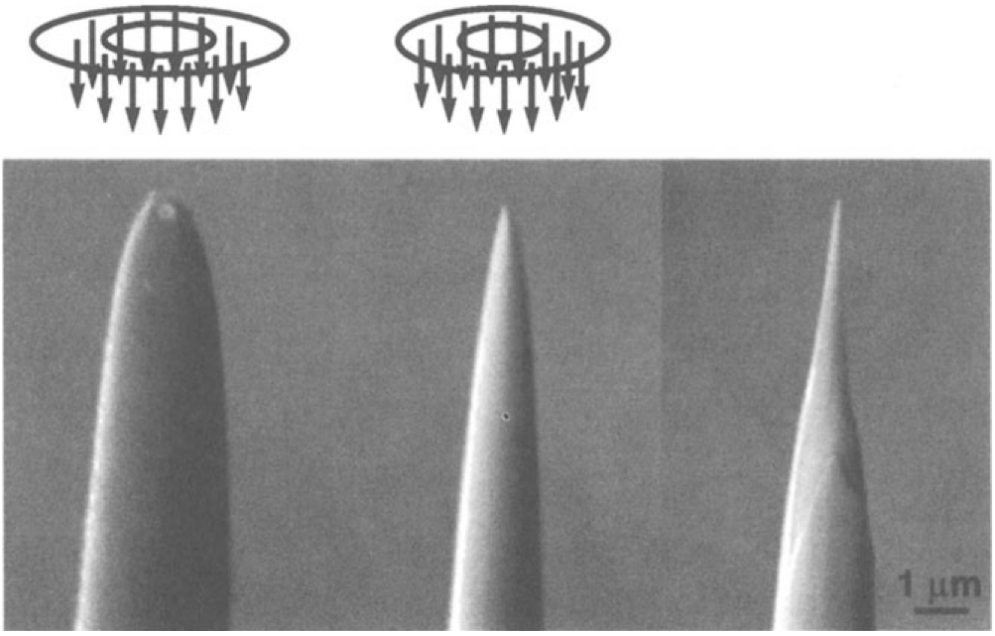

Figure 2.8: Annular milling with a focussed ion beam [89].

The entire silicon coupon was installed into a CAMECA local electrode atom probe

Table 2.5: Parameters for a typical annular milling process

Ion energy (keV)	Ion Current (pA)	Annular Diameter (μm) Outer	Inner	Milling depth (μm)	Milling time
30	3000	6	4	0.3	
30	1000	4.5	2	0.3	
30	300	4	1.5	0.2	
30	300	3.5	1	0.2	
30	100	3	0.75	0.2	
30	100	2.5	0.5	0.2	
30	30	2	0.3	0.1	
30	30	1.5	0.25	0.1	
5	48	*	0		$\sim$20 sec
2	27	*	0		$\sim$1 min

* Final polishing. Set outer diameter large enough to cover the needle entirely.

(LEAP) of model 4000X HR to acquire APT data. Figure 2.9 shows the schematic diagram of a 3-dimensional atom probe. The APT needle was cryogenically-cooled by mounting it on a cryogenically cooled goniometer. With the applied high voltage, the atoms field-evaporated from the surface were recored by the single atom position-sensitive detector, determining their spatial coordinates and mass-to-charge ratios. The arrangement of the atoms can be visualized and characterized by data reconstruction in a computer. The software used in this study is the Integrated Visualization and Analysis Software (IVAS). Detailed introduction of APT can also be found in the textbook by M.K. Miller [89].

Multiple APT needle were analyzed for each irradiation condition to verify data reliability and consistency. For each APT needle, the atom probe continued to collect atoms until the maximum voltage is reached or a major specimen fracture occurred. In general, only the very tip volume of the needle (roughly 50 nm $\times$ 50 nm $\times$ 150 nm or 10^5 to 10^6 atoms) were examined.

2.4.2 Isoconcentration surface analysis

The Cr-riched α' precipitates were visualized with the use of isoconcentration surfaces, or isosurfaces for short. An isosurface is a surface of designated concentration in three dimen-

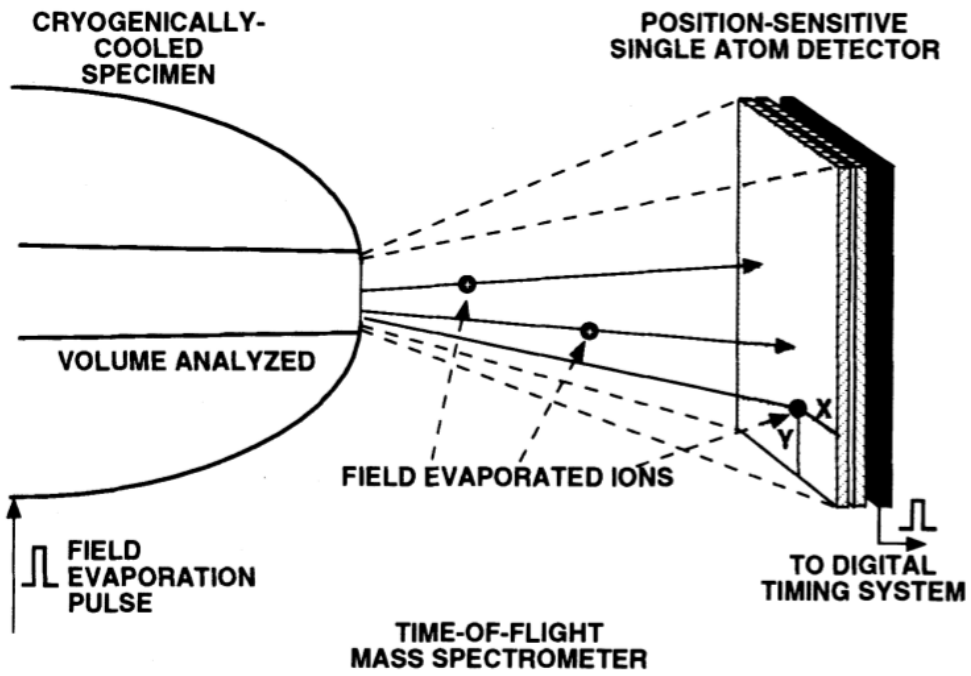

Figure 2.9: Schematic diagram of a 3-D atom probe. The are of analysis was defined by the active area of the single atom detector [89].

sions. In order to make comparison among specimens of various characteristics (Cr content, irradiation temperature, dose etc.), one single Cr concentration was used to define the α' precipitates. In this study, 20%Cr was selected since it reveals suitably the precipitates in all of the 1 dpa specimens. The size and density of α' precipitates were obtained by measuring the precipitates defined by the isosurfaces. The density N_p was calculated according to Equation 2.11 and Equation 2.12 [91].

$$N_P = \frac{N_{\alpha 1} + 0.5 \times N_{\alpha 2}}{V} \tag{2.11}$$

$$V = \frac{N_{Fe,Cr}/(detectionefficiency)}{a^3/2} \tag{2.12}$$

$N_{\alpha 1}$ is the number of α' precipitates well inside the boundary of the reconstruction data. $N_{\alpha 2}$ is the number of α' precipitates located at the edge of the boundary. As an estimate, half of the precipitates at the edge of the boundary were assumed to contribute to the density. V is the specimen volume estimated using lattice constant a (2.87 $\mathring{A}$ [60]), total number of

Fe and Cr ions, NFe,Cr, and the detection efficiency.

For the precipitates well inside the boundary of the reconstruction data, the sizes were clearly defined by the isosurfaces and could be readily obtained. For precipitates located at the edge of the boundary, however, their sizes were not obtainable. Therefore, the mean size of α' precipitates was calculated by considering only the precipitates well inside the boundary.

2.4.3 Proximity histogram analysis

A proximity histogram, or proxigram, was used to study the Cr concentration profile along the phase boundary normal of the α' precipitates. Following Hellman et al. [90], a proxigram is generated with three steps: (1) a sampling to generate a grid of concentration point from the atom position data; (2) an interpolation to construct an isosurface; (3) a correlation between the initial atomic position, their elemental identity and the constructed isosurface. The steps (1) and (2) are basically to construct an isosurface. After step (3), a one-dimensional plot of local concentration versus the proximity to the isosurface is generated. Figure 2.10 is an example of constructing a proxigram.

Multiple precipitates of similar sizes were combined to plot the proxigram in this study for better statistical significance. Although the Cr concentration profile of a single α' precipitate could also be acquired by using the region of interest (ROI) across the precipitate boundary. The boundary curvatures of the α' precipitates in this study were too large (due to the small sizes of 1-2 nm) for ROI method to appropriately accommodate [87].

2.4.4 Frequency distribution analysis

The frequency distribution analysis reveals the degree of Cr segregation in a statistical fashion. Following Moody et al. [88], frequency distribution analysis is a grid based technique when applied to the APT data set. The analysis was carried out with several steps: (1) The 3-dimensional data was partitioned into N discrete blocks containing an equal number of n_b atoms; (2) The occurrence frequency of solute atoms in each block is counted; (3) The

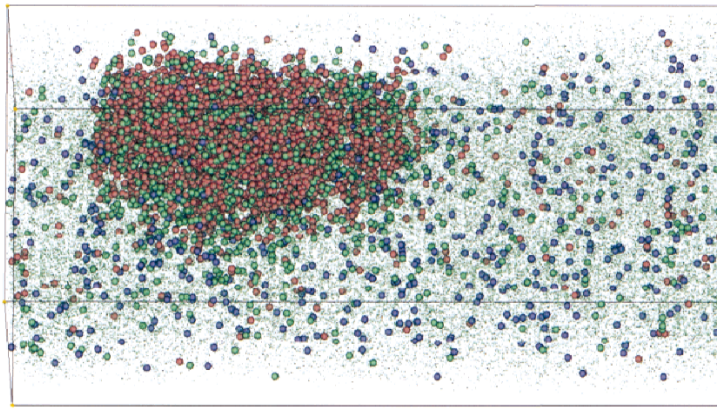

(a) Original atomic data

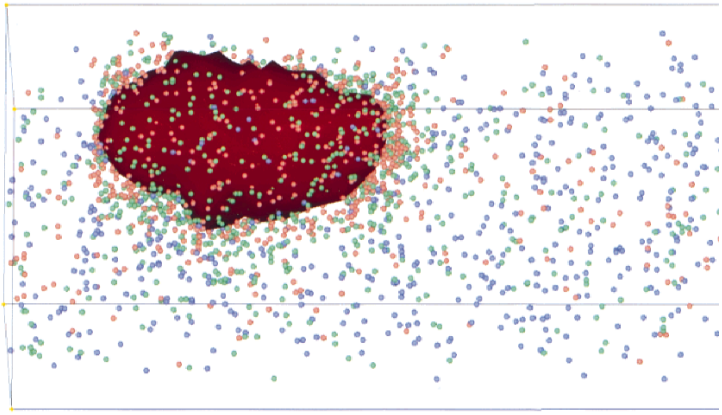

(b) Constructing isosurface

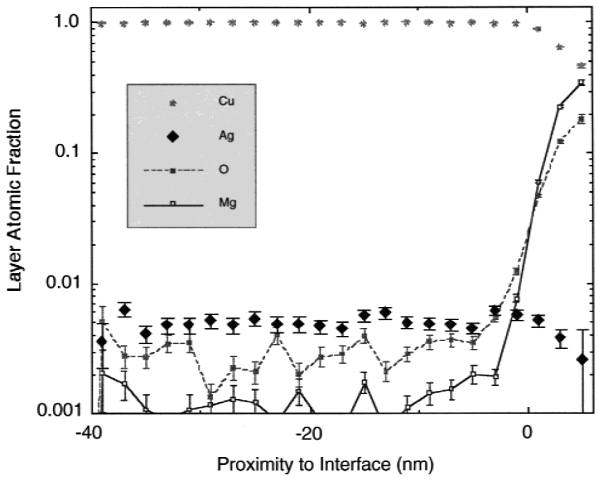

(c) Proxigram

Figure 2.10: (a) 3-dimensional reconstruction of an internally oxidized Cu(Mg, Ag) alloy where Mg, O, Ag and Cu atoms were presented with red, green blue spheres and small green dots. The cell size is 17 nm × 17 nm × 40 nm. (b) The isosurface of 11 at.% Mg. (c) The proxigram of the species in the sample with respect to the Mg 11% isosurface [90].

frequency *e(n)* is then compared with the corresponding binomial distribution *f(n)* (equation 2.13), the theoretical distribution of solutes randomly distributed throughout the solution.

$$f(n) = Np_B(n) = N\frac{n_b!}{n!(n_b-n)!}c_A^n(1-c_A)^{(n_b-n)} \tag{2.13}$$

The n is the number of solute atoms and c_A is the bulk concentration. Deviation of the actual frequency distribution from the binomial distribution indicates phase separation. Figure 2.11(a) is an example of frequency distribution analysis showing the Cr segregation in Al-1.7at%Cu under aging. The spreading of the frequency of Cu atom occurrence from the binomial distribution is significant, indicating that many blocks are Cu-segregated, and many are Cu-depleted.

In this study, the Pearson coefficient, μ-index, was used to quantify the deviation of the measured frequency distribution from the binomial distribution

$$\mu = \sqrt{\frac{\chi^2}{N+\chi^2}} \tag{2.14}$$

The χ^2 is defined as

$$\chi^2 = \sum_{n=0}^{n_b}\frac{(e(n)-f(n))^2}{f(n)} \tag{2.15}$$

where n_b is the block size. The value of ranges between 0 and 1, corresponding to random distribution and complete decomposition, respectively. Figure 2.11(b) is the μ-index of the same data set of Figure 2.11(a).

2.5 Hardness Measurements

2.5.1 Vickers microhardness

Hardness measurements provide a link connecting the microstructure and the mechanical property. Two types of hardness tests were performed: microhardness and nanohardness. The micro-hardness tests was carried out in the LAMBDA laboratory at ORNL using a Vickers diamond pyramid indenter. Figure 2.12 is a schematic diagram of the Vickers micro-

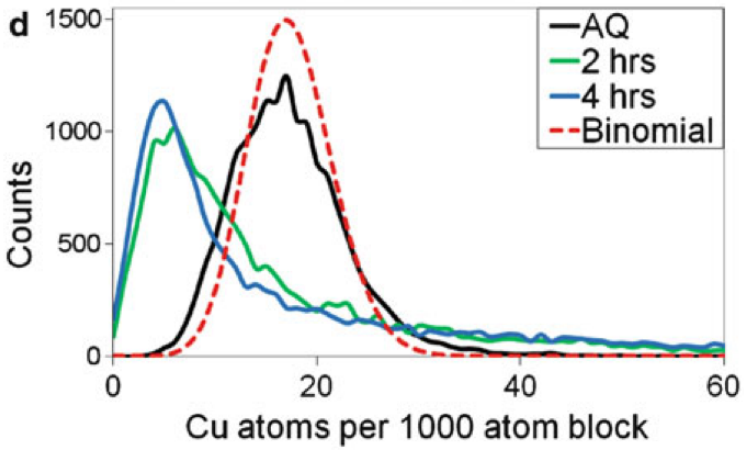

(a) Frequency distribution analysis

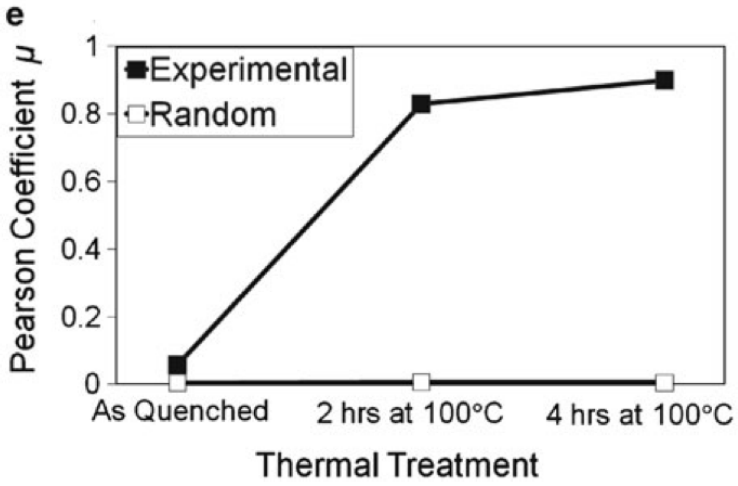

(b) μ-index

Figure 2.11: (a)The frequency distribution analysis and (b) corresponding μ-index of Cu in Al-1.7 at%Cu under thermal treatment of (1) as quenched (AQ), (2) 2 hr at 100°C and (3) 4 hr at 100°C. [92]

hardness measurement labeled with parameters of load force (F) and the indent diagonals (d_1 and d_2). The hardness, HV number, is defined as

$$HV = \frac{F}{A} \tag{2.16}$$

$$A = \frac{d^2}{2sin(\frac{136°}{2})} \approx \frac{d^2}{1.8544} \tag{2.17}$$

$$d = 0.5 \times (d_1 + d_2) \tag{2.18}$$

where F is in kgf and d is in millimeters.

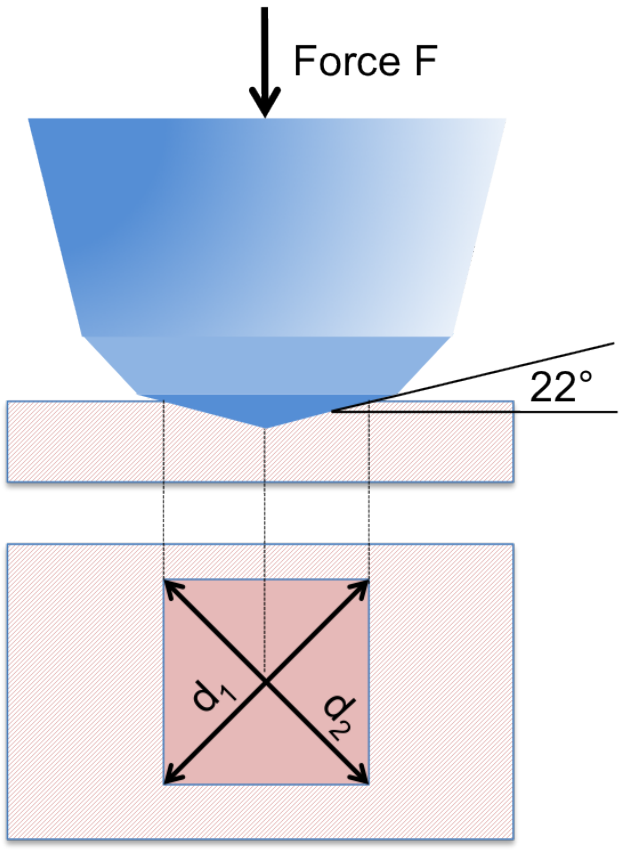

Figure 2.12: Schematic diagram of Vickers microhardness test

Normally, the Vickers is expressed as a number only (without unit). To report HV in SI unit involves converting from kgf/mm^2 to newton/m^2 and lead to the formula

$$Hardness(MPa) = 9.807 \times Hardness(HV) \tag{2.19}$$

Ten specimens were tested with Vickers microhardness test. Before indentation, the specimens were mechanical polished with sand papers to a thickness of 80-100 nm so the specimens could be jet-polished for TEM examination immediately after the hardness tests. The load setting is 100 g load and 15 seconds dwell time for all tests. At least 7 indents were performed for each specimen.

2.5.2 Nanoindentation

The nanoindentation was performed in the CAES facility. Nanoindentation measures the hardness using a much smaller load and indent depth comparing to microhardness measurement. Typically, nanoindentation is for testing thin films or coatings because it is capable of probing very small volumes of material. In the field of radiation damage in nuclear materials, it is useful to study ion irradiation because the damage depth of ion irradiation is around hundreds of nanometers to a few micrometers [93]. In this study, nanoindentation is actually not necessary since the examined specimens of this study were bulk specimens (i.e. size in the order of millimeters). The nanoindentation was utilized simply due to the readily accessibility of the nanoindenter in the CAES facility where microhardness indentor was not available.

The theory of nanoindentation/nanohardness is similar to microhardness. The hardness is defined as

$$H = \frac{P}{A_r} \tag{2.20}$$

where A_r is the residual area of indentation and P is the maximum load. The curve of load versus displacement is recorded during the indentation. A typical load versus displacement curve is shown in Figure 2.13. Different to the microhardness, the area A_r is not estimated from direct measuring the diagonal d of each indent. Instead, the final displacement (depth) was used to obtain the residual area according the depth-to-area curve. The depth-to-area curve is obtained by indenting the Si single crystal with an array of indents of varying load up to 2 N. The residual areas and the corresponding final displacements are plotted to generate the depth-to-area curve.

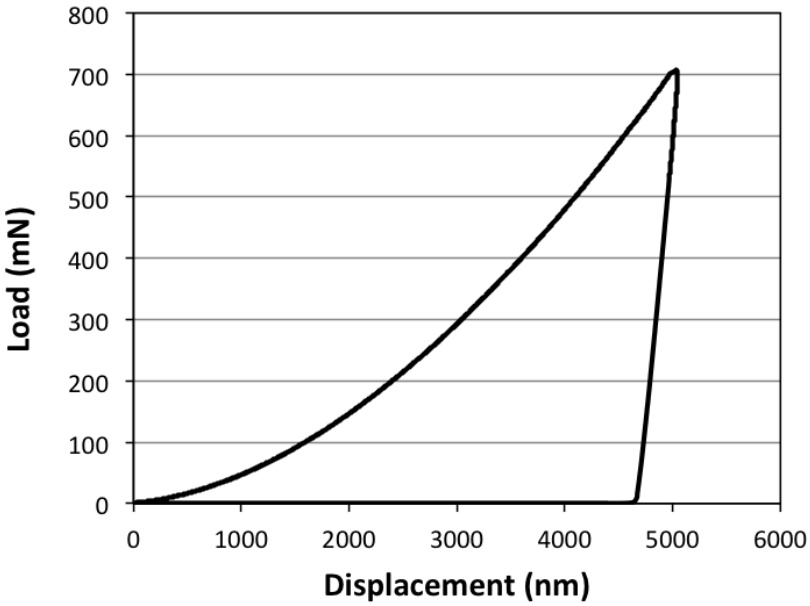

Figure 2.13: A typical load versus displacement curve from the nanoindentation on a unirradiated iron specimen.

All of the specimens (21 experimental conditions) were tested in a Hysitron TI-950 TriboIndenter with a high load Berkovich indentation head. Before indentation, specimens in the form of 2.3 mm disc were mechanically polished, and then jet-polishing for about 10 seconds to achieve mirror-like surface. For nanoindentation, it important to make the surface as flat as possible since it is very sensitive to the surface roughness. Polished specimens were then mounted on a SEM pin stubs with super glue, and were installed in the indenter. Before indenting the specimens, the curve of area-to-depth ratio was calibrated.

The indentations were performed in a constant displacement mode that a uniform 5 μm depth was used for all indents. This is to eliminate the influence of indentation size effect between indents [94]. A minimum of 10 indents were performed for each specimen.

CHAPTER 3

EXPERIMENTAL RESULTS

3.1 Transmission Electron Microscopy (TEM)

3.1.1 Unirradiated Fe poly-crystals

The microscopy of the unirradiated Fe specimens was not performed due to time restrictions. Its microstructure is thought to be close to the Fe specimen irradiated at 300°C to 0.01 dpa where very low radiation damage was observed. As will be shown in details later, the dislocation density in 300°C-irradiated Fe do not change with irradiation doses, therefore a roughly equal amount of dislocations is expected in the unirradiated Fe. In addition, EBSD examinations show no grain growth with irradiation, so the grain size of the unirradiated Fe specimen should be equal to the irradiated ones.

3.1.2 Unirradiated Fe-10Cr poly-crystals

The TEM micrograph of the archive Fe-10Cr poly-crystal (unirradiated) specimen is shown in Figure 3.1. A wide area was examined in order to show the structure of the dislocations. The foil thickness at the center of Figure 3.1 is 420 nm, estimated by counting the thickness fringes in dark field. The distribution of dislocations is not uniform. Figure 3.2(a) shows the area with a low dislocation density, and Figure 3.2(b) shows the area with a clustering of dislocations. The average dislocation density, measured over a wide area including both low density area and clustering area, is $1.2\text{x}10^{13}\frac{1}{m^2}$. For the clustering area alone, the dislocation density is roughly $7.3\text{x}10^{13}\frac{1}{m^2}$, which is significantly higher than the average.

In addition to the regional clustering of dislocations, two-dimensional dislocation cell walls

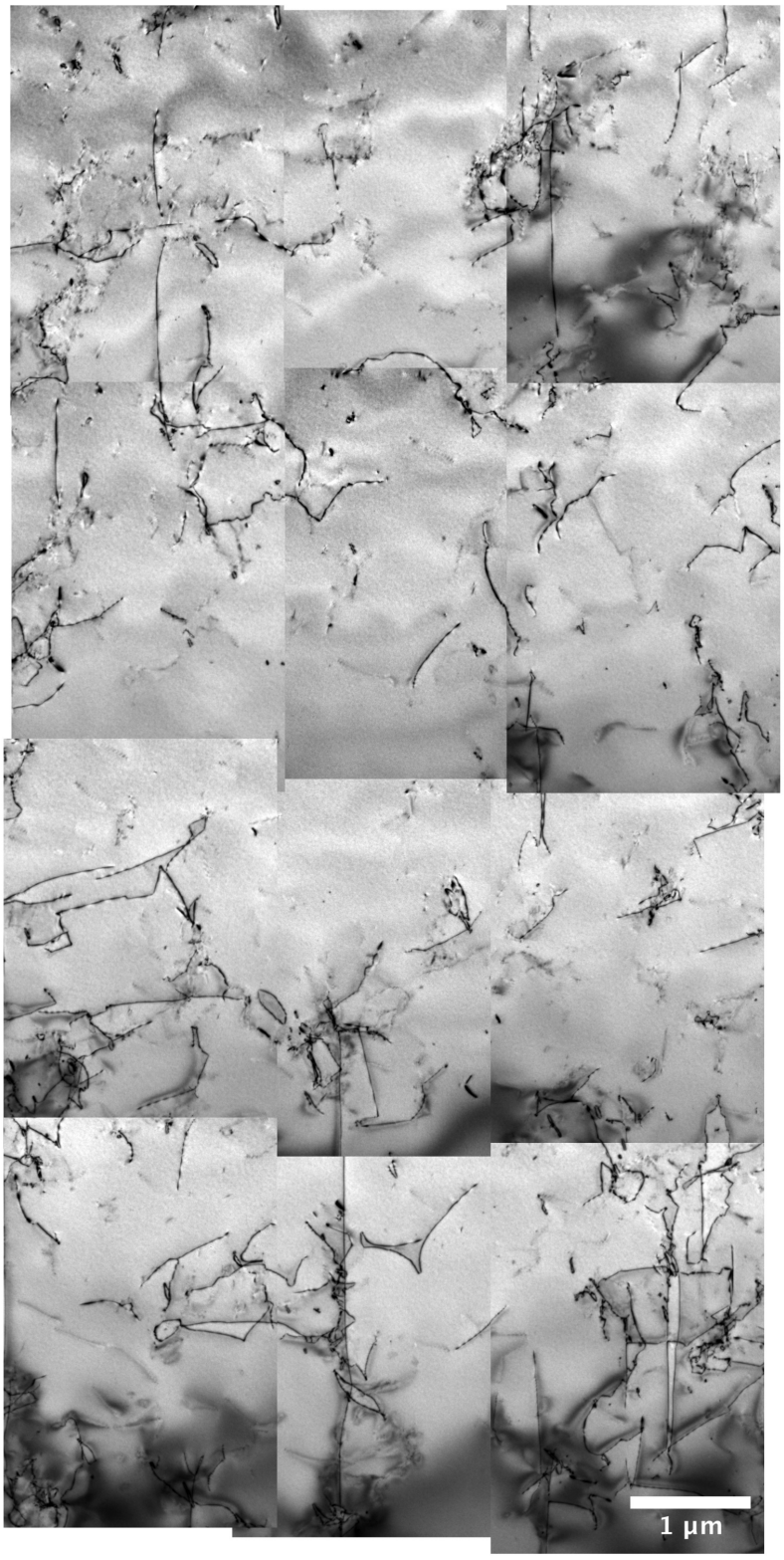

Figure 3.1: TEM images of unirradiated Fe-10Cr poly-crystals. The imaging condition is g= 110 (g, 3g). The electron beam was close to the [$1\bar{1}0$] direction.

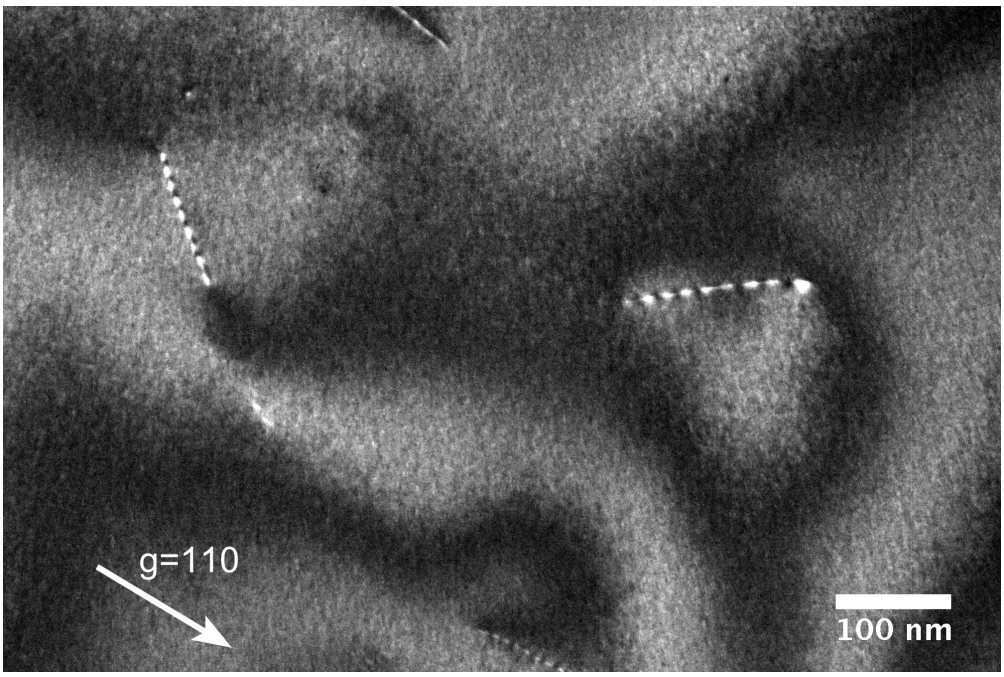

(a) Low Density Area

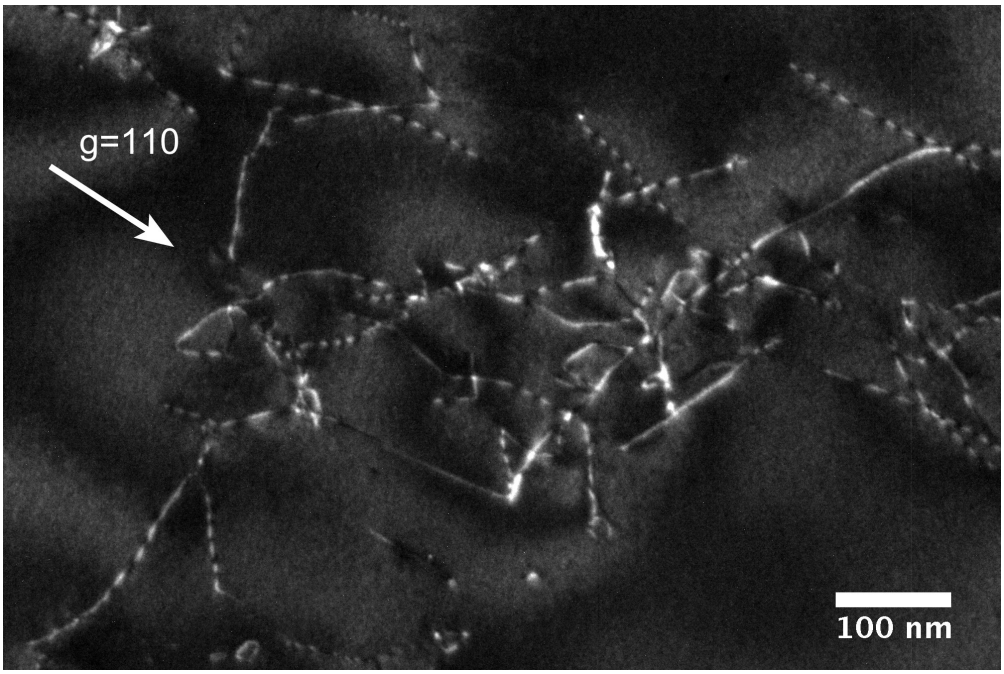

(b) Area of Clustering Dislocations

Figure 3.2: TEM images of unirradiated Fe-10Cr poly-crystals. The imaging condition is g= 110 (g, 4.3g) dark field. The electron beam was close to the [001] direction. The foil thickness at the center of all of the images is estimated to be about 180 nm. The oscillating contrast of some dislocations indicates that these dislocations have gone through multiple extinction distances (34.3 nm) across the foil thickness.

were observed throughout the specimen. Figure 3.3 shows two tripple-junctions of cell wall; one is more edge-on and the other is more flat-on. The driving force for the formation of dislocation cell walls is to reduce the total elastic energy by clustering [95]. The cell walls result in small small orientation differences between the cells, and can be regarded as small-angle grain boundaries of sub-grains. The EBSD results in Figure 2.2 show small sub-grains with tiny orientation differences in each grain, which is consistent with the TEM observations. The dislocations inside the cell walls were not considered in the above measurements of dislocation density.

Finally, a low density of dislocation loops was observed in the unirradiated Fe-10Cr poly-crystals, as shown in Figure 3.4. Their sizes vary from tens to hundreds of nanometers. The origin of these dislocation loops is not clear. Surely, they were not induced by irradiation since it had not been irradiated. A Frank-Reed source mechanism during deformation is a possible explanation. At any rate, the origin of these dislocation loops is beyond the scope of this study. However, they were recorded as a reference to discriminate themselves from the *real* irradiation-induced dislocation loops in the irradiated specimens.

3.1.3 Unirradiated Fe-14Cr single-crystals

Figure 3.5 is the TEM micrograph of the archive Fe-14Cr single crystal. The density of line dislocations is $2.8\times10^{12}\frac{1}{m^2}$ in average, obtained by measuring an area of 100 μm^2. This density is about five-times lower than the dislocation density in Fe-10Cr poly-crystals. In addition to the line dislocations, features with a size of 20-40 nm were observed. These features were not fully characterized. Through-thickness examinations show that their areal density does not have an clear dependence on the foil thickness. Surface contamination, if it exists, does not depend on foil thickness as well, and is, therefore, consistent with this observation. However, there are other evidence indicating that the features are not surface contaminations. Firstly, contamination is usually amorphous and is not visible in dark-field images; these features do have contrast in the dark-field counterparts in Figure 3.5(b). In addition, in some micrographs, such as Figure 3.6, the black dots form a straight line in BF, which is an unlikely arrangement for surface contamination.

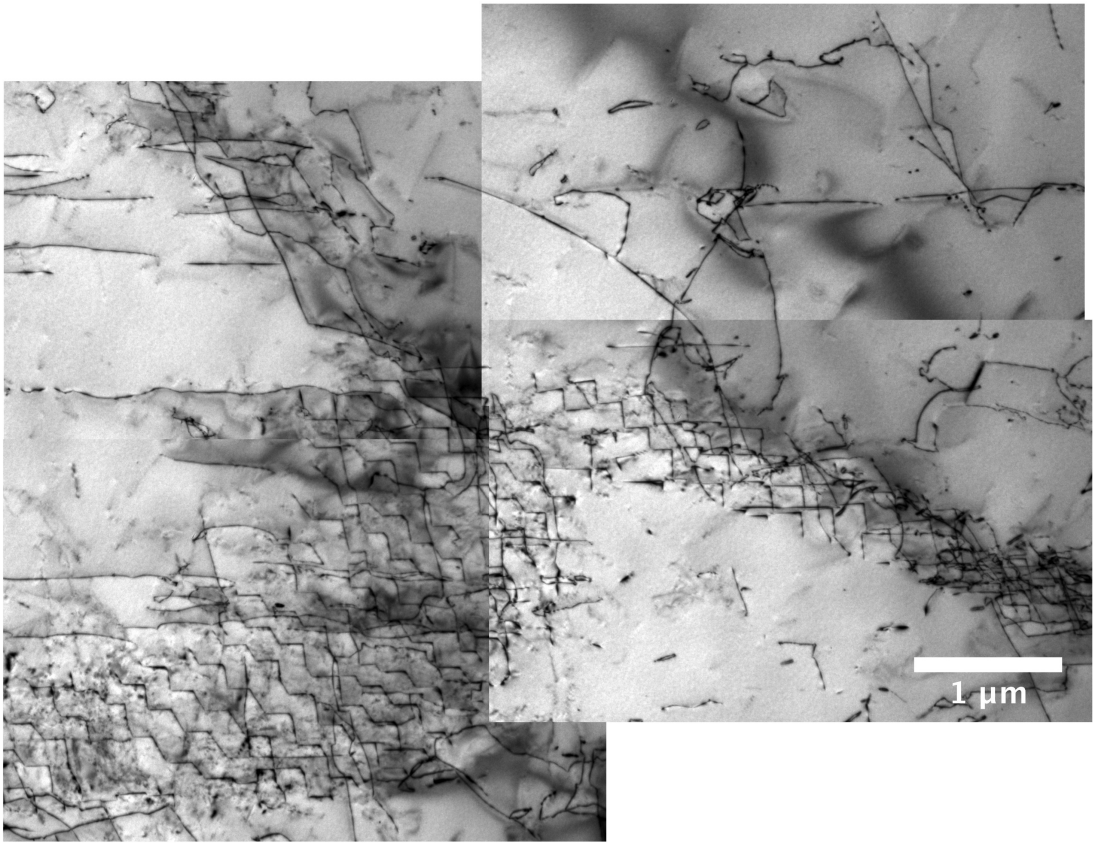

(a) BF Inclined Dislocation Cell Wall

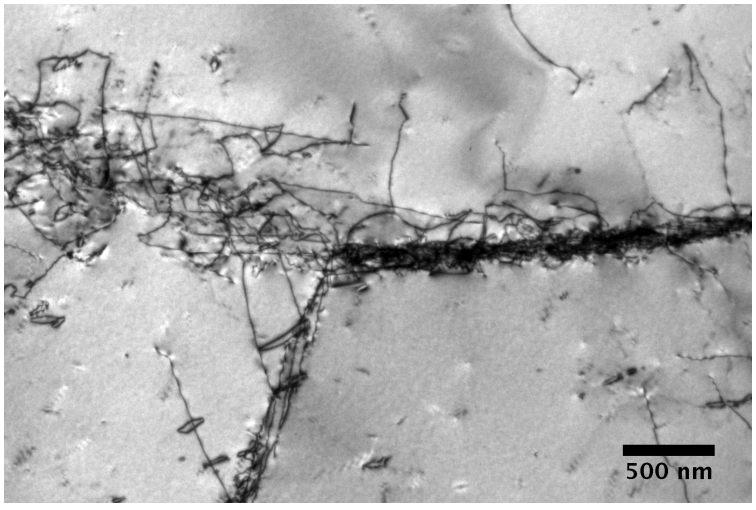

(b) BF Edge-on Dislocation Cell Wall

Figure 3.3: TEM images of unirradiated Fe-10Cr poly-crystals. The imaging condition is g= 110 kinematic BF. The electron beam was close to the $[1\bar{1}0]$ direction.

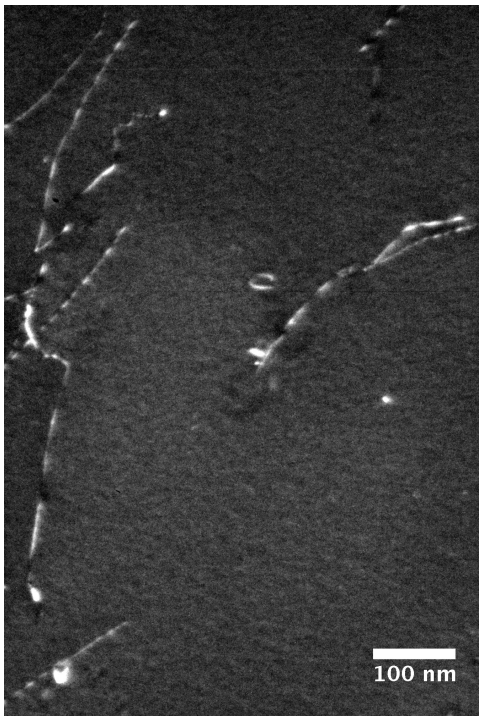

(a) DF Area 1

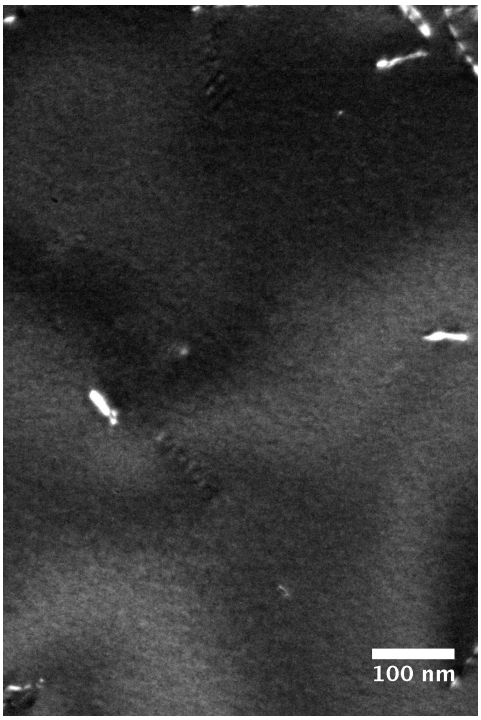

(b) DF Area 2

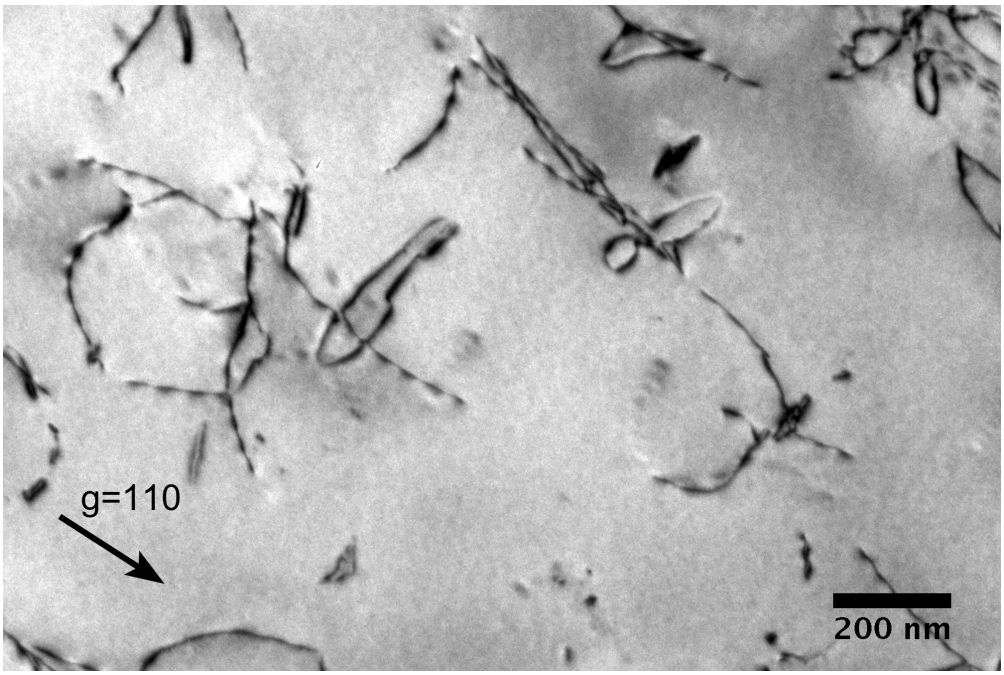

(c) BF Area 3

Figure 3.4: TEM images of unirradiated Fe-10Cr poly-crystals. The imaging condition is g= 110. The electron beam was close to the [001] direction.

Dislocation loops are possible candidates since some of the larger ones exhibit a lobe-lobe or loop contrast. Also, dislocation loop line-up has been reported in bcc Fe-Cr model alloys irradiated by Fe ions [49]. However, the specimen examined here is unirradiated, and no dislocation loops could have been induced by irradiations unless a Frank-Reed mechanism were involved. In addition, deformation process is unlikely to form such a line-up structure shown in Figure 3.6. Nevertheless, the average density of these dot features is low and their effect on the irradiation damage should not be significant.

3.1.4 Fe poly-crystals irradiated at 300C to 0.01dpa

Figure 3.7 is the TEM micrograph of an Fe poly-crystal irradiated at 300°C to 0.01 dpa. Due to the low irradiation dose (0.01 dpa), these dislocations are unlikely a result of the irradiation damage, and should be a pre-irradiation microstructure. The distribution of dislocations is not uniform. Cell walls in a fashion of a net of dislocations as shown in the middle of the figure was frequently observed throughout the specimen.

Figure 3.8 shows the TEM micrographs of another area with diffraction condition g = $1\bar{1}0$. Figure 3.7 and Figure 3.8 show that the irradiation damage in this specimen is minimal. Dislocation loops appearing as small dots in a size of 1-2 nm were only observed occasionally. For instance, these dislocation loops are indicated by the arrows in Figure 3.7. Because of the rareness of dislocation loops, there are not sufficient statistics to show if the dislocation loops were associated with the pre-irradiation line dislocations.

Overall, a similar microstructure was observed in each grain: a moderate amount of line dislocations (1.1×10^{14} $\frac{1}{m^2}$) and few small dislocation loops ((1.9×10^{20} $\frac{1}{m^3}$)). However, there was an exception. Figure 3.9 shows the observation of a group of larger dislocation loops with an average size of 11 nm . Since this was only observed once and was localized within a small volume of roughly 200 nm by 200 nm by 100 nm, it is not a general feature of the irradiation damage in this specimen. However, this observation should not be ignored. It shows how inhomogeneous, spatially, the radiation damage could be in Fe irradiated at 300°C.

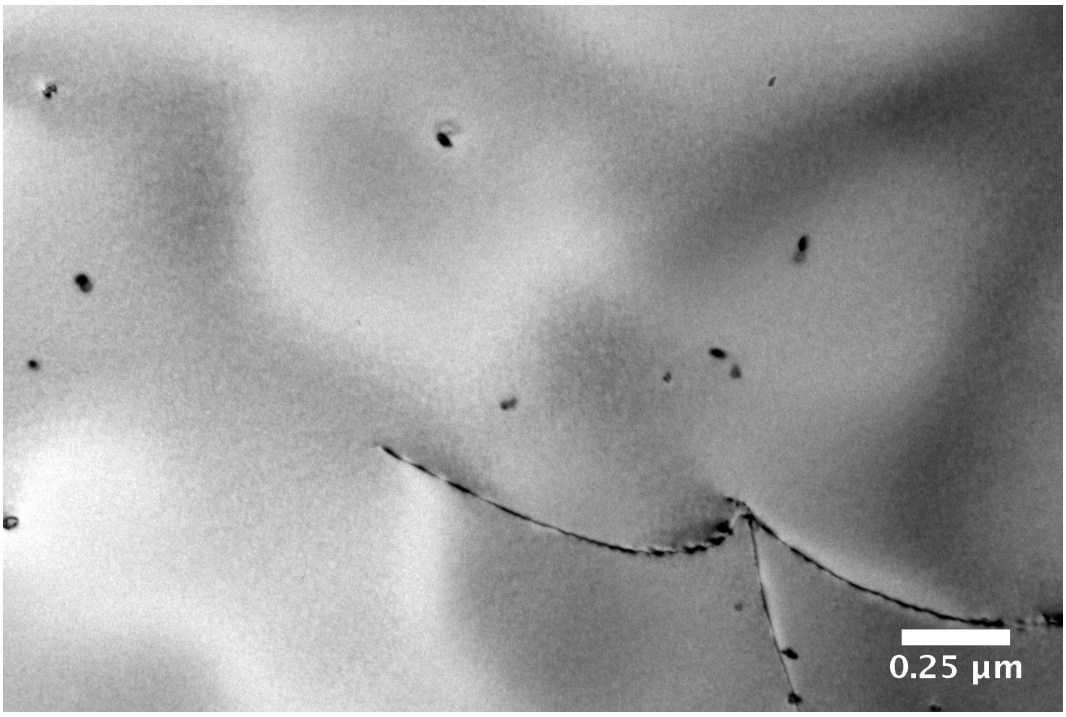

(a) Kinematic bright field

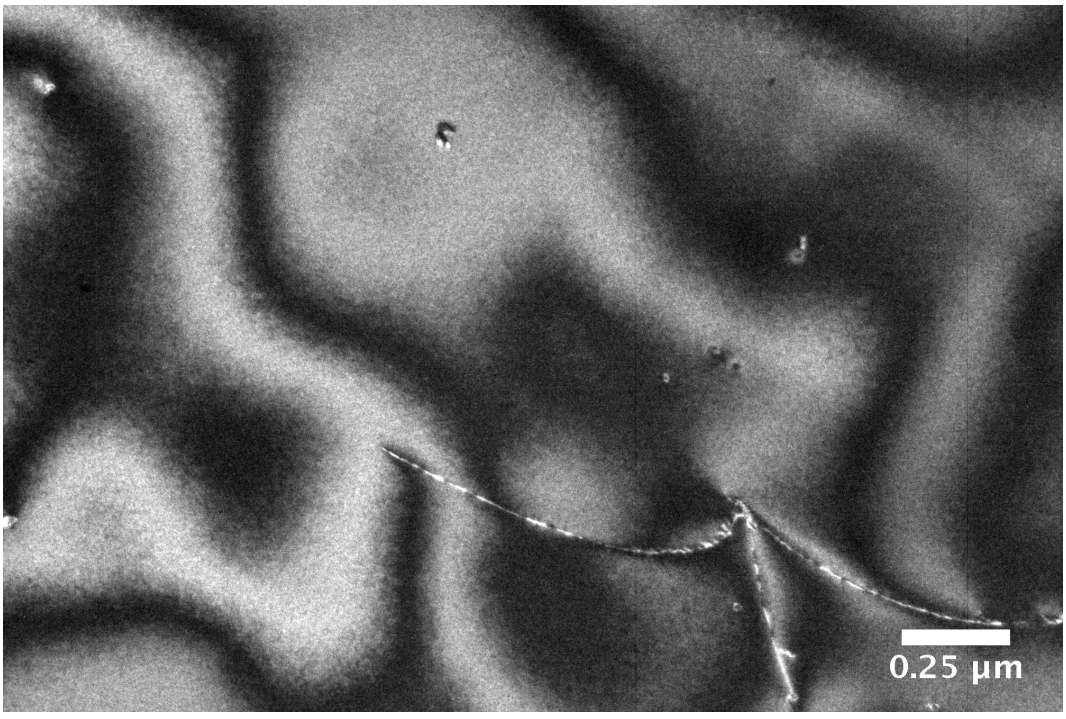

(b) dark field

Figure 3.5: TEM image of unirradiated Fe-14Cr single crystal. The imaging condition is g = 110 kinematic for bright field and (g, 4.3g) for dark field with beam direction close to [001]. The foil thickness at the center of the micrograph is estimated to be 120 nm.

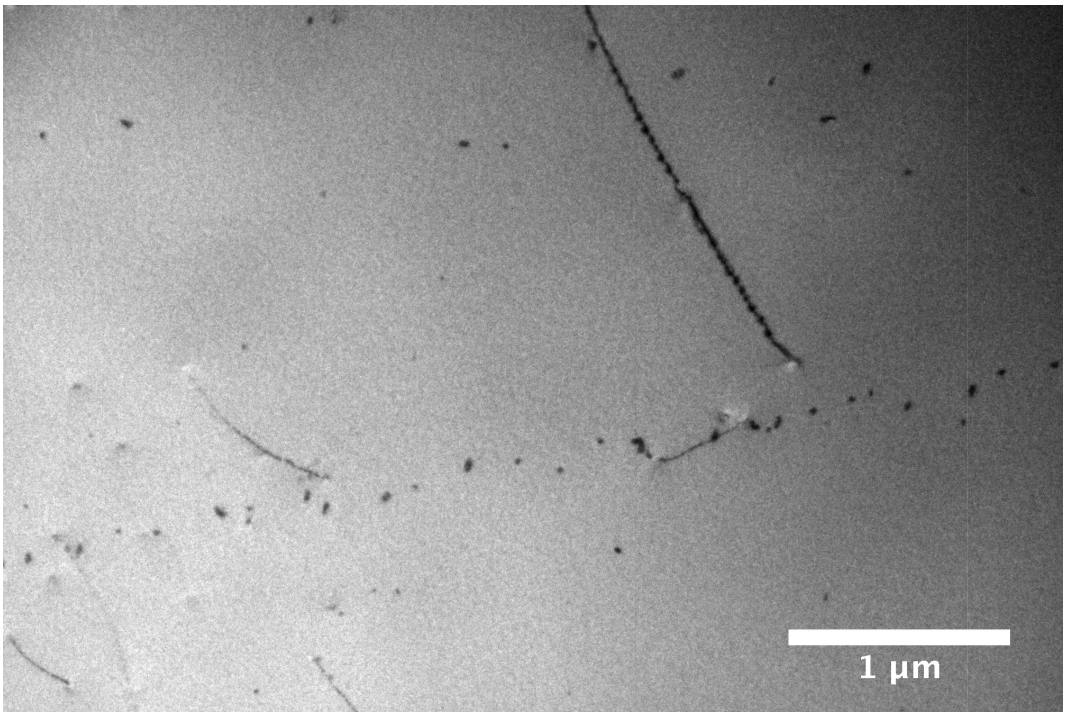

Figure 3.6: TEM image of unirradiated Fe-14Cr single crystal. Bright field imaging condition is kinematic using g = 110 with beam direction close to [001]. The foil thickness at the center of the micrograph is estimated to be more than 400 nm.

3.1.5 Fe poly-crystals irradiated at 300C to 0.1dpa

The TEM specimen preparation for Fe irradiated at 300°C to 0.1 dpa was not successful. The specimen was severely oxidized and an oxidation layer was formed all over the TEM specimen surface. Only one area is relatively clean for further characterization.

The Fe-300°C-0.1dpa specimen, like other Fe specimens, is poly-crystalline with a moderate amount of line dislocations existing. The density of line dislocations is $1.9\times10^{14}\frac{1}{m^2}$. As shown in Figure 3.10, radiation damage took the form of dislocation loops with a size ranging from a few nanometer (dots) to ∼30 nm (resolvable loops). The distribution of dislocation loops is not uniform. More loops reside in the vicinity of line dislocations than in the regions short of line dislocations. The dislocation loops found in the matrix (away from line dislocations) is about 15% of the total. Since the line dislocations have $\mathbf{b} = \frac{1}{2}\langle111\rangle$, all of the dislocations are visible with diffraction condition g = 002 in Figure 3.10(a) and Figure 3.11(a). The possibility of wrongly recognizing an dislocation-containing area as a dislocation-deficient area is eliminated. The foil thickness in the region of Figure 3.10

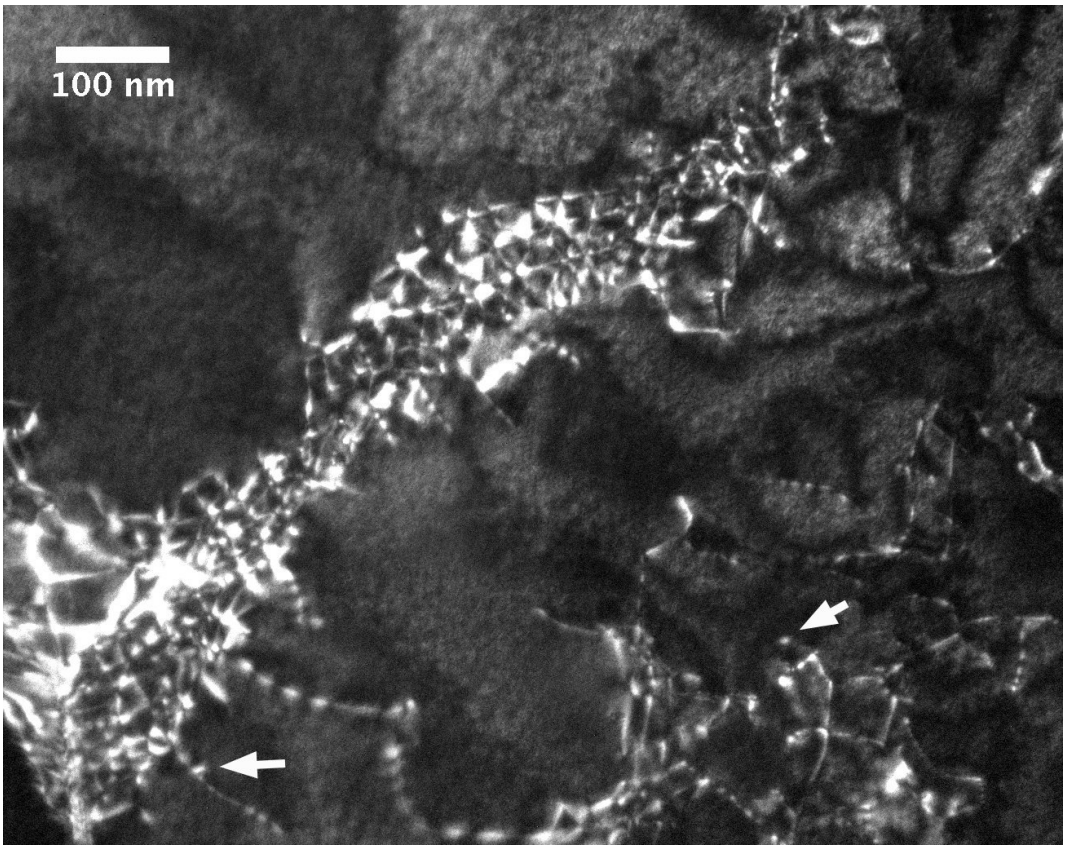

Figure 3.7: TEM image of Fe poly-crystal irradiated at 300°C to 0.01 dpa. The electron beam was close to the [110]. The diffraction condition is g = 002 (g, 3g)

and 3.11 was estimated with CBED to be 112 nm. The loop density was measured to be $1.17\times10^{21}\ \frac{1}{m^3}$.

The Burgers vector of irradiation-induced dislocation loops was studied with Figure 3.10. Based on the assumption that loops exhibit either $\mathbf{b} = \frac{a}{2}\langle111\rangle$ or a$\langle100\rangle$, the Burgers vector should be a[100] or a[010] for those loops marked with 'a' in the figures because they are invisible with g = 002 but visible with g = $1\bar{1}0$, . For the loops invisible with g = $1\bar{1}0$ but visible with g = 002, their Burgers vector could be a[001], $\frac{a}{2}[111]$ or $\frac{a}{2}[11\bar{1}]$. To further determine the exact Burgers vectors, the orientations of loop inclination were considered. The loops marked with 'b' exhibit habit planes that are consistent with (001) and not with (111) or $(11\bar{1})$, indicating that they are dislocation loops with $\mathbf{b}$ = a[001]. For the loops marked with 'c', their size is too small to determine their habit plane orientation, and their Burgers vector could be either a[001], $\frac{a}{2}[111]$ or $\frac{a}{2}[11\bar{1}]$.

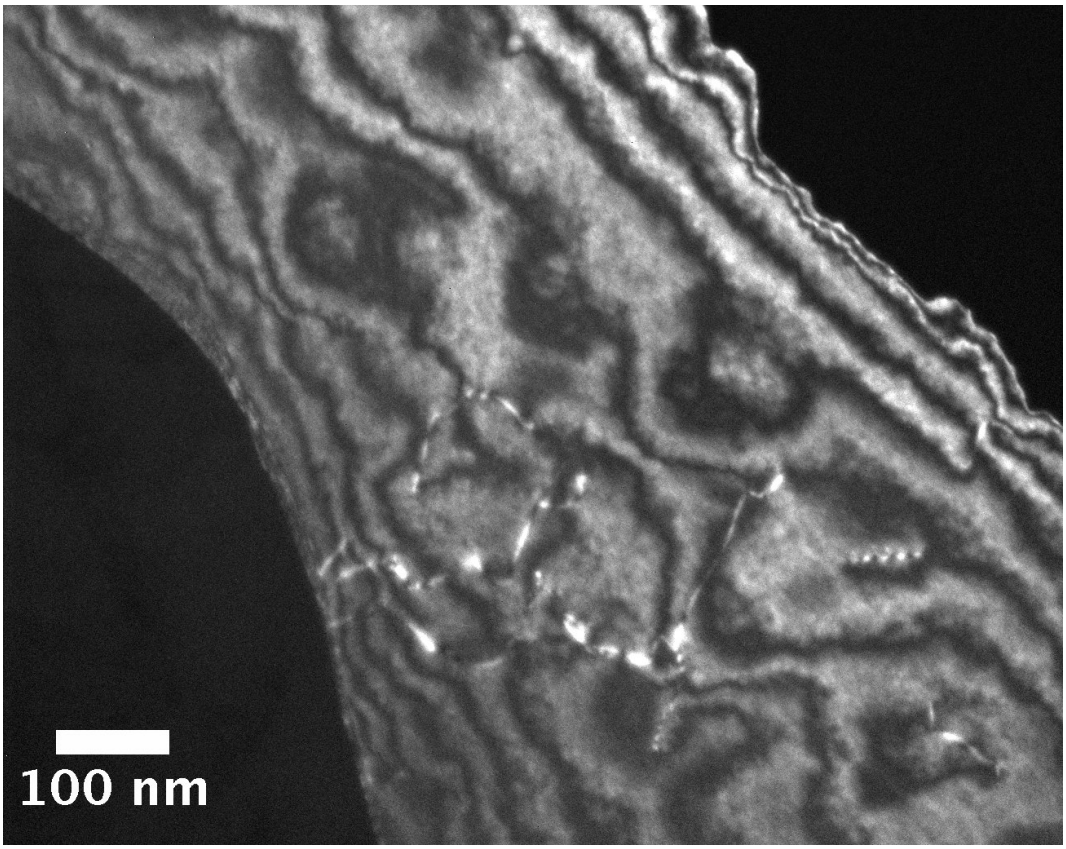

Figure 3.8: TEM images of Fe poly-crystal irradiated at 300°C to 0.01 dpa. The electron beam was close to the [110]. The diffraction condition is dark field g = $1\bar{1}0$ (g, 4.3g)

Figure 3.12 shows the under-over focus analysis to search for the irradiation-induced voids. In the under-focused image 3.12(a), the white contrast (two of the largest are marked with arrows) indicate the existence of low density cavity, voids. In the over-focused image Figure 3.12(b), however, no evident dark contrast appeared in the corresponding spots (marked with arrows). Rigorous void analysis requires consistent bright and dark contrast under under and over focused conditions, therefore the existence of voids in this specimen remains a question mark.

3.1.6 Fe poly-crystals irradiated at 300C to 1dpa

Figure 3.13 and 3.14 are the TEM micrographs of the same area of an Fe poly-crystal irradiated at 300°C to 1 dpa with varying magnifications. The irradiated specimen contained a high density of line dislocations ($1.2\times10^{14}\frac{1}{m^2}$), characterized by a cell structure as shown in

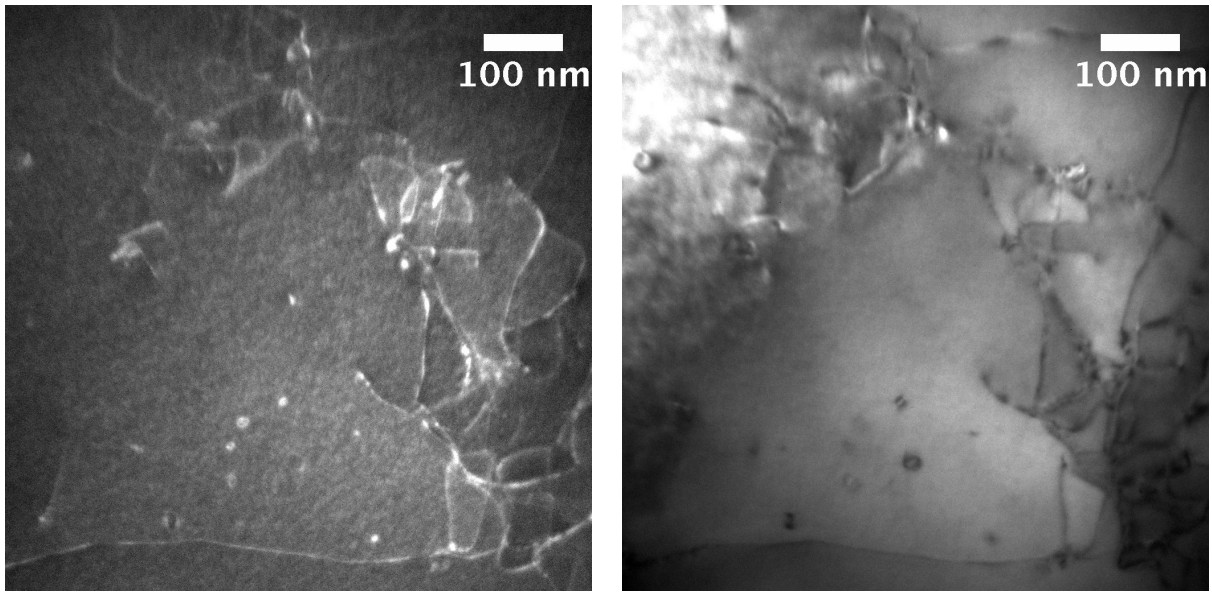

(a) DF (b) BF

Figure 3.9: TEM images of Fe poly-crystal irradiated at 300°C to 0.01 dpa. The electron beam was close to the [110]. The diffraction condition is (a) g = $1\bar{1}0$ (g, 4.3g) and (b) g = $1\bar{1}0$ kinematic.

Figure 3.13. The line dislocations are decorated with small dislocation loops. By contrast, in the areas at a distance from the line dislocations, the density of dislocation loops is extremely low.

The high-magnification micrograph of Figure 3.14 shows that the size of dislocation loops varies from small ones like dots to large ones with resolvable shapes. The average loop size is 5.9 nm. The loop density was measured to be 9.3×10^{21} $\frac{1}{m^3}$, based on Figure 3.14. However, the distribution of dislocation loops is very inhomogeneous (dislocation decoration), the loop density shown in Figure 3.14 is higher than the average. Considering the dislocation distribution in Figure 3.13, the average loop density of the entire specimen was estimated to be around 5×10^{21} $\frac{1}{m^3}$.

This observation, that the damage was confined mainly to dislocation lines, is consistent with the work by Horton [28] et al. and Robertson et al. [29] on Fe poly-crystal irradiated with neutrons at ambient temperature and around 300°C, respectively. However, the phenomenon that large loops on one side of the dislocation line and small dislocation loops on the other side observed in Ref in [29] is not clearly seen in Figures 3.13 to 3.14. The

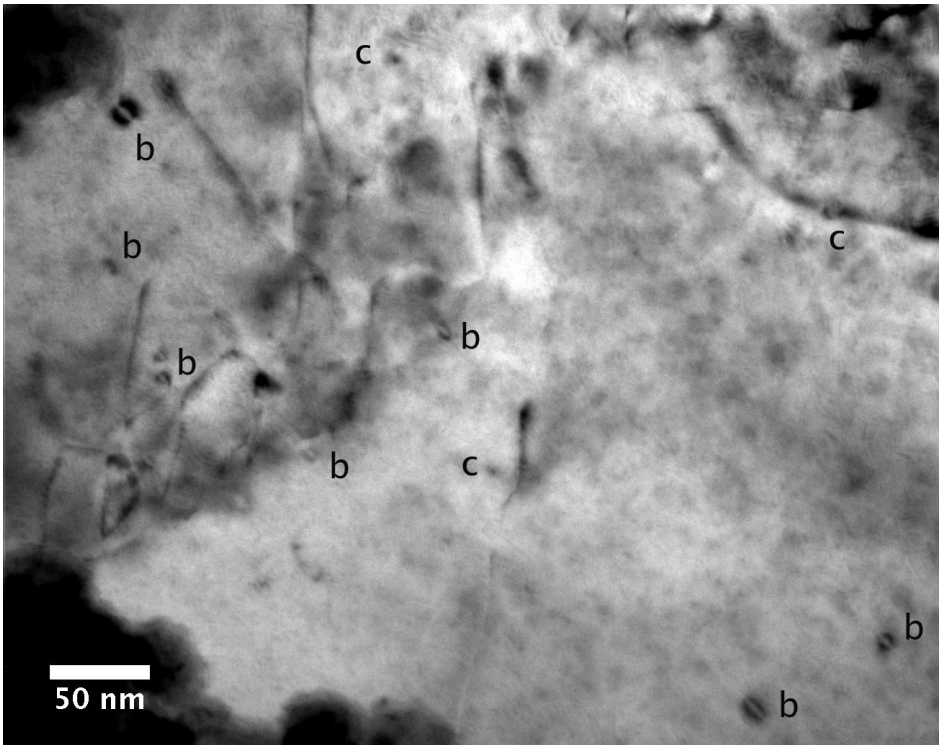

(a) Area A, BF g = 002

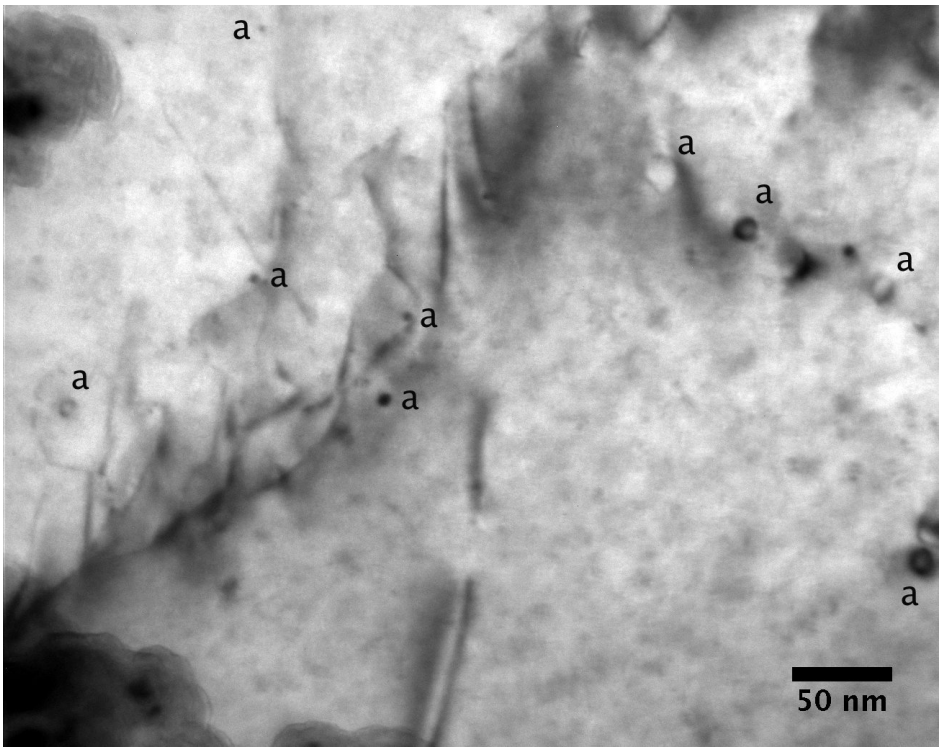

(b) Area A, BF g = $1\bar{1}0$

Figure 3.10: TEM images of Fe poly-crystal irradiated at 300°C to 0.1 dpa. The electron beam was close to the [110] with (a) g = 002 and (b) g = $1\bar{1}0$

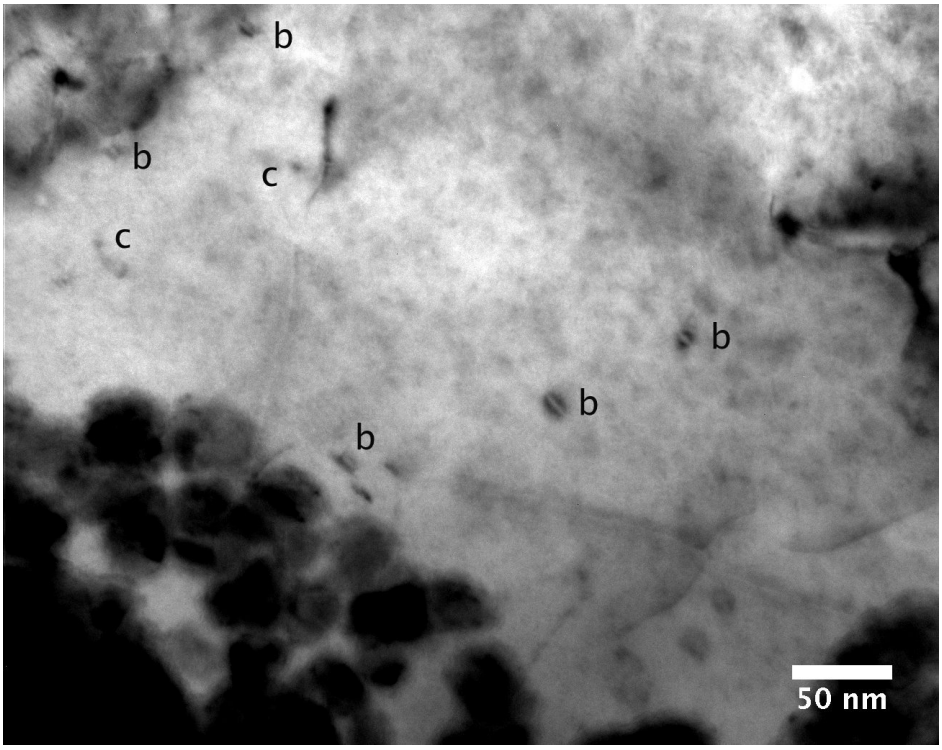

(a) Area B, BF g = 002

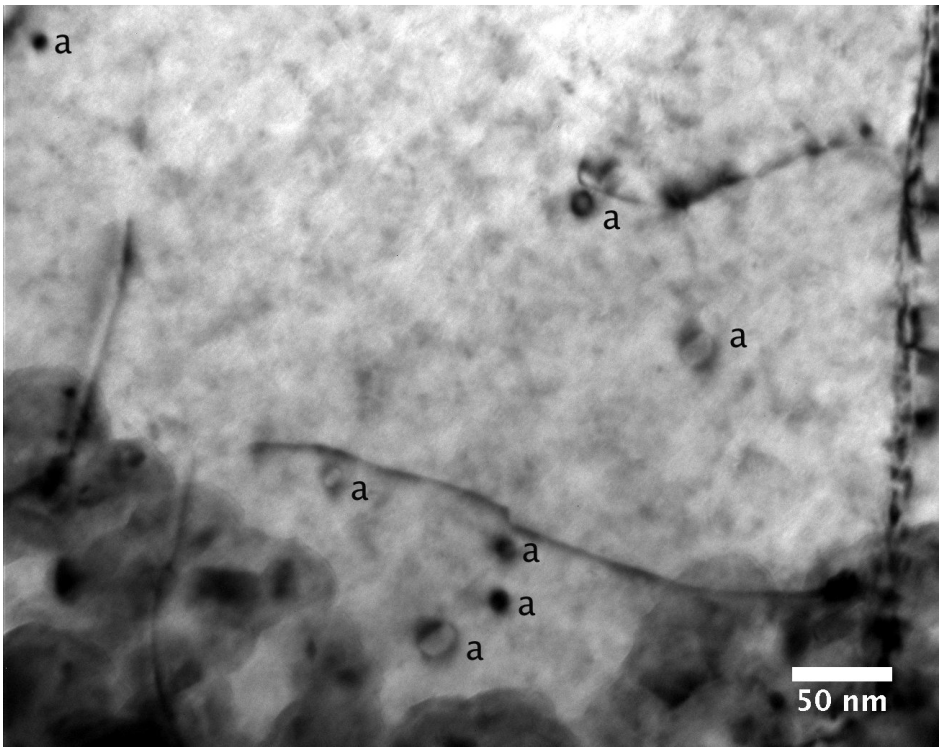

(b) Area B, BF g = $1\bar{1}0$

Figure 3.11: TEM images of Fe poly-crystal irradiated at 300°C to 0.1 dpa. The electron beam was close to the [110] with (a) g = 002 and (b) g = $1\bar{1}0$

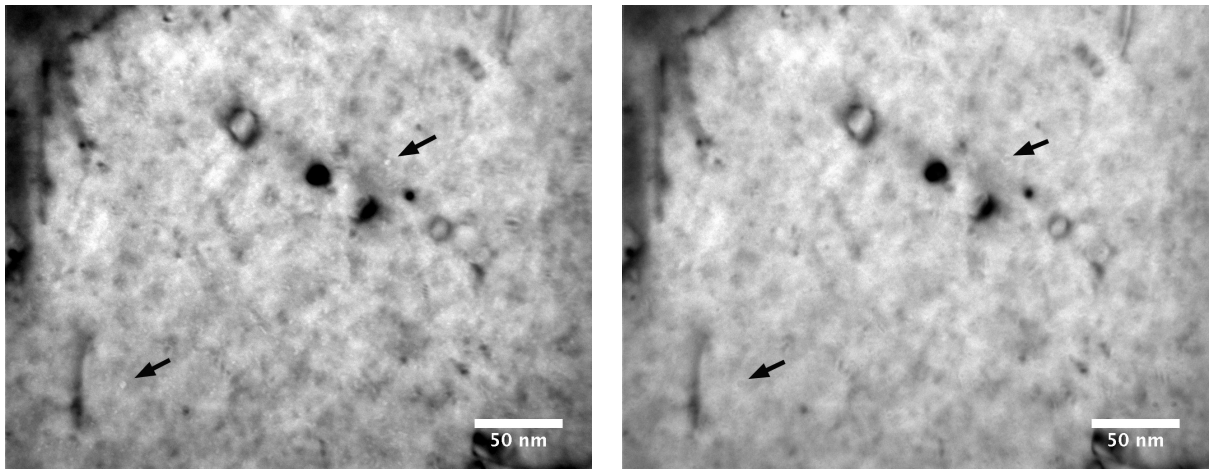

(a) Kinematic BF Under-focused (b) Kinematic BF Over-focused

Figure 3.12: TEM images of Fe poly-crystal irradiated at 300°C to 0.1 dpa. The electron beam was close to the [110] with g = $1\bar{1}0$.

dislocation densities in these images might be too high to show this type of structure.

A FIB sample was independently lifted-out from the same irradiated Fe specimen, and its TEM micrograph is shown in Figure 3.15. In this micrograph, the dislocation loops stay mainly on one side of the line dislocation, which is similar to the result in [29]. However, this loop-dislocation correlation was observed only on one occasion among all the micrographs. It is not clear if it represents a general case or actually an exception. In addition, a comparison of TEM micrographs between FIB sample (Figure 3.15) and jet-polished sample (e.g. Figure 3.14) shows that additional contrast of gray strips and dots appeared uniformly in the FIB sample. These contrast features were artificial defects introduced by the Ga ions during the FIB preparation, and were not a result of neutron irradiation.

Irradiation-induced voids are shown in Figure 3.16 where the same area was imaged with in-focused, under-focused and over-focused conditions. The distribution of voids was not associated with either line dislocations nor the dislocation loops. In addition, their distribution is reasonably uniform but with some size variations. An example of clusters of large voids is indicated by an arrow in the figure. The average size of the voids is 1.8 nm with the largest size of 5.0 nm.

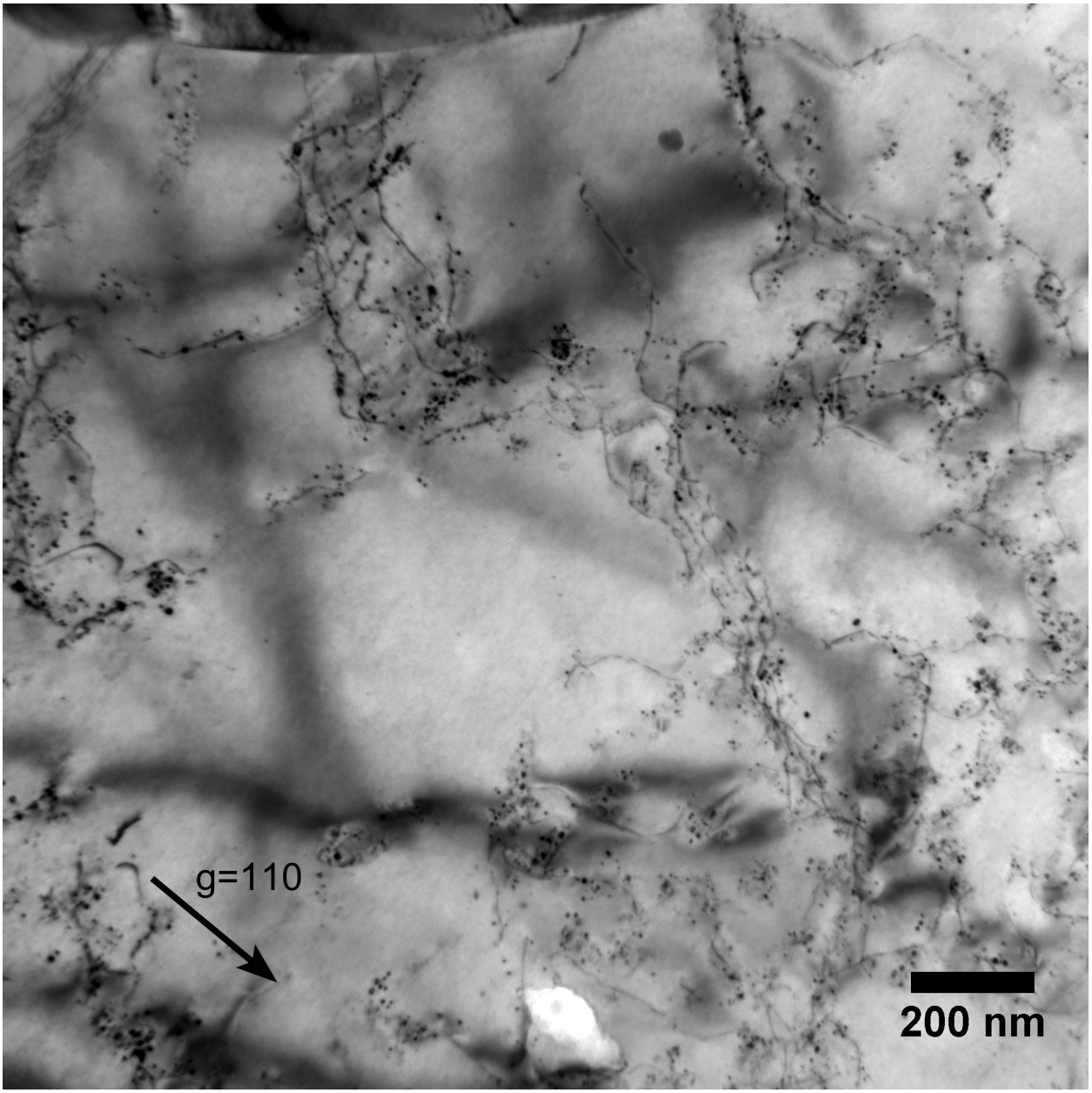

Figure 3.13: Low magnification TEM images of Fe poly-crystal irradiated at 300°C to 1 dpa. The electron beam was close to the [111] direction of the crystal. The imaging condition was kinematic bright field g = $1\bar{1}0$.

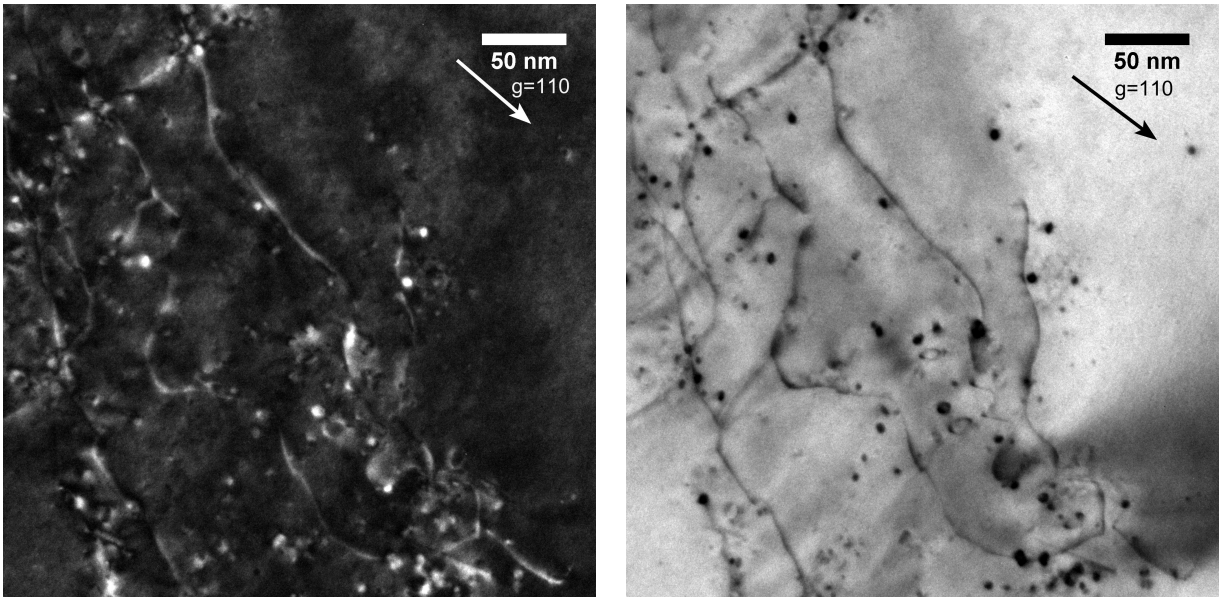

(a) High Mag DF (b) High Mag BF

Figure 3.14: High magnification TEM images of Fe poly-crystal irradiated at 300°C to 1 dpa. The electron beam was close to the [111] direction of the crystal. The imaging condition was g = $1\bar{1}0$ kinematic for bright field and (g, 4.3g) for weak-beam dark field.

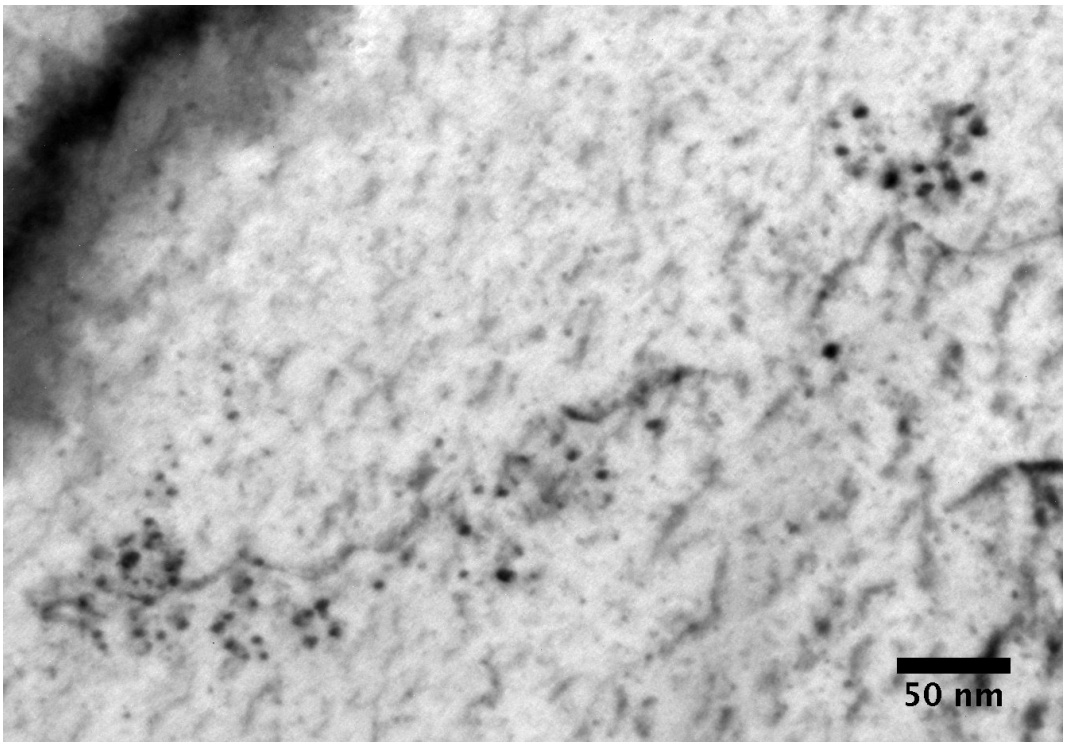

Figure 3.15: TEM image of Fe poly-crystal irradiated at 300°C to 1 dpa. Bright field imaging condition is kinematic g = $1\bar{1}0$ with beam direction close to [111].

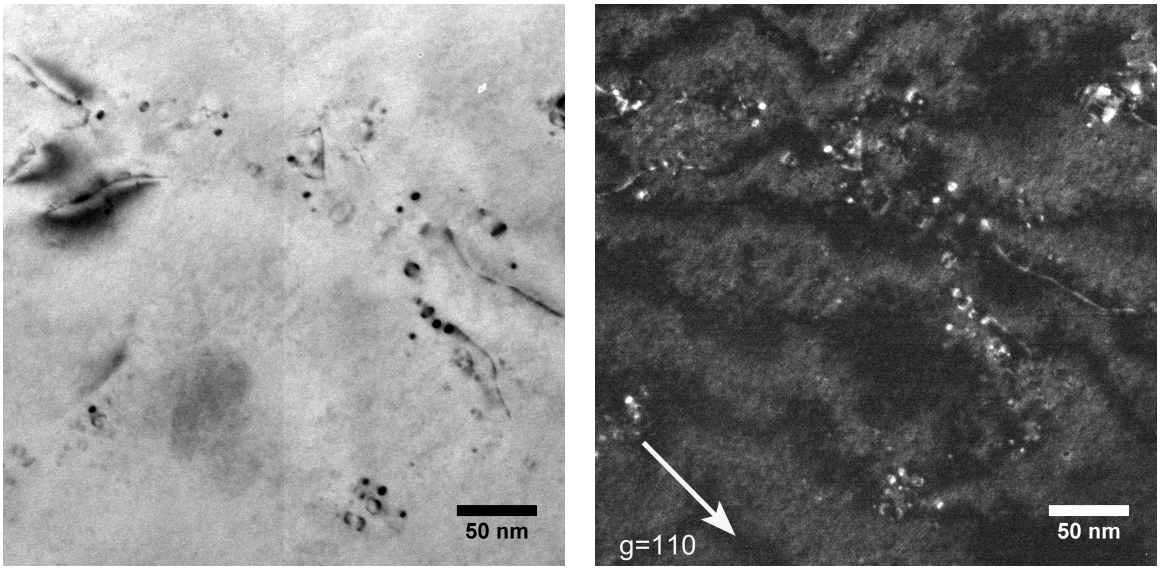

(a) BF In-focused

(b) DF In-focused

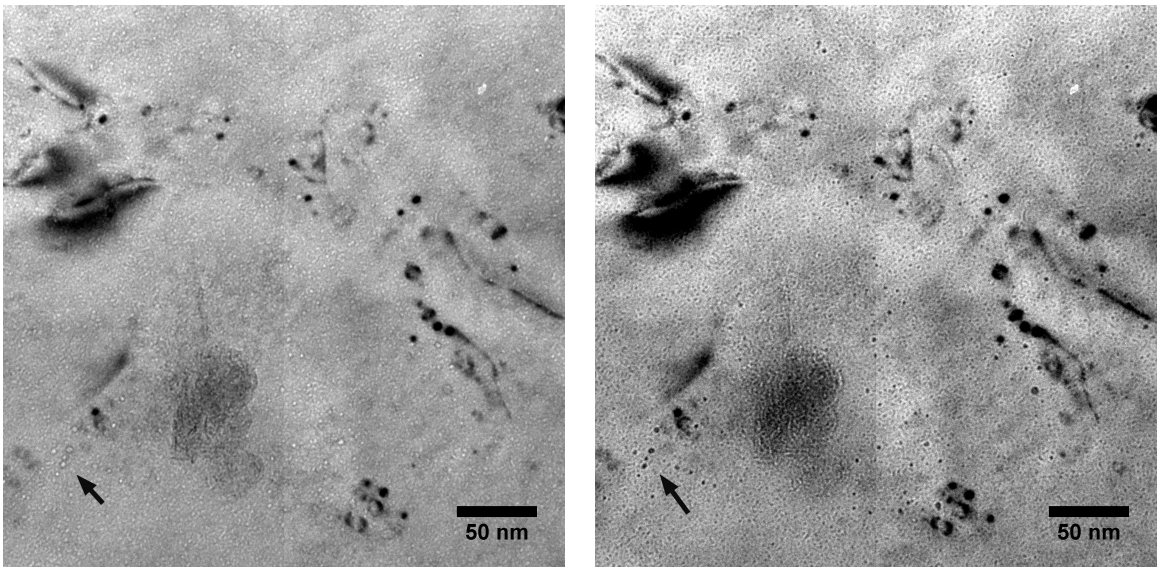

(c) BF Under-focused

(d) BF Over-focused

Figure 3.16: TEM images of Fe poly-crystal irradiated at 300°C to 1 dpa. Images were taken in the same area with (a)(b) in-focused, (c) under-focused and (d) over-focused in order to reveal the voids. The diffraction condition is g = 110.

3.1.7 Summary of Fe poly-crystals irradiated at 300C

The microstructural evolution in Fe irradiated at 300° as a function of irradiation dose is shown in Figure 3.17. The irradiation damage accumulated mainly in the vicinity of pre-existing dislocation lines. This observation of dislocation decoration is similar to those observed by Horton et al. [28] and Robertson et al. [29] where Fe was irradiated at 300°C and RT to comparable doses. Burgers vector analysis was performed on the 0.1 dpa specimen, and most of the loops exhibit Burgers vectors of a⟨100⟩, consistent with Nicol et al. [30].

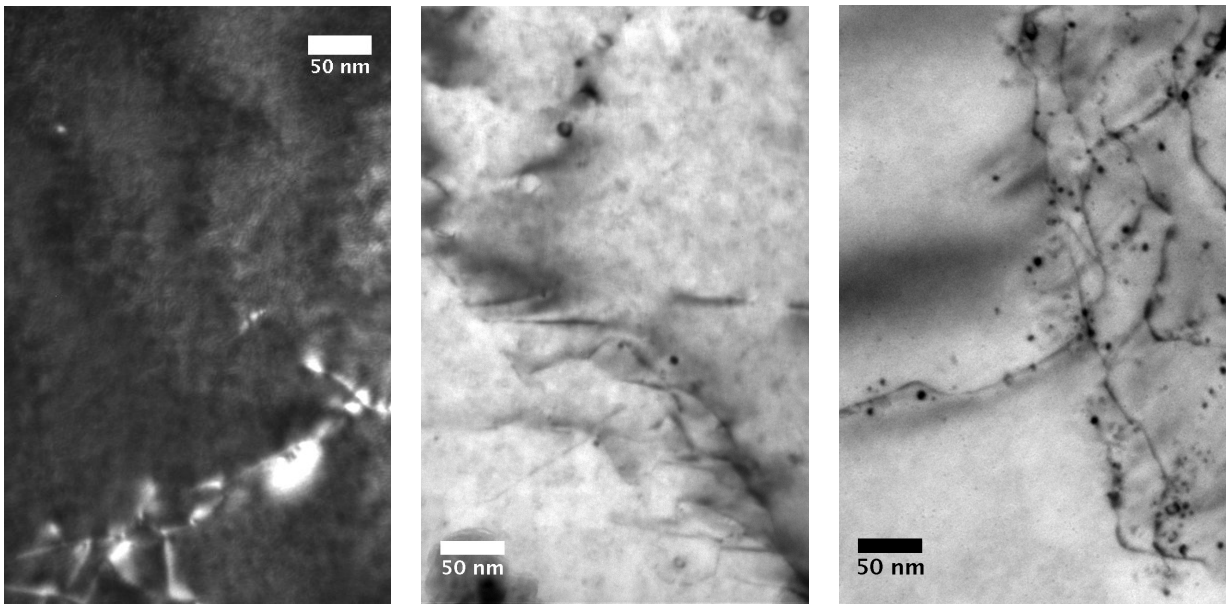

(a) 0.01 dpa (b) 0.1 dpa (c) 1 dpa

Figure 3.17: TEM micrographs of Fe polycrystals irradiated at 300°C as a function of irradiation dose.

The quantitative data regarding dislocation loops and voids is shown in Table 3.1. An increase in loop density with dose is obvious. Compared to the density, the dependence of loop size on the irradiation dose is not straightforward nor monotonic. In general, the mean loop size is 6-8 nm for all three doses. Figure 3.18 indicates that their size distributions do not differ much from each other. The data scattering for 0.01 dpa and 0.1 dpa specimens is a result of insufficient data statistics.

The density of line dislocations do not change with irradiation, as shown in the table, which indicates that no irradiation annealing occurred at this irradiation temperature of

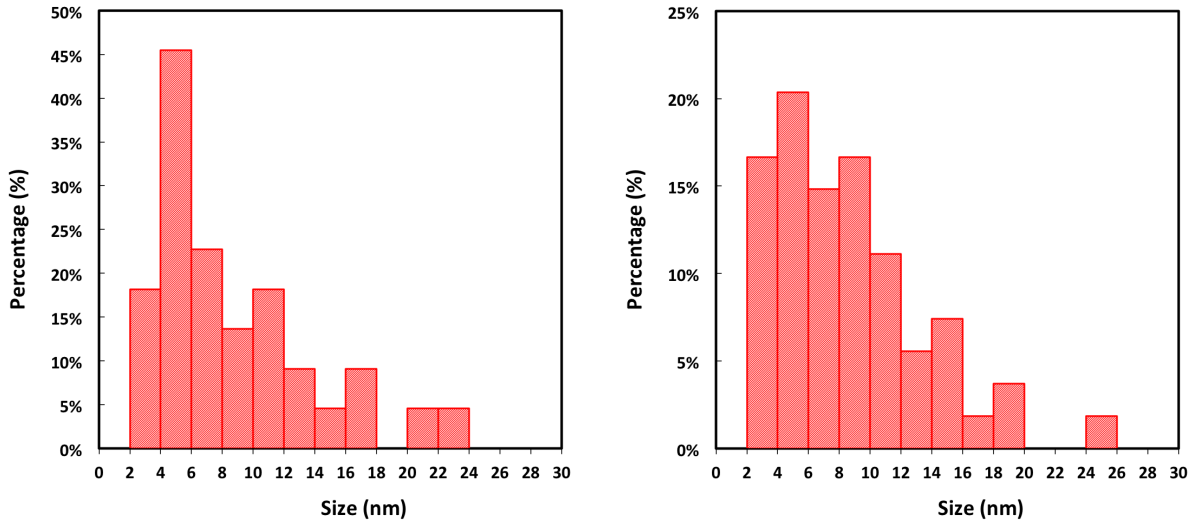

(a) 0.01 dpa Loops

(b) 0.1 dpa Loops

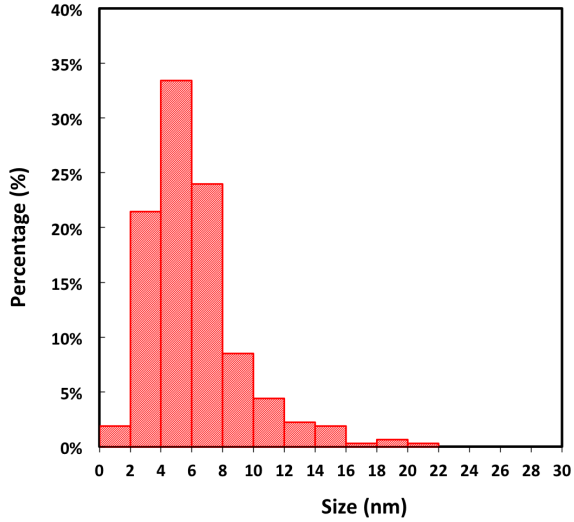

(c) 1 dpa Loops

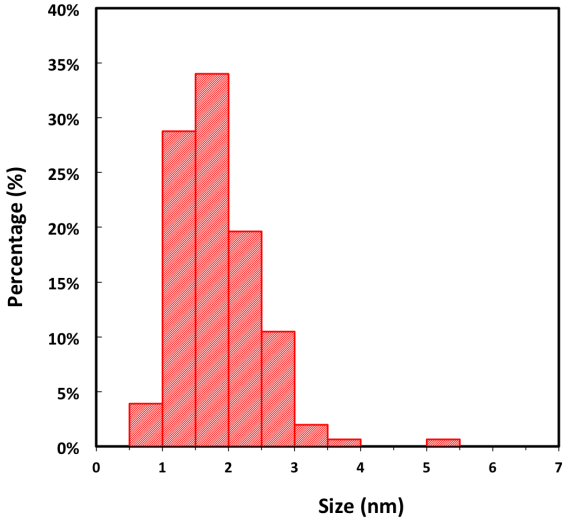

(d) 1 dpa Voids

Figure 3.18: The size distribution of (a)(b)(c) dislocation loops and (d) voids in Fe polycrystals irradiated at 300°C as a function of irradiation dose. The distribution in (a) also include the data from the exceptional area of Figure 3.9

Table 3.1: Microstructure data for Fe irradiated at 300°C

	0.01 dpa	0.1 dpa	1 dpa
Dislocation density (10^{14} $\frac{1}{m^2}$)	1.1	1.2	1.2
$\bar{d}_{loop}$ (nm)	6.1 (8.5 [a])	8.5	6.0
$d_{loop,Max}$ (nm)	10.9 (22.0 [a])	19.2	20.54
N_{loop} (10^{20} $\frac{1}{m^3}$)	1.9	11.7	50
$\bar{d}_{void}$ (nm)	-	-	1.8
$d_{void,Max}$ (nm)	-	-	5.0

[a] If the exceptional area of Figure 3.9 is included.

300°C. The voids, with a size larger than TEM resolution limit, do not form until 1 dpa. The size of voids is comparably larger (5.0 nm maximum) than that observed in Fe irradiated at room temperature to 0.79 dpa (1.5 nm maximum [31]).

3.1.8 Fe-10Cr poly-crystals irradiated at 300C to 0.01dpa

Figure 3.19 is the TEM micrographs of a Fe-10Cr polycrystalline specimen irradiated at 300°C to 0.01 dpa. When the specimen was being examined, it had been stored in dehydrated ethanol for about one and half months. A layer of contamination formed on the TEM foil surface, which significantly degraded the quality of TEM images. Particularly, the contamination layer seems to have certain stresses that resulted in some features with a contrast similar to dislocation loops. These artificial contrasts greatly confused the real dislcoation loops induced by irradiations.

Hence, plasma cleaning with low energy argon ions was used to removed the contamination. Plasma cleaning was a known technique to effectively remove the carbon-based contamination on TEM foils without inducing much artificial irradiation damages that may raise confusions. Figure 3.19 is the TEM micrographs obtained after the plasma cleaning. Although there was still a little contamination not being removed as shown with the black arrows in the figure, the quality of TEM image had been greatly improved.

The density of line dislocations is 8.6×10^{12} $\frac{1}{m^2}$. The line dislocations were original microstructure and were not induced by irradiations. The density of visible irradiation-induced

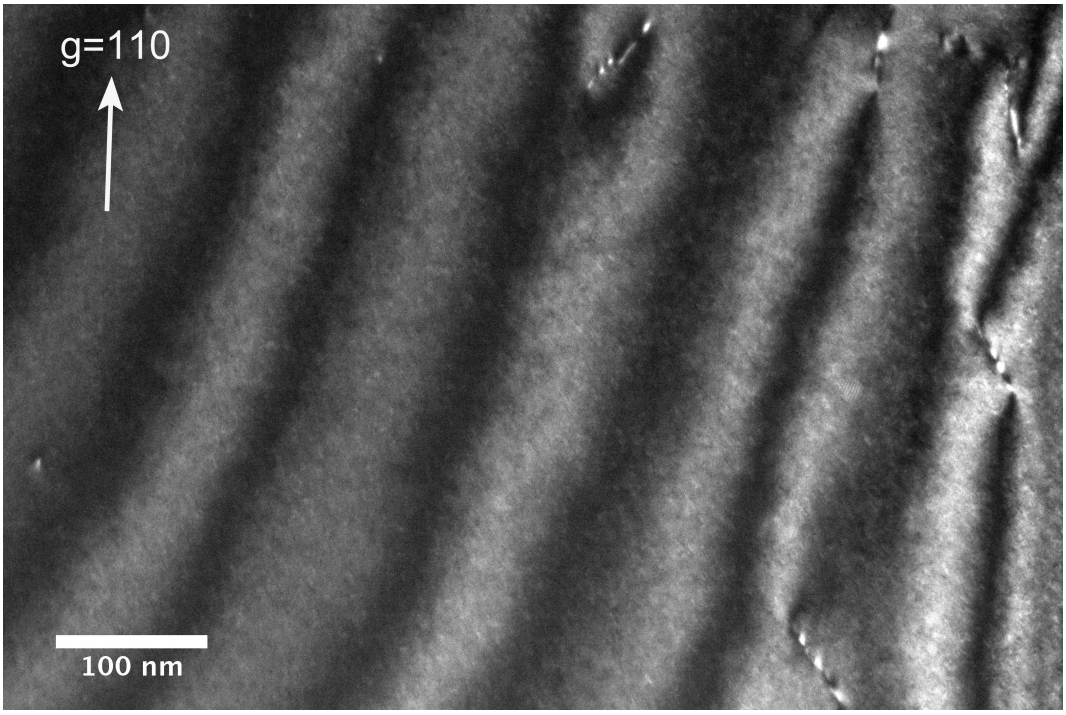

(a) DF

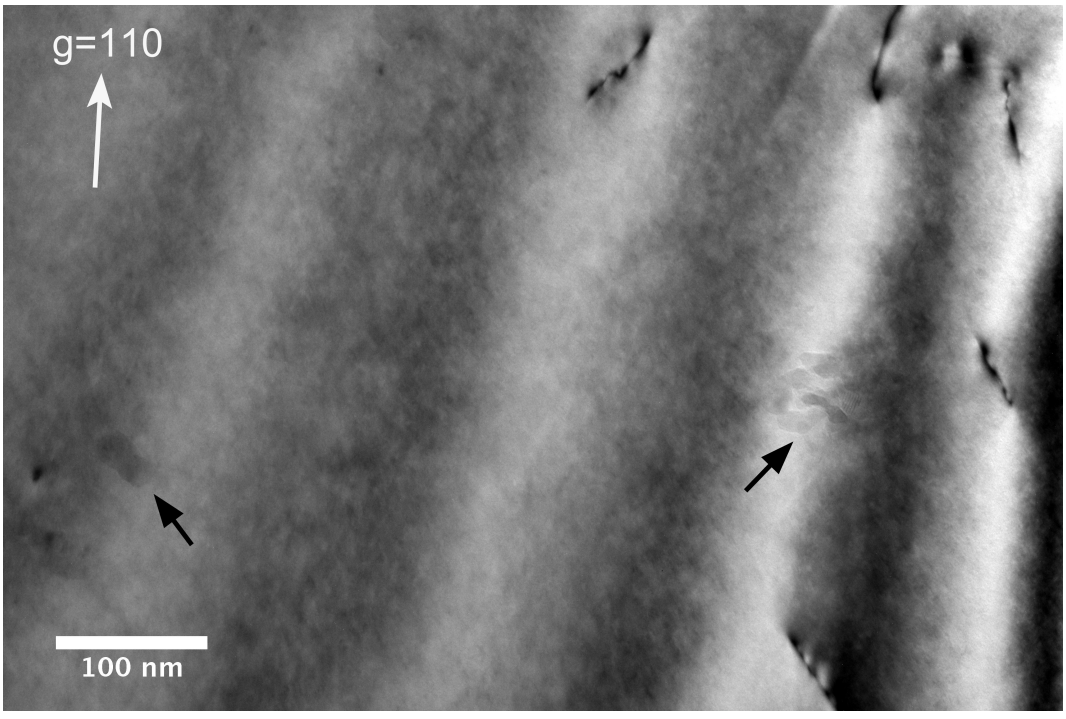

(b) BF

Figure 3.19: TEM images of Fe-10Cr poly-crystal irradiated at 300°C to 0.01 dpa. The imaging condition is g = 110 kinematic for BF and (g, 4.3g) for the DF. The foil thickness at the center of the image is roughly 40 nm

dislocation loops is 1.7×10^{19} $\frac{1}{m^3}$, which is fairly low. As shown in Figure 3.19, only one or two dislocation loops with a size around 3 nm were observed in the examined areas. No dislocation decoration were noted in this specimen.

3.1.9 Fe-10Cr poly-crystals irradiated at 300C to 0.1dpa

Figure 3.20 shows the TEM micrographs of a Fe-10Cr poly-crystalline specimen irradiated at 300°C to 0.1 dpa. The mean density of line dislocations is $5.43\times10^{12}\frac{1}{m^2}$ by measuring a total area of 70 μm^2. Figure 3.21 is the zoomed-in TEM micrographs that show the small defect clusters caused by the neutron irradiations. In each micrograph, only one or two evident dislocation loops with a size of 3-4 nm were observed. The background seems to be more noisy compared to the 0.01 dpa specimen (ex. Figure 3.19), implying the specimen might contain a high density of very small loops. However, their contrast is too small and too dim to be dislocation loops for sure. In terms of the visible loops (the sure loops), their density is measured to be 7.31×10^{19} $\frac{1}{m^3}$.

Some line dislocations were found decorated by small dislocation loops. In Figure 3.22(a), the small dislocation loops were observed to attach at one side of the line dislocation. This is in line with the observations in Fe-10Cr single-crystalline specimen of the same irradiation condition (Chapter 3.1.13). In Figure 3.22(b), small dislocation loops were observed to be in the vicinity of line dislocations and not in the matrix. However, the phenomenon of one-sided decoration is not evident since the amount of small dislocation loops is too low to have sufficient statistics. While line dislocation decoration is a commonplace in the Fe-10Cr single crystalline specimen of the same irradiation condition, most of the line dislocations in this Fe-10Cr poly-crystalline specimen were not decorated (e.g. the line dislocations in Figure 3.21).

3.1.10 Fe-10Cr poly-crystals irradiated at 300C to 1dpa

Figure 3.23 shows the TEM micrographs of the same area in a Fe-10Cr poly-crystal irradiated at 300°C to 1 dpa with varying magnifications. The irradiation damage took the form of

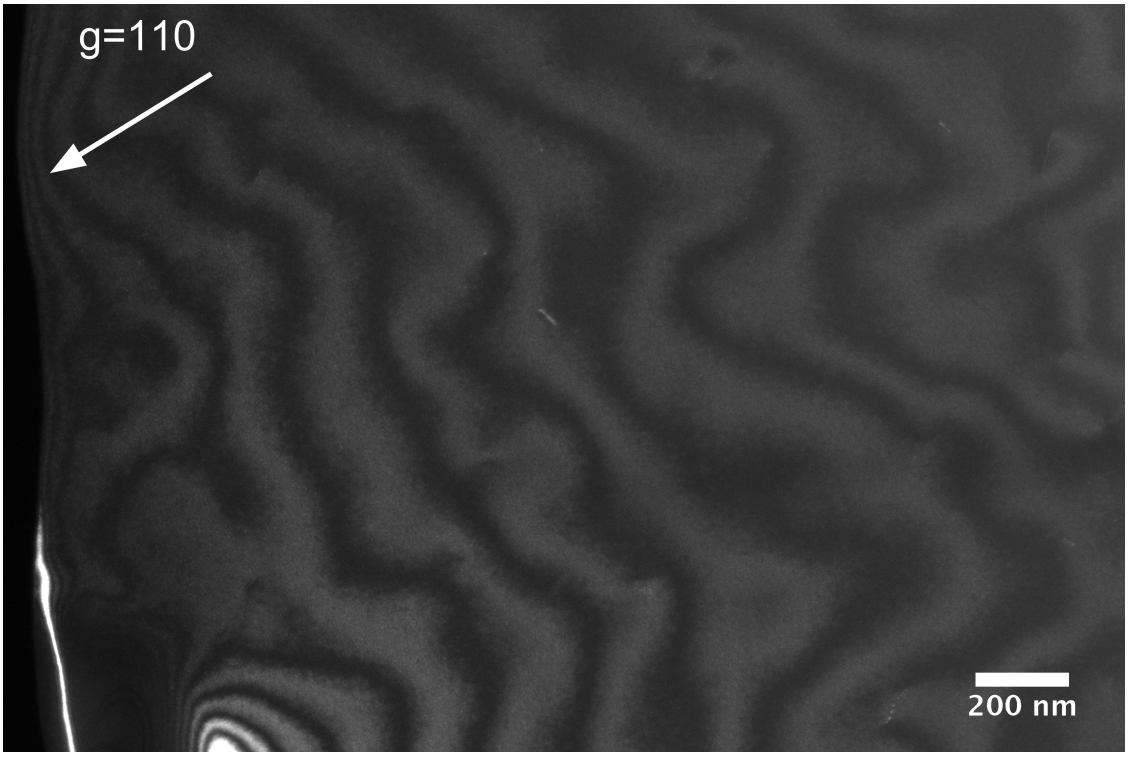

Figure 3.20: Low magnification TEM images of Fe-10Cr poly-crystal irradiated at 300°C to 0.1 dpa. The imaging condition is g = 110 (g, 4.3g) DF.

uniformly-distributed small dislocation loops 6.5 nm with average size of 6.0 nm and density of $1.0\times10^{22}\frac{1}{m^3}$. There are hardly any visible dislocation lines in Figure 3.23. This observation implies that this specimen was very *clean* before irradiation.

Figure 3.24, 3.25 and 3.26 are nearby areas imaged with different diffraction conditions: g = 110, 200 and 020, respectively. All of the images were taken close to (001) zone axis. Although these three data sets were not taken in the exact same area, the Burgers vector of dislocation loops in these images could be readily identified considering the projection shapes and the invisibility results of the dislocation loops. A mixture of $\langle100\rangle$ and $\frac{1}{2}\langle111\rangle$ dislocation loops was observed. In Figure 3.24, selected loops marked with letters 'a' are inclined dislocation loops consistent with a Burger vectors of $\frac{a}{2}[111]$ or $\frac{a}{2}[\bar{1}\bar{1}1]$ and a habit plane of, respectively, (111) and $(\bar{1}\bar{1}1)$. The dislocation loops marked with 'b' and 'c' are edge-on loops with a habit plane, respectively, on (100) and (010), which is 45° rotated from loops 'a'. Considering their visibility under g = 200 and g = 020 in Figure 3.25 and 3.26, they are concluded to be a[100](100) and a[010](010) loops. Dislocation loops of $\frac{a}{2}[\bar{1}1\bar{1}](\bar{1}1\bar{1})$,

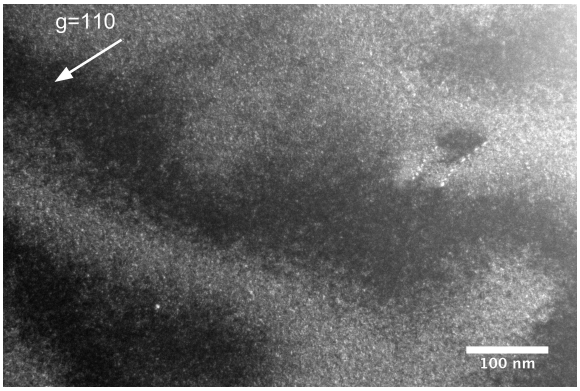

(a) WBDF Area 1

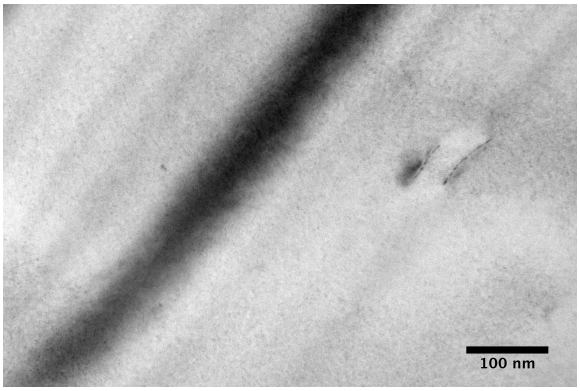

(b) BF Area 1

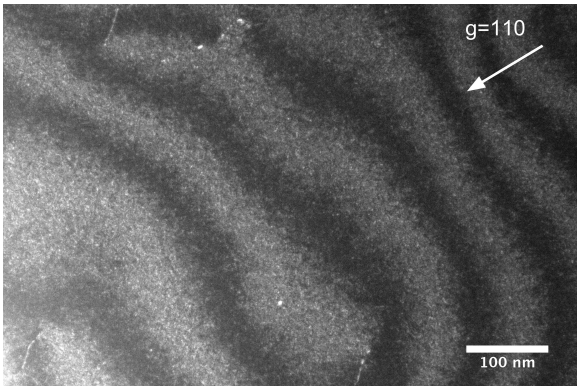

(c) WBDF Area 2

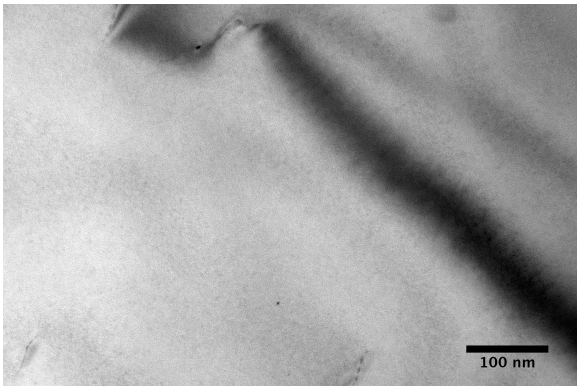

(d) BF Area 2

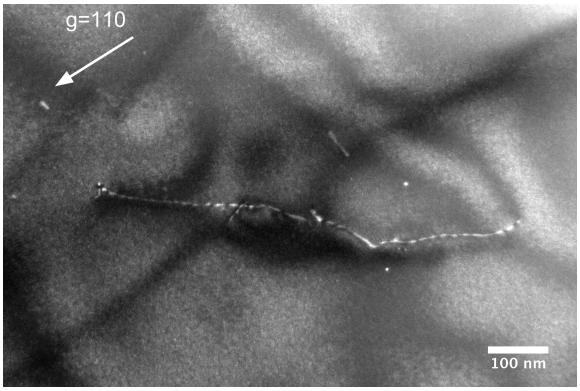

(e) WBDF Area 3

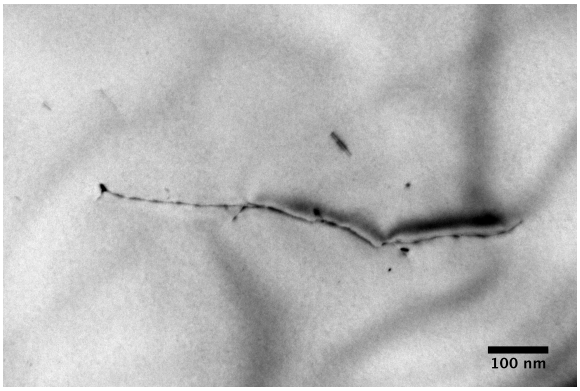

(f) BF Area 3

Figure 3.21: TEM images of Fe-10Cr poly-crystal irradiated at 300°C to 0.1 dpa. The imaging condition is g = 110 (g, 3g) for BF and (g, 4.3g) for the DF. The foil thickness at the center of Area 1 and Area 2 is estimated to be 90 nm and 140 nm, respectively. The thickness for Area 3 was not determined.

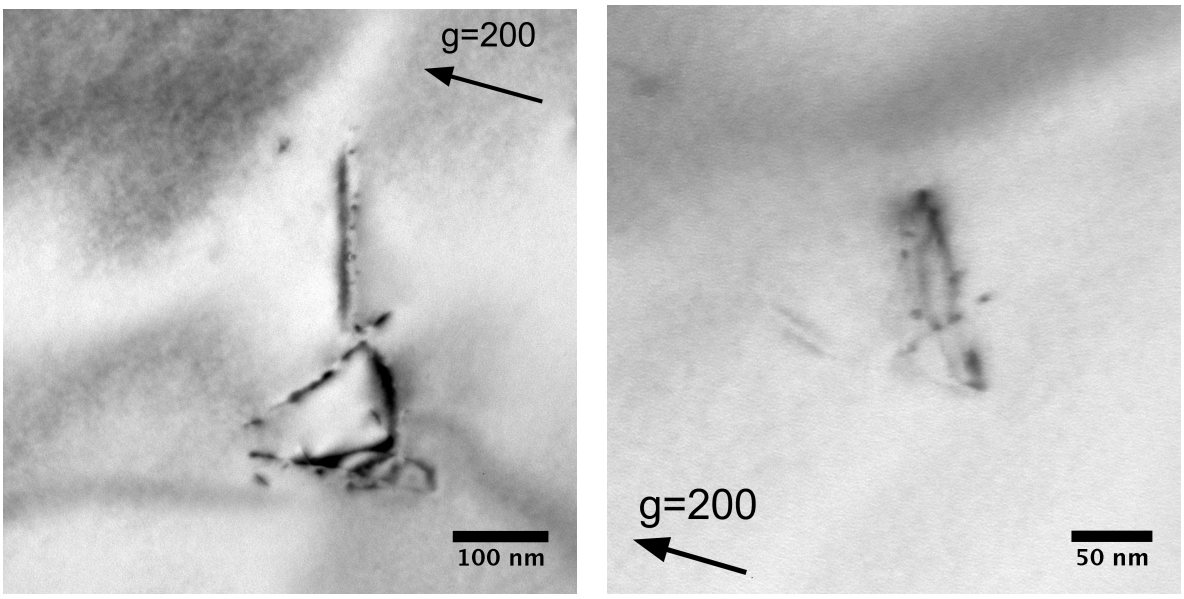

(a) WBDF (b) BF

Figure 3.22: TEM images of Fe-10Cr poly-crystal irradiated at 300°C to 0.1 dpa. The imaging condition is g = 200 with the electron beam close to [001] direction.

$\frac{a}{2}[1\bar{1}1](1\bar{1}1)$ and a[001](001) are invisible in Figure 3.24 because they satisfy the invisibility criterion g·b = 0. The percentage of a⟨100⟩ and $\frac{a}{2}\langle 111\rangle$ dislocation loops was measured based on Figure 3.24. 47% and 24% (roughly 2:1) of the loops are a⟨100⟩ loops and $\frac{a}{2}\langle 111\rangle$ loops. The Burgers vector of 28% of the loops could not be determined mostly because of their small size that made it impossible to determine their habit planes. The above result is not corrected with the fact that some loops are invisible under g=110 imaging condition. If it is taken into account, a ratio of 3:2 between a⟨100⟩ loops and $\frac{a}{2}\langle 111\rangle$ loops are estimated.

Finally, voids formation had been investigated with the use of under-over focus techniques, as shown in 3.27. Features with contrast similar to voids (i.e. dark when over-focused and white when under-focused) exists, however it was very small and indistinct. Also, if these features were voids, the observed areal density of voids should be proportional to the TEM foil thickness. In Figure 3.27, such proportionality is not evident. Therefore, it is considered that the contrast was surface features such as surface roughness or oxidation, and not as real voids or bubbles.

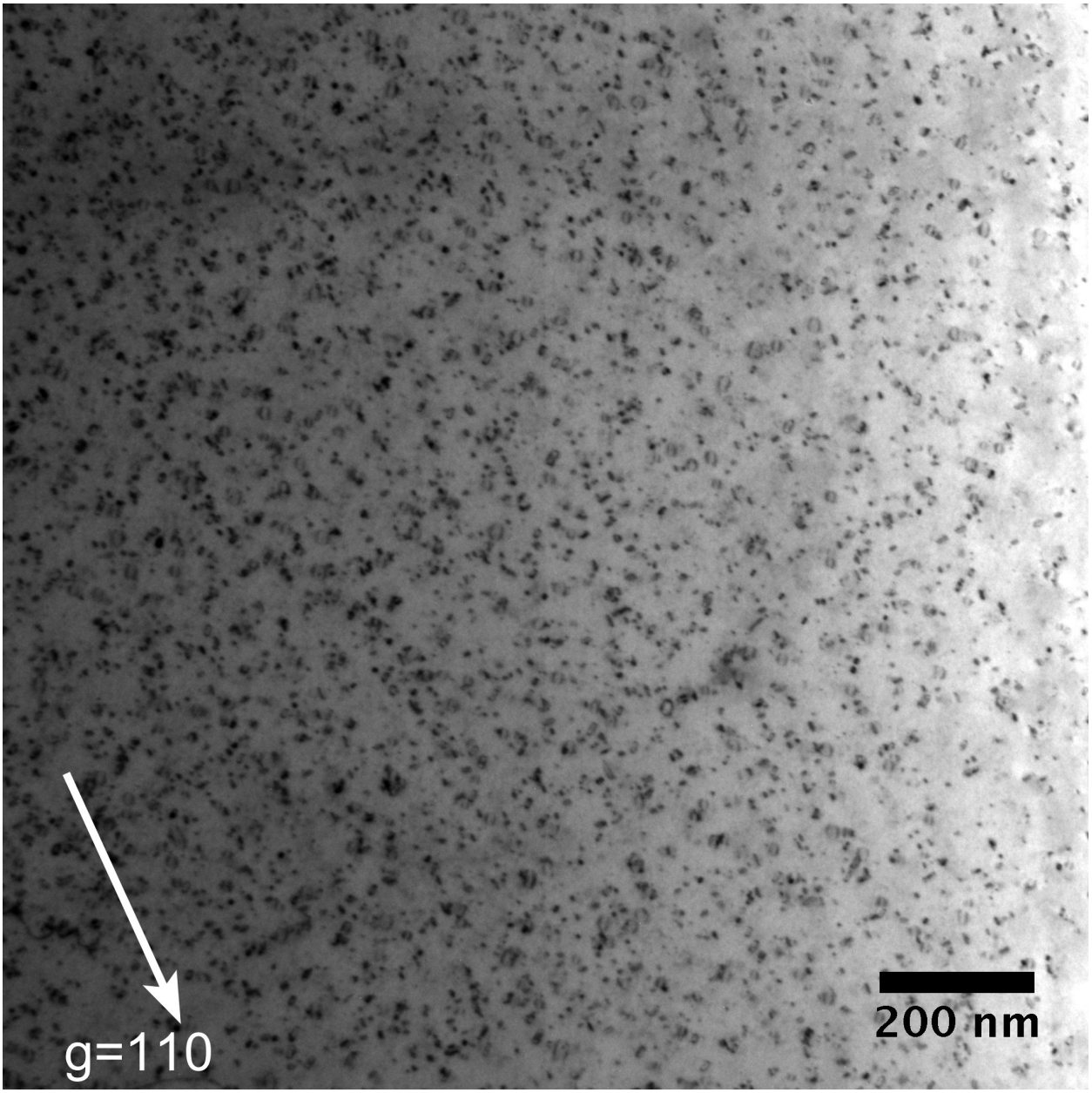

Figure 3.23: TEM images of Fe-10Cr poly-crystal irradiated at 300°C to 1 dpa. Images were taken at the same area with different magnifications. The imaging condition was g = 110 (g, 3g).

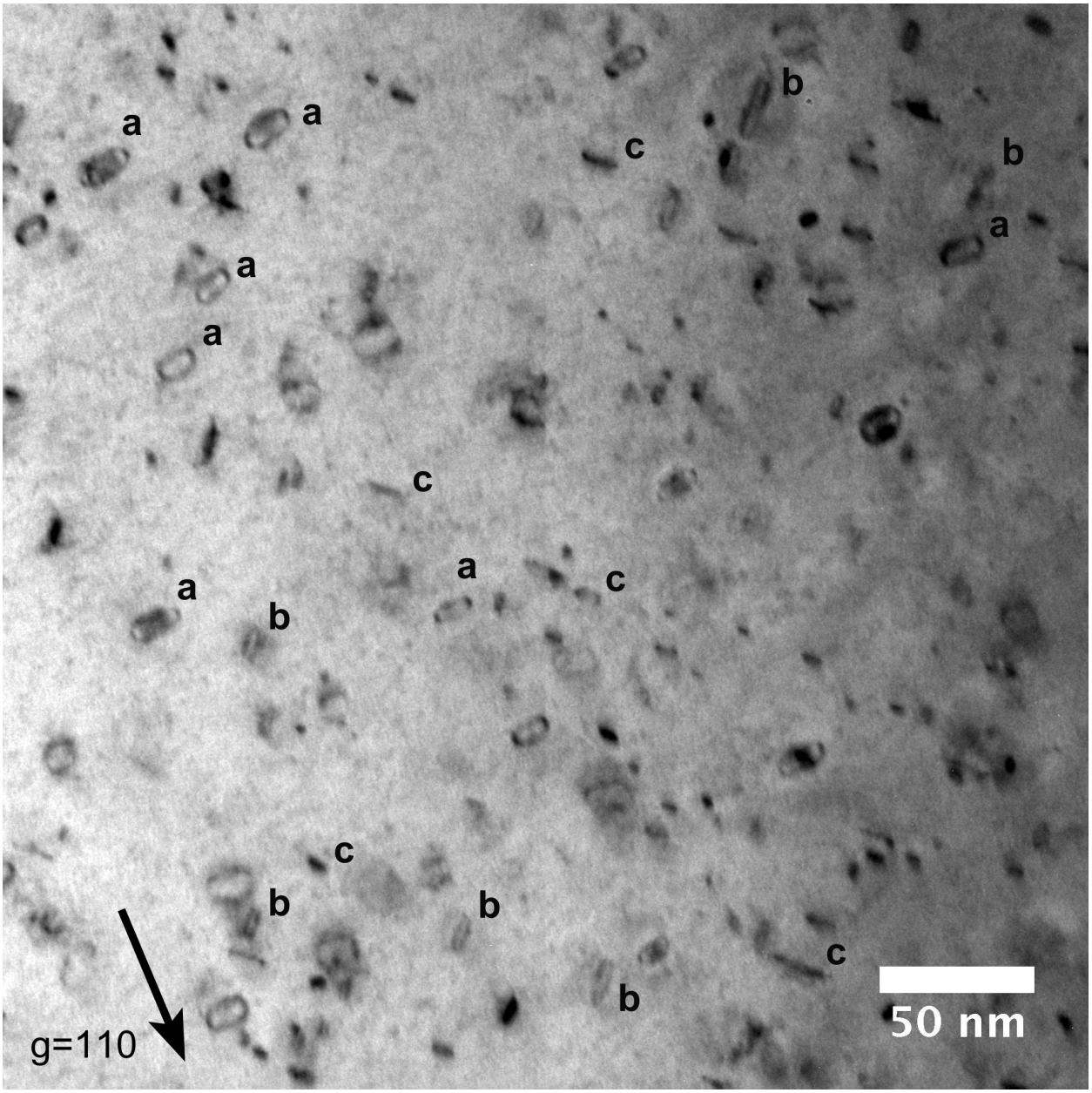

Figure 3.24: TEM images of Fe-10Cr poly-crystal irradiated at 300°C to 1 dpa.The electron beam was close to the [001] direction of the crystal. The imaging condition was g = 110 (g, 3g) for bright-field.

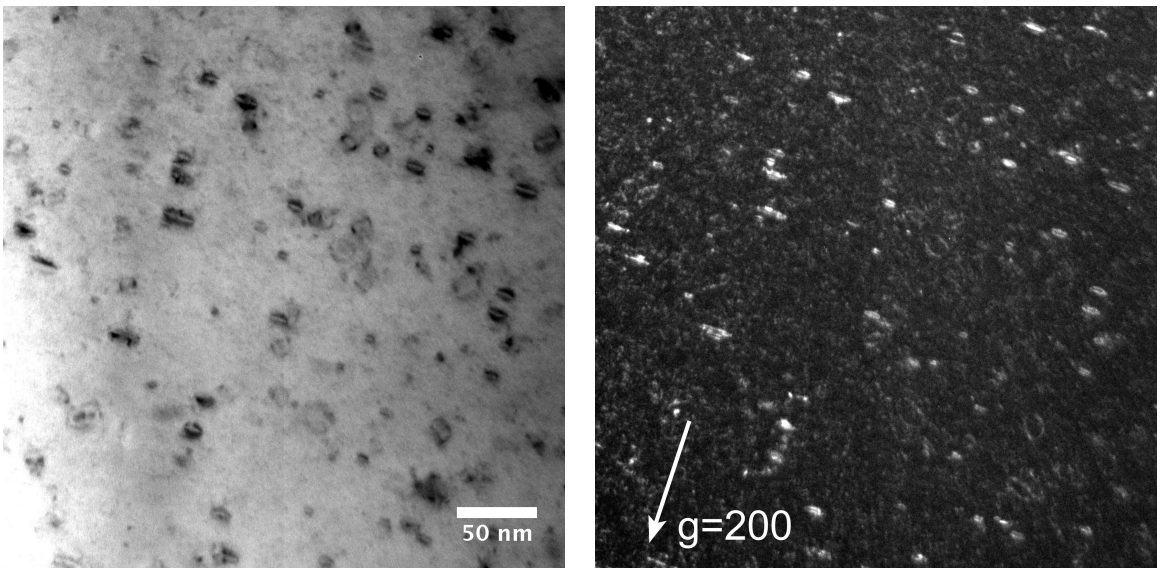

(a) BF (b) WBDF

Figure 3.25: TEM images of Fe-10Cr poly-crystal irradiated at 300°C to 1 dpa. The electron beam was close to the [001] direction of the crystal. The imaging condition was g = 200 (g, 3g) for dark-field and kinematic for bright-field.

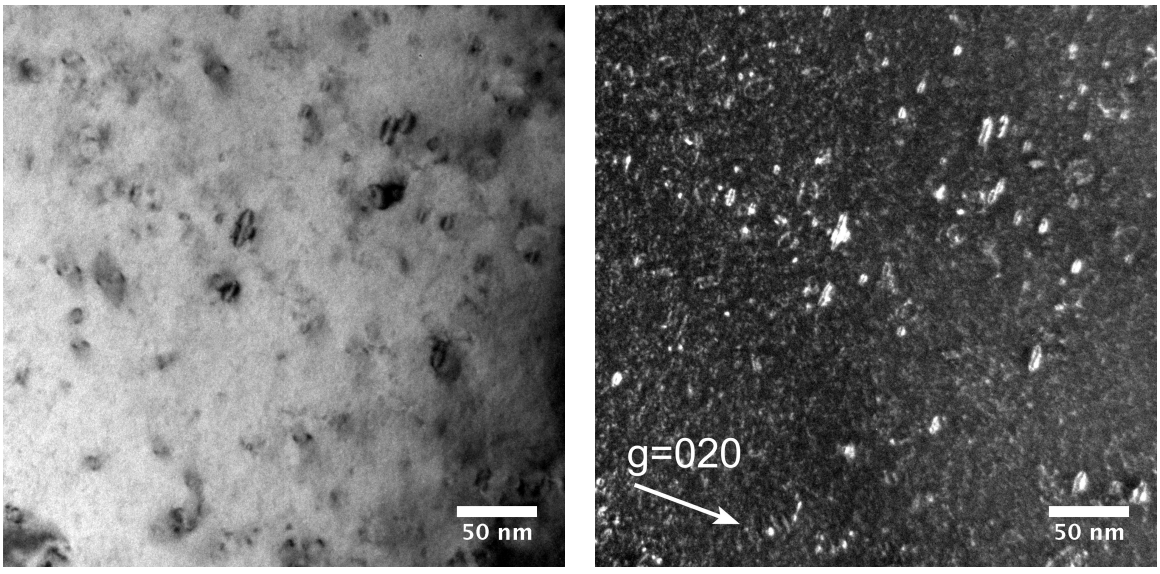

(a) BF g = 020 (b) WBDF g = 020

Figure 3.26: TEM images of Fe-10Cr poly-crystal irradiated at 300°C to 1 dpa. The electron beam was close to the [001] direction of the crystal. The imaging condition was g = 020 (g, 3g) for DF and kinematic for BF.

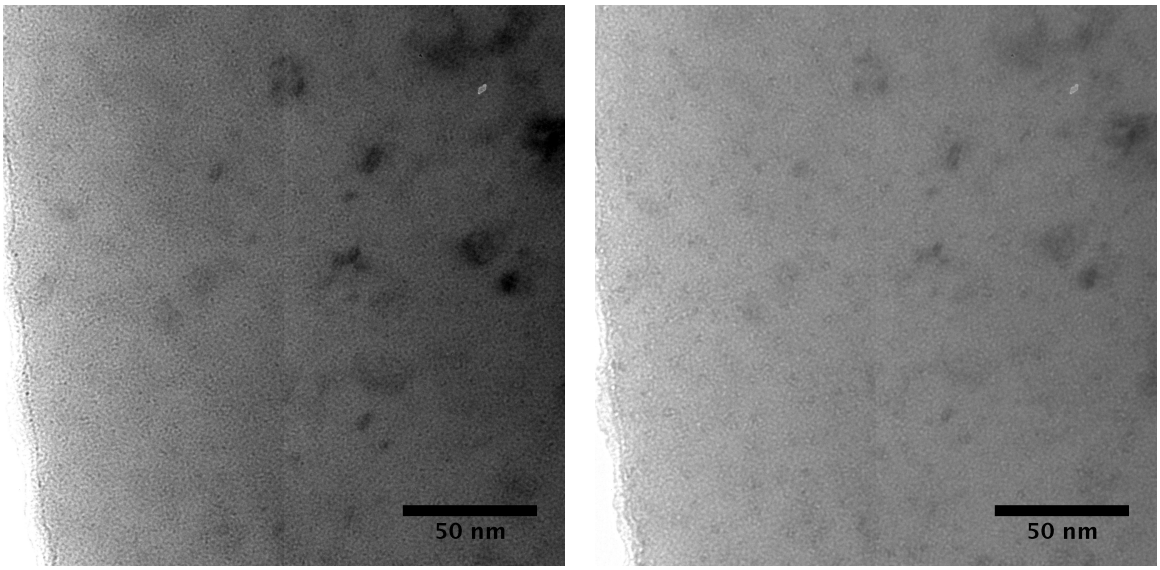

(a) BF Over-focused (b) BF Under-focused

Figure 3.27: TEM images of Fe-10Cr poly-crystal irradiated at 300°C to 1 dpa. The electron beam was close to the [001] direction of the crystal. The imaging condition was over and under-focused g = 110 kinematic BF.

3.1.11 Summary of Fe-10Cr poly-crystals irradiated at 300C

The TEM micrographs of Fe-10Cr polycrystals irradiated at 300° to 0.01, 0.1 and 1 dpa are compared in Figure 3.28. The quantitative measurements of defect and defect clusters are shown in Table 3.2. Both 0.01 dpa and 0.1 dpa Fe-10Cr specimens exhibit a very low loop density. The 1 dpa Fe-10Cr specimen has a significantly higher loop density, about 2-3 orders of magnitude higher. While 0.01 and 0.1 dpa Fe-10Cr specimens exhibit only 'dot' dislocation loops with a size around 3-4 nm, the 1 dpa Fe-10Cr specimen contains much larger loops with an average size of 6.5 nm. Many loops in 1 dpa specimens are as large as 10-20 nm and have resolvable shapes. The size distribution of the dislocation loops for 1 dpa Fe-10Cr polycrystal specimen is shown in Figure 3.29. The Burgers vector of these resolvable loops is a mixture of both $\frac{a}{2}\langle 111\rangle$ and $a\langle 100\rangle$ with a ratio estimated as 2:3. No evident voids were found in all of the three 300°C specimens.

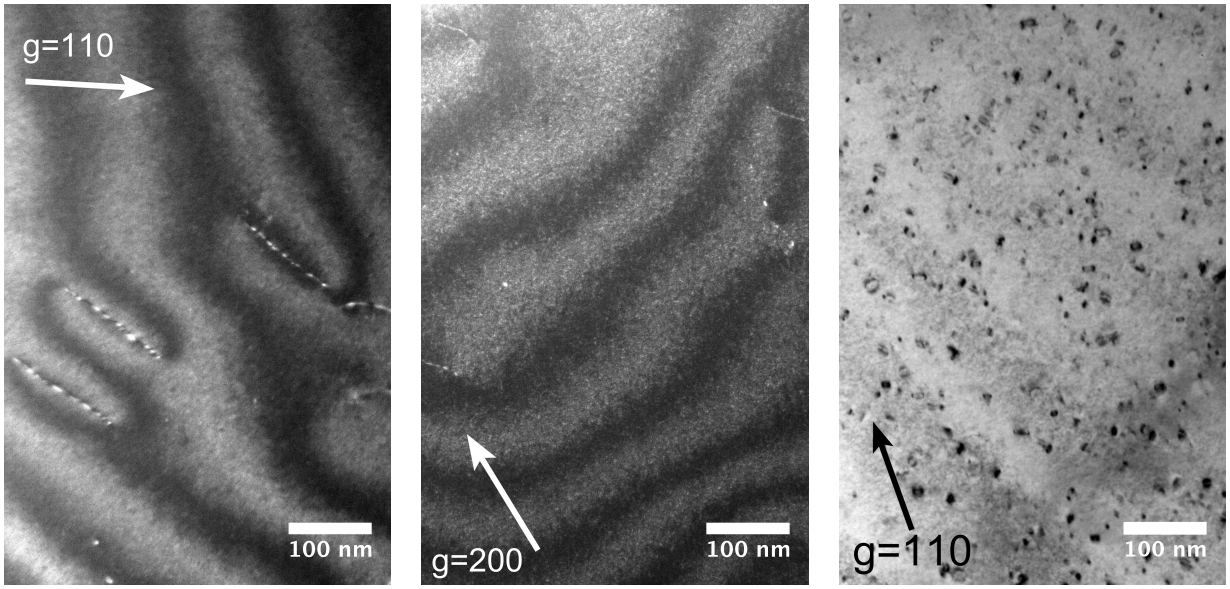

(a) 0.01 dpa (b) 0.1 dpa (c) 1 dpa

Figure 3.28: TEM micrographs of Fe-10Cr polycrystals irradiated at 300°C as a function of irradiation dose.

Table 3.2: Microstructure data for Fe-10Cr polycrystals irradiated at 300°C

	0.01 dpa	0.1 dpa	1 dpa
Dislocation density (10^{12} $\frac{1}{m^2}$)	8.6	5.43	-
$\bar{d}_{loop}$ (nm)	3.5	3.5	6.5
$d_{loop,Max}$ (nm)	4.95	6.59	19.03
N_{loop} (10^{20} $\frac{1}{m^3}$)	0.17	0.73	100
$\bar{d}_{void}$ (nm)	Not observed		
$d_{void,Max}$ (nm)	Not observed		

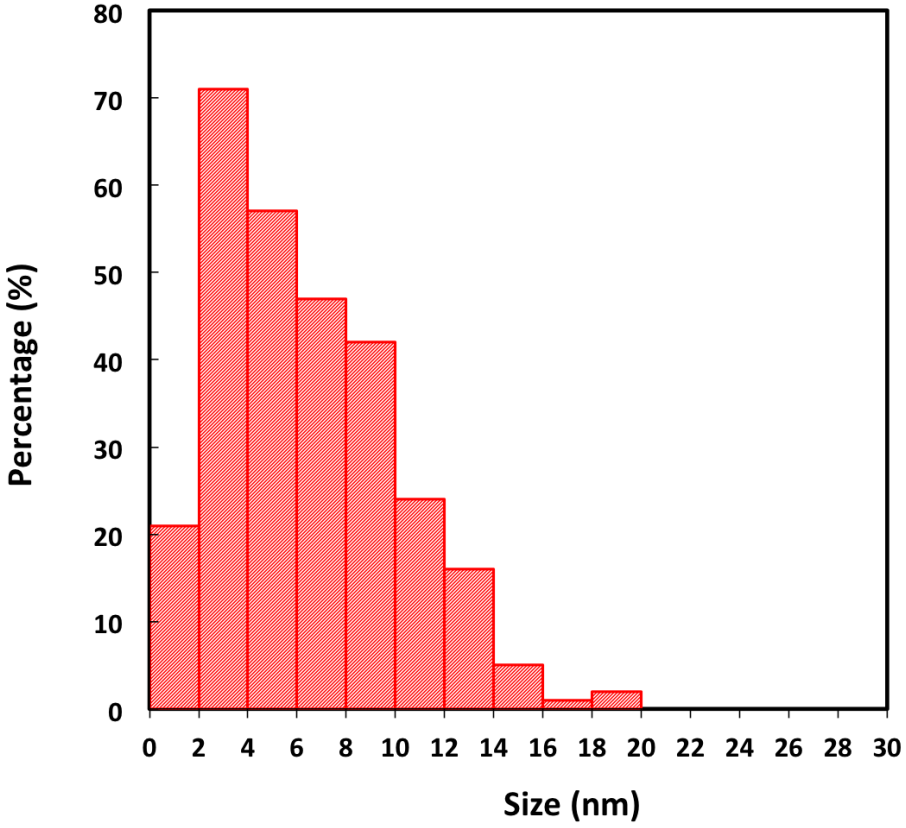

Figure 3.29: The size distribution of dislocation loops in Fe-10Cr polycrystals irradiated at 300°C to 1 dpa.

3.1.12 Fe-14Cr single-crystals irradiated at 300C to 0.01dpa

The TEM micrographs of Fe-14Cr single crystal irradiated at 300°C to 0.01 dpa are shown in Figure 3.30 and Figure 3.31 with two magnifications and two diffraction conditions (g = 110 and g = 200). The density of line dislocations is less than 10^6 $\frac{1}{m^2}$, which is negligible. Radiation damage took the form of uniformly-distributed dislocation loops. The loops are small, having an average size $\bar{d}_{loop}$ of 2.6 nm.

The small size of the dislocation loops posed difficulties for density measurement because it is sometimes hard to distinguish dislocation loops from the noise. The noise resembles the look of small dislocation loops (small white spots in WBDF) and could overwhelm the contrast of dislocation loops for certain diffraction conditions. For instance, the left two white bands in Figure 3.30(e) have a stronger diffraction condition (perhaps due to slight bending), resulting a higher noise that make it hard to identify the real dislocation loops. The right-hand side of Figure 3.30(e), on the other hand, was in a better diffraction condition and the dislocation loops can be recognized with much higher certainty.

This issue is especially serious when it comes to Figure 3.31. The high magnification micrographs 3.31(e)(f) exhibit a high density of white dots contrast, indicating a much higher density of dislocation loops than it appeared in the low magnification micrographs 3.31(a)(b)(c)(d). The densities of dislocation loops are 1.1 $\times 10^{21}$ $\frac{1}{m^2}$ and 3.3 $\times 10^{21}$ $\frac{1}{m^2}$ by measuring lower and higher magnification micrographs, respectively.

It is difficult to justify which measurement is more correct. Measurement on lower magnification micrographs might under-estimate by overlooking the very small dislocation loops. On the other hand, the measurements on the higher magnification micrographs might over-estimate by counting the noise. Although a further refined measurement is not available, the densities reported above should correspond to the upper and lower bounds of the true density of dislocation loops.

Finally, Figure 3.32 shows the under-and-over-focused TEM micrographs. Features appeared in correspondence to the focus change, but not in a way that resemble the voids. The feature is uniformly distributed over the entire surface, and might be related to contamination or oxidation. These contamination or oxidation are the possible cause for the

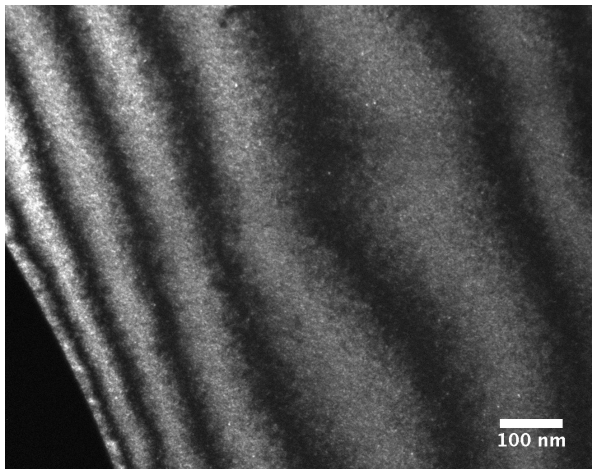

(a) DF Area 1

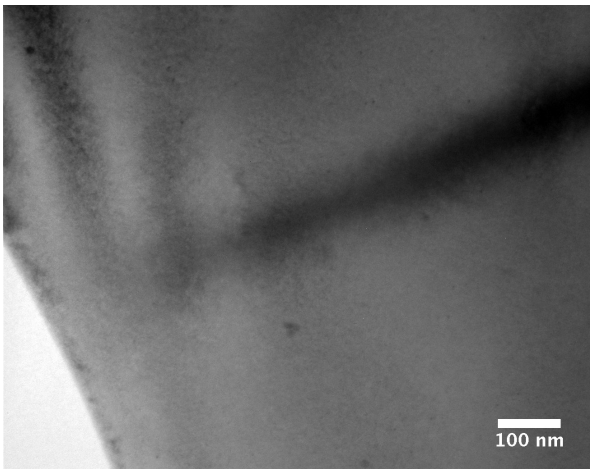

(b) BF Area 1

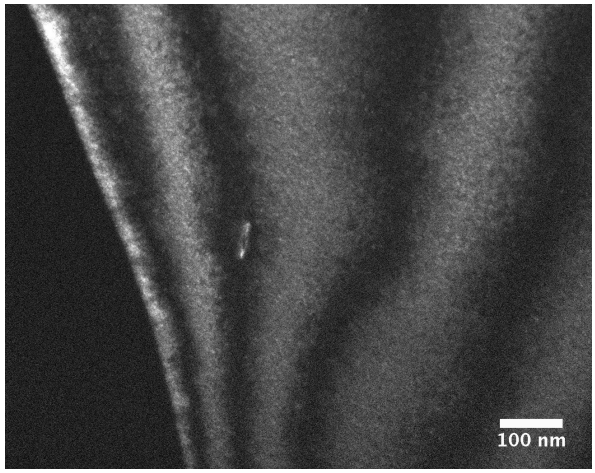

(c) DF Area 2

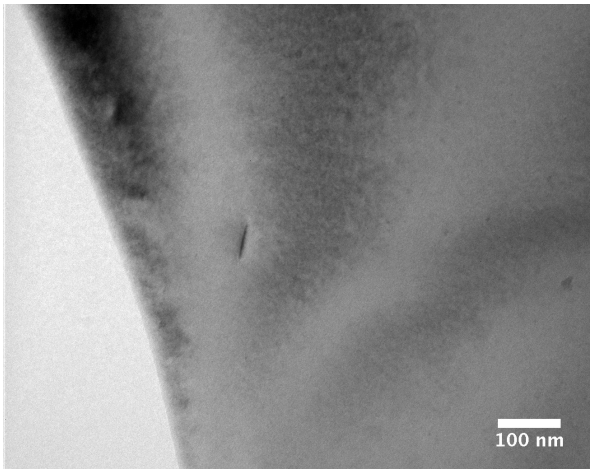

(d) BF Area 2

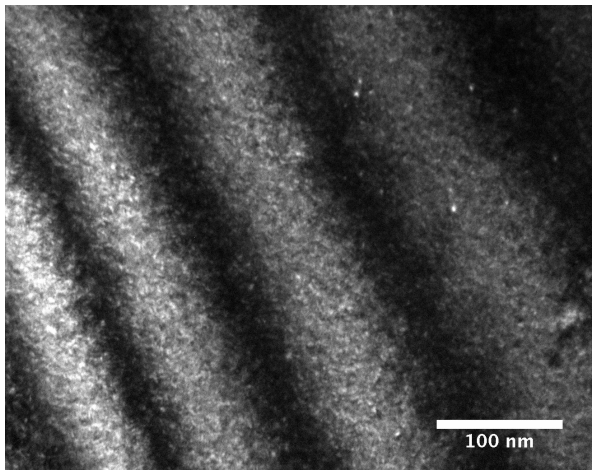

(e) DF High Mag Area 1

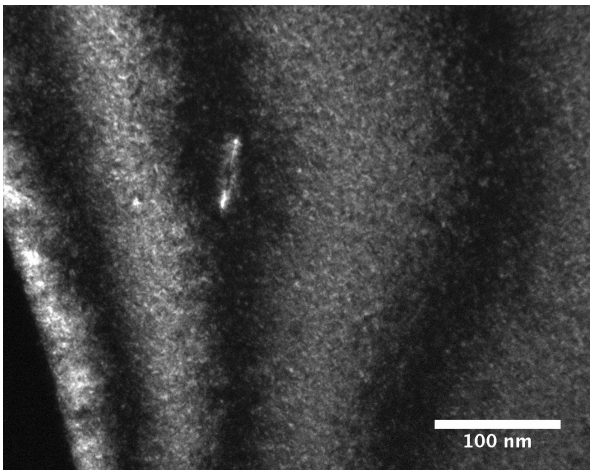

(f) BF High Mag Area 2

Figure 3.30: TEM images of Fe-14Cr single-crystal irradiated at 300°C to 0.01 dpa.The electron beam was close to the [001] direction of the crystal. The imaging condition was g = 110 (g, 4.3g) for DF and kinematic for BF.

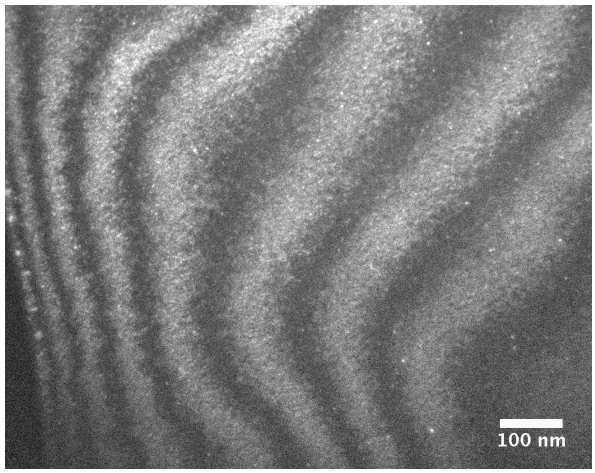

(a) WBDF Area 1

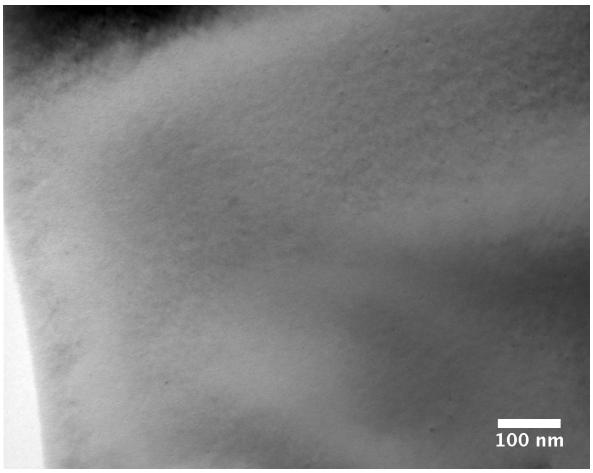

(b) BF Area 1

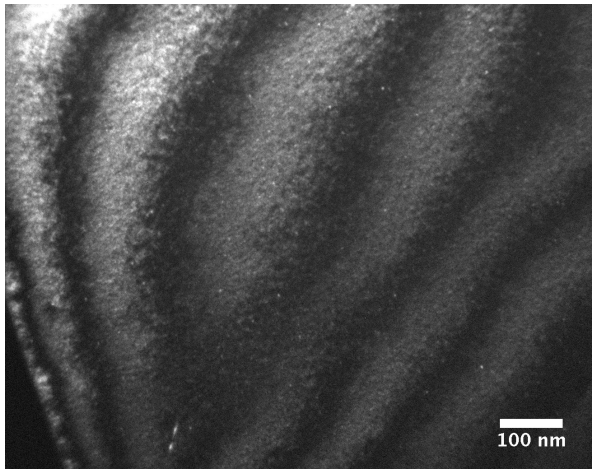

(c) WBDF Area 2

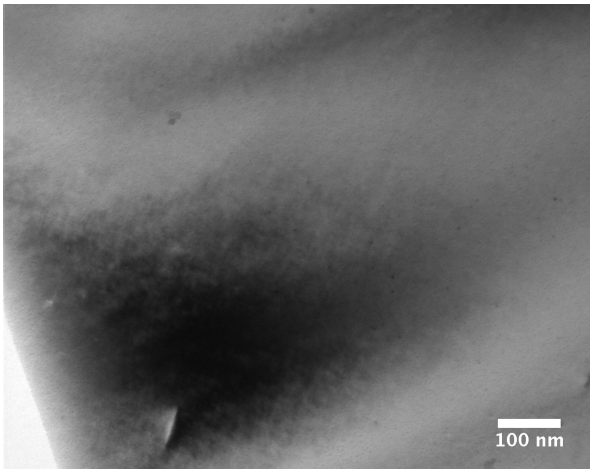

(d) BF Area 2

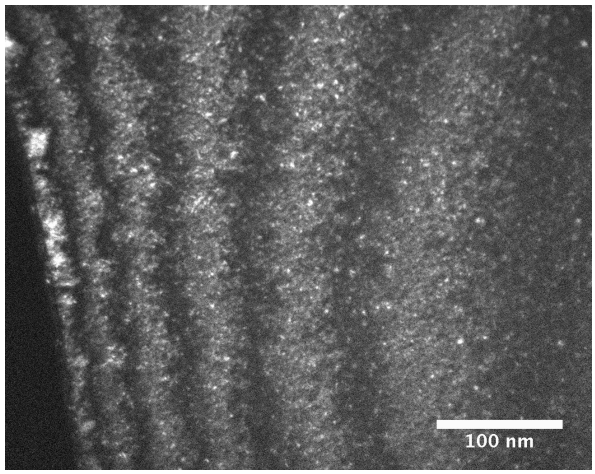

(e) DF Area 1 High Mag

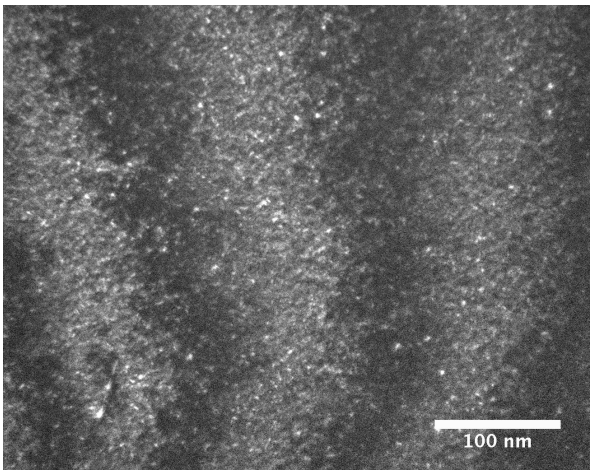

(f) DF Area 2 High Mag

Figure 3.31: TEM images of Fe-14Cr single-crystal irradiated at 300°C to 0.01 dpa.The electron beam was close to the [001] direction of the crystal. The imaging condition was g = 200 (g, 3g) for DF and kinematic for BF.

'dot' contrast that confuse with the real dislocation loops in those high-magnification TEM micrographs sunch as Figure 3.31(e)(f). However, this suggestion is just a speculation, and is not justified.

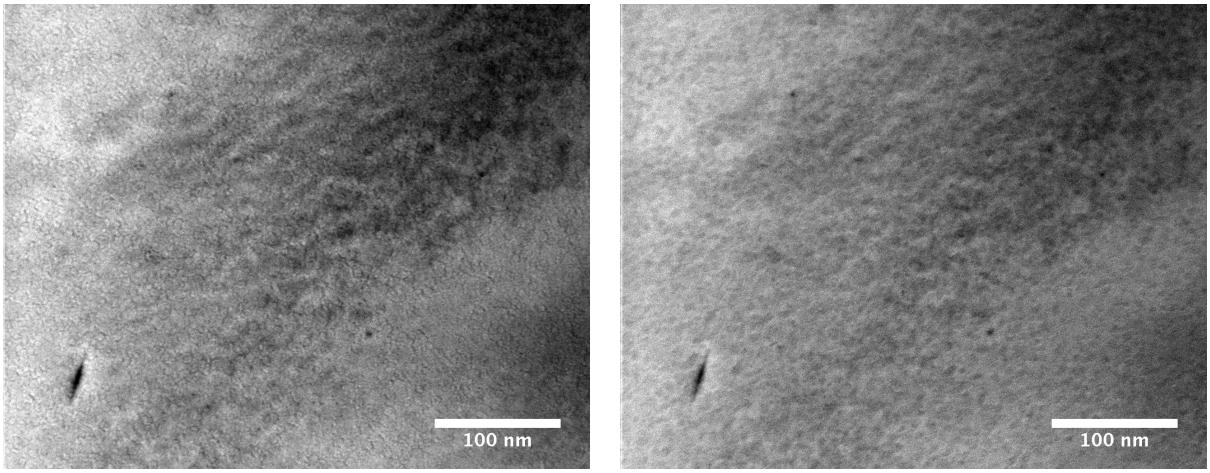

(a) BF under-focused (b) BF over-focused

Figure 3.32: The under and over-focused TEM micrographs of Fe-14Cr single crystal irradiated at 300° to 0.01 dpa. Contrast changes with focus change, but the features turning bright in the under-focused do not match those turning dark in the over-focused.

3.1.13 Fe-10Cr single-crystals irradiated at 300C to 0.1dpa

Figure 3.33 is a low magnification TEM micrograph of Fe10Cr single crystal irradiated at 300°C to 0.1 dpa. The density of line dislocations is higher ($1.4\times10^{13}\frac{1}{m^2}$) in this specimen than in other single crystal specimens of equivalent irradiation dose or lower. Those line dislocations were not caused by irradiations because of the low irradiation dose and temperature. Instead, these dislocations should have existed before irradiation.

Zoomed-in micrograph Figure 3.34 shows that the neutron radiation produced little damage: a fairly low density ($3.2\text{x}10^{20}\ \frac{1}{m^3}$) of small dislocation loops ($\bar{\text{d}}_{loop}$ = 5.21 nm) was observed. While some dislocation loops were occasionally observed in the matrix, many more of the dislocation loops (68%) were found attached to one side of the line dislocations, as shown in Figure 3.35 and 3.36. This inhomogeneity of loop distribution is similar to Fe specimens irradiated at the same temperature of 300°C (section 3.1.6). The Burgers vectors

of the dislocation loops in this specimen could not be determined due to the small size of the loops and the insufficient data from diffraction conditions.

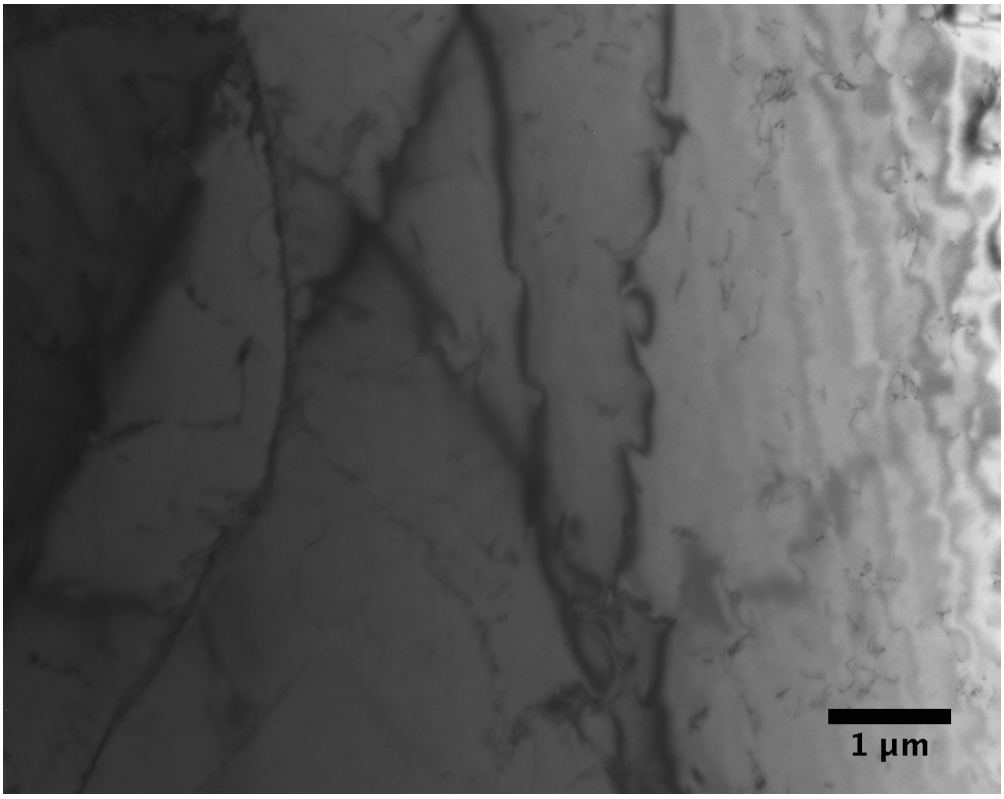

Figure 3.33: TEM image of Fe poly-crystal irradiated at 300°C to 0.1 dpa. The imaging condition is kinematic g = 110 with beam direction close to [001].

3.1.14 Fe-16Cr single-crystals irradiated at 300C to 1dpa

Figure 3.37 shows the TEM micrographs of the same area in a Fe-16Cr single crystal irradiated at 300°C to 1 dpa with various magnifications. The images of the lowest magnification, Figure 3.37(a)(d), show a large examination area featuring a uniform distribution of small dislocation loops. The volume density is $1.5\times10^{22}\frac{1}{m^3}$. The dislocation loops appear as white dots in WBDF and black dots in BF. Figures 3.37(b)(c)(e)(f) are of higher magnification. Many loops are large resolvable loops. The average size $\bar{d}_{loop}$ is 4.88 nm. Note the 90° rotation between Figure 3.37(b)(e) and Figure 3.37(c)(f). This is characteristic of FEI Tecnai TEM. The image rotations between different magnifications were not corrected in this microscope.

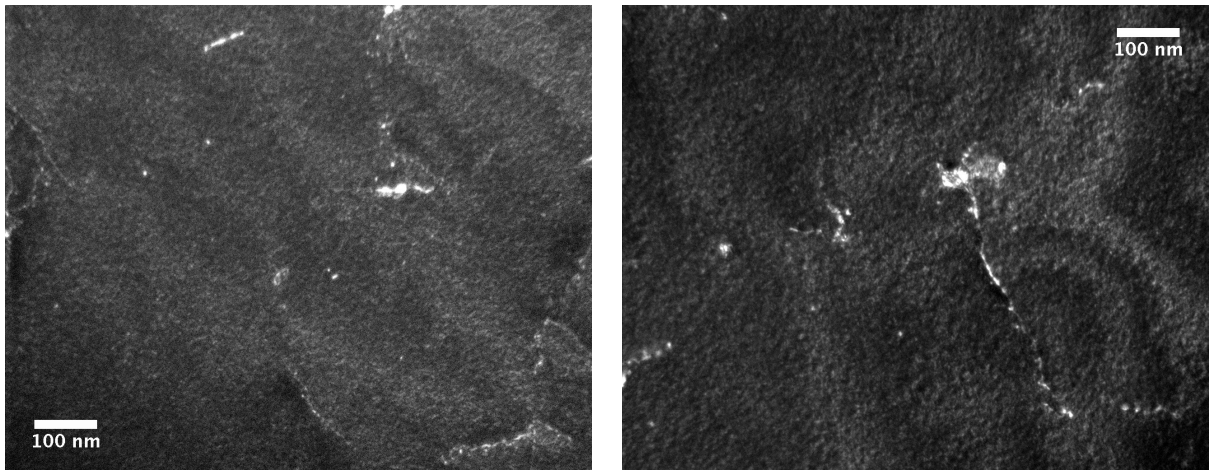

(a) 110g DF (b) 020g DF

Figure 3.34: TEM images of Fe-10Cr single-crystal irradiated at 300°C to 0.1 dpa. Images were taken at (different but nearby) areas with (a) g = 110 (g, 4.3g) and (b) g = 020 (g, 3g). The electron beam was close to the [001] direction of the crystal.

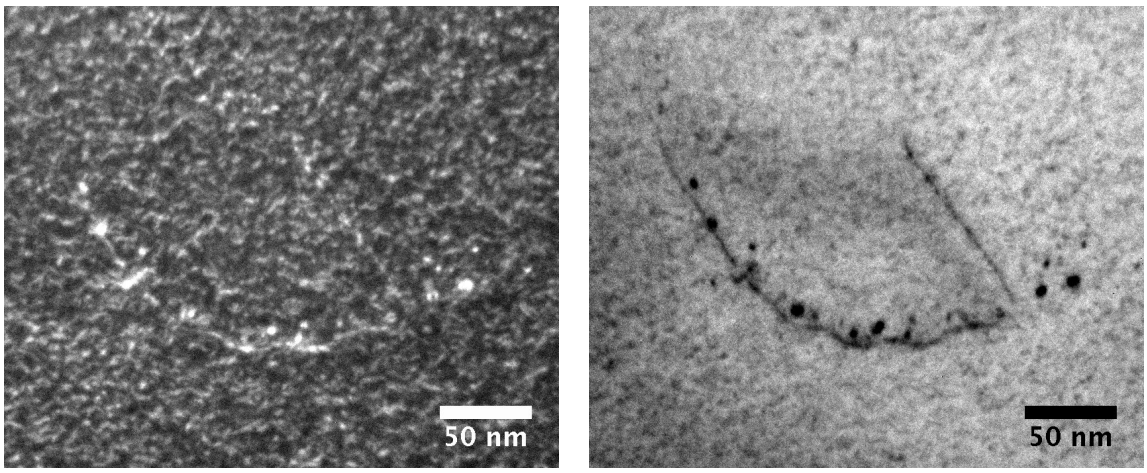

(a) DF (b) BF

Figure 3.35: TEM images of Fe-10Cr single-crystal irradiated at 300°C to 0.1 dpa with a higher magnification to show the microstructure of dislocation decoration. The imaging condition is g = 110 (g, 4.3g) for DF (a) and kinematic for BF (b). The electron beam is close to [001] orientation of the crystal.

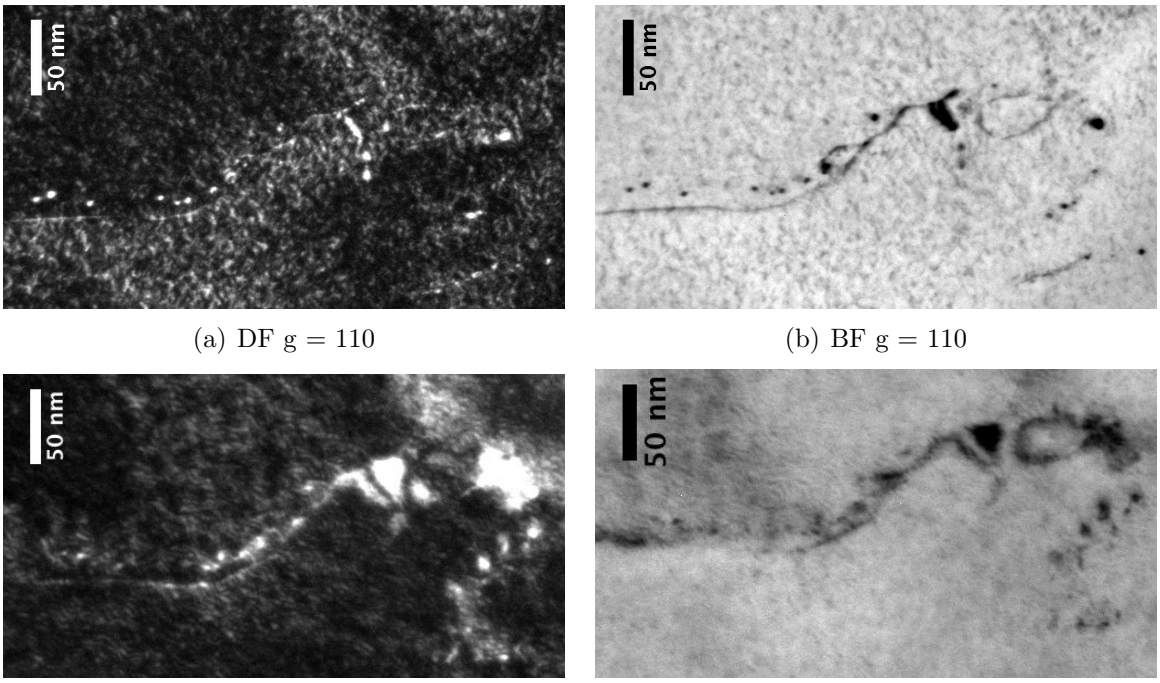

(a) DF g = 110 (b) BF g = 110

(c) DF g = 020 (d) BF g = 020

Figure 3.36: TEM images of Fe-10Cr single-crystal irradiated at 300°C to 0.1 dpa with a higher magnification to show the microstructure of dislocation decoration.

Figure 3.37 also indicates that the specimen exhibits a very low dislocation line density. Only one localized region containing a high density of dislocation lines and bending was observed, as shown in Figure 3.38(a). Because of the co-existence of bending and the dislocations, and also because this observation is localized, these dislocations should be resulted from the deformation due to specimen preparation. Figure 3.38(b) shows the zoomed-in area of 3.38(a) at the edge of the high dislocation region. The dislocation line density dropped and the microstructure resumed to a uniform distribution of small dislocation loops.

Figure 3.39 and in Figure 3.40 shows the same area TEM micrograph using three different g vectors (110, 200, 020) in the same crystal orientation close to (001) zone. A mixture of $\langle 100 \rangle$ and $\frac{1}{2}\langle 111 \rangle$ was observed. Burgers vector g·b analysis shows that a$\langle 100 \rangle$ dislocation loops dominate comprising 84% of the total loops, while it is 16% for $\frac{a}{2}\langle 111 \rangle$ loops.

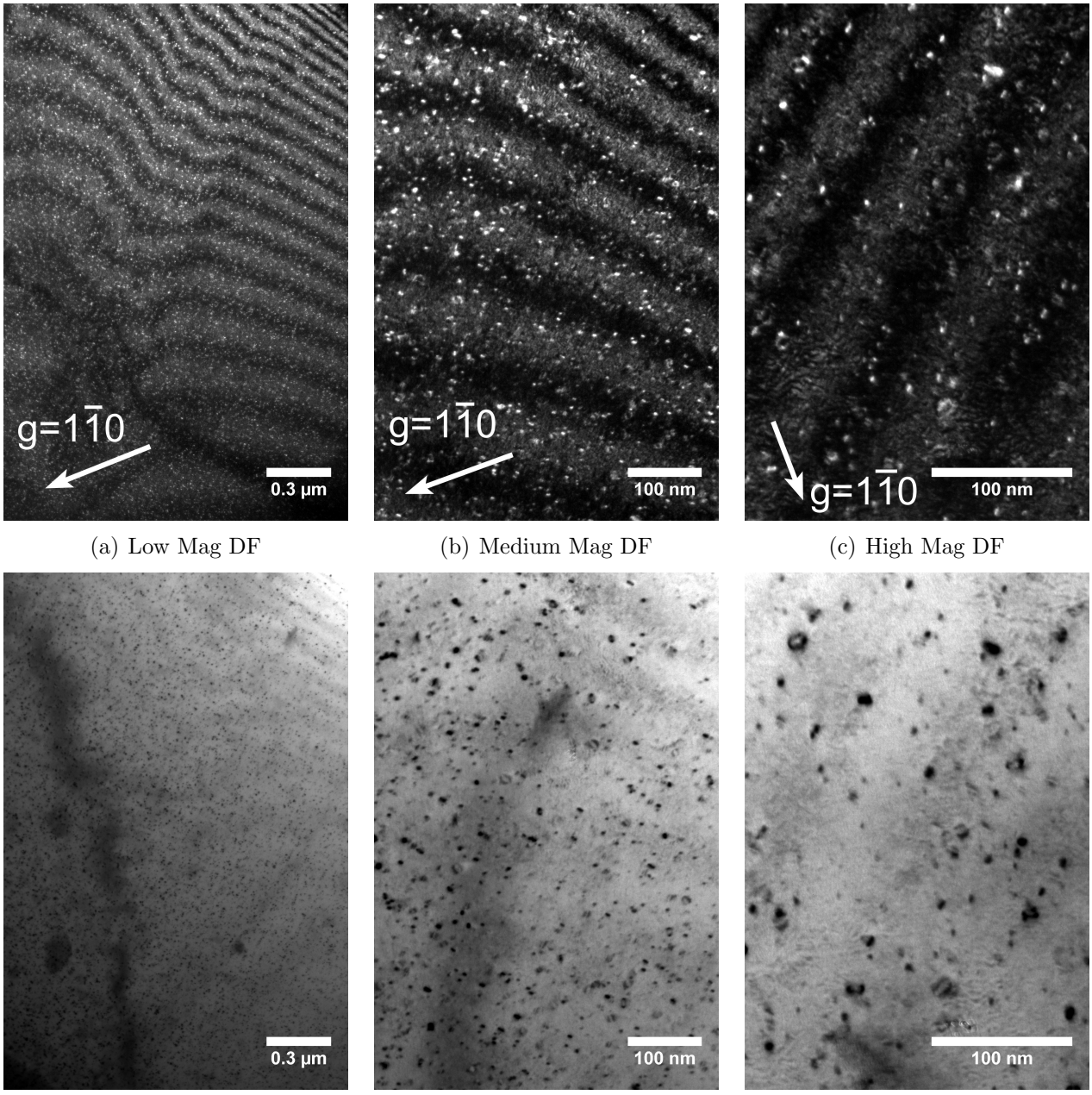

(a) Low Mag DF (b) Medium Mag DF (c) High Mag DF

(d) Low Mag BF (e) Medium Mag BF (f) High Mag BF

Figure 3.37: TEM images of Fe-16Cr single crystal irradiated at 300°C to 1 dpa. Images were taken at the same area with different magnifications. The electron beam was close to the [111] direction of the crystal. The imaging condition was g = 1$\bar{1}$0 (g, 4.3g) for dark-field and kinematic for bright-field.

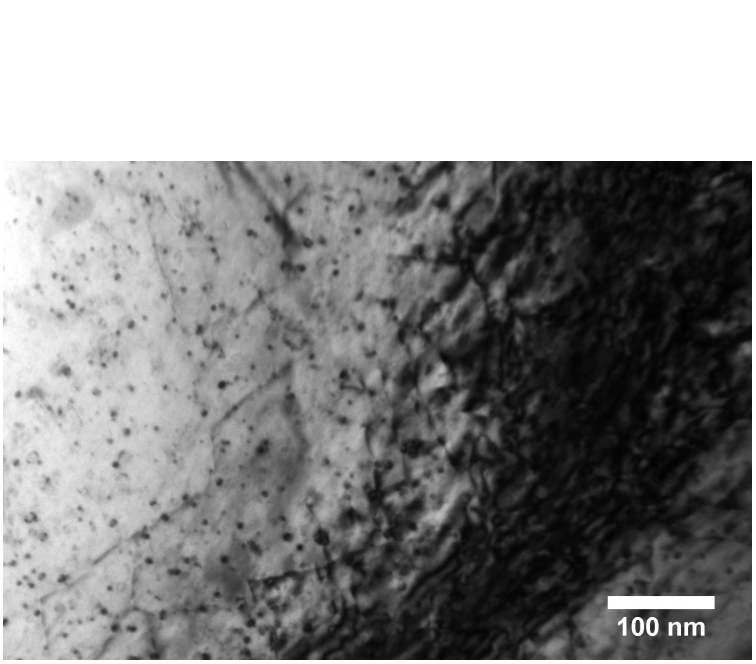

(a) Low Mag BF

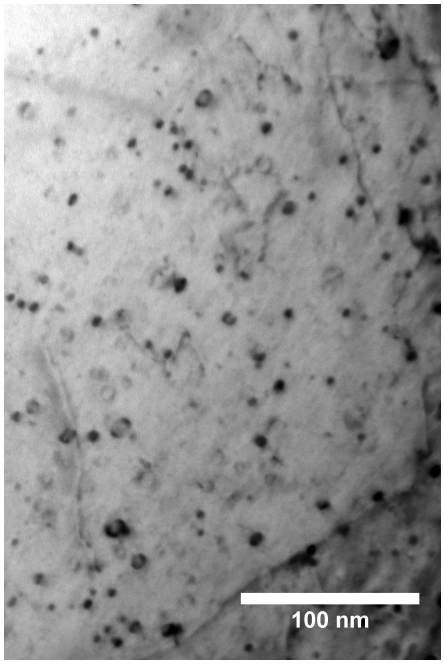

(b) High Mag BF

Figure 3.38: BF TEM images of Fe-16Cr single crystal irradiated at 300°C to 1 dpa (a)Lower magnification image showing the deformed-region containing a high density of dislocations, and the nearby region. (b)High magnification image showing the region close to the deformed region.

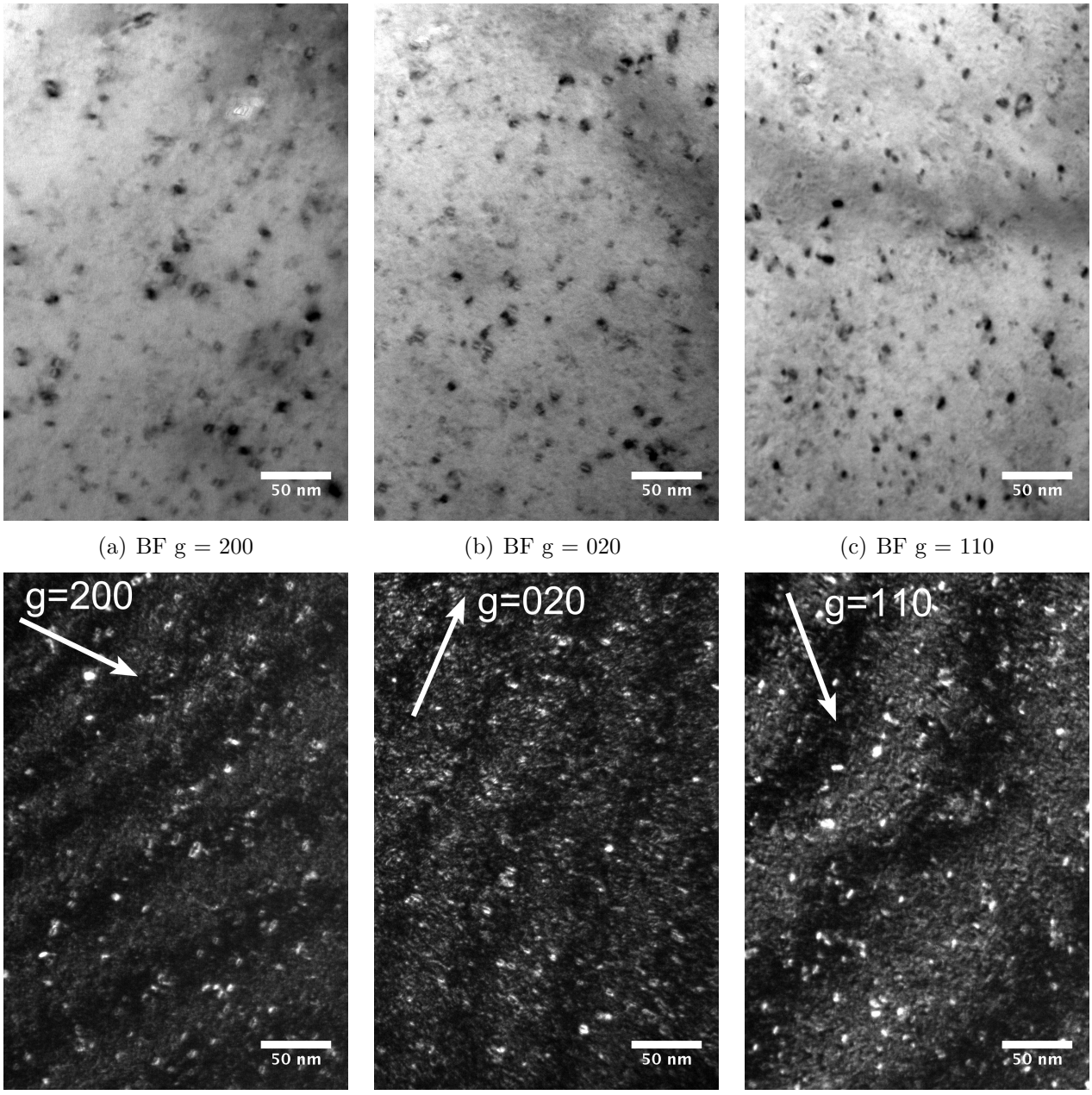

(a) BF g = 200 (b) BF g = 020 (c) BF g = 110

(d) DF g = 200 (e) DF g = 020 (f) DF g = 110

Figure 3.39: TEM images of Fe-16Cr single crystal irradiated at 300°C to 1 dpa. Images were taken at the same area with different diffraction conditions. The electron beam was close to the [001] direction of the crystal.

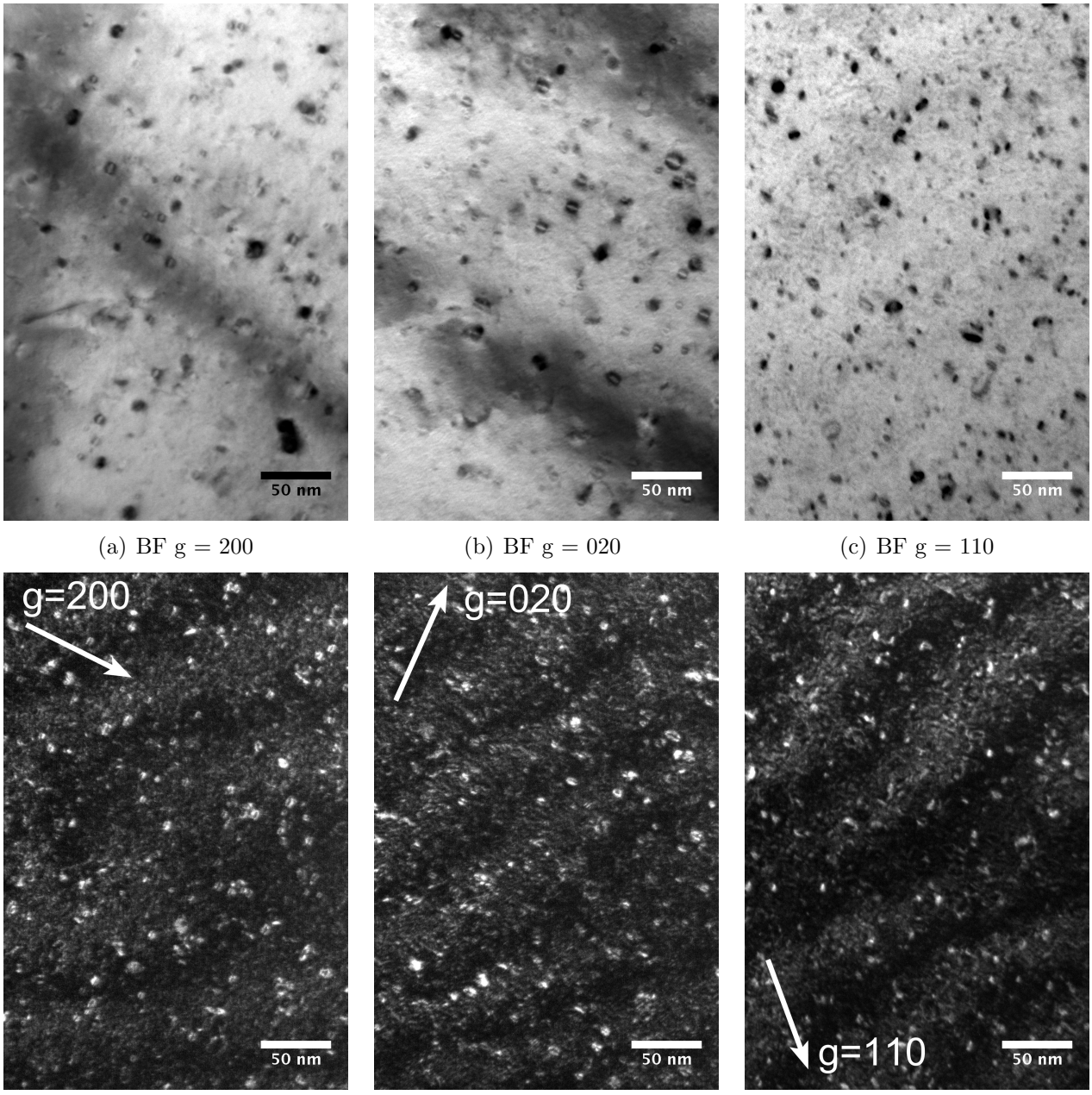

(a) BF g = 200 (b) BF g = 020 (c) BF g = 110

(d) DF g = 200 (e) DF g = 020 (f) DF g = 110

Figure 3.40: TEM images of Fe-16Cr single crystal irradiated at 300°C to 1 dpa. Images were taken at the same area with different diffraction conditions. The electron beam was close to the [001] direction of the crystal.

3.1.15 Summary of Fe-Cr single-crystals irradiated at 300C

Figure 3.41 shows the typical microstructure in Fe-Cr single crystal irradiated at 300°C to 0.01, 0.1 and 1 dpa. The quantitative data is shown in Table 3.3 and Figure 3.42. The dislocation density in 1 dpa specimen is significantly higher than in 0.01 dpa and 0.1 dpa specimens. Uniform distribution of dislocation loops were observed in 0.01 dpa and 1 dpa specimens, whereas dislocation decoration was observed in the 0.1 dpa specimen. Burgers vector analysis was performed in the 1 dpa specimen. The a⟨100⟩ loops are the majority comprising about 84% of the total loops. No voids were observed in either of the three specimens.

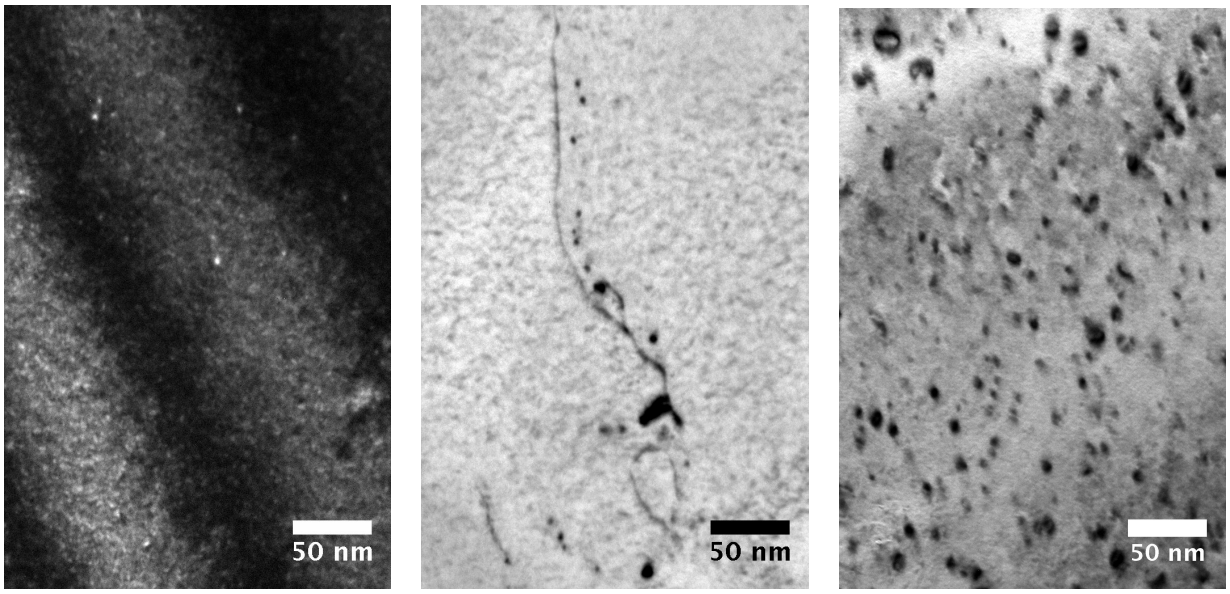

(a) 0.01 dpa (b) 0.1 dpa (c) 1 dpa

Figure 3.41: TEM micrograph of Fe-Cr single crystal irradiated at 300°C

3.1.16 Fe poly-crystals irradiated at 450C to 0.01dpa

Figure 3.43 is the TEM micrograph of a Fe poly-crystal irradiated at 450°C to 0.01 dpa, showing a microstructure composed of line dislocations and low-angle grain boundaries (dislocation net).These dislocations were the original microstructure, and were not a result of radiation damage. Note that the subgrain at the center-top of the figure has a slightly darker

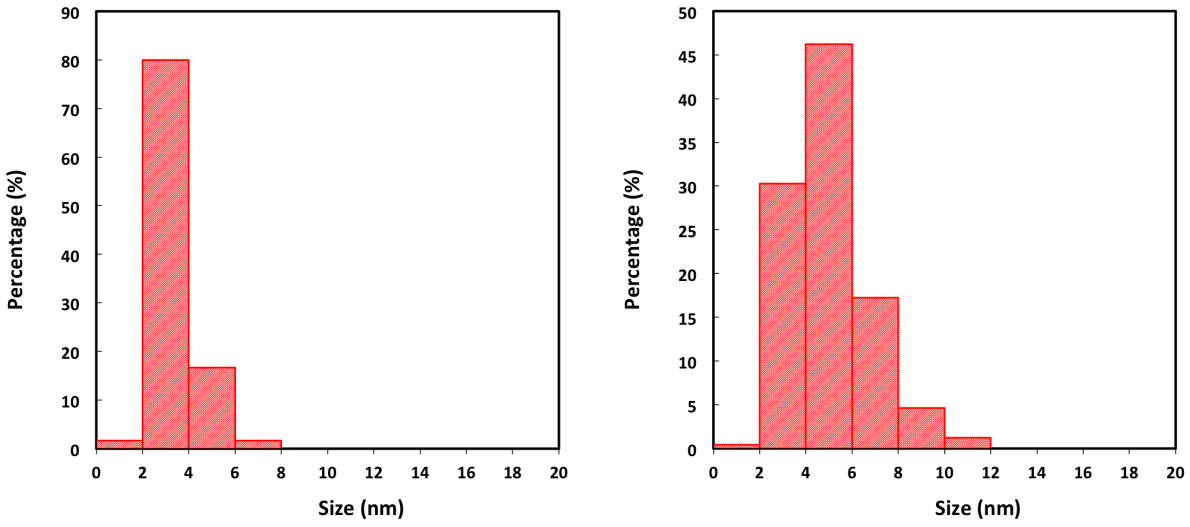

(a) 0.01 dpa

(b) 0.1 dpa

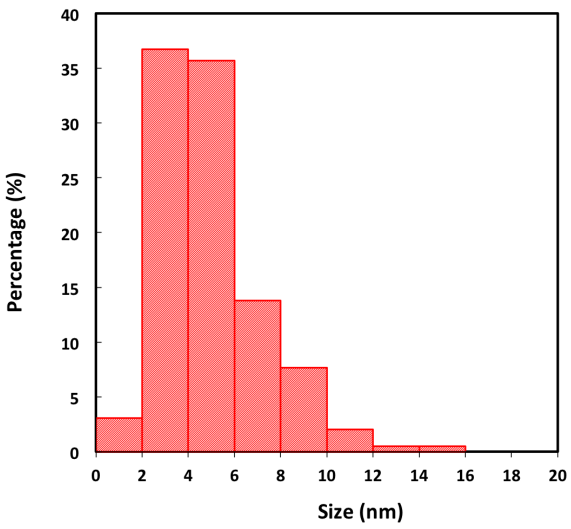

(c) 1 dpa

Figure 3.42: The size distribution of dislocation loops in Fe-Cr single crystals irradiated at 300°C as a function of irradiation dose.

Table 3.3: Microstructure data for Fe-Cr single crystals irradiated at 300°C

	0.01 dpa Fe-14Cr	0.1 dpa Fe-10Cr	1 dpa Fe16Cr
Dislocation density ($\frac{1}{m^2}$)	$<10^6$	1.4×10^{13}	very low [1]
$\bar{d}_{loop}$ (nm)	2.6	5.2	4.88
$d_{loop,Max}$ (nm)	6.1	10.73	15.58
N_{loop} (10^{21} $\frac{1}{m^3}$)	1.1-3.3	0.32	15
$\bar{d}_{void}$ (nm)		Not observed	
$d_{void,Max}$ (nm)		Not observed	

[1] If the area of Figure 3.38 is not considered

(stronger) contrast than the neighboring subgrain below. This is an indication showing that the low-angle grain boundary causes slight mis-orientations between subgrains. Excluding those dislocations composing a low-angle grain boundary, the density of line dislocations is measured to be $4.7\times10^{13}\frac{1}{m^2}$, which is about half of its 300°C counterpart.

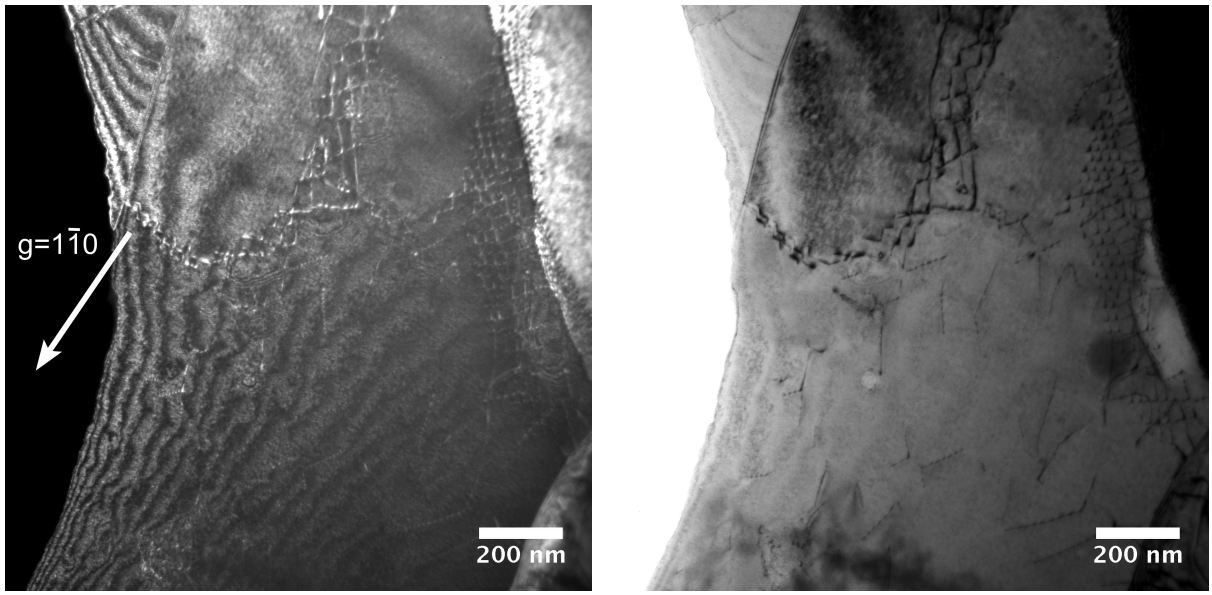

(a) DF (b) BF

Figure 3.43: TEM images of Fe poly-crystal irradiated at 450°C to 0.01 dpa. Images were taken under g = $\bar{1}$10 dark field (g, 4.3g) and kinematic bright field with beam direction close to [111].

In addition to the line dislocations, a few irradiation-induced dislocation loops were observed, as shown with black arrows in Figure 3.44. Similar to Fe-300°C-0.01dpa specimen,

the density of dislocation loops is low ($5.0\times10^{19}\frac{1}{m^2}$). No correlation could be established about the location of the occurrence of dislocation loops to the original dislocation structure because of insufficient statistics, which is again similar to the situation of counterpart 300°C specimen. The difference between two specimens lies in the size of dislocation loops. The loop size in 450°C specimen is significnatly larger ($\bar{d}_{loop}$ = 14.4 nm) than that in 300° specimen ($\bar{d}_{loop}$ = 2.6 nm).

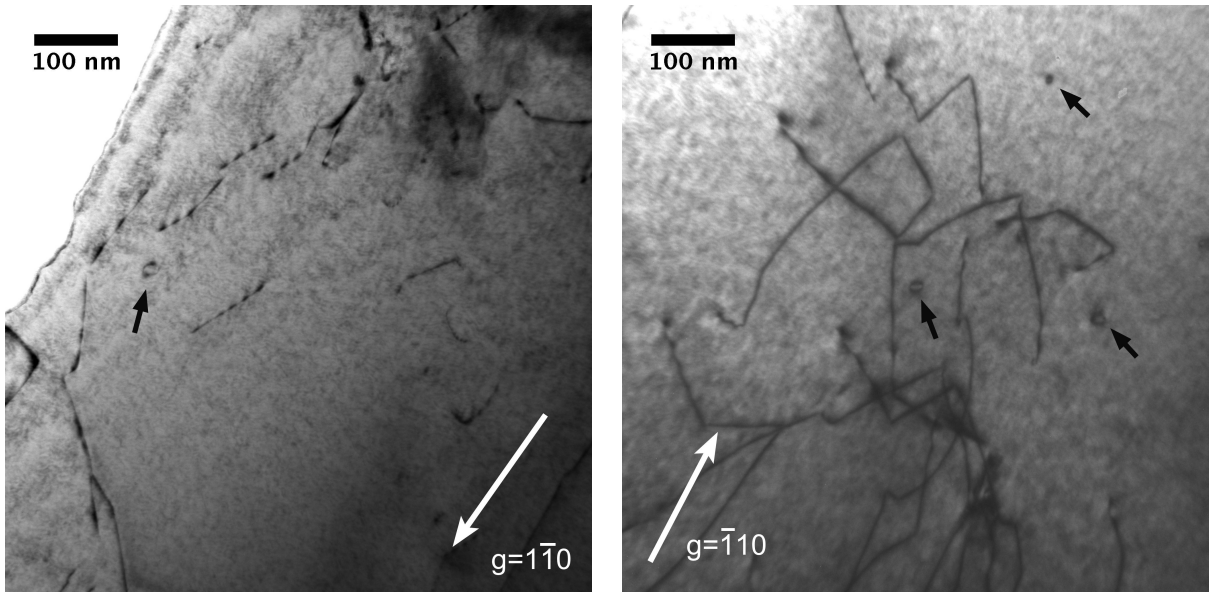

(a) Area 1 (b) Area 2

Figure 3.44: High magnification TEM images of Fe poly-crystal irradiated at 450°C to 0.01 dpa. Images taken under kinematic bright field g = $\bar{1}$10 and g = 1$\bar{1}$0 with beam direction close to [111].

3.1.17 Fe poly-crystals irradiated at 450C to 0.1dpa

The microstructure of Fe poly-crystal irradiated at 450°C to 0.1 dpa is shown in Figure 3.45 to Figure 3.47. In Figure 3.45, the microstructure is similar to the 0.01 dpa specimen (lower dose) (see Figure 3.44). It is composed of sparsely-distributed dislocation loops ($22.2\times10^{19}\frac{1}{m^3}$) and a moderate amount of line dislocations (($4.7\times10^{13}\frac{1}{m^2}$)). The density of dislocation loops is low that there are only 2-3 dislocation loops in a micrograph of regular magnification (marked with arrows). The size of the largest loop in Figure 3.45 is about 30

nm. However, the other observed dislocation loops in this specimen are often much larger. As shown in Figure 3.46, the loop size could be as large as hundreds of nanometers. Figure 3.47 shows a group of large dislocation loop. This kind of clustering of multiple dislocation loops was not observed in the Fe polycrystal specimen irradiated at 450°C to 0.01 dpa.

The dislocation loop in the center of Figure 3.47 is thought to be a $\langle 100 \rangle (100)$ loop because of the following reasons. Firstly, the prevailing Burgers vector of dislocation loops in Fe at this irradiation temperature of 450°C is b = $\langle 100 \rangle$ according to the results of *in-situ* self-ion irradiation and neutron irradiations discussed in Chapter 1.3.1[45][28]. Also, the equilibrium shape of $\frac{1}{2}\langle 111 \rangle$ and $\langle 100 \rangle$ dislocation loops are hexagonal and square, respectively [96]. The shape in Figure 3.47 is not a projection of hexagonal. When the crystal orientation is exactly at (110) zone axis, 1: 0.71 is the ratio between the long side and the short side of the projection of loops with b= [100] or b = [010]. The measured ratio is 1: 0.74, which is fairly close considering the crystal orientation is slightly off the (110) zone axis. Finally, a comparison between the diffraction pattern and the image shows that the shape and the orientation of the loop projection is consistent with the loop as a[100](100) loop or a[010](010) loop.

3.1.18 Fe poly-crystals irradiated at 450C to 1dpa

Figure 3.48 to 3.50 shows the low-magnification and high-magnification TEM micrographs of the same area in an Fe poly-crystal irradiated at 450°C to 1 dpa. A couple of grains are shown in Figure 3.48. Most of the grains, except for the top-left one, are in contrast and show a high density of resolvable dislocation loops and dislocation lines. The density of line dislocations is measured to be $2.2\times10^{13}\frac{1}{m^2}$, which is about 5 times less than that in the 0.01 dpa Fe specimen irradiated at 300°C. No evident denuded zone was observed at the grain boundary. The average size and the density of dislocation loops are 13.6 nm and 1.9x10^{21} 1/m^3, respectively.

The spatial distribution of dislocation loops is not uniform. In Figure 3.49, some areas are free of dislocation loops while some areas exhibit many dislocation loops. Besides, the dislocation loops do not seem to associate with the pre-existing dislocations, which is different

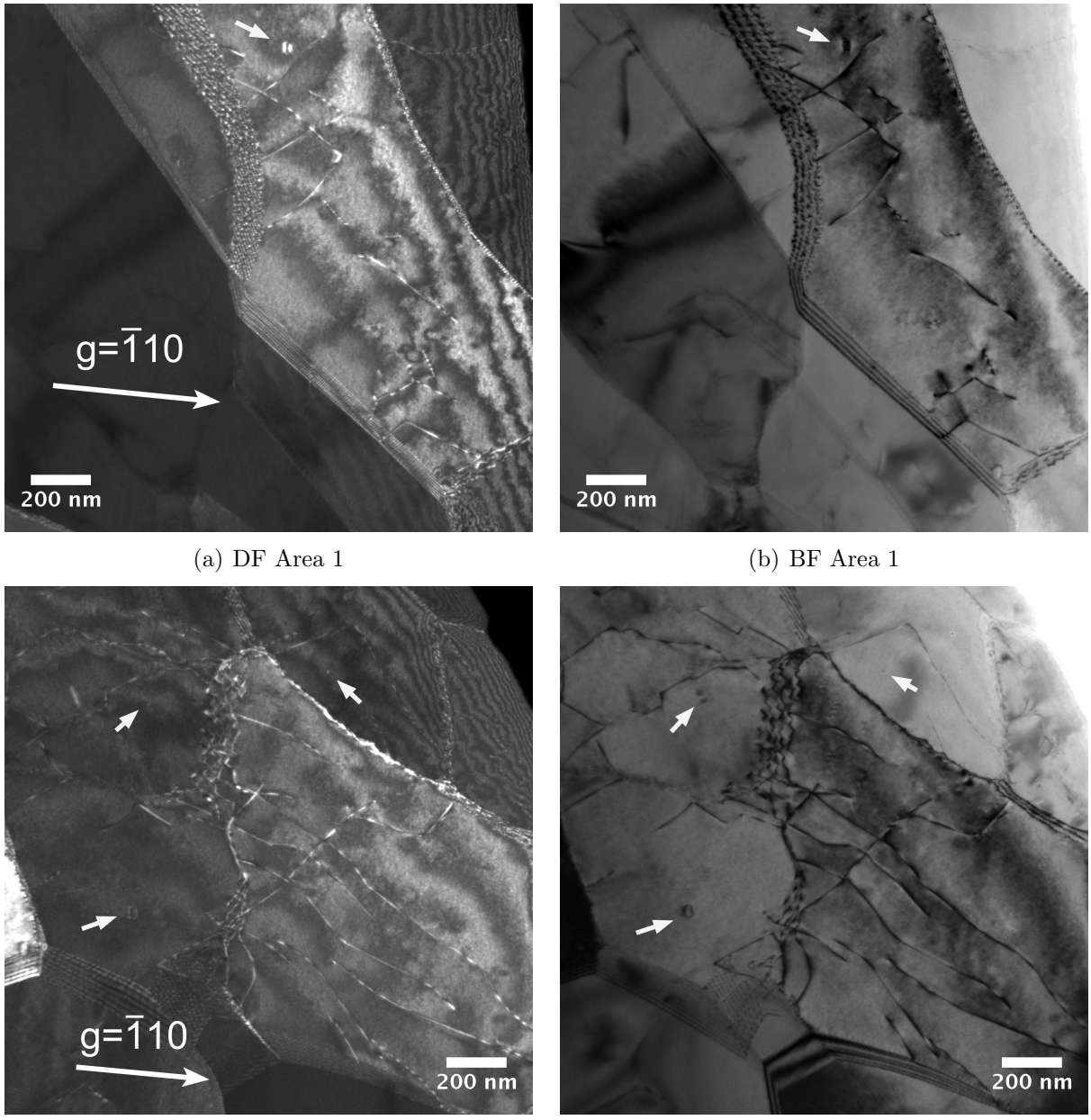

(a) DF Area 1

(b) BF Area 1

(c) DF Area 2

(d) BF Area 2

Figure 3.45: TEM images of Fe poly-crystal irradiated at 450°C to 0.1 dpa. Images were taken under g = $\bar{1}$10 kinematic BF and g = $\bar{1}$10 (g, 4.3g) DF with beam direction close to [110].

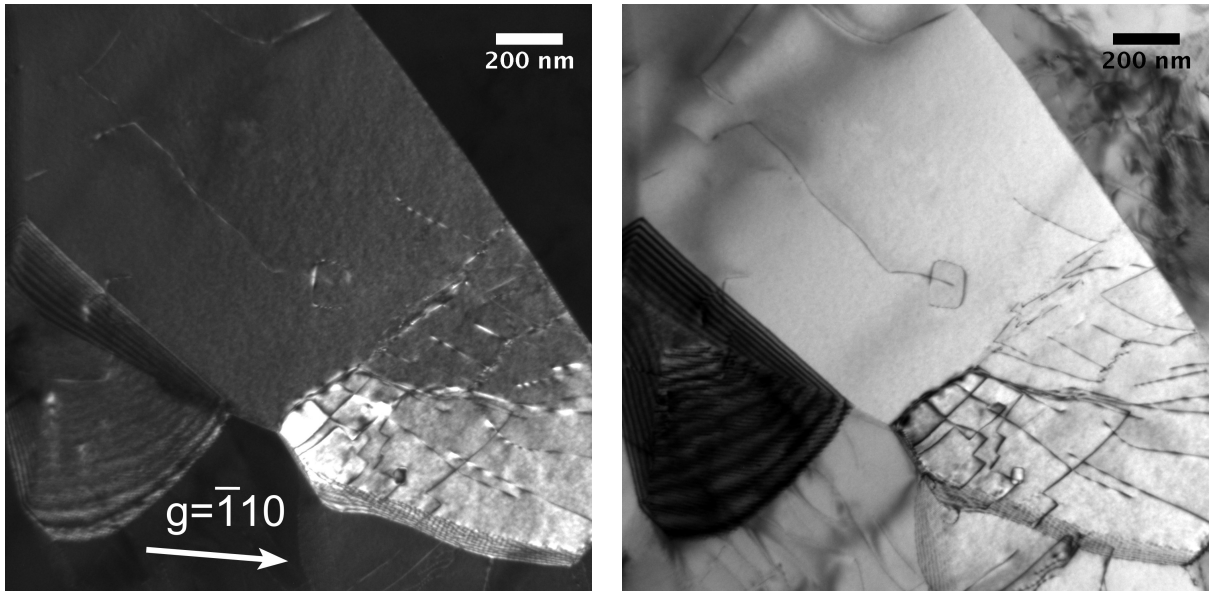

(a) DF Area 3 (b) BF Area 3

Figure 3.46: TEM images of Fe poly-crystal irradiated at 450°C to 0.1 dpa. Imaging conditions were g = $\bar{1}$10 (g, 4.3g) for DF and g = $\bar{1}$10 kinematic for BF with beam direction close to [110].

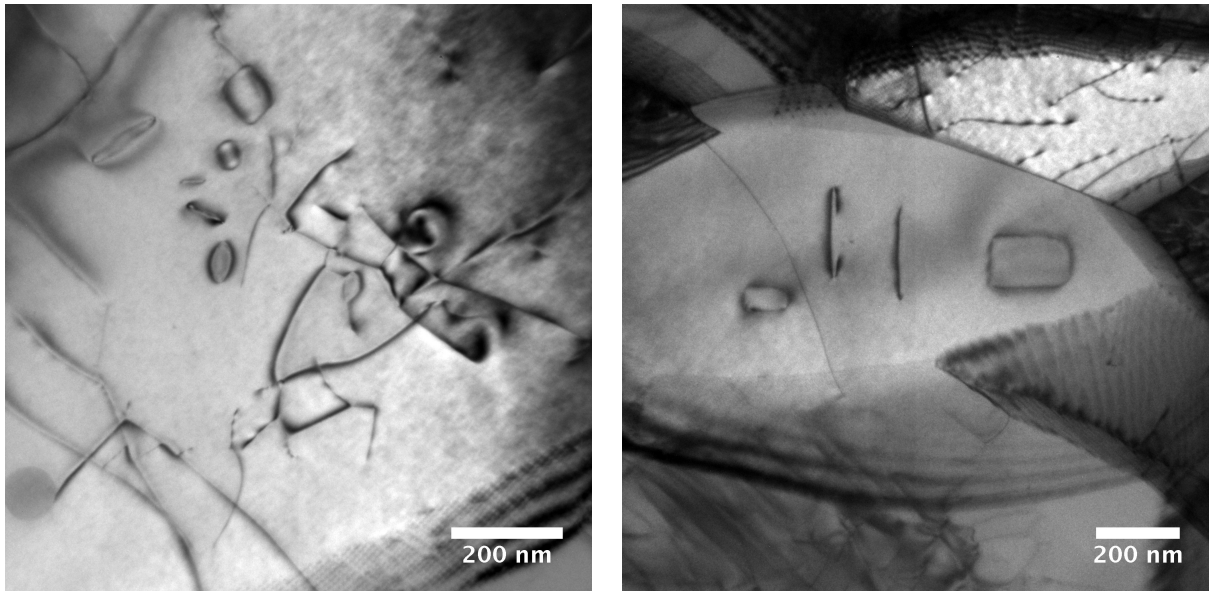

(a) BF Area 4 (b) BF Area 5

Figure 3.47: TEM images of Fe poly-crystal irradiated at 450°C to 0.1 dpa.

from the Fe specimen irradiated at 300°C (section 3.1.10). This observation of dislocations-loop-free area (inhomogeneity) is not due to the imaging condition. The argument for this observation will be given later when the Burgers vector of the dislocation loops is discussed.

Figure 3.50 shows the higher magnification images of the same area and a set of under/over focused images that reveal the voids. The average size of the visible voids are 3.6 nm, roughly twice as large as that in the Fe polycrystal irradiated at 300°C to 1 dpa.

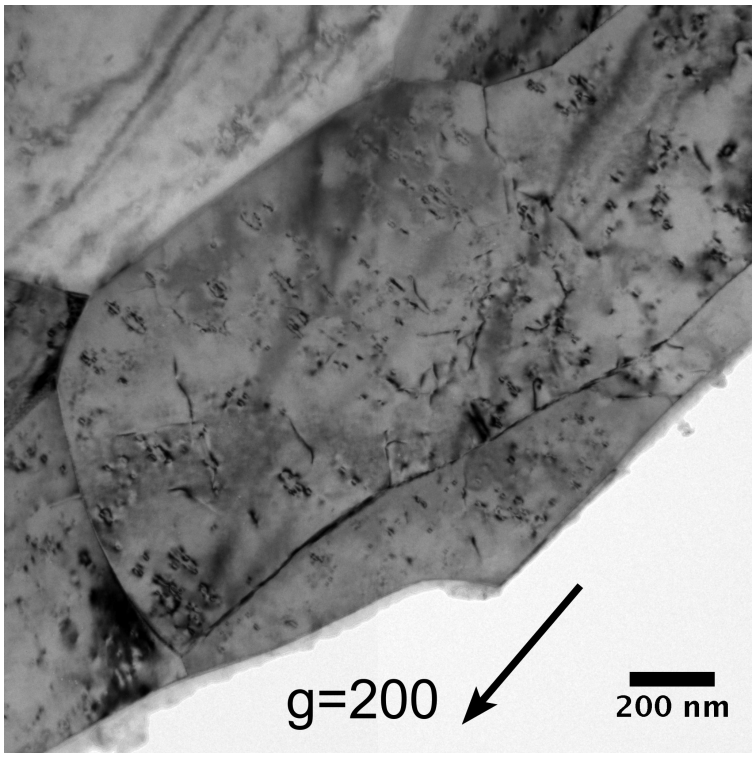

Figure 3.48: Low magnification TEM image of Fe poly-crystal irradiated at 450°C to 1 dpa. Kinematic bright field imaging condition is g = 200 with beam direction close to [011].

The Burgers' vector of most dislocation loops is b = ⟨100⟩. The proof is shown in Figure 3.51 to 3.53 where a series of the same area micrographs were taken with various diffractions conditions (g = 110, 200 and 020). The grain orientation was close to the (001) zone. The loops are edge-on with habit planes on (100) and (010). The loops on (100) plane are invisible with g = 020 and, oppositely, the loops on (010) planes are invisible with g = 200. In addition, dislocation loops on (100) and (010) planes are both visible with g = 110. With the assumption that only Burgers vector b = ⟨111⟩ and b = ⟨100⟩ are considered and the invisibility observations in Figure 3.51 to 3.53, it is concluded that the majority of the

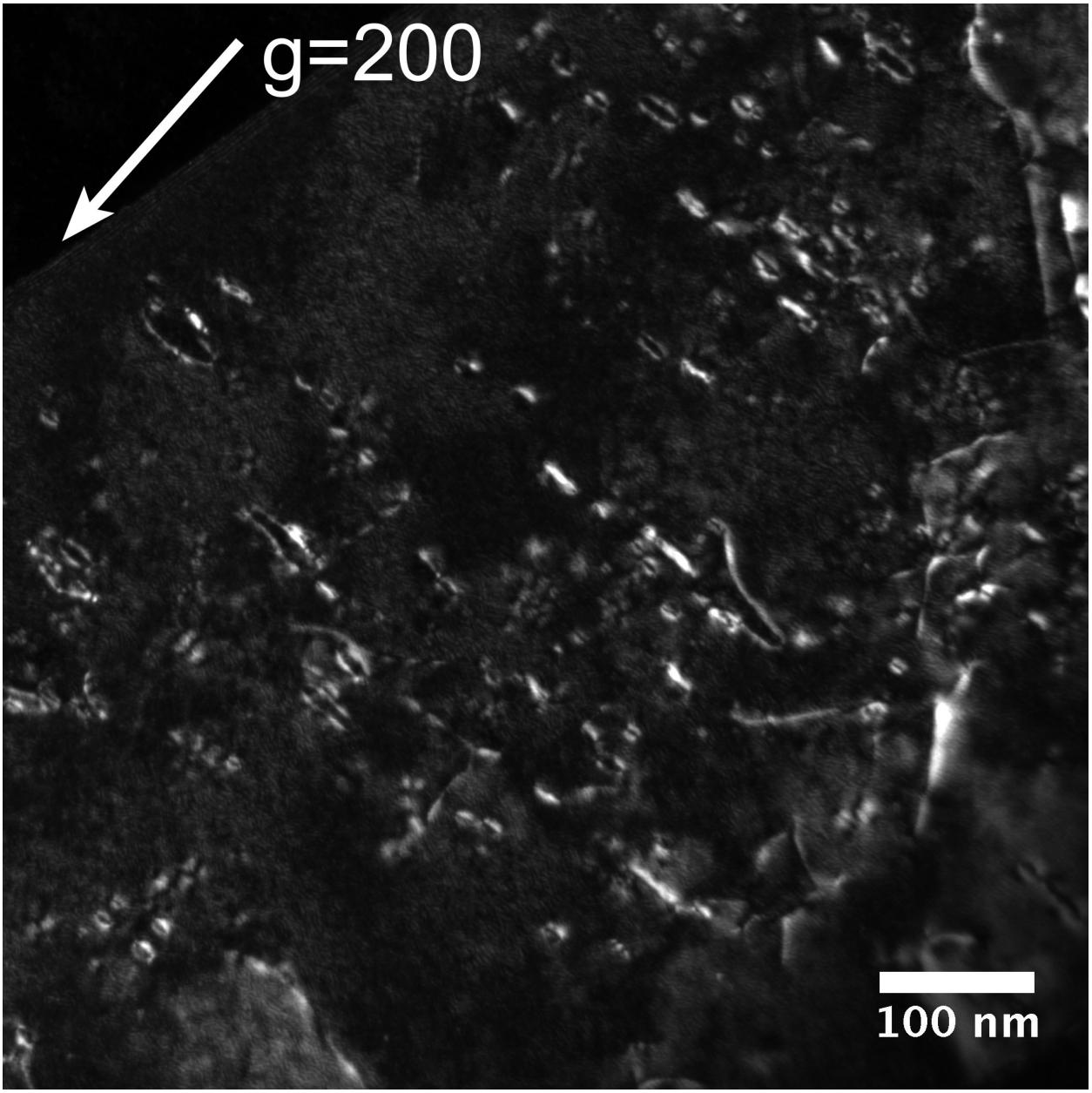

Figure 3.49: TEM images of Fe poly-crystal irradiated at 450°C to 1 dpa. Dark-field images taken under g = 200 (g, 3g) with beam direction close to [011].

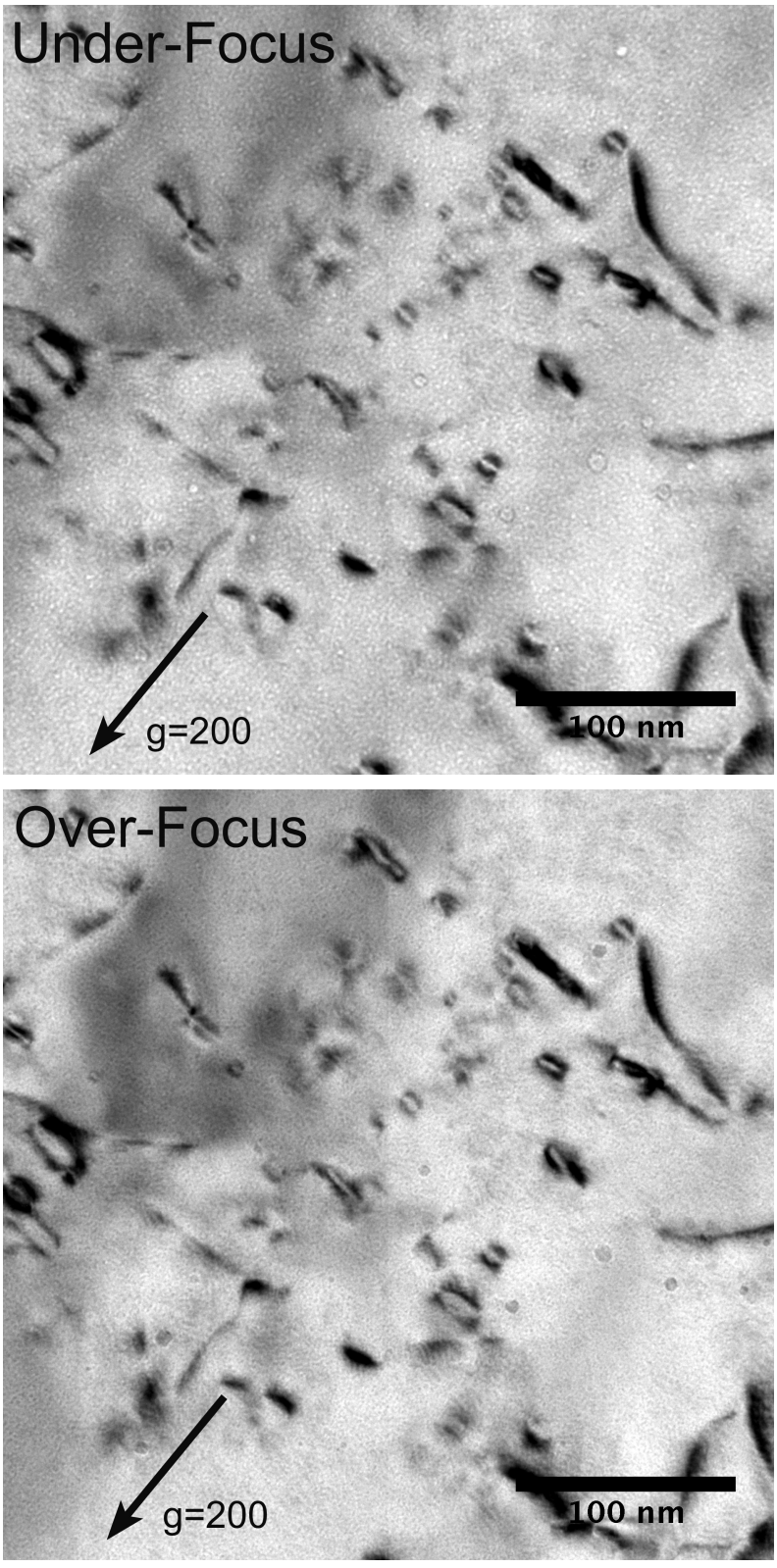

Figure 3.50: Uner and over-focus TEM images of Fe poly-crystal irradiated at 450°C to 1 dpa. Kinematic BF images taken under g = 200 with beam direction close to [011].

dislocation loops is $\langle 100 \rangle \{100\}$ loops.

The inhomogeneous distribution of dislocation loops is apparent in Figure 3.51 to 3.53. An example area with negligible dislocation loops are marked with letter 'a'. Note that this loop-free area appears within all of the three images representing three different diffraction conditions. Because both [100] and [010] loops are visible with g = 110, there are only two possibilities for the invisibility. One is that there were simply no dislocation loops. The other possibility is that the extinction area was composed of [001] loops that were invisible under g = 110. The second one is not plausible and is explained as follows.

The area with many loops were composed of a mixture of [100] and [010] loops. Since [001] loops is crystallographically symmetric to the rest of the two $\langle 100 \rangle$ loops, it is unlikely that [001] loops behave differently and stay in another area (extinction area) alone. [001] loops should exist also in the area with many loops but out of contrast due to invisibility criterion. The extinction area is indeed free of dislocation loops, and the distribution of dislocation loops is indeed inhomogeneous.

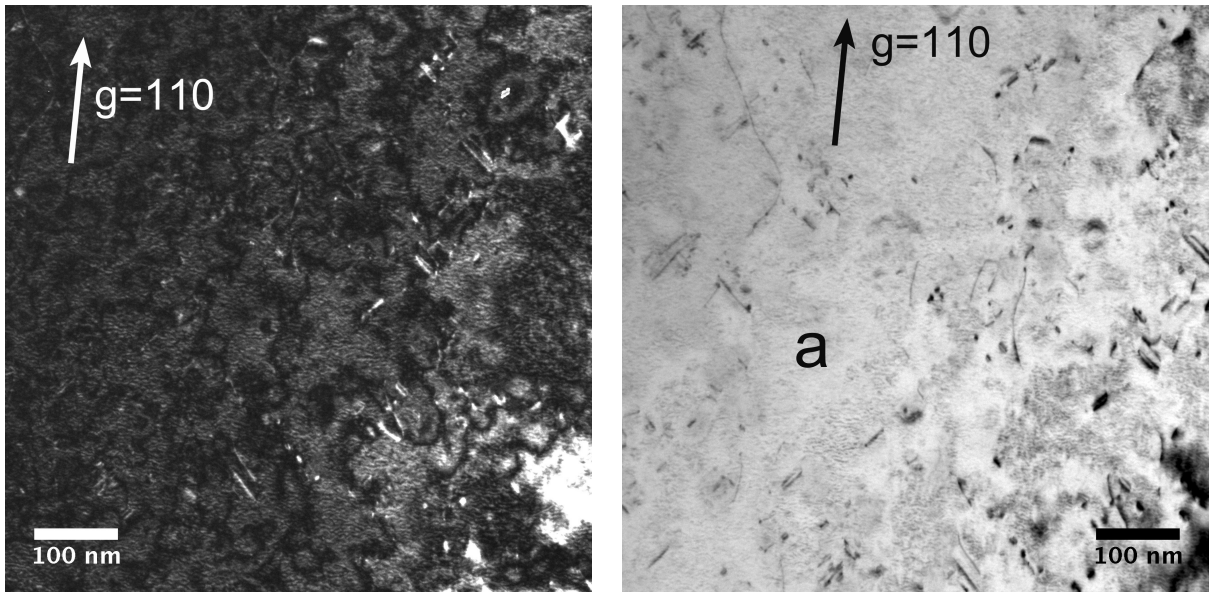

(a) DF (b) BF

Figure 3.51: TEM images of Fe poly-crystal irradiated at 450°C to 1 dpa. Images taken under g=110 (g, 4.3g) DF and kinematic BF with beam direction close to [001].

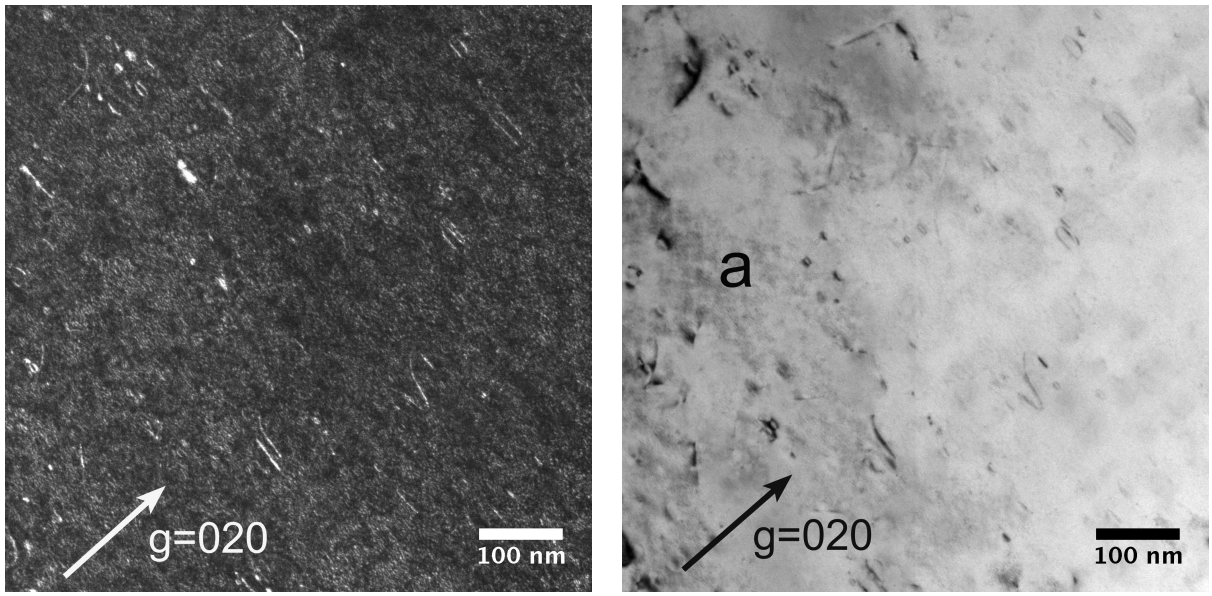

(a) DF (b) BF

Figure 3.52: TEM images of Fe poly-crystal irradiated at 450°C to 1 dpa. Images taken under g = 020 (g, 3g) DF and kinematic BF with beam direction close to [001].

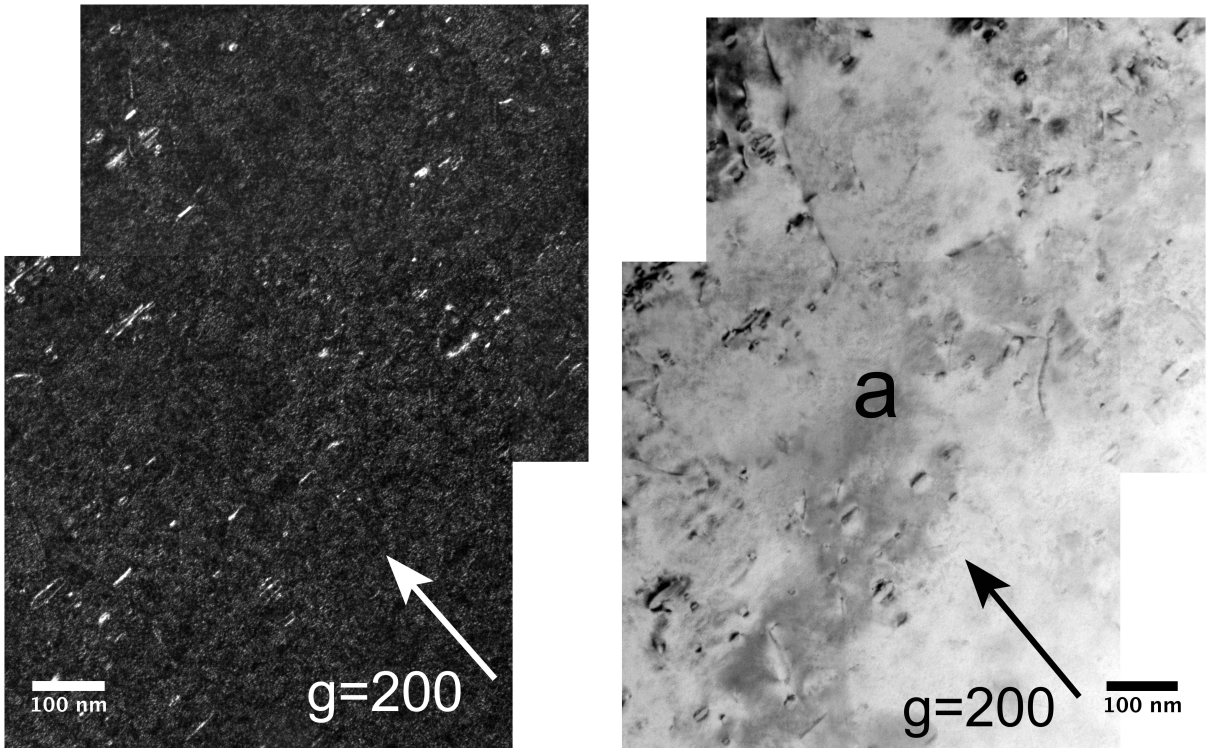

(a) DF (b) BF

Figure 3.53: TEM images of Fe poly-crystal irradiated at 450°C to 1 dpa. Image conditions are g = 200 (g,3g) DF and kinematic BF with beam direction close to [001].

3.1.19 Summary of Fe poly-crystals irradiated at 450°C

A comparison of the microstructure of Fe poly-crystals irradiated at 450° as a function of irradiation dose is shown in Figure 3.54. The quantitative measurement results are summarized in Table 3.4. Compared with the density in the 0.01 dpa-300° Fe ($1.1\times10^{14}\frac{1}{m^2}$), the lower line dislocation density in the 0.01 dpa and 0.1 dpa Fe poly-crystals irradiated at 450° ($4.7\times10^{13}\frac{1}{m^2}$) and the further decreases in 1 dpa specimen ($2.2\times10^{13}\frac{1}{m^2}$) indicates the occurrence of irradiation-enhanced annealing.

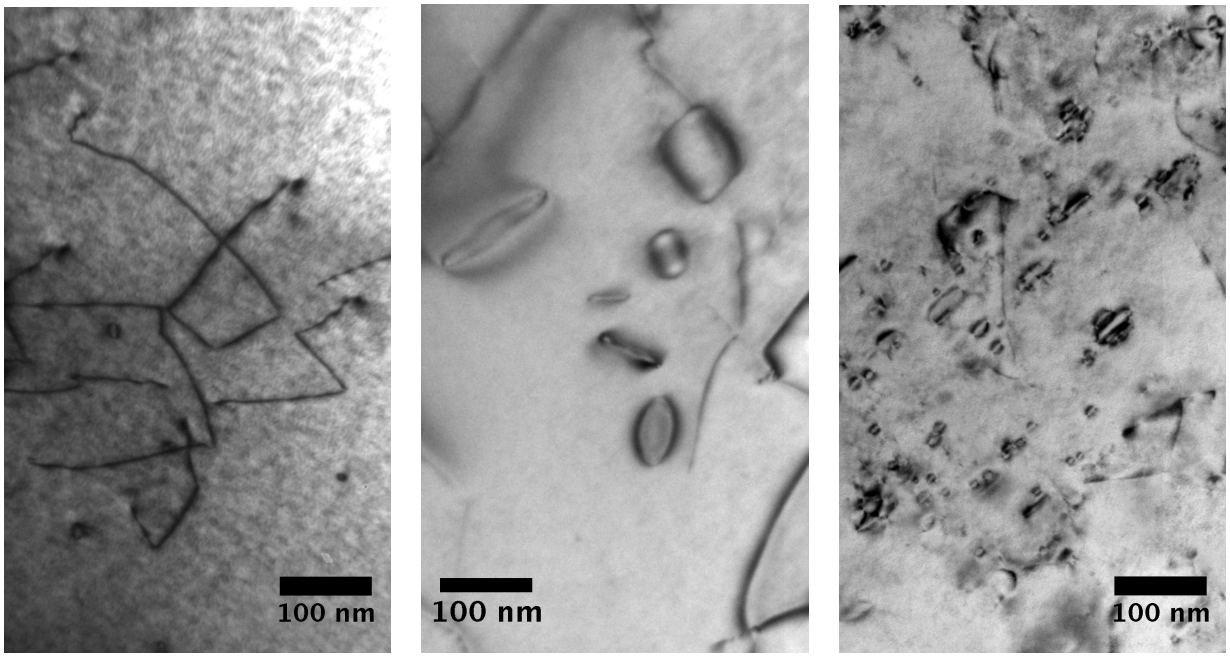

(a) 0.01 dpa (b) 0.1 dpa (c) 1 dpa

Figure 3.54: TEM micrograph of Fe polycrystals irradiated at 450°C

Table 3.4: Microstructure data for Fe poly-crystals irradiated at 450°C

	0.01 dpa	0.1 dpa	1 dpa
Dislocation density ($\frac{1}{m^2}$)	4.7×10^{13}	4.7×10^{13}	2.2×10^{13}
$\bar{d}_{loop}$ (nm)	14.4	71.8	13.6
$d_{loop,Max}$ (nm)	34.4	215.4	62.5
N_{loop} (10^{19} $\frac{1}{m^3}$)	5.0	2.2	190
$\bar{d}_{void}$ (nm)	-	-	3.6
$d_{void,Max}$ (nm)	-	-	8.2

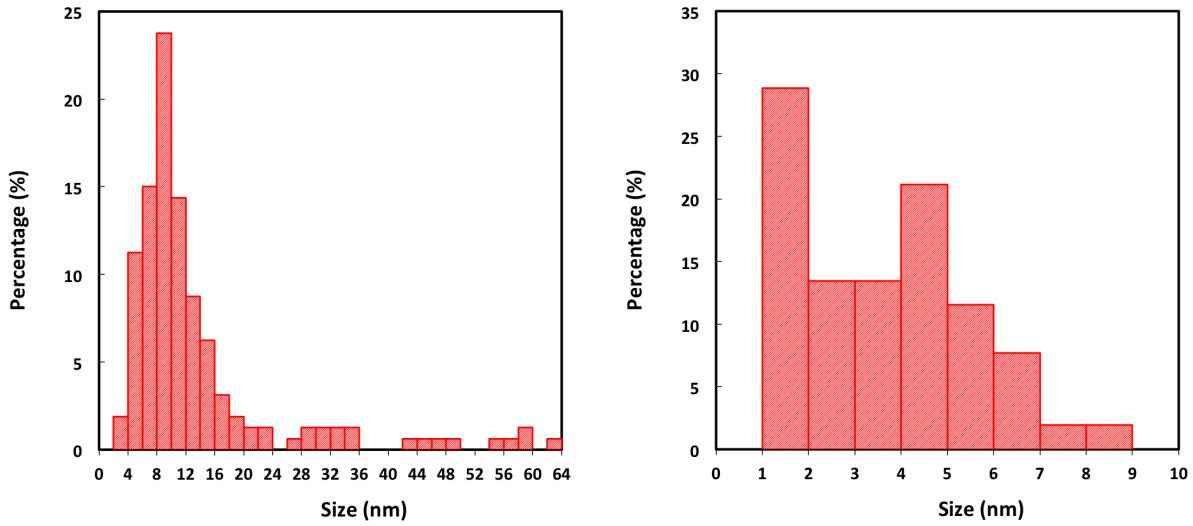

(a) 1 dpa Loops

(b) 1 dpa Voids

Figure 3.55: The size distribution of (a) dislocation loops and (b) voids in Fe polycrystals irradiated at 450°C to 1 dpa.

The 0.01 dpa and 0.1 dpa specimens exhibit a very low density of resolvable dislocation loops, while 1 dpa specimen exhibits a much higher density of dislocation loops. Size-wise, most dislocation loops observed in Fe specimens irradiated at 450° are fairly larger than the other irradiation conditions investigated in this study. The loop size increases significantly from 0.01 dpa to 0.1 dpa. However, the size is obviously smaller in 1 dpa specimen than in 0.1 dpa specimen, both in terms of the average size or the maximum size. It indicates that the irradiation temperature is lower for 1 dpa specimen than for the 0.1 dpa specimen, in despite of the same target irradiation temperature of 450°C.

The dislocation loops in 0.1 dpa and 1 dpa specimens were determined to have a Burger vector of a⟨100⟩{100}, which is consistent with other neutron and ion irradiation studies [75][45][44]. Dislocation decoration was not observed in either of the three specimens. However, the distribution of dislocation loops in 1 dpa specimens were not uniform, indicating that some loop-loop interactions exist. For 0.01 and 0.1 dpa specimens, the number density of dislocation loops is too low to show if similar loop clustering also exists. Finally, Voids were observed in the 1 dpa specimen, but not in 0.1 and 0.01 dpa specimens.

3.1.20 Fe-10Cr poly-crystals irradiated at 450C to 0.01dpa

Figure 3.56 shows the typical microstructure of the Fe-10Cr poly-crystals irradiated at 450 °C to 0.01 dpa. The line dislocation density (pre-irradiation microstructure) in this specimen is $2.4\times10^{13}\frac{1}{m^2}$, which is relatively high compared to other Fe-10Cr samples. The shaded band at the bottom of Figure 3.56(a) are the Moiré fringes corresponding to an overlapping of two crystals of different crystallographic orientation. Since the diffraction conditions were similar on both sides of the band, the mis-orientation was not significant. The shaded band should be an small angle grain boundary between the two sub-grains.

Irradiation damage took the form of dislocation loops. The dislocation loops can be divided into two groups: the tiny loops and the large loops. The group of tiny loops exhibits a high density (2.9×10^{21} $\frac{1}{m^3}$) and a small size (3.8 nm). The large loops (indicated with orange arrows in the figure) have a much lower density (1.45×10^{20} $\frac{1}{m^3}$) then the tiny loops and a distinctly large loop size (22.9 nm). There is no clear transition between the two groups of dislocation loops as the their sizes were sharply different and no dislocation loops of middle sizes were observed.

The nature of the loops of both groups were characterized with three diffraction conditions g = 110, g = 200 and g = 020 near the (001) zone (i.e. the g·b anaysis), as shown in Figure 3.57 and in Figure 3.58. The analysis shows that, considering both groups, $\frac{1}{2}\langle111\rangle$ and $\langle100\rangle$ loops constitute 15% and 82%, respectively, of the total loops observed in the TEM micrographs. The Burgers vectors of 3% of the loops could not be determined. For the large loops, all of them were $\frac{1}{2}\langle111\rangle$ loops. In addition to the g·b anaysis, an examination of the loop orientation indicated that the b = $\frac{1}{2}\langle111\rangle$ loops have their habit planes on $\{111\}$. Since large $\frac{1}{2}\langle111\rangle$ loops of comparable sizes were already observed in the unirradiated Fe-10Cr specimens (ex.Figure 3.4). In addition, no trace could be observed about these smaller loops evolving to larger ones. The large $\frac{1}{2}\langle111\rangle$ loops appeared in the irradiated specimen here should be of original microstructure and not from irradiation damage. The tiny loops were considered to be the only defect clusters induced by irradiations. For tiny loops alone, 86% and 11% of them were composed of $\langle100\rangle$ and $\frac{1}{2}\langle111\rangle$ loops, respectively. 3% of them could not be determined.

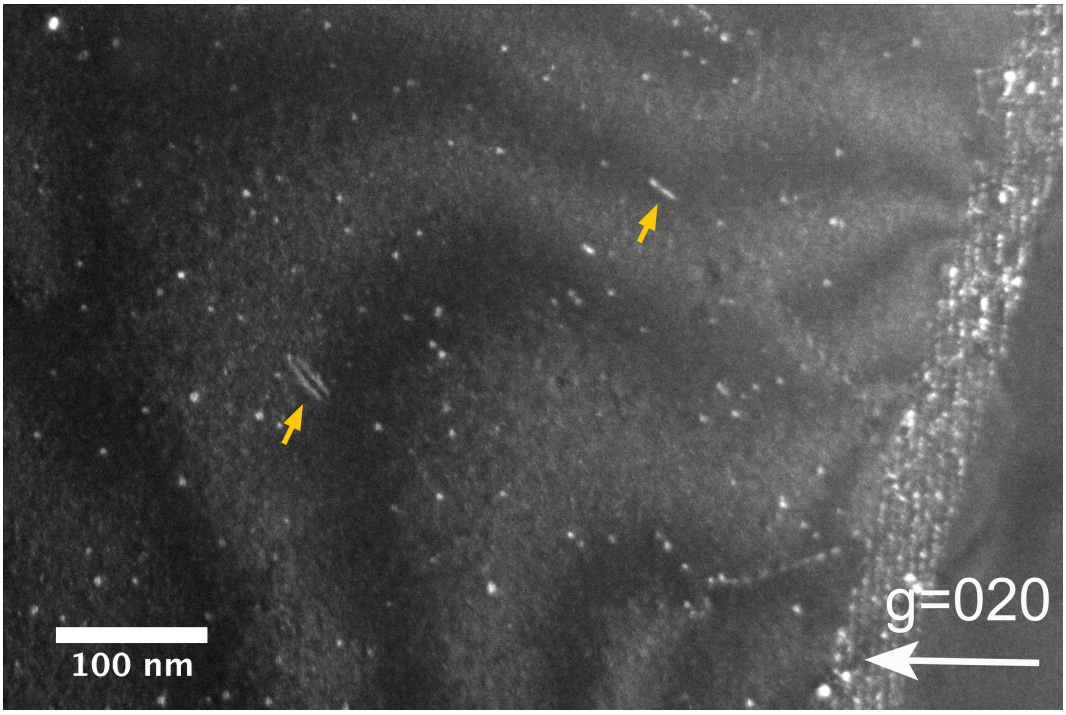

(a) Area One DF

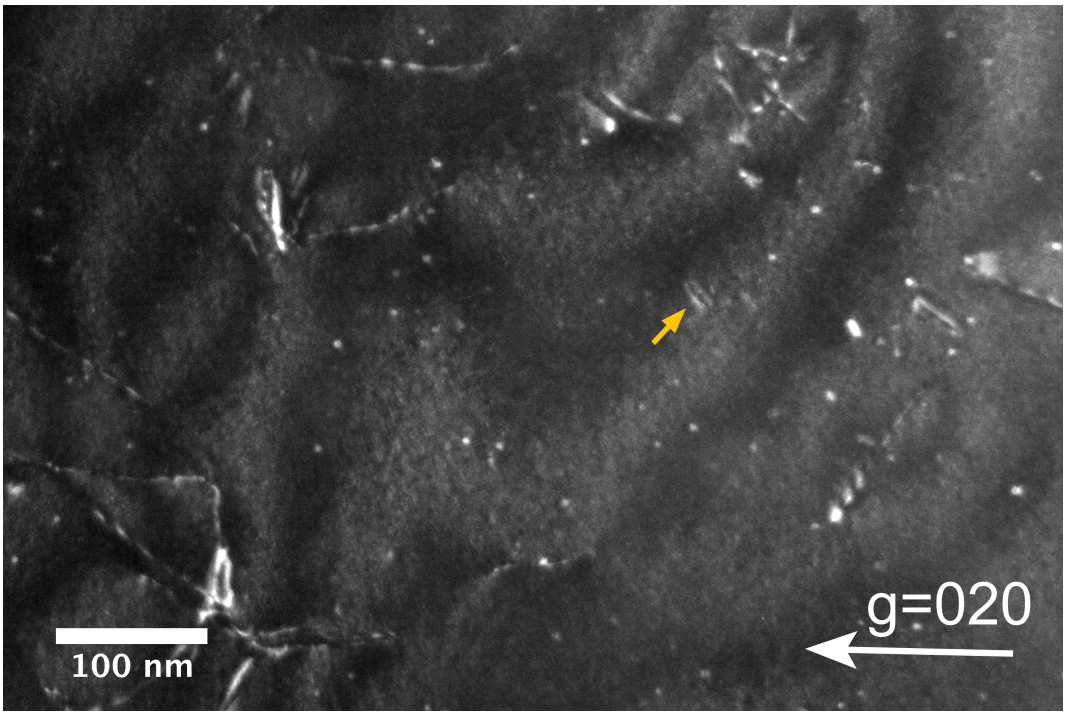

(b) Area Two DF

Figure 3.56: Low magnification TEM images of Fe-10Cr poly-crystal irradiated at 450°C to 0.01 dpa. Dark-field images taken under g = 020 (g, 3g) with beam direction close to [001].

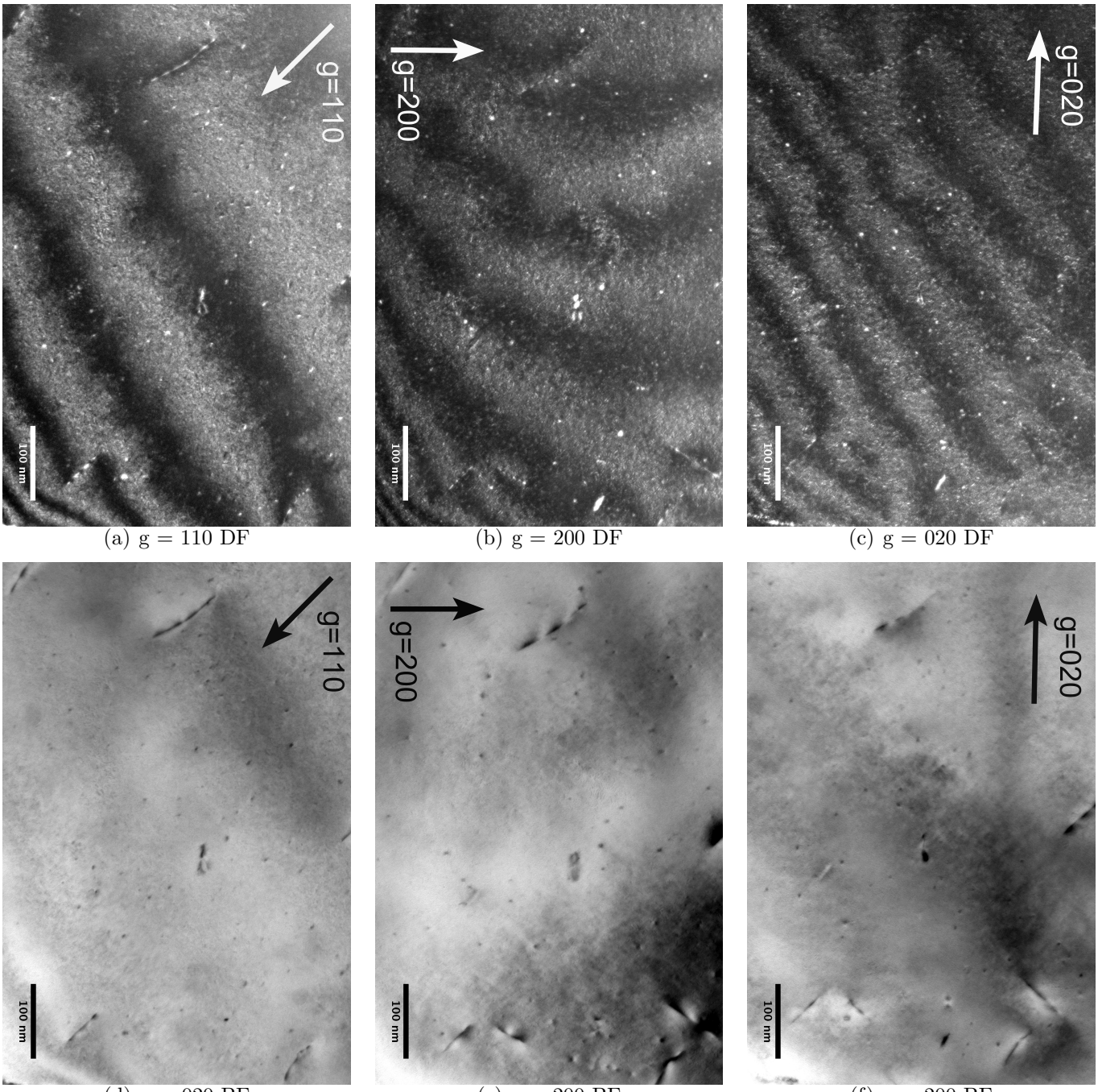

(a) g = 110 DF (b) g = 200 DF (c) g = 020 DF

(d) g = 020 BF (e) g = 200 BF (f) g = 200 BF

Figure 3.57: Same area TEM images of Fe-10Cr poly-crystal irradiated at 450°C to 0.01 dpa. DF and BF images were taken with different diffraction conditions: g = 110, g = 020 and g = 200 where the electron beam is close to [001] direction.

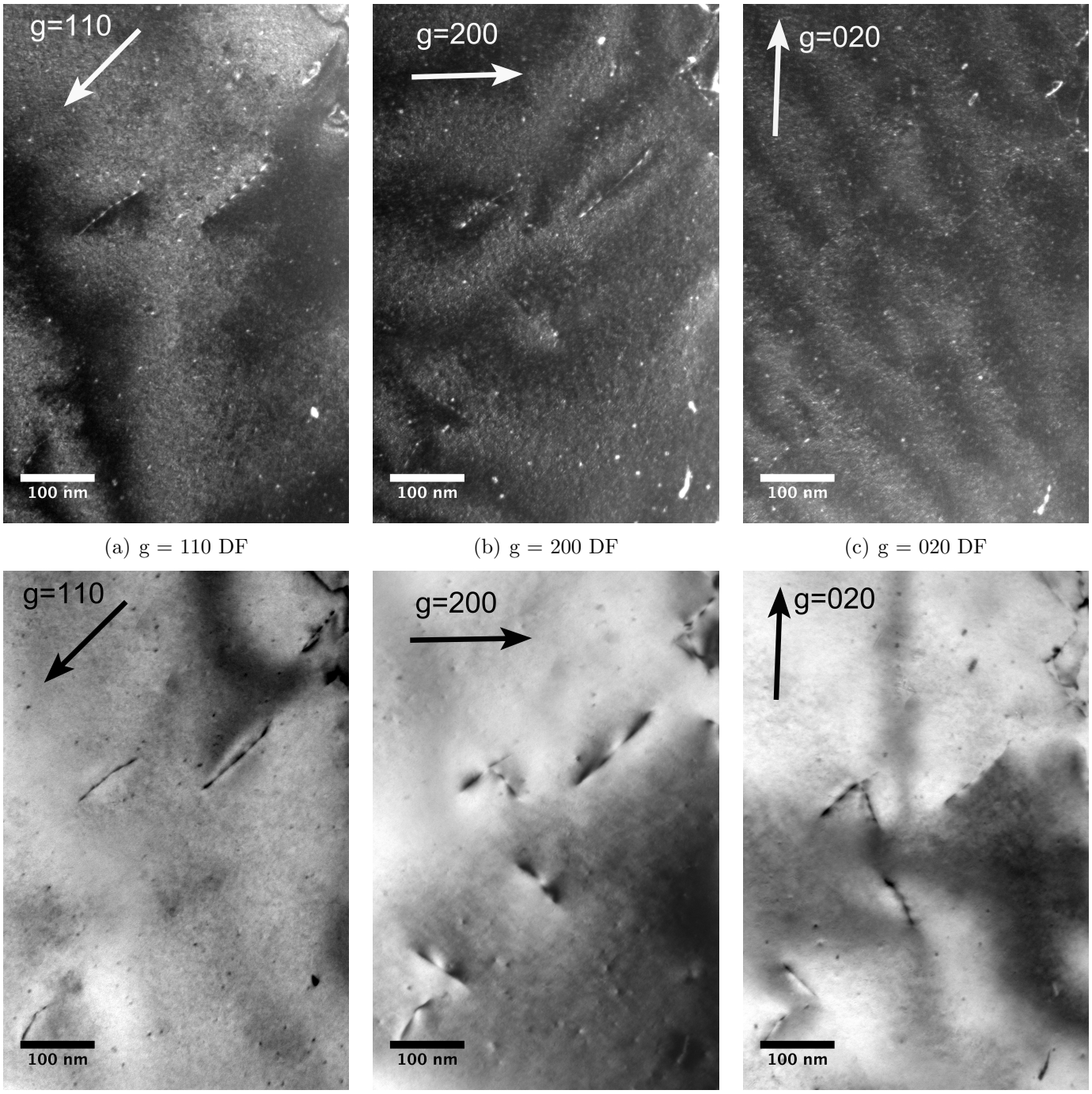

(a) g = 110 DF (b) g = 200 DF (c) g = 020 DF

(d) g = 110 BF (e) g = 200 BF (f) g = 020 BF

Figure 3.58: Same area TEM images of Fe-10Cr poly-crystal irradiated at 450°C to 0.01 dpa. DF and BF images were taken with different diffraction conditions: g = 110, g = 020 and g = 200 where the electron beam is close to [001] direction.

3.1.21 Fe-10Cr poly-crystals irradiated at 450C to 0.1dpa

Figure 3.59 and Figure 3.60 shows the TEM micrographs of the same area near the (111) zone in a Fe-10Cr poly-crystal irradiated at 450°C to 0.1 dpa with various magnifications. The images of the lowest magnification, Figure 3.59, show a large examination area featuring a uniform distribution of dislocation loops and a low density of dislocation lines ($1.78\times10^{12}\frac{1}{m^2}$). Different from the 0.01 dpa specimen in Chapter 3.1.20, it does not exhibit a 'two-size-groups' morphology of dislocation loops. In other words, dislocation loops of particularly large sizes (than the majority of loops) were not observed. Figure 3.60 is higher magnification micrograph showing that dislocation loops are large resolvable loops. The average size $\bar{d}_{loop}$ is 7.3 nm when measured with g = 200, and 9.59 nm when measured with g = $0\bar{1}1$. The volume density of dislocation loops was measured to be $7.8\times10^{21}\frac{1}{m^3}$.

Figure 3.61 is the TEM micrographs of the same area using g = $1\bar{1}0$ and g = 200 diffraction conditions close to (011) zone. According to the orientation of loop projections and the invisibility conditions, it was concluded that the majority of dislocation loops has a Burgers' vector b = $\langle 100\rangle$ and a habit plane on $\{100\}$ perpendicular to their Burgers' vector. The $\langle 100\rangle$ loops constitute 95% of the total observed dislocation loops, and the other 5% is $\frac{1}{2}\langle 111\rangle$ loops.

Clustering (but not coalescence) of dislocation loops was frequently observed. Figure 3.62 shows a few examples. When size measurements were performed, the loops constituting clusters were treated as separate loops.

3.1.22 Fe-10Cr poly-crystals irradiated at 450C to 1 dpa

In the Fe-10Cr poly-crystal irradiated at 450° to 1 dpa, the distribution of defects, both irradiation-induced and pre-existing, is inhomogeneous. Figure 3.63 is a low magnification TEM micrograph showing the morphology of line dislocations (presumably pre-existing) in a region with a thickness of 550 nm. It is dislocation-dense on the bottom and dislocation-sparse on the top. This inhomogeneous distribution of line dislocations appeared uniformly across the specimen. In addition, it is similar to the morphology of line dislocations in the unirradiated control specimen shown in Figure 3.1, indicating that 1 dpa irradiation at 450°C

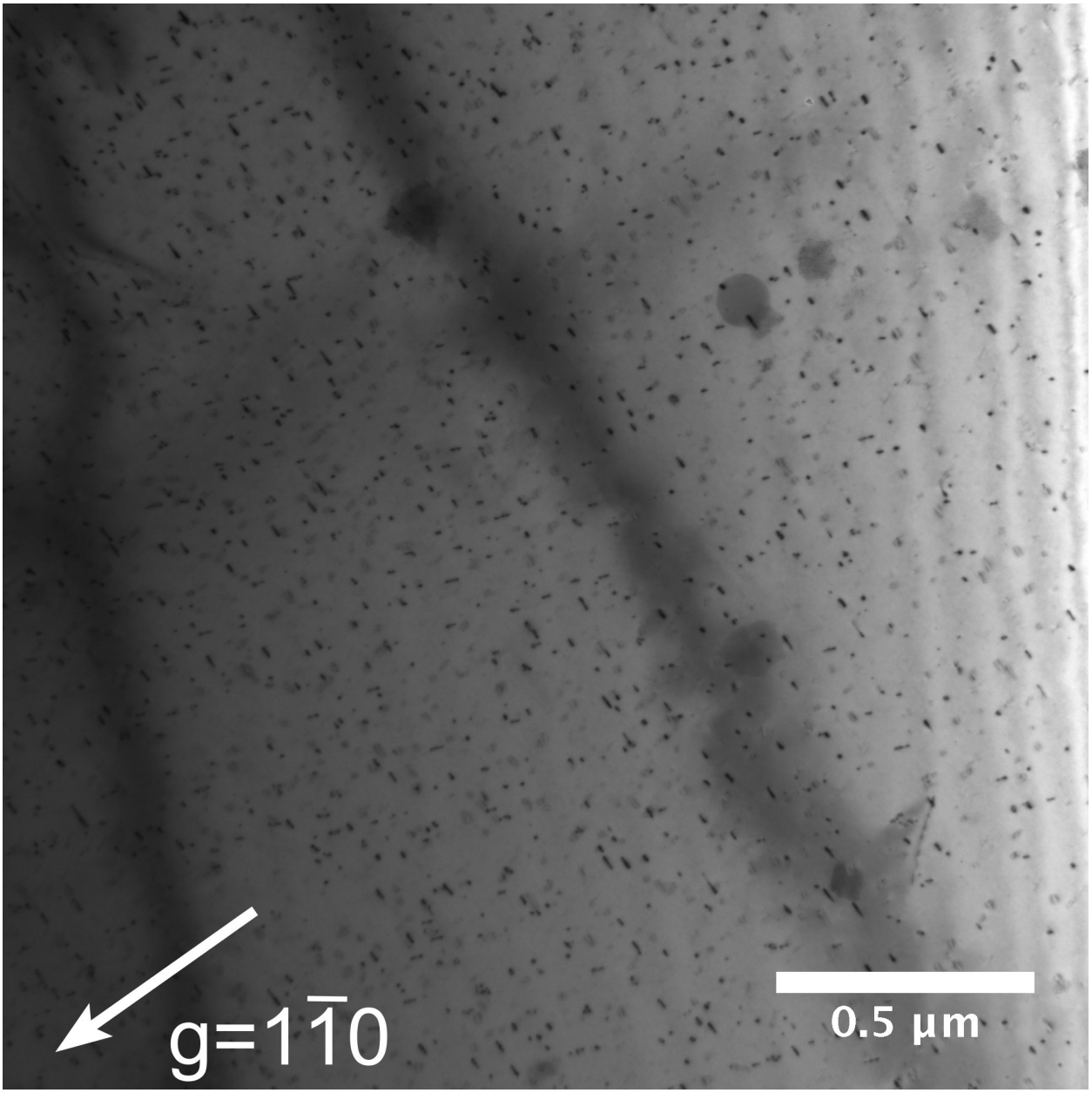

Figure 3.59: Low magnification TEM image of Fe-10Cr poly-crystal irradiated at 450°C to 0.1 dpa. Image was taken under kinematic bright field g = 1$\bar{1}$0 condition with beam direction close to [111].

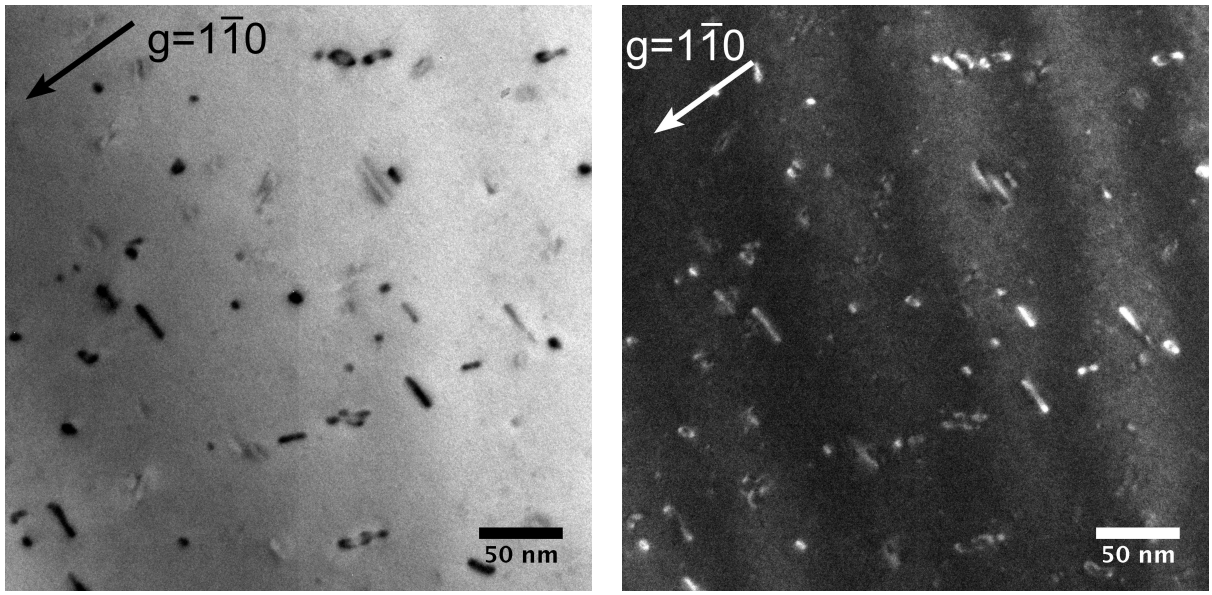

(a) Bright field (b) Dark field

Figure 3.60: High magnification TEM images of Fe-10Cr poly-crystal irradiated at 450°C to 0.1 dpa. TEM images were taken under g = 1$\bar{1}$0 kinematic bright field and (g, 4.3g) dark field with beam direction close to [111].

did not significantly change the structure of pre-existing line dislocations in the Fe-10Cr poly-crystals. The dislocation densities were measured over a wide area (roughly 100 μm^2) covering several dislocation-dense and dislocation-sparse regions. Excluding irradiation-induced dislocation loops, the average density of line dislocation was estimated to be 4.6x10^{12} $\frac{1}{m^2}$.

The Burgers vectors of the line dislocations were characterized with three diffraction conditions $\mathbf{g} = 1\bar{1}0$, $\mathbf{g} = 0\bar{1}1$ and $\mathbf{g} = 200$. Figure 3.64 shows the TEM micrographs of the same area as the lower-left portion of Figure 3.63 using g = 1$\bar{1}$0 and g = 200. Figure 3.63 used g = 0$\bar{1}$1. The invisibility criterion of line dislocations in these three diffraction conditions indicates that their Burgers' vectors **b** are 1/2$\langle 111 \rangle$. The glide planes of the line dislocations are deduced from their orientations. Figure 3.63 and Figure 3.64(b) are both close to the (111) zone, and their (1$\bar{1}$0), (10$\bar{1}$) and (01$\bar{1}$) planes are nearly edge-on (vertical to paper). Compared with diffraction pattern taken at (111) zone axis, the orientations of the three sets of line dislocations are found in coincidence with (1$\bar{1}$0), (10$\bar{1}$) and (01$\bar{1}$) planes, indicating that the glide planes are {110}.

In addition to the pre-existing line dislocations, irradiation-induced microstructure change

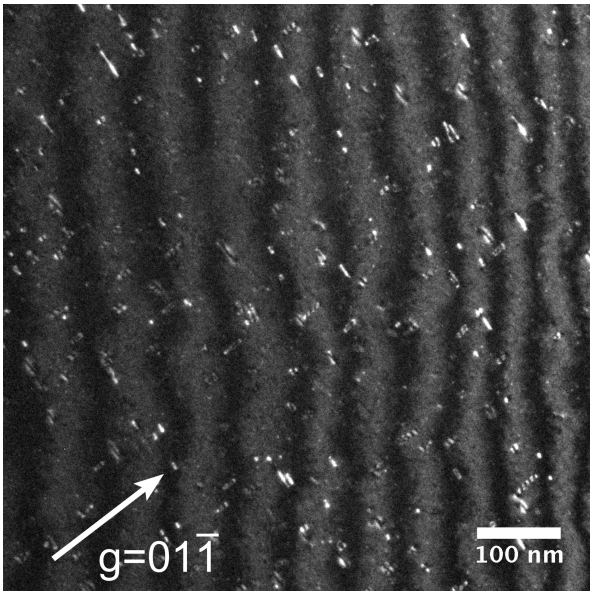

(a) Dark-field g = 01$\bar{1}$

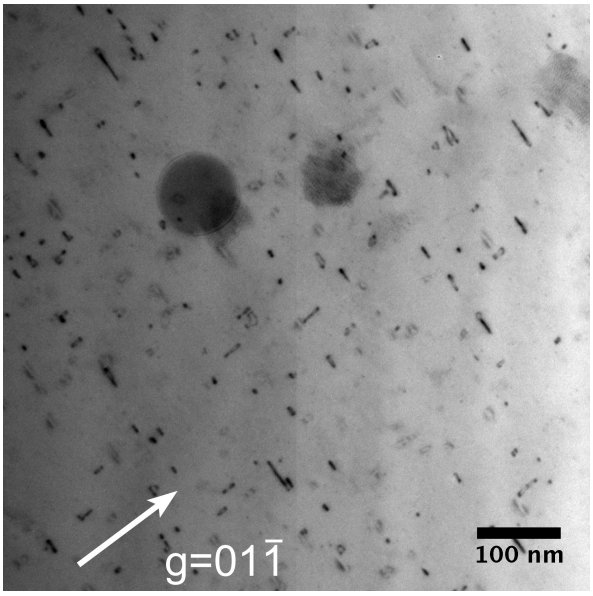

(b) Bright-field g = 01$\bar{1}$

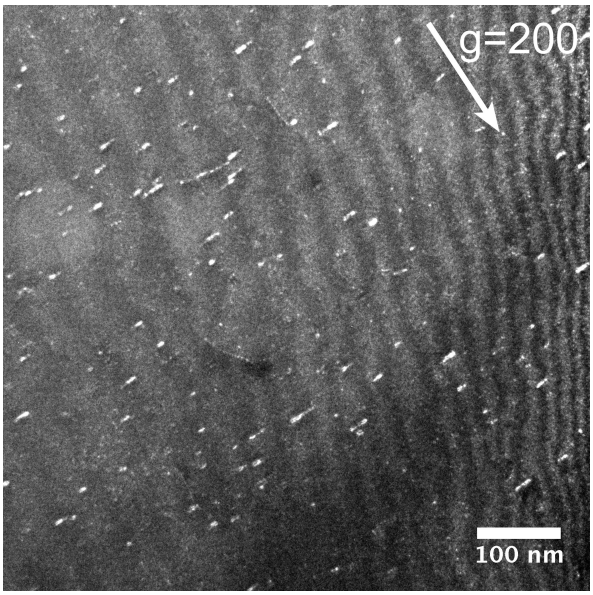

(c) Dark-field g = 200

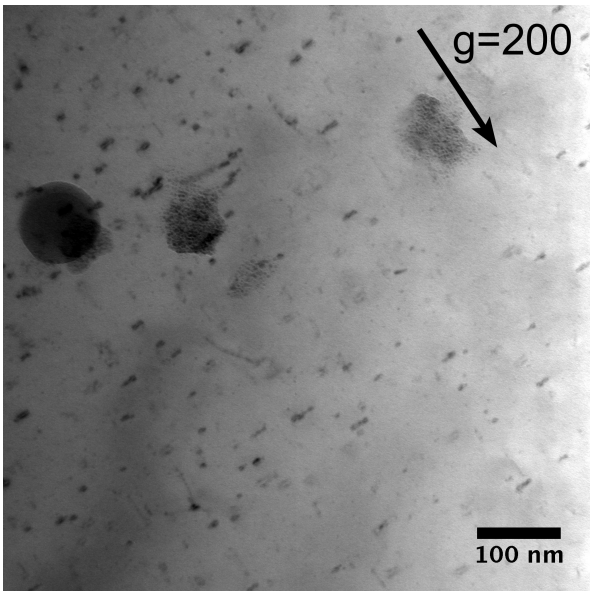

(d) Bright-field g = 200

Figure 3.61: TEM images of the same area of a Fe-10Cr poly-crystal irradiated at 450°C to 0.1 dpa. DF images were taken under with (a) g = 01$\bar{1}$ (g, 4.3g) and (c) g = 200 (g, 3g). BF images were taken under kinemetical condition. The beam direction is close to [011] for all images. The images were taken from the same area as Figure 3.59 and 3.60

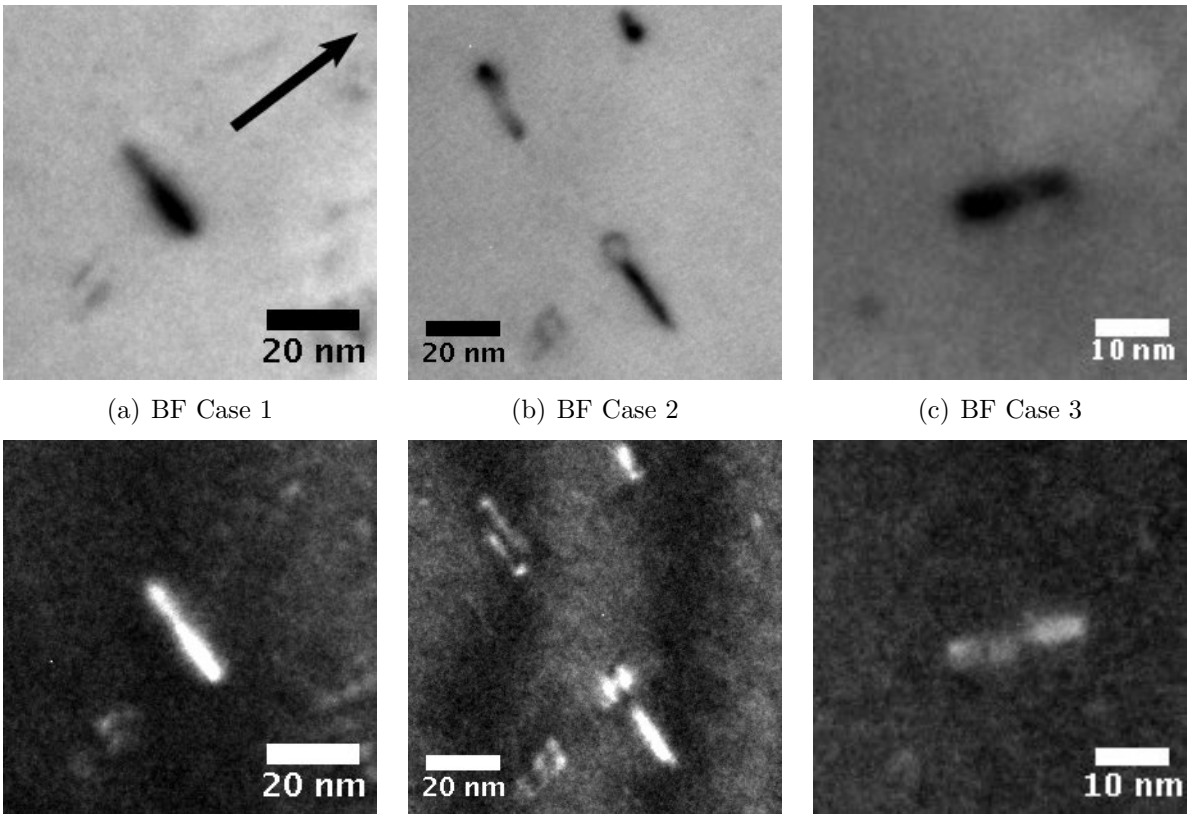

(a) BF Case 1 (b) BF Case 2 (c) BF Case 3

(d) DF Case 1 (e) DF Case 2 (f) WBDF Caes 3

Figure 3.62: Zoomed-in TEM micrographs of Fe10Cr specimen irradiated at 450°C to 0.1 dpa, focusing on individual clusters of dislocation loops. The imaging condition was g = $01\bar{1}$ where the electron beam was close to (a)(d)(b)(e) [011] direction and (c)(f) [111] direction. BF was taken under kinematic condition and DF was taken under (g, 4.3g) imaging conditions. The g vectors are the same for all of the six images.

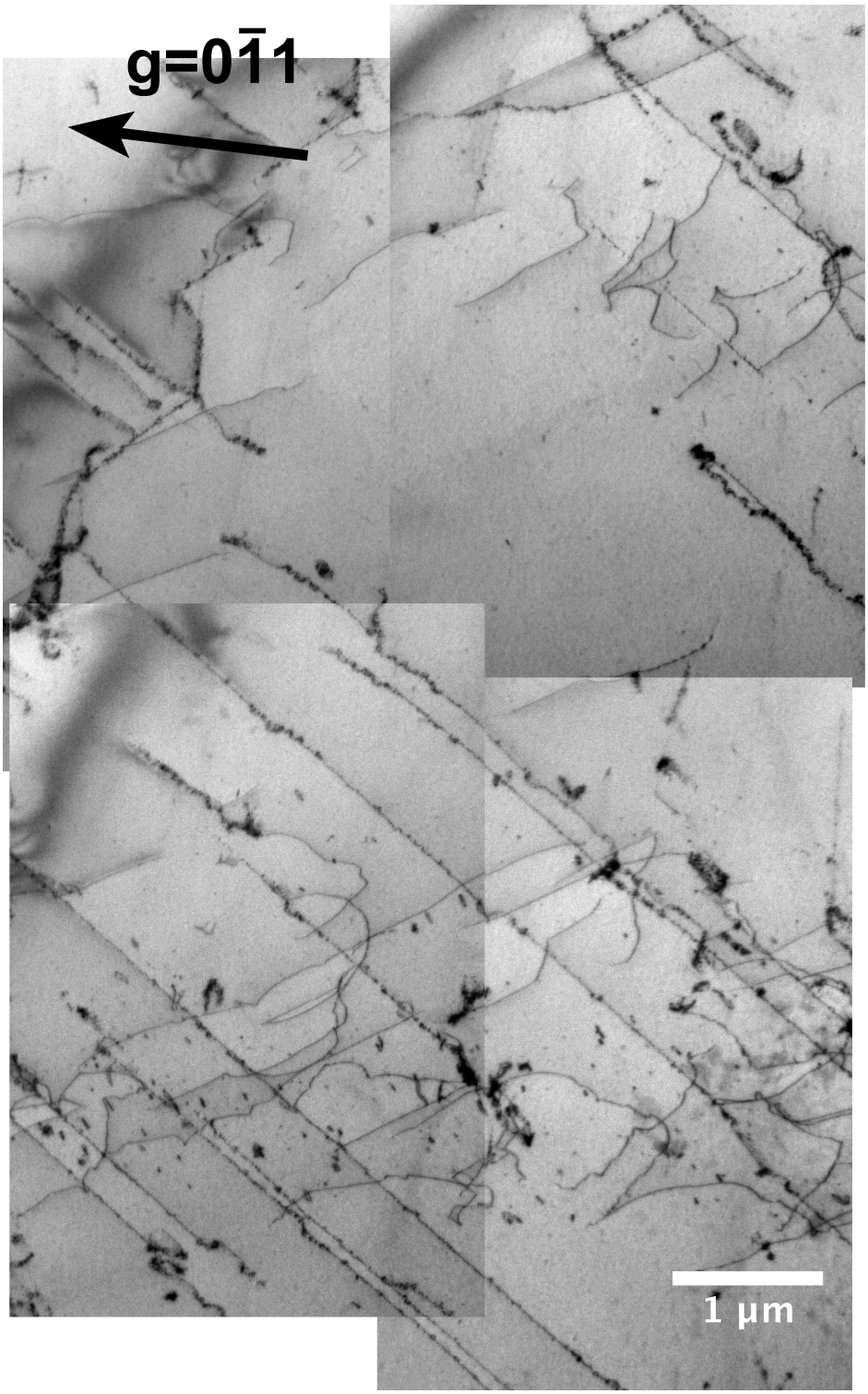

Figure 3.63: TEM images of Fe-10Cr poly- crystal irradiated at 450°C to 1 dpa. The imaging condition is g = 0$\bar{1}$1 kinematic BF where the electron beam is close to [111] direction. The foil thickness at the center of the image is 550 nm, obtained with EELS measurements.

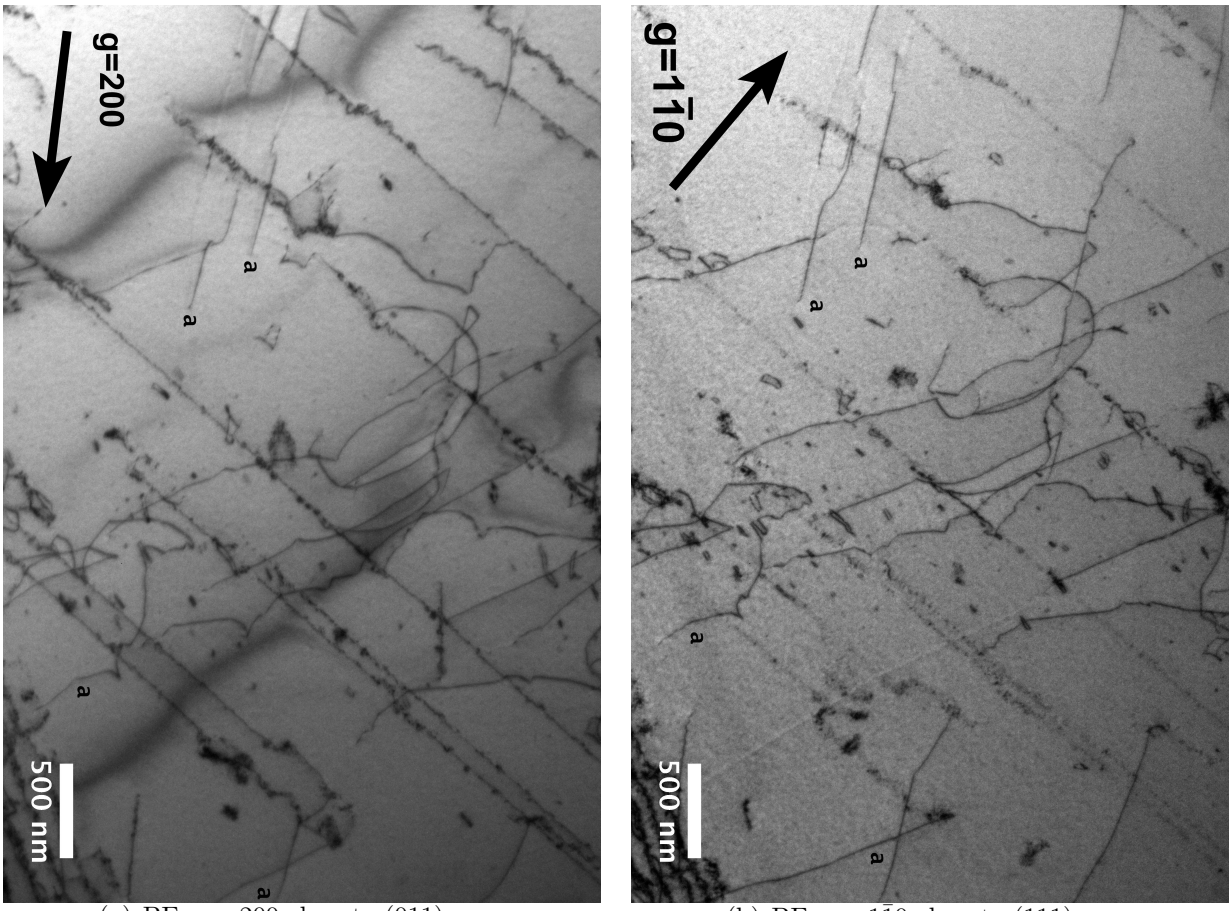

(a) BF g = 200 close to (011) zone

(b) BF g = 1$\bar{1}$0 close to (111) zone

Figure 3.64: TEM images of Fe-10Cr poly-crystal irradiated at 450°C to 1 dpa with two different imaging conditions and orientation. The thickness at the center of the micrograph are 600 nm. The thickness was measured with EELS.

was observed as a) uniform dispersion of small dislocation loops b) clustering of large dislocation loops and c) line dislocation decoration. Figure 3.65 shows the TEM micrograph of a (line) dislocation-sparse region. The radiation damage took the form of a uniform distribution of small dislocation loops of average size $\bar{d}_{loop-matrix}$ = 3.5 nm and density $\bar{N}_{loop-matrix}$ = 1.4x10$^{21}\frac{1}{m^3}$. While the area shown in Figure 3.65 contains only small dislocation loops, Figure 3.66 shows that there is a group of larger dislocation loops (marked with arrows in the figure) coexisting with the small dislocation loops. The size of the larger loops in Figure 3.66 varies from 7 to 41 nm, which is significantly larger than the uniformly-dispersed small dislocation loops. Also, there is no apparent transition (in size) between the small and the large dislocation loops, suggesting that the two groups might have different characteristics (i.e. Burgers' vector, habit planes and nature).

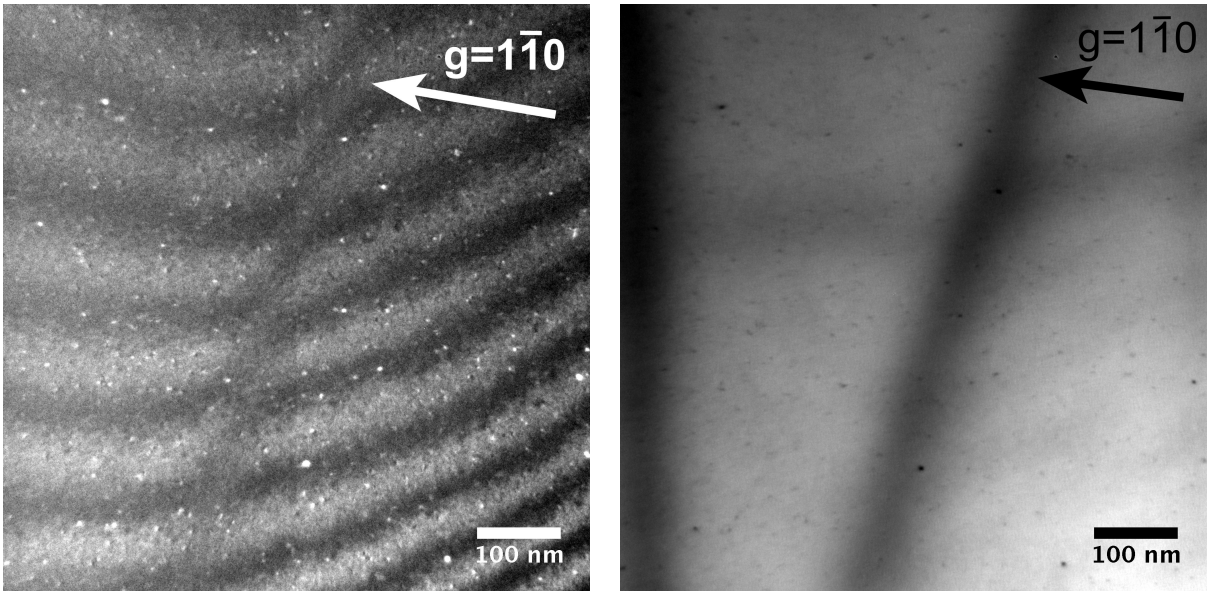

(a) DF (b) BF

Figure 3.65: TEM images of Fe-10Cr poly-crystal irradiated at 450°C to 1 dpa. The diffraction condition is $\mathbf{g} = 1\bar{1}0$ at (110) zone. The foil thickness at the center of the image was estimated to be 170 nm.

Because of their low volume density, quite often they were not observed in a TEM micrograph when the foil thickness of the viewing area is small (ex. Figure 3.64). In addition, the rate of their appearance is positively correlated to the density of line dislocations, as shown in Figure 3.63 and Figure 3.64. A more evident example of the (large) loop associating

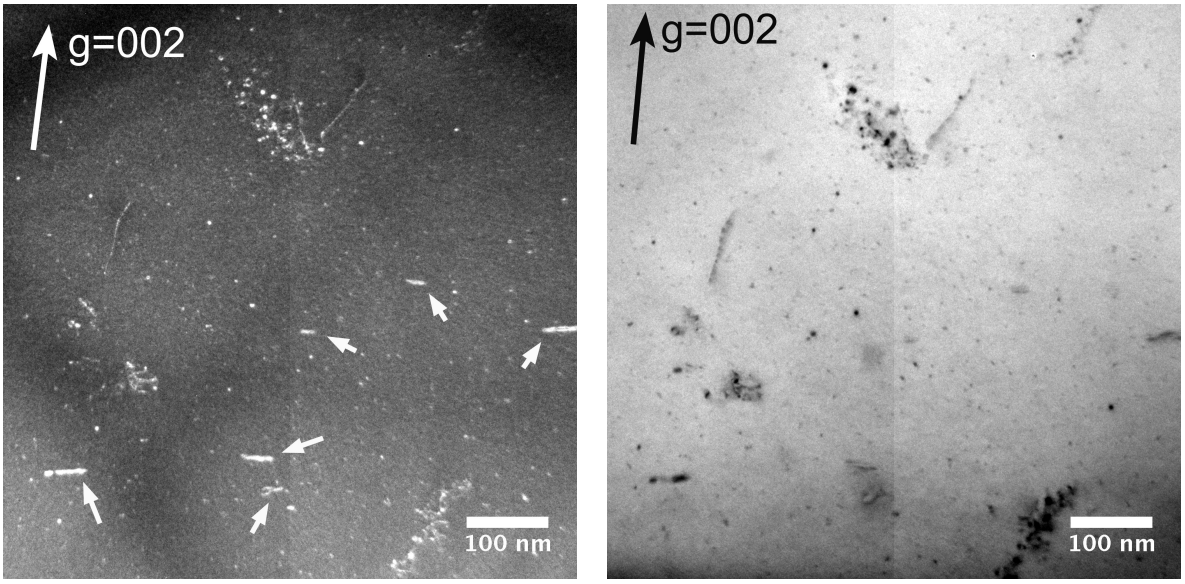

(a) DF (b) BF

Figure 3.66: TEM images of Fe-10Cr poly-crystal irradiated at 450°C to 1 dpa. The diffraction condition is $\mathbf{g} = 002$ at (110) zone. The foil thickness of the image was estimated to be 340 nm.

with (not decorating) line dislocations is shown in Figure 3.67 to Figure 3.69. These figures are the same-area TEM micrographs taken with different diffraction conditions ($\mathbf{g} = 200$, $\mathbf{g} = 1\bar{1}0$ and $\mathbf{g} = 0\bar{1}1$) at a thicker area of 800 nm. Note that the small dislocation loops (3.5 nm) should still exist uniformly within the volume, but they were not visible at this combination of high thickness and low magnification (both degrades the resolution). The size of largest loop observed in this region is 190 nm. The volume density of the large loops in this region was measured to be $4.6\text{x}10^{19}\frac{1}{m^3}$, which is about 4% of the density of small dislocation loops. Considering the heterogeneous distribution of these large dislocation loops, the average density of loops across the entire crystal should be smaller than this number.

Many line dislocations were decorated by dislocation loops. Figure 3.70(a)(b) shows a line-up of dislocation loops along a line dislocation. The line dislocation itself is invisible because the diffraction condition satisfies the invisibility criterion $\mathbf{g}\cdot\mathbf{b} = \mathbf{0}$. The micrographs also indicate that some line dislocations were not decorated. It is a general observation that some of the line dislocations are decorated and some are not. Going back to Figure 3.64, the line dislocations marked with A are not decorated by dislocation loops in both diffraction

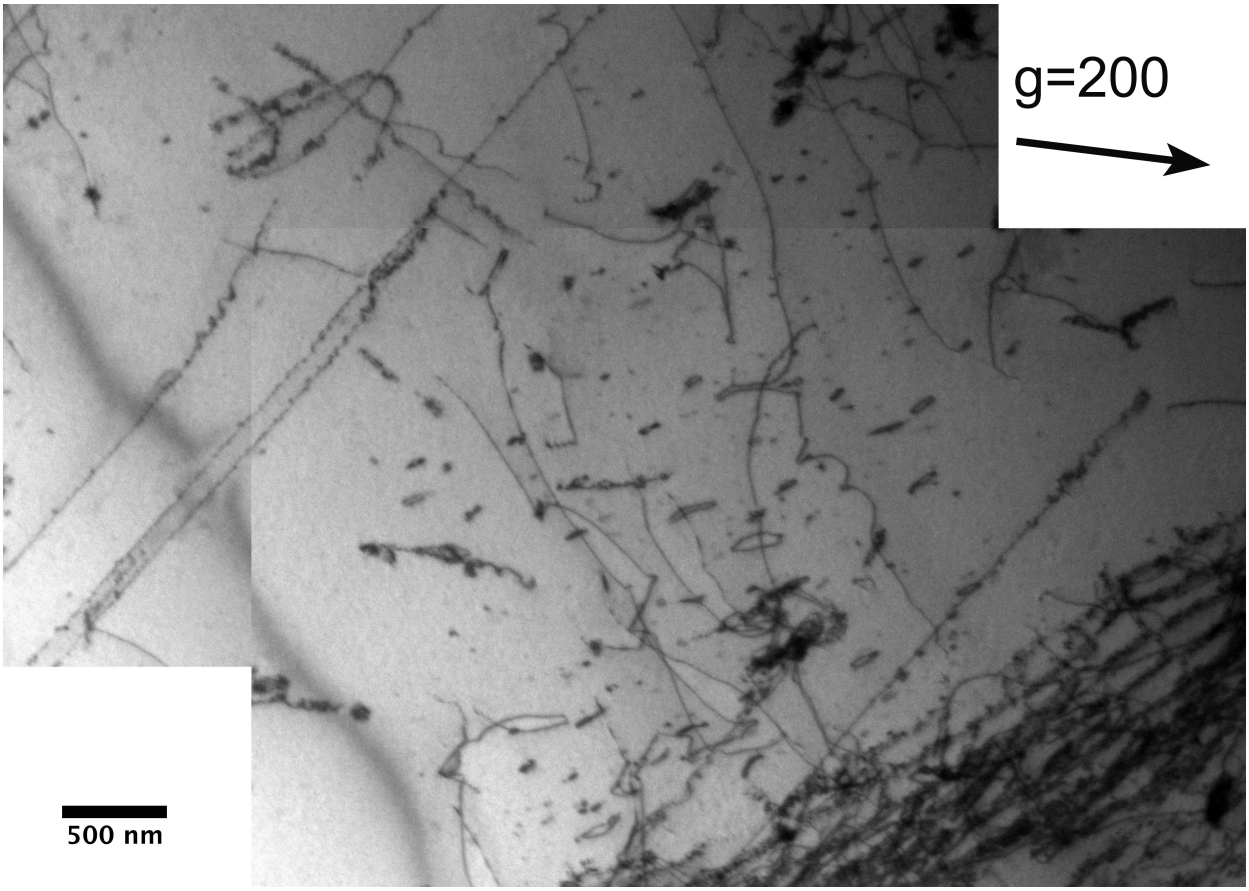

Figure 3.67: TEM images of Fe-10Cr poly-crystal irradiated at 450°C to 1 dpa. The imaging condition is g = 200 close to (011) zone. The thickness at the center of the micrograph is 800 nm. The thickness was measured with EELS.

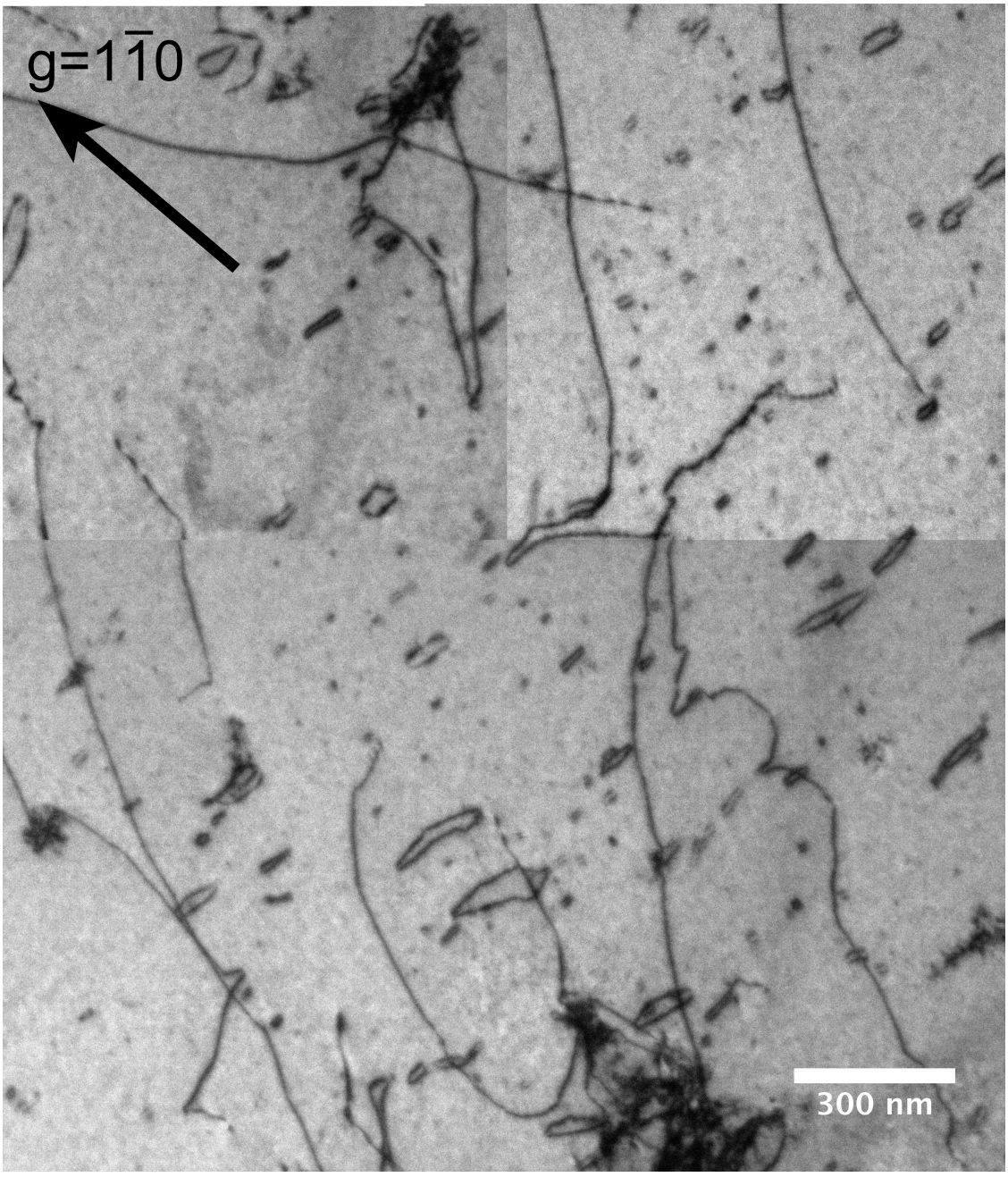

Figure 3.68: TEM images of Fe-10Cr poly- crystal irradiated at 450°C to 1 dpa.The image condition is g = 1$\bar{1}$0 close to (111) zone.

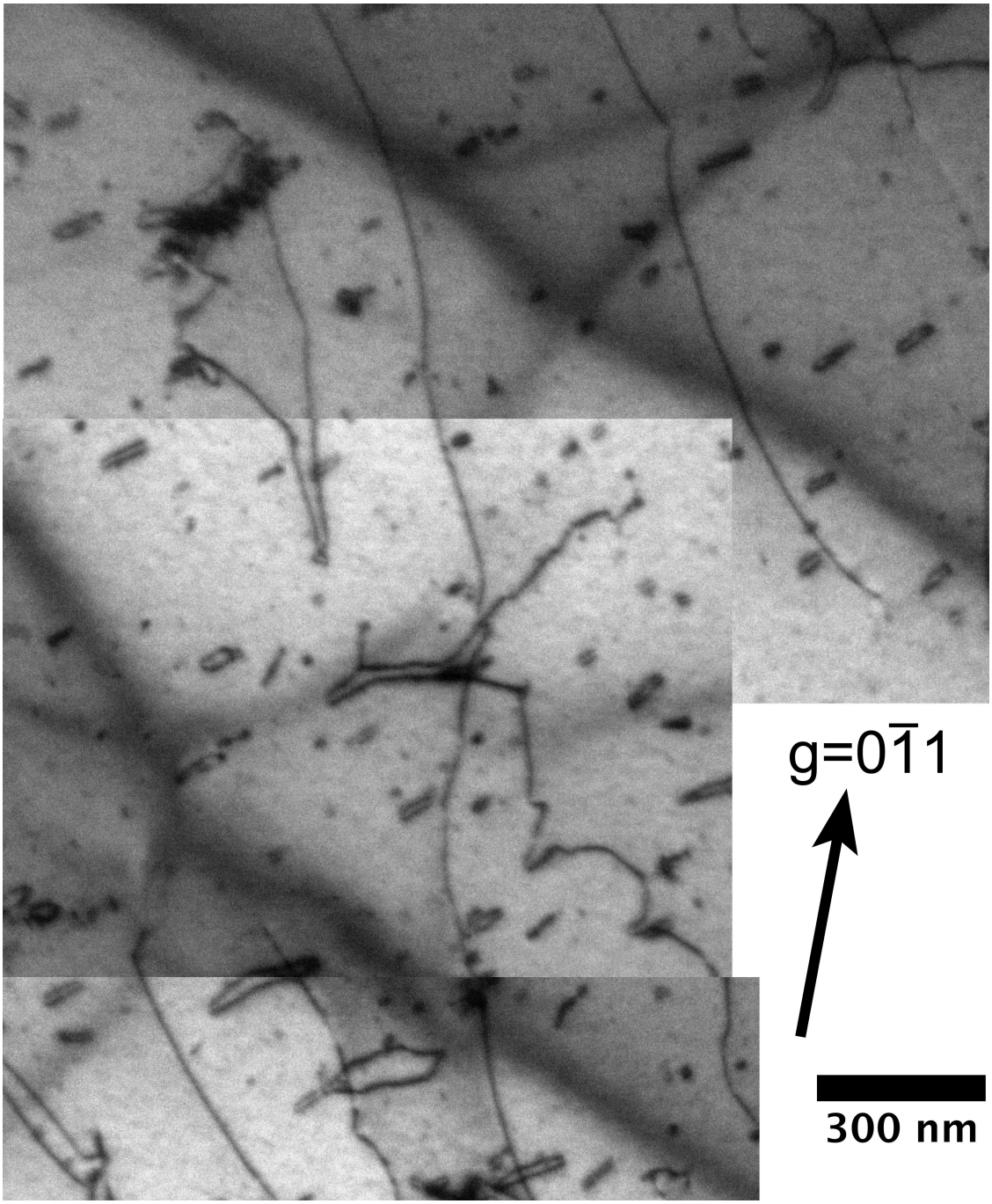

Figure 3.69: TEM images of Fe-10Cr poly- crystal irradiated at 450°C to 1 dpa. The image condition is g = 0$\bar{1}$1 close to (011) zone.

conditions. This indicates that the absence of decorating loops on line dislocations 'a' is truly due to a missing of decorating loops, and is not due to imaging conditions.

Another instance of dislocation decoration is shown in Figure 3.70(c)(d). In this case, the line dislocation was decorated on one side. However, microstructure like Figure 3.70(c)(d) was only observed occasionally. It is more frequent to observe decorations on both sides (e.g. Figure 3.70(e)(f)) or as a straight line (e.g. Figure 3.70(c)(d)).

Finally, the dislocations composing the low-angle grain boundaries were observed to be decorated by small dislocation loops as well. Figure 3.71 shows a set of TEM images of a triple-junction of low-angle grain boundaries. Sub-figure 3.71(a) shows the diffraction pattern taken at the grain boundary. The diffraction pattern indicates that the crystallographic orientations of nearby grains is nearly identical. This is consistence with the fact that the image contrast of each grain in Figure 3.71(b) is similar. A small tilting between the two grains could be inferred from the split of the $\bar{2}\bar{2}0$ diffraction spot shown in the inset of 3.71(a). The grain boundaries are fairly close to edge-on, especially for the one at the top-right. The width of decoration from the grain boundary is roughly 200 nm.

3.1.23 Summary of Fe-10Cr poly-crystals irradiated at 450C

Figure 3.72 shows the comparison of microstructures between 0.01, 0.1 and 1 dpa Fe-10Cr poly-crystals irradiated at 450°C. For consistency, the images compared here are all taken from the thin region (∼100 nm) of the TEM foils. The corresponding quantitative measurement data is shown in Table 3.5. For the lower dose specimens of 0.01 dpa and 0.1 dpa, the microstructure is composed of a uniformly distributed a$\langle 100 \rangle$ (majority) and $\frac{a}{2}\langle 111 \rangle$ (minority) dislocation loops. The loop size increases significantly from 0.01 dpa to 0.1 dpa as well as the density. However, for 1 dpa specimen, the loop size oddly dropped to a size and density similar to 0.01 dpa.

In addition to the uniformly-distributed dislocation loops, 1 dpa specimen also exhibit heterogeneous-distributed dislocation loops that decorating (Figure 3.70) or being associated with (Figure 3.67) line dislocations, while 0.01 dpa and 0.1 dpa do not exhibit such heterogeneous microstructure. Those loops that found associated with the line dislocations

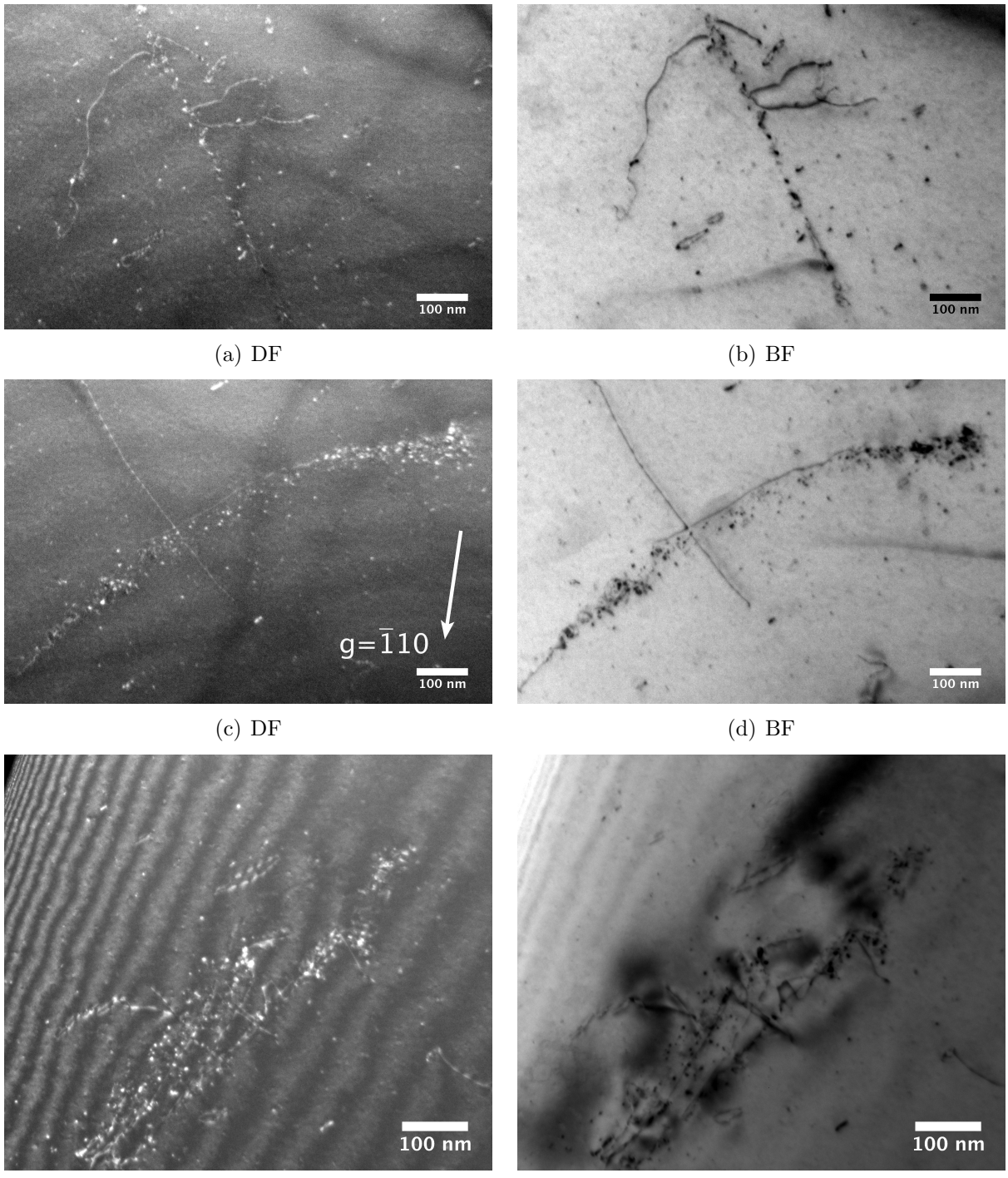

(a) DF (b) BF

(c) DF (d) BF

(e) BF (f) DF

Figure 3.70: TEM images of Fe-10Cr poly-crystal irradiated at 450°C to 1 dpa. The imaging condition is g = $\bar{1}$10 at (111) zone for all of the images. The g vector shown in (c) applies for all of the six micrographs.

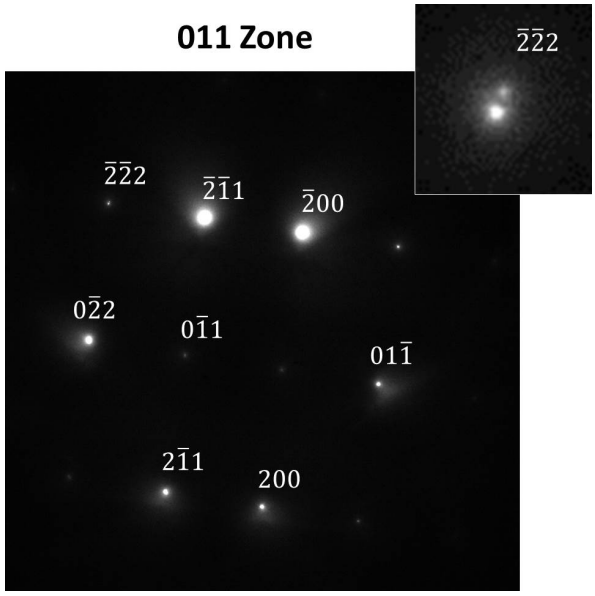

(a) Diffraction pattern

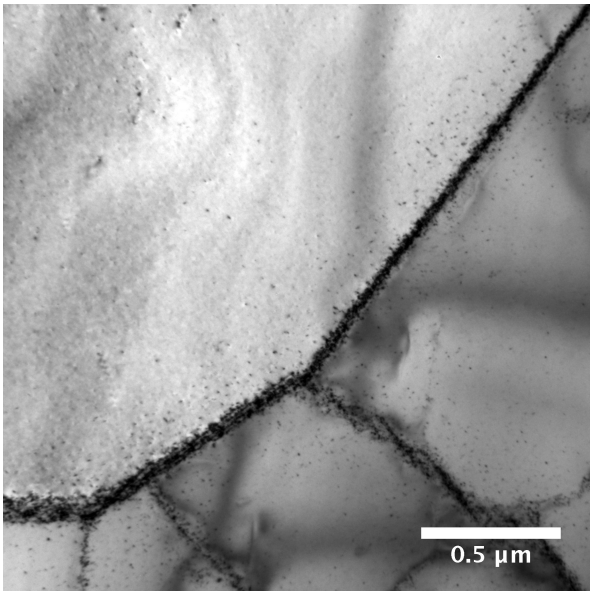

(b) BF Low Mag

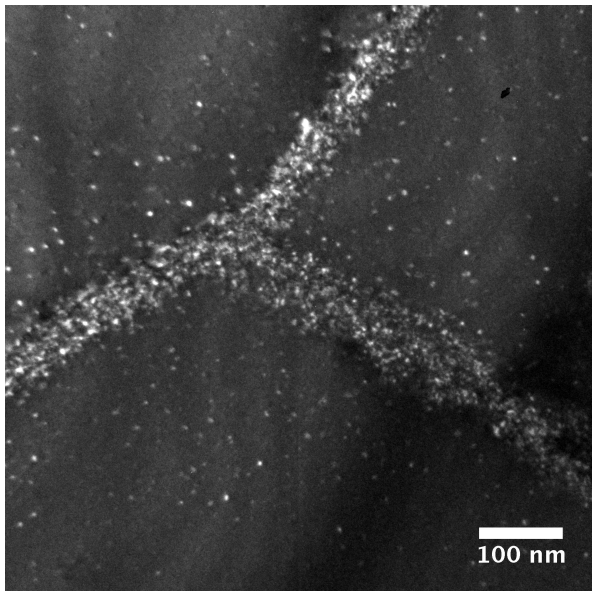

(c) DF High Mag

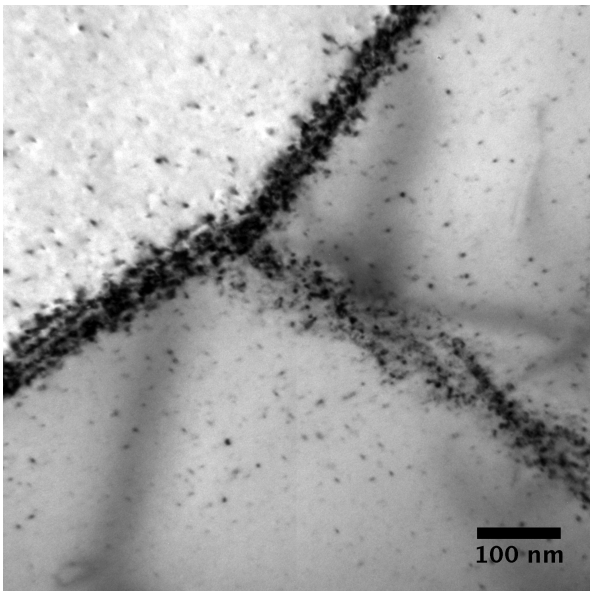

(d) BF High Mag

Figure 3.71: (a)The (011) zone axis diffraction pattern taken at the boundary of two sub-grains.The inset is an enlarged image of $\bar{2}\bar{2}0$ spot. (b)-(d)TEM images of Fe-10Cr poly-crystal irradiated at 450°C to 1 dpa. Dark-field images taken under g = $01\bar{1}$ kinematic BF and (g, 4.3g) DF with beam direction close to [011].

in 1 dpa specimen are much larger. Finally, no voids formation were observed in any of the Fe-10Cr polycrystalline specimens irradiated at 450°C.

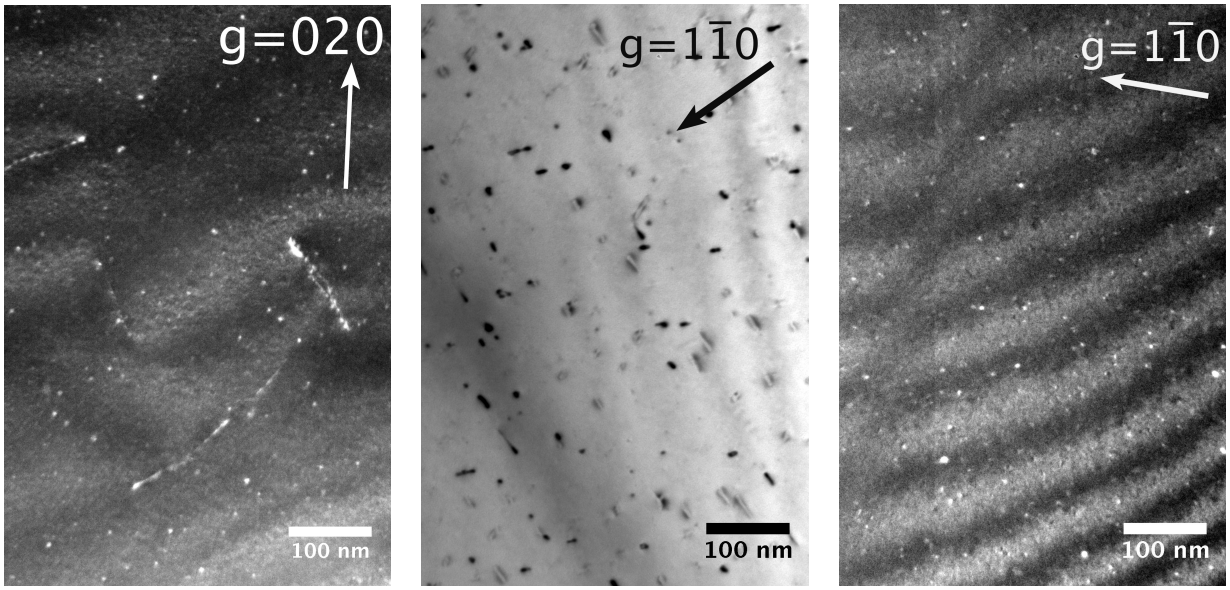

(a) 0.01 dpa (b) 0.1 dpa (c) 1 dpa

Figure 3.72: TEM micrograph of Fe10Cr polycrystals irradiated at 450°C. The foil thickness for the three images are all roughly 100-200 nm.

3.1.24 Fe-14Cr single-crystal irradiated at 450C to 0.01 dpa

Figure 3.74, 3.75 and 3.76 show the TEM micrographs of the Fe-14Cr single crystal irradiated at 450°C to a dose of 0.01 dpa with various foil thickness. Neutron damage taking the form of a high density of ($5.7\times10^{21}\frac{1}{m^3}$) small (3.0 nm) dislocation loops is visible as white dots in WBDF images or as dark dots in BF images. The fact that the areal density of visible dislocation loops increases with the foil thickness from Figure 3.74 to 3.76 is a good indication that the dot contrasts are indeed from volumetric defects and not from surface features. For surface features, their areal density should not be proportional on foil thickness.

A low density of dislocation lines can be observed in Figure 3.74 to 3.76. The density of the line dislocations was measured to be $1.7\times10^{13}\frac{1}{m^2}$. The distribution of dislocation loops in the crystal is uniform and is irrelevant to the pre-existing dislocations, suggesting that there was negligible interactions between visible dislocation loops and the dislocations.

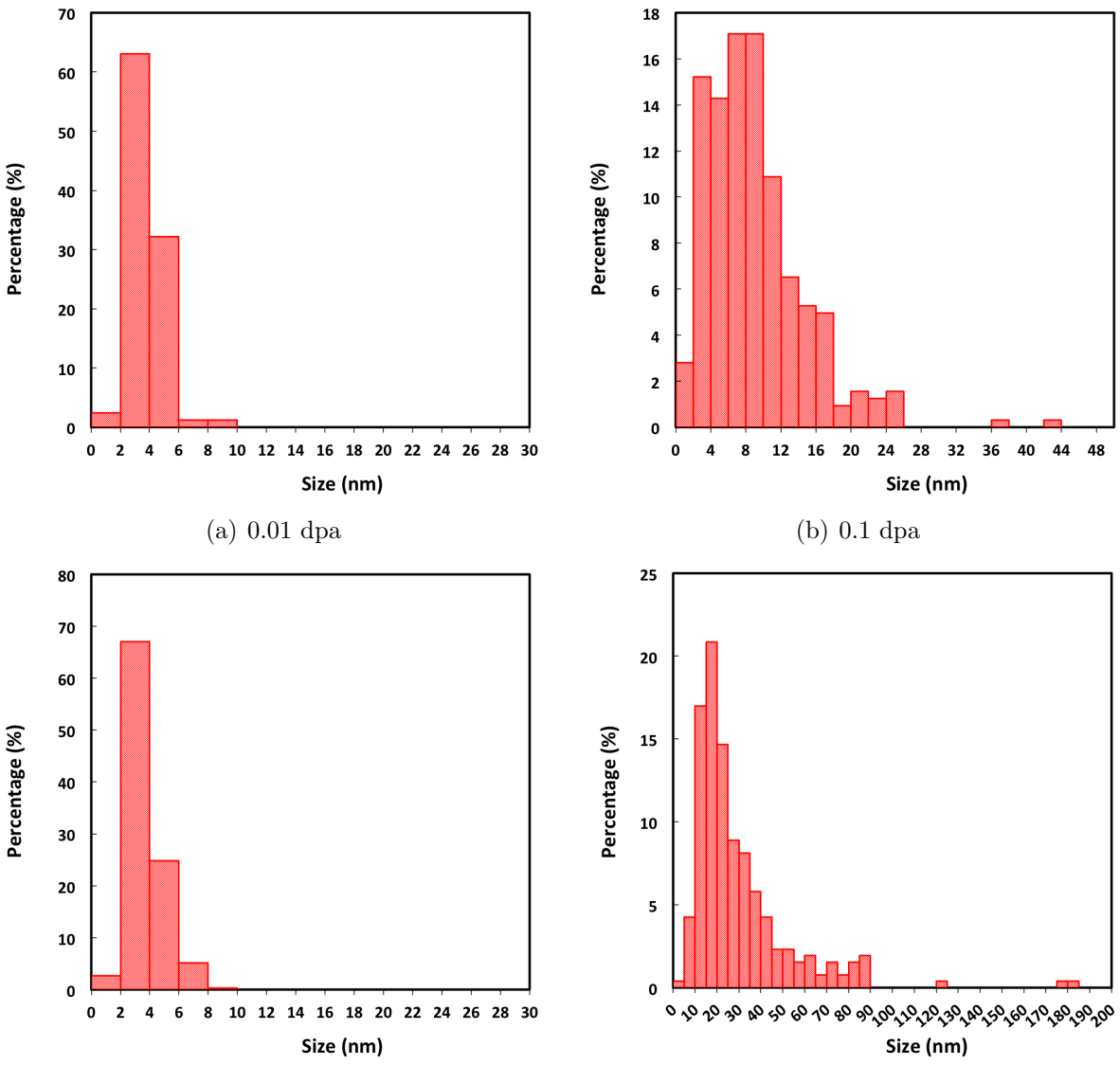

(a) 0.01 dpa

(b) 0.1 dpa

(c) 1 dpa small uniform loops

(d) 1 dpa large heterogeneously-distributed loops

Figure 3.73: The size distribution of dislocation loops in Fe-10Cr polycrystals irradiated at 450°C as a function of irradiation dose.

Table 3.5: Microstructure data for Fe-10Cr poly-crystals irradiated at 450°C

	0.01 dpa	0.1 dpa	1 dpa
Dislocation density (10^{12} $\frac{1}{m^2}$)	24	1.8	4.6
$\bar{d}_{loop}$ (nm)	3.8	8.5[a]	3.5(31.1)[b]
$d_{loop,Max}$ (nm)	8.4	42.1	9.81 (182.9)[b]
N_{loop} (10^{21} $\frac{1}{m^3}$)	2.9	7.8	1.4(0.05)[b]
$\bar{d}_{void}$ (nm)	Not observed		
$d_{void,Max}$ (nm)	Not observed		

[a] Average of the measurement from g = {110} and g={200}
[b] Uniform small loops in the matrix (large loops associated with dislocations. Ex. Figure 3.68)

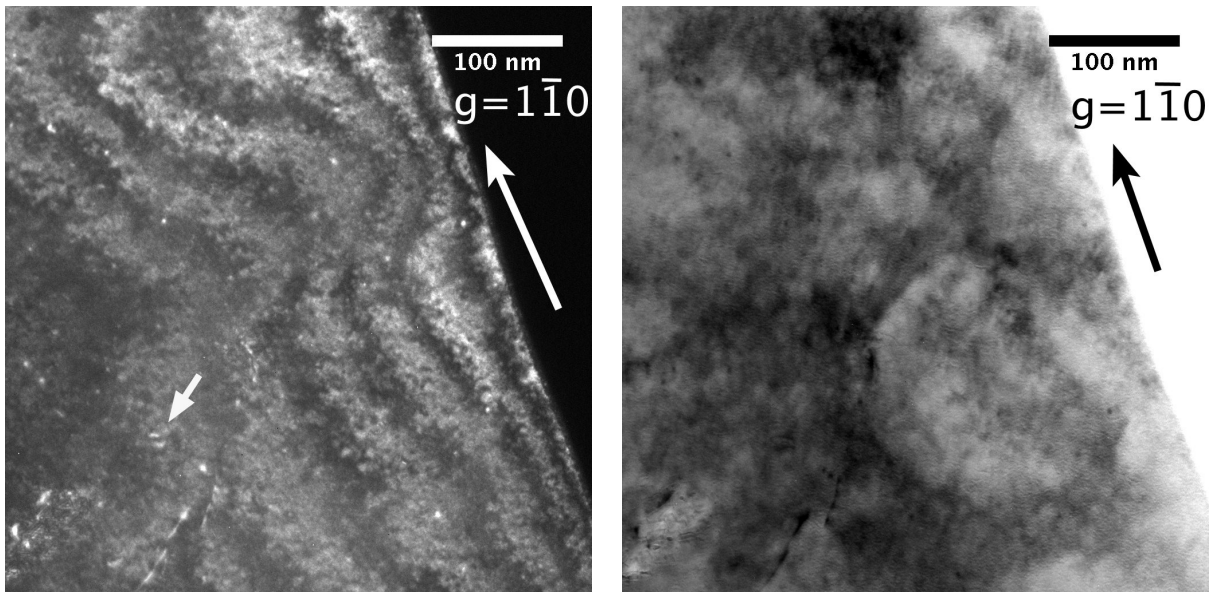

(a) Dark-field (b) Bright-field

Figure 3.74: TEM images of Fe-14Cr single crystal irradiated at 450°C to 0.01 dpa. Images were taken under g = 1$\bar{1}$0 (g, 4.3g) DF and kinematic BF with beam direction close to [111]. The images were taken at the edge of the perforation.

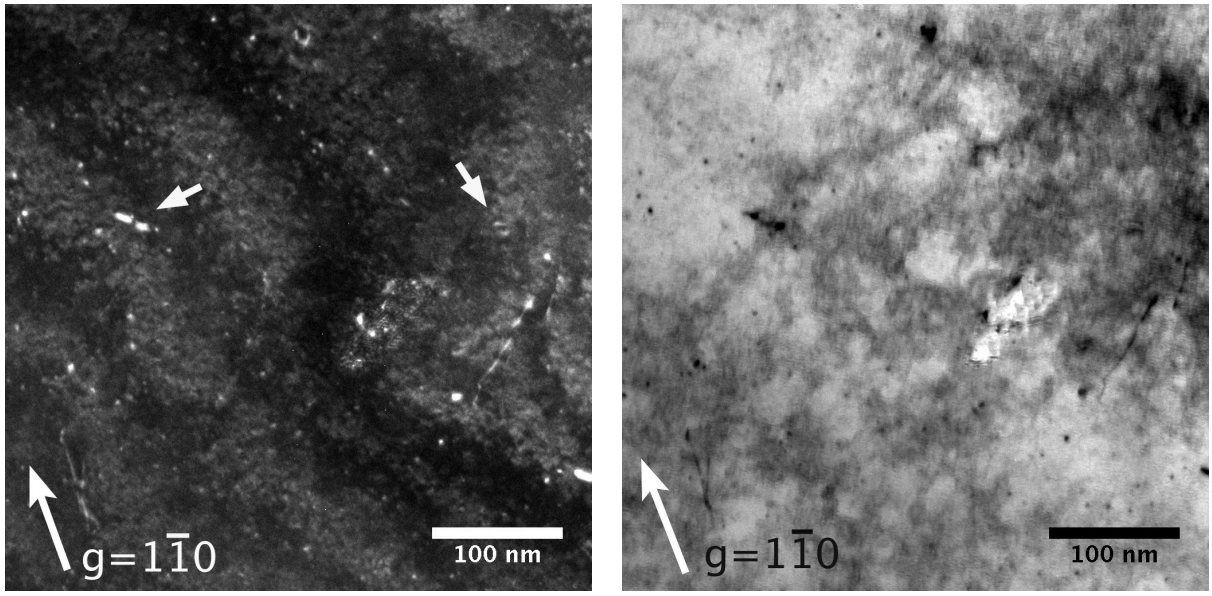

(a) Dark-field (b) Bright-field

Figure 3.75: TEM images of Fe-14Cr single crystal irradiated at 450°C to 0.01 dpa. Images were taken under g = 1$\bar{1}$0 (g, 4.3g) DF and kinematic BF with beam direction close to [111]. The thickness at the image center is estimated as 66 nm.

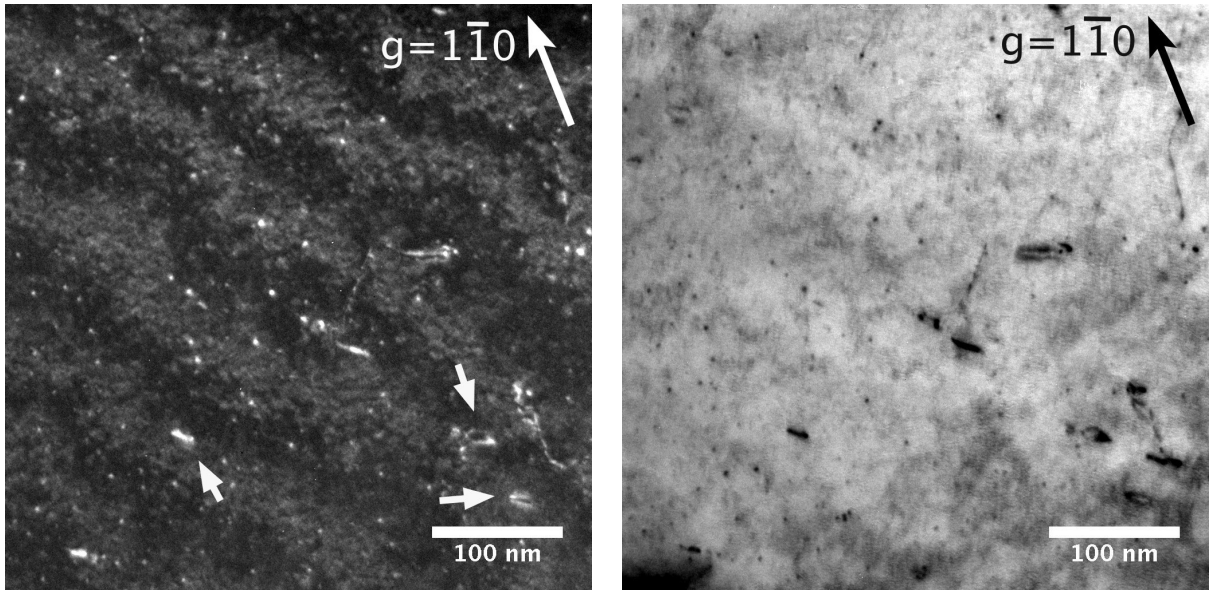

(a) Dark-field image (b) Bright-field image

Figure 3.76: TEM images of Fe-14Cr single crystal irradiated at 450°C to 0.01 dpa. Images were taken under g = 1$\bar{1}$0 (g, 4.3g) DF and kinematic BF with beam direction close to [111]. The thickness at the image center is estimated as 103 nm

The Burgers vector of these small dislocation loops have not been characterized rigorously. However, since their irradiation-induced microstructure is very similar to the Fe-10Cr polycrystalline specimen of the same irradiation condition, their Burgers vector is likely mostly a$\langle 100 \rangle$.

In addition to the small dislocation loops, a few large resolvable dislocation loops was observed as shown with the arrows in in Figure 3.74 to 3.76. Their size (10-20 nm) is abruptly larger than the uniformly-distributed small dislocation loops (3 nm), and no continuous transition between the small and large size groups can be evidently recognized, indicating the large loops have a different nature or origin from the small ones.

The origin and the nature of these larger dislocation loops is not clear. On one hand, similar observation have been found in the Fe-10Cr polycrystal irradiated at 450°C to 0.01 dpa (See Chapter 3.1.20). The coincident microstructure appearing in two individual specimens of identical irradiation condition is an indication that these large loops were induced by irradiations. On the other hand, features of unknown nature (loops or something else. See Chapter 3.1.3) of comparable size and density were observed in the archive un-irradiated specimen. It should not be excluded that the larger loops in the irradiated specimens are actually the same as those uncharacterized features in the un-irradiated specimens. At any rate, the volume density of these large loops is much less than the small dislocation loops, about two orders of magnitude less, and their role in the irradiation-hardening is considered to be limited.

3.1.25 Fe-14Cr single-crystals irradiated at 450C to 0.1 dpa

Figure 3.77 shows the TEM micrographas of the Fe-14Cr single crystal irradiated at 450°C to a dose of 0.1 dpa. Images were taken in nearby areas with orientations close to the same (111) zone with different diffraction conditions of g = $01\bar{1}$, $1\bar{1}0$ and $10\bar{1}$. The average size of dislocation loops in the 0.1 dpa specimen is significantly larger (8.9 nm) than that in the 0.01 dpa specimen (3.0 nm). In addition, Figure 3.77 shows the increasing areal density of dislocation loops with foil thickness. This is an evidence that the observed loop-contrasts are indeed from volumetric defects and are not from surface features. The volume density

of the dislocation loops was measured to be $5.5\times10^{21}\ \frac{1}{m^3}$.

Overall, the density of line dislocations is similar to the 0.01 dpa Fe-14Cr single crystal specimen irradiated at 450°C (section 3.1.24). However, in some micrographs, Figure 3.78 for instance, the dislocation density is much higher. In addition, most dislocations in Figure Figure 3.78 exhibit a bowing-and-pinned shape, indicating that these dislocations had experienced obstacles (i.e. dislocation loops) while gliding. This observation further implies that the specimen had been deformed after irradiation possibly during TEM specimen preparation. In addition to the dislocation produced by deformation, another possibility for the origin of these bowing dislocation segments are the coalescence of dislocation loops. $\frac{a}{2}\langle111\rangle$ loops are known to align and coalescence to form bigger finger-shaped loops [49]. Since most of the dislocation segments observed in this specimen is not paired or having a finger shape, the coalescence of dislocation loops as an explanation is not favored. The dislocation density in the 0.1 dpa-450°C specimen was measured to be $2.2\times10^{13}\frac{1}{m^2}$ by averaging all of the available TEM micrographs including Figure 3.78.

The TEM micrographs imaged using g = 200 and 020 in neighborhood areas are shown in Figure 3.79. The majority of the dislocation loops are determined to have a Burger's vector of b = $\langle100\rangle$ and a habit plane $\{100\}$ perpendicular to their Burger's vector. In Figure 3.79(a), dislocations loops with a habit planes on (010) is visible while the loops on (100) is invisible. In Figure 3.79(b), the observation is opposite. With the assumption that only $\langle100\rangle$ and $\frac{1}{2}\langle111\rangle$ dislocation loops exist and the invisibility observations in Figure 3.79, it is concluded that the majority of the dislocation loops has Burgers' vectors b = $\langle100\rangle$.

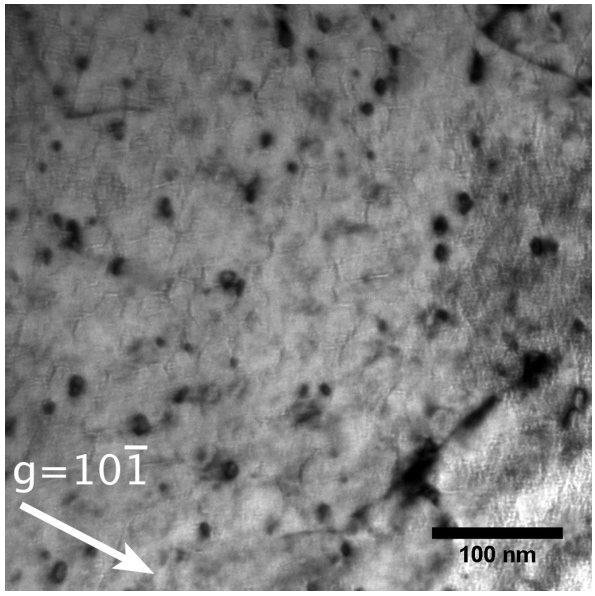

(a) g = 10$\bar{1}$

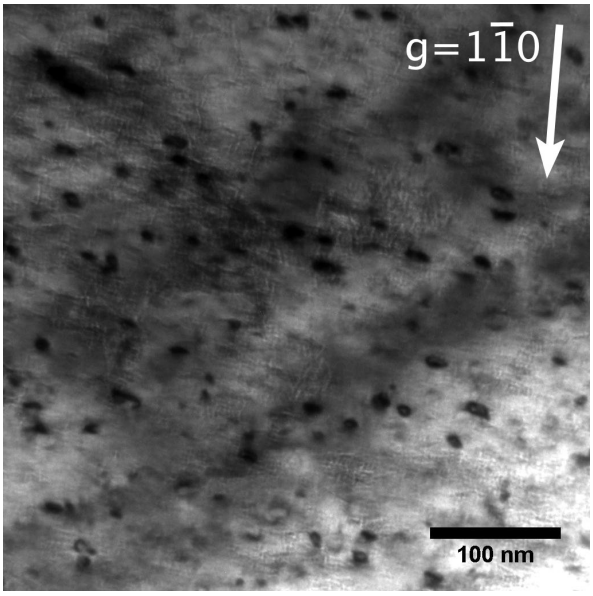

(b) g = 1$\bar{1}$0

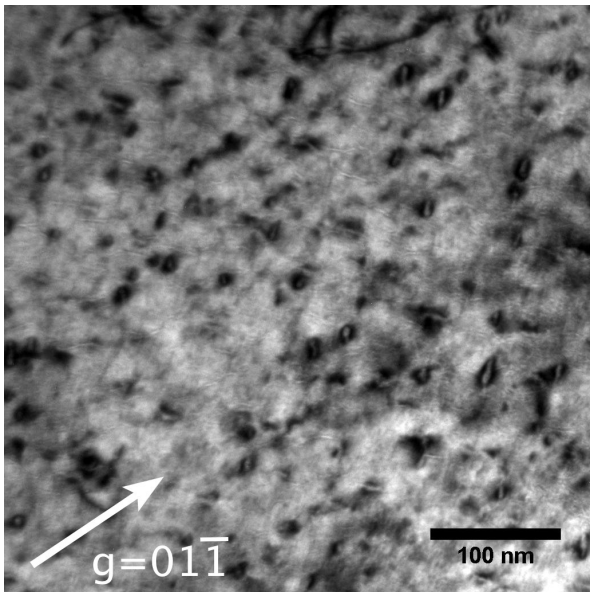

(c) g = 01$\bar{1}$

Figure 3.77: TEM images of Fe-14Cr single crystal irradiated at 450°C to 0.1 dpa. Bright field images were taken under kinematic conditions with g = (a) 10$\bar{1}$, (b) 1$\bar{1}$0 and (c) 01$\bar{1}$ with beam direction close to [111]. The thickness at the image center is estimated as (a) 113 nm, (b) 121 nm and (c) 160 nm

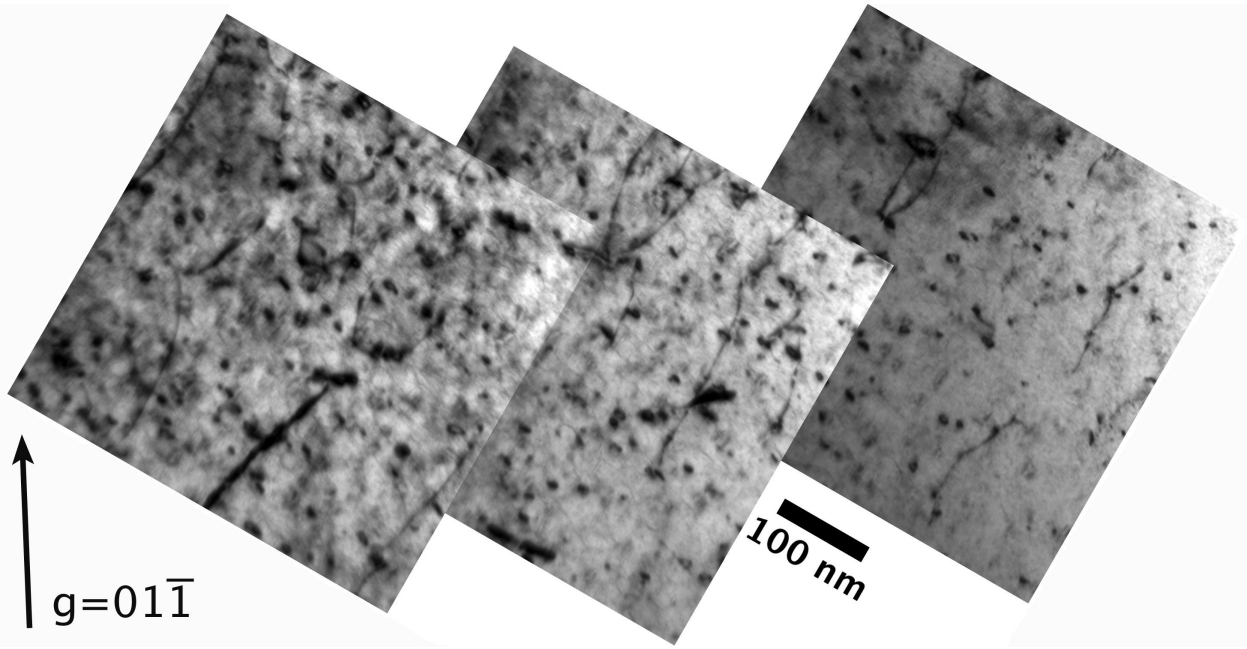

Figure 3.78: TEM images of Fe-14Cr single crystal irradiated at 450°C to 0.1 dpa. The image was taken under kinematic condition g = 01$\bar{1}$ with beam direction close to [111].

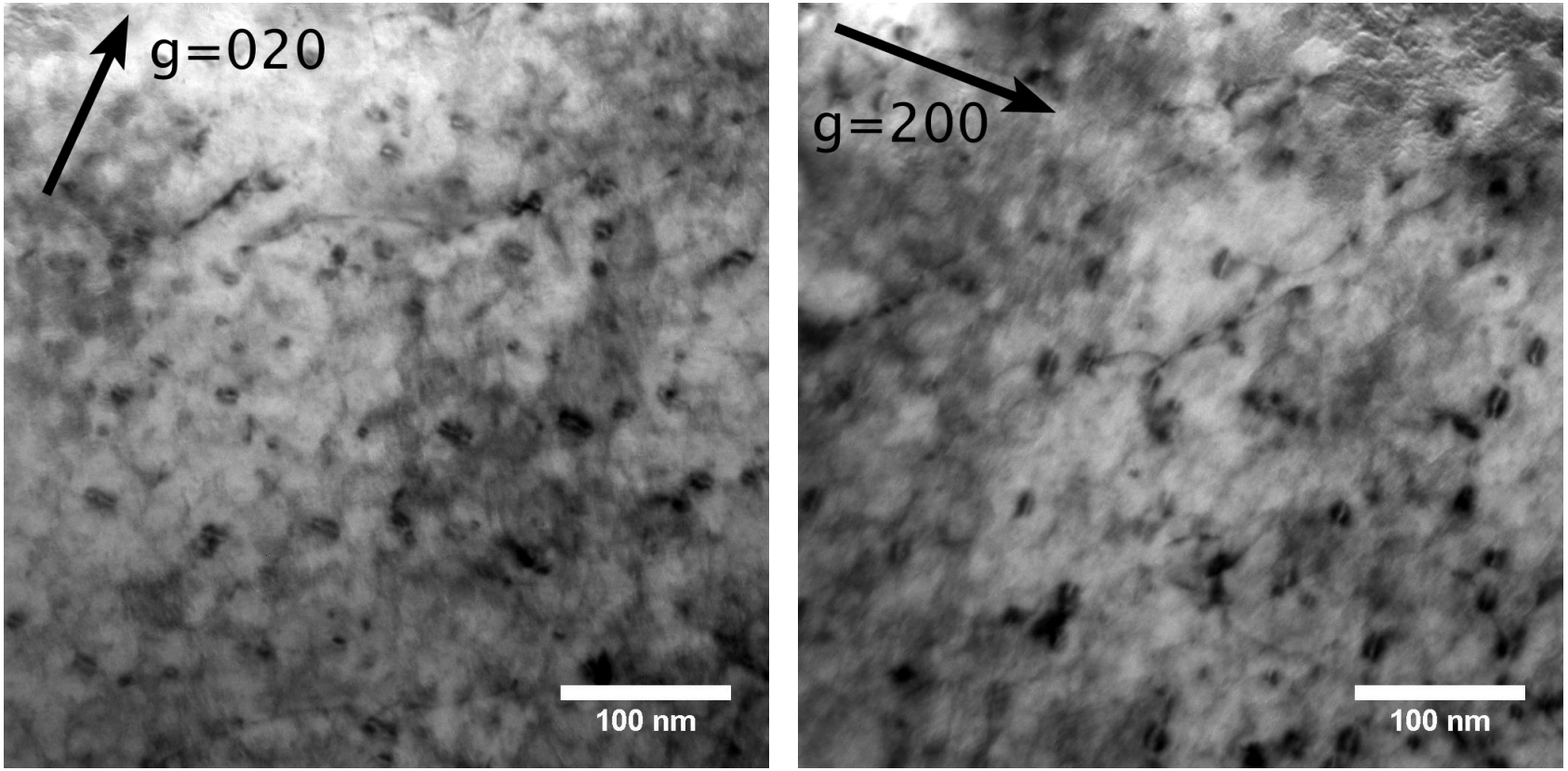

Figure 3.79: TEM images of Fe-14Cr single crystal irradiated at 450°C to 0.1 dpa. Images were taken under kinematic BF condition with g = 020 and g = 200 with beam direction close to [001].

3.1.26 Fe-13Cr single-crystals irradiated at 450C to 1 dpa

Figure 3.80 shows a low magnification TEM micrograph of a Fe-13Cr single crystal irradiated at 450°C to 1 dpa. The micrograph covers a wide range of foil thickness from perforation edge to roughly 600 nm. Normally, a foil thickness around 100 nm is used for microstructure characterization in TEM as a trade-off between image resolution (resolution decreases with increasing foil thickness) and image representivity to the complete microstructure (examined volume increased with increasing foil thickness). However, the dislocation density of the dislocation network in this specimen is low to some extent, and it is necessary to examine the thick area in order to reveal the network structure.

As shown in Figure 3.80, a dislocation network had formed with a density of 3.4×10^{13} $\frac{1}{m^2}$. Unlike the irradiated Fe-10Cr poly-crystalline specimen , the distribution of dislocation network is fairly uniform (section 3.1.22). Since no dislocation network was observed in the unirradiated Fe-Cr single crystal (section 3.1.3), the dislocation network appeared in the irradiated specimen should be irradiation-induced. The Burgers' vectors of the line dislocations have not been characterized completely due to the strong magnetic field that pose difficulty to fully perform the g·b analysis.

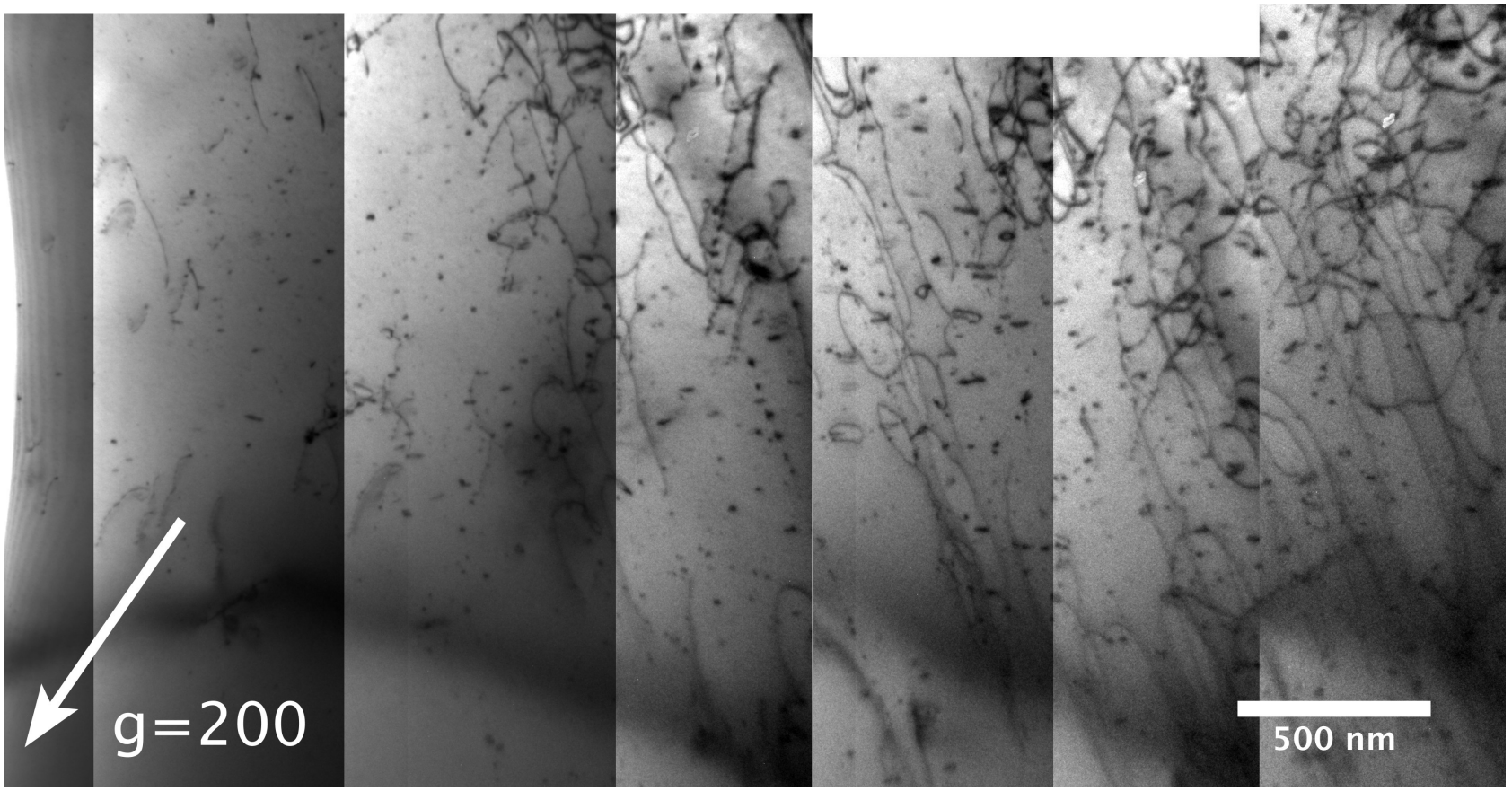

Figure 3.80: TEM images of Fe-13Cr single crystal irradiated at 450°C to 1 dpa. The BF images were taken under the kinematic condition with g = 200 and beam direction close to [012].

In addition to the line dislocations, dislocation loops were distributed uniformly within the dislocation network. Figure 3.81 and Figure 3.82 are micrographs of higher magnification that shows the thin area (perforation edge) and thick area (350 nm), respectively. Due to the large wedge angle, the original micrograph of Figure 3.81 has very uneven brightness between the thin side (bottom-left) and the thick side (top-right). In order to show the details of both sides, the brightness and contrast of each side was adjusted individually with image processing software.

In both micrographs, there are dislocation loops existing within the line dislocations. Similar to the case in Fe-10Cr polycrystal irradiated at 450° to 1 dpa, it is convenient to sort dislocation loops into two groups: small loops (<6 nm) and large loops (>6 nm). For the large loops, the observed areal density is indeed linear to the foil thickness. This is reasonable because the damage from neutron irradiation is uniform and the areal density of dislocation loops should be proportional to the TEM foil thickness, providing no significant foil surface effect during the TEM specimen preparation and TEM examination. The estimated density and average size of the large dislocation loops are is 4.2×10^{20} $\frac{1}{m^3}$ and 18 nm, respectively.

The small loops, however, does not follow the same linear correlation to the TEM foil thickness. The observed areal density is actually higher in the thinner area (1.8×10^{20} $\frac{1}{m^2}$, Figure 3.81) than in the thicker area (9.7×10^{18} $\frac{1}{m^2}$, Figure 3.82) . The reduced visibility of the small loops in the thicker area were possibly due to the reduced ability to reveal small loops with increasing foil thickness. Also, it is more difficult to align the electron beam and focus in the thick area. Therefore, the density of small loops obtained from the micrograph of the thin area (ex. Figure 3.82) is considered to be more representative. The total volume density of large (>6 nm) and small (<6 nm) dislocation loops would then add up to 5.9×10^{20} $\frac{1}{m^2}$.

In Figure 3.82, a chain of dislocation loops is visible at the bottom-left corner. Similar observation is shown in Figure 3.83 where the line dislocation at the center was decorated with dislocation loops, implying that the chain of dislocation loops in Figure 3.82 is also a decorated dislocation with the line dislocation itself being invisible due to the invisibility criterion $\mathbf{g}\cdot\mathbf{b}=\mathbf{0}$. Also, in both Figure 3.83 and Figure 3.82, only one of the dislocations was heavily decorated. The rest of them were either not decorated or were only slightly

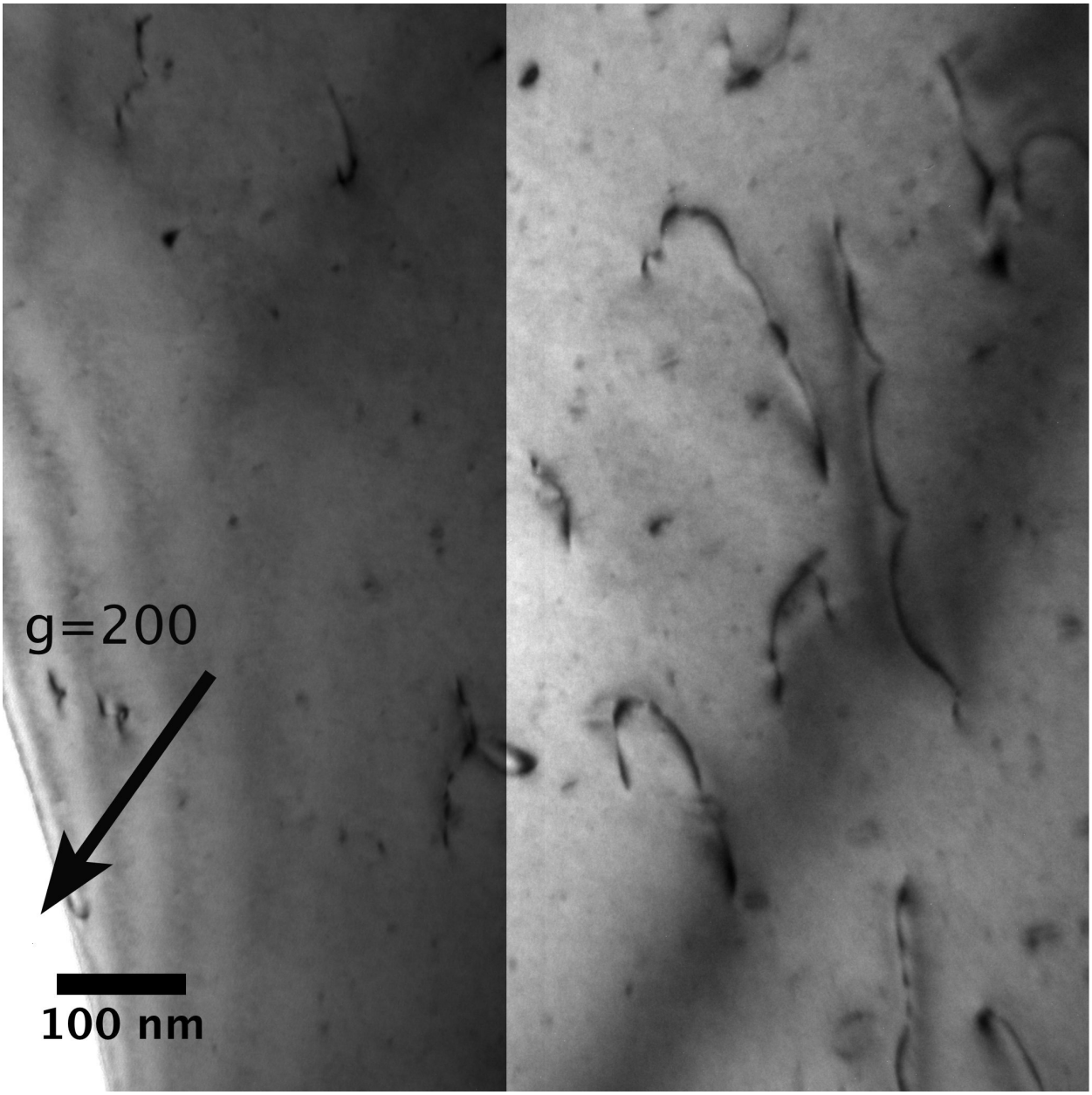

Figure 3.81: TEM images of Fe-13Cr single crystal irradiated at 450°C to 1 dpa. The images taken under the kinematic condition with g = 200 and beam direction close to [001].

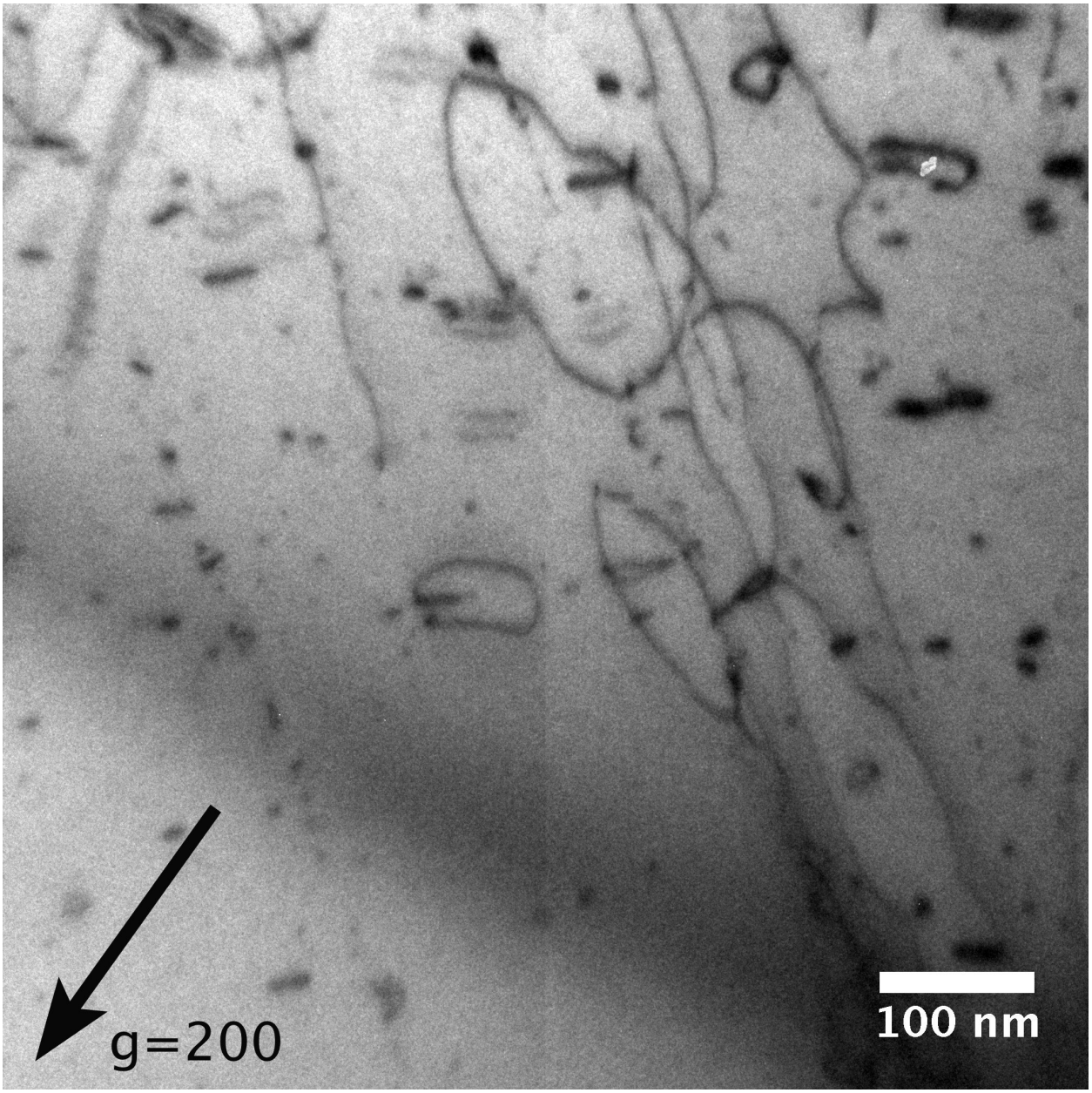

Figure 3.82: TEM images of Fe-13Cr single crystal irradiated at 450°C to 1 dpa. The images taken under the kinematic condition with g = 200 and beam direction close to [012]. The foil thickness at the center of the image is roughly 350 nm.

decorated. This uneven distribution of dislocation decoration was observed consistently in both Fe-13Cr single crystal and Fe-10Cr polycrystal specimens.

3.1.27 Summary of Fe-Cr single-crystals irradiated at 450C

The TEM micrographs comparing Fe-Cr single crystals irradiated at 450°C to 0.01, 0.1 and 1 dpa were shown in Figure 3.84 where all micrographs were taken from areas with a foil thickness of 100-200 nm. The quantitative data is summarized in Table 3.6 and Figure 3.85. The microstructure evolution is highly similar to the corresponding Fe-10Cr polycrystals (Figure 3.72). At the lowest dose, 0.01 dpa, radiation damage took the form of a high density of uniform dislocation loops in a size of ∼3 nm. The size increased with dose to ∼9 nm at 0.1 dpa while the density unchanged.

At 1 dpa, dislocation networks had formed. In addition, dislocation loops with a size of a few nanometer up to 171 nm were observed within the dislocation network, while small dislocation loops (roughly <6 nm) are barely visible in thick area (roughly >200 nm). In contrast to the 1 dpa-450°C Fe-10Cr polycrstalline specimen, the distribution of dislocation loops are fairly uniform and seems independent to the line dislocations (except for those decorating dislocations).

Table 3.6: Microstructure data for Fe-Cr single-crystals irradiated at 450°C

	0.01 dpa Fe-14Cr	0.1 dpa Fe-14Cr	1 dpa Fe-13Cr
Dislocation density (10^{13} $\frac{1}{m^2}$)	1.7	2.2	3.4
$\bar{d}_{loop}$ (nm)	3.0[b]	8.9	4.72 (18.0)[a]
$d_{loop,Max}$ (nm)	6.7[b]	18.68	171.4
N_{loop} (10^{21} $\frac{1}{m^3}$)	5.7[b]	5.5	0.18(0.42)[a]
$\bar{d}_{void}$ (nm)		Not observed	
$d_{void,Max}$ (nm)		Not observed	

[a]Small dislocation loops with size <6 nm (>6 nm) measured in areas with foil thickness of 0-200 nm (0-600 nm).
[b] The exceptionally large loops are excluded.

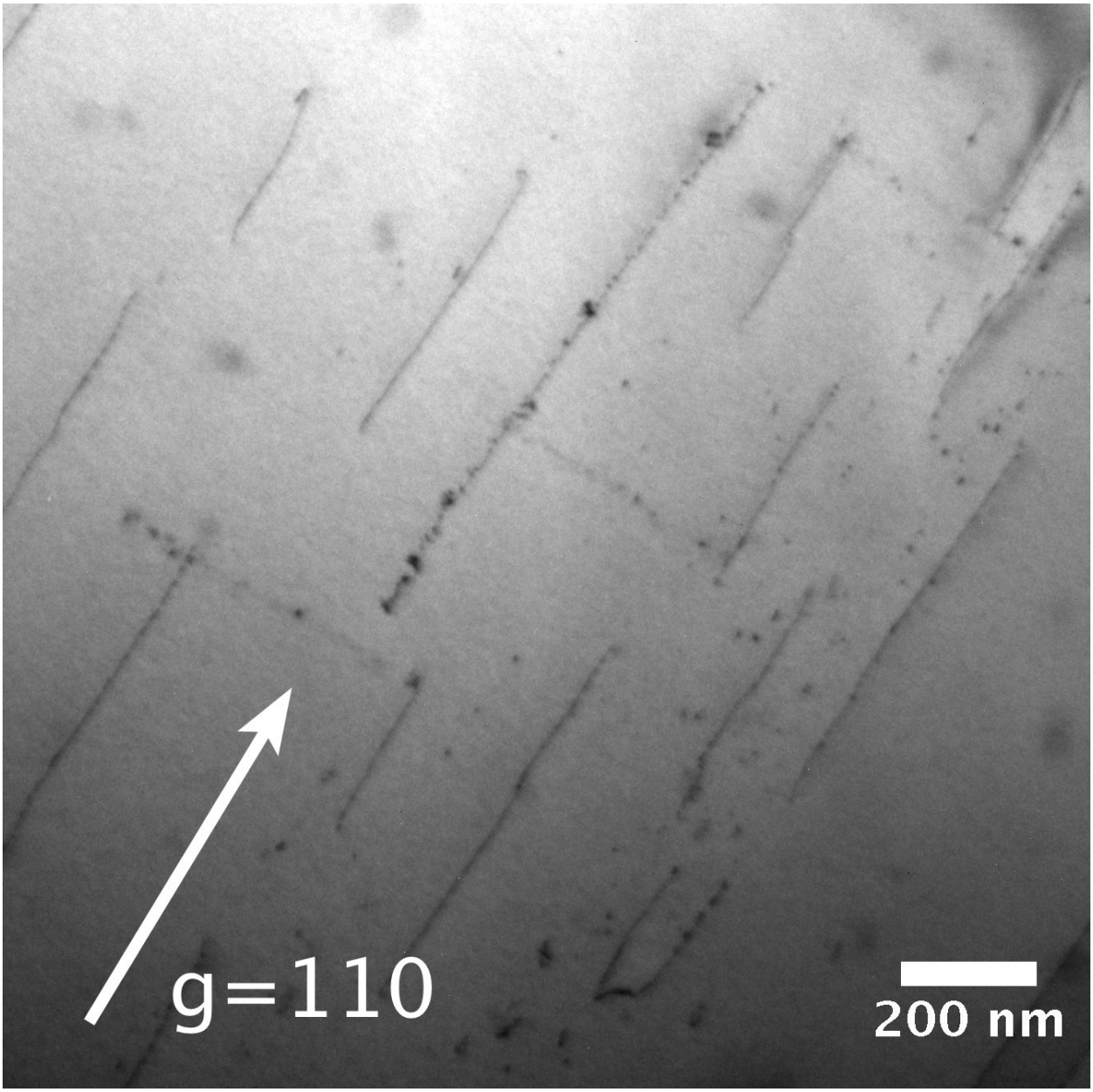

Figure 3.83: TEM images of Fe-13Cr single crystal irradiated at 450°C to 1 dpa. The BF image was taken under kinematic condition with g = 110 and beam direction close to [001]. The orientation of line dislocations is in parallel to (110) and $(1\bar{1}0)$ planes.

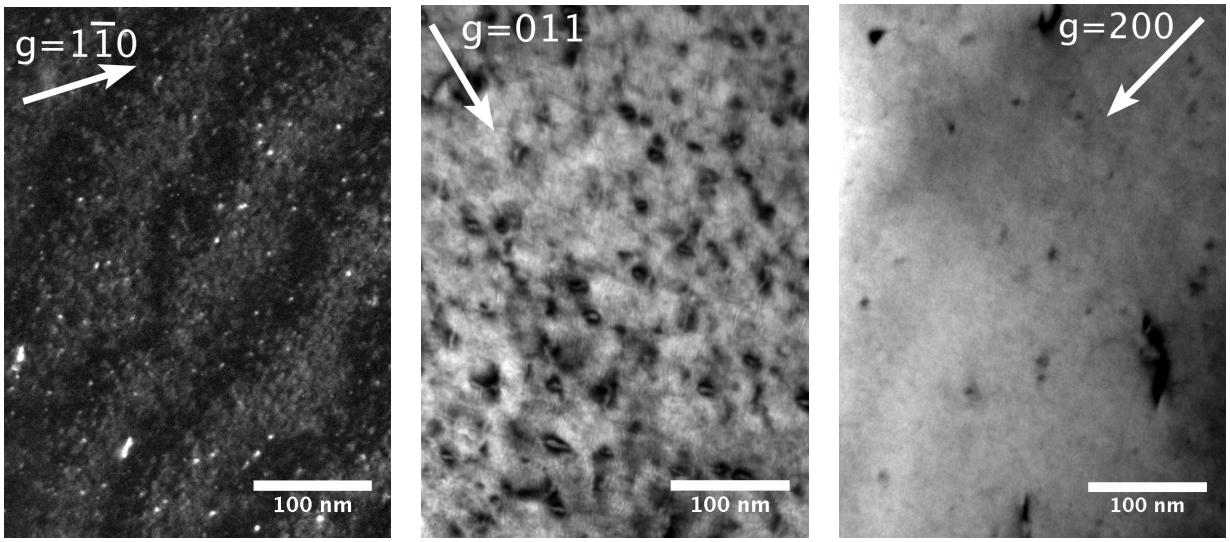

(a) Fe-14Cr 0.01 dpa (b) Fe-14Cr 0.1 dpa (c) Fe-13Cr 1 dpa

Figure 3.84: TEM micrograph of Fe-Cr single crystals polycrystals irradiated at 450°C. The foil thickness for the three images are all roughly 100-200 nm.

3.2 Atom Probe Tomography (APT)

The APT was performed in the CAES facility in Idaho Falls, ID. Multiple specimens for each condition were examined to ensure data reliability. The APT was used to study the α' precipitation and to examine the chemical composition. For α' precipitation, three techniques were utilized to analyze the APT data: isoconcentration surface analysis, proximity histogram analysis and frequency analysis. The basic description of each technique was discussed earlier in Chapter 2.4.2 to 2.4.4. The results of each analyzing technique are reported individually in the following Sections 3.2.1, 3.2.2 and 3.2.3.

3.2.1 Isoconcentration surface analysis

For the specimens of a dose equal and less than 0.1 dpa, few α' precipitates were found by using isosurfaces of 20%Cr or lower. Contrarily, α' precipitates were observed in all of the 1 dpa specimens. Figure 3.86 shows the 20%Cr isosurface. Each red sphere is a Cr-rich α' precipitate. Figure 3.87 shows their size distribution. The value of size ($r_{\alpha'}$), density $N_{\alpha'}$ and volume fraction $f_{\alpha'}$ are summarized in Table 3.7.

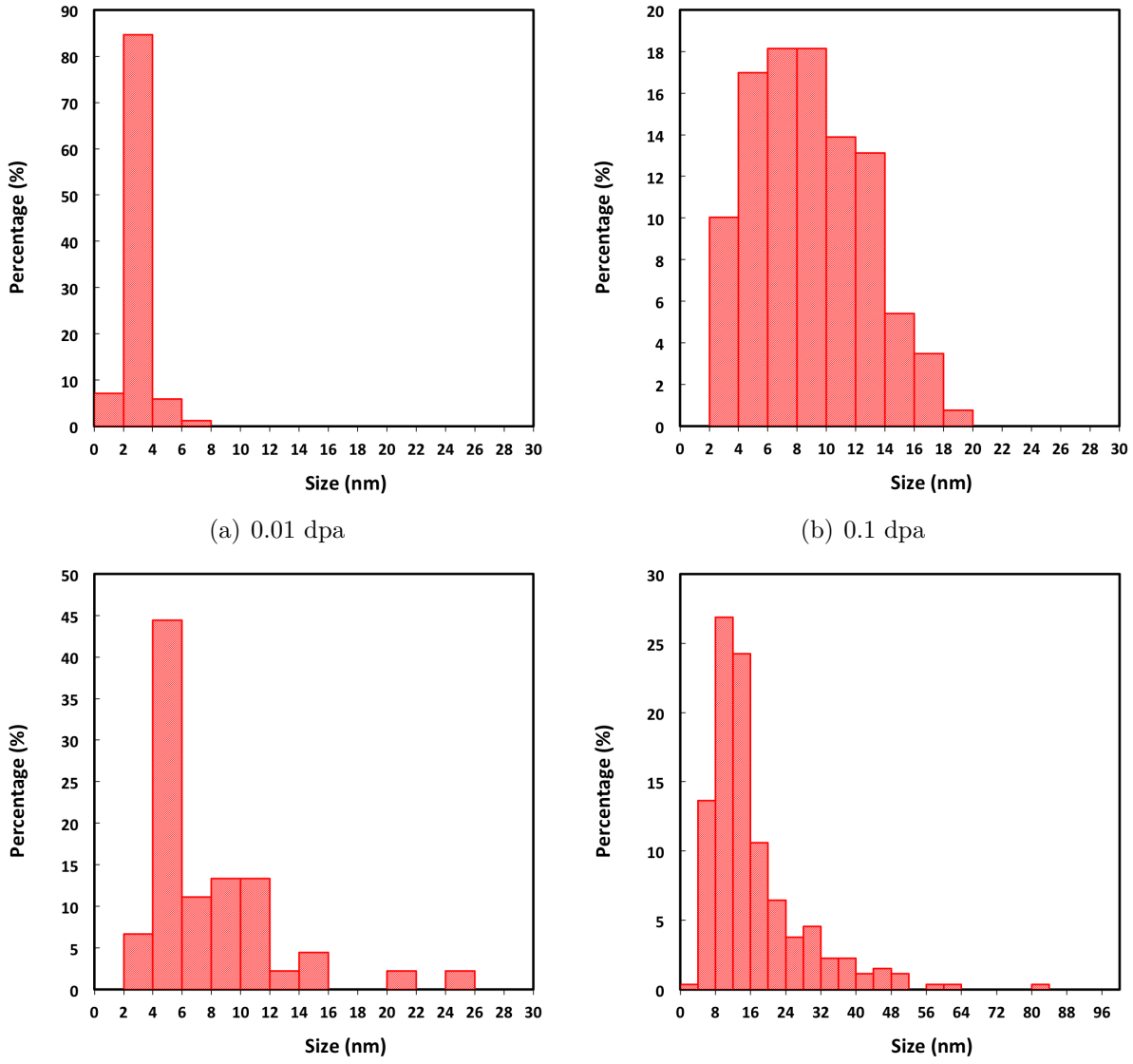

(a) 0.01 dpa

(b) 0.1 dpa

(c) 1 dpa Thinner region

(d) 1 dpa Thicker region

Figure 3.85: The size distribution of dislocation loops in Fe-13Cr single crystals irradiated at 450°C as a function of irradiation dose. (c) Measurements performed on Figure 3.81 where many small loops (<6 nm) are still visible at this thickness of 0-200nm. (d) Measurements performed over areas with thicker foil thickness of 200 nm-600 nm where small loops <6 nm are mostly invisible.

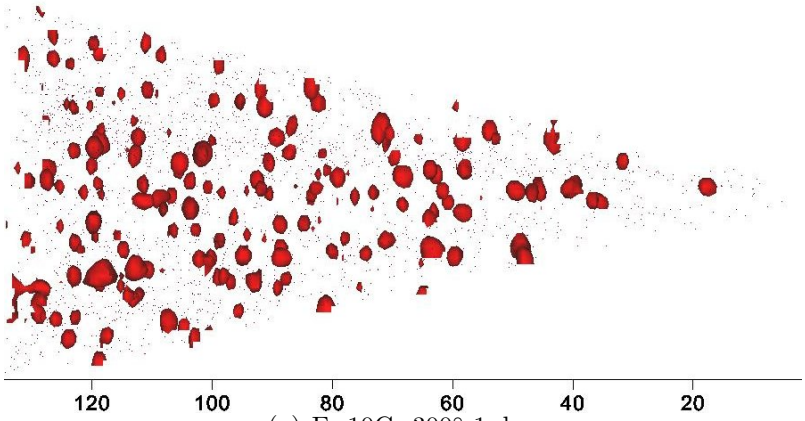

(a) Fe-10Cr 300° 1 dpa

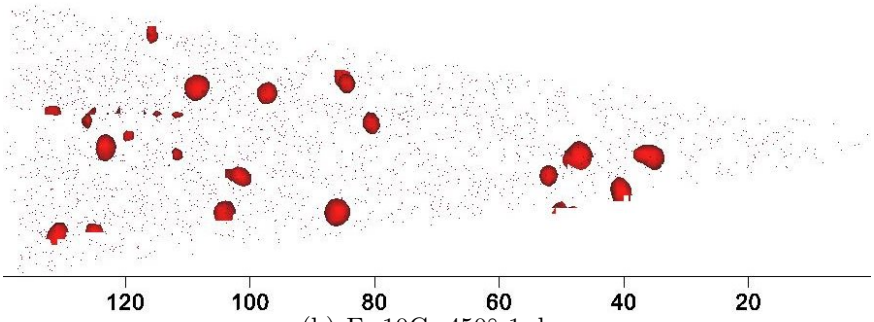

(b) Fe-10Cr 450° 1 dpa

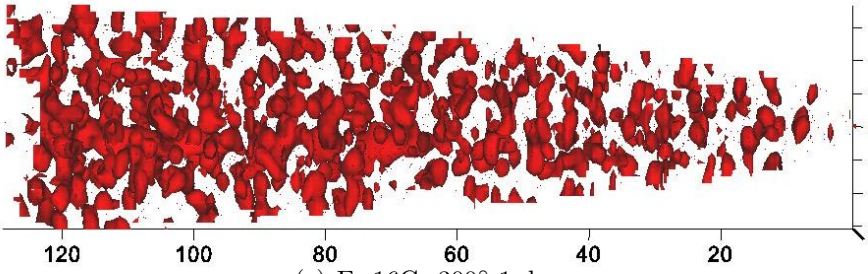

(c) Fe-16Cr 300° 1 dpa

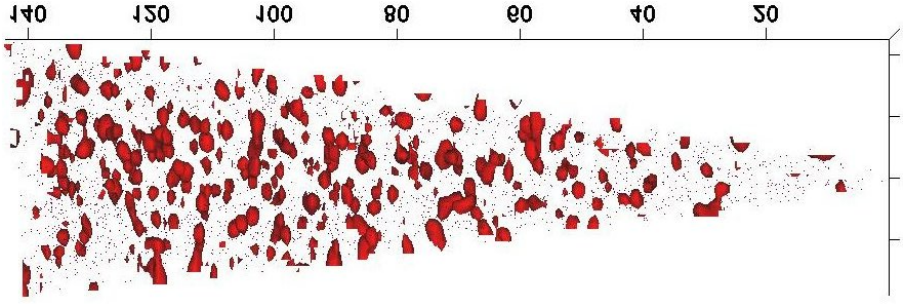

(d) Fe-13Cr 450° 1 dpa

Figure 3.86: The reconstructed APT images of the 20%Cr isosurfaces of Fe-Cr model alloys irradiated by neutrons to a dose of 1 dpa at 300°C and 450°C

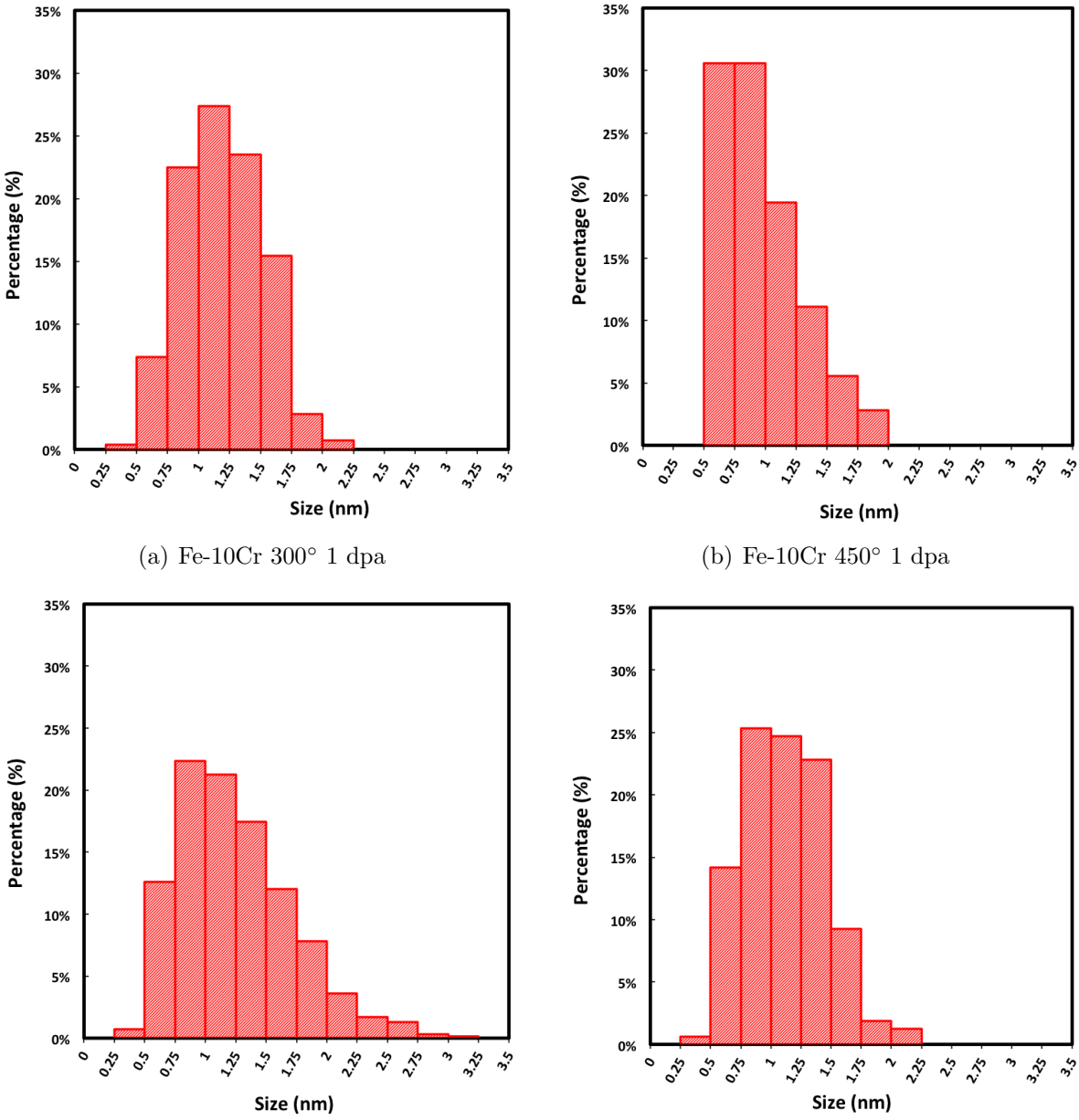

(a) Fe-10Cr 300° 1 dpa

(b) Fe-10Cr 450° 1 dpa

(c) Fe-16Cr 300° 1 dpa

(d) Fe-13Cr 450° 1 dpa

Figure 3.87: The size distribution of α' precipitates in 1 dpa Fe-10Cr polycrystals and Fe-Cr single crystals. The precipitates were defined by the 20%Cr iso-surfaces.

Table 3.7: The density, mean size and volume fraction of α' precipitates in Fe-Cr model alloys irradiated to 1 dpa

Specimen	$N_{\alpha'}$ ($\times 10^{23}$ $\frac{1}{m^3}$)	$r_{\alpha'}$ (nm)	$f_{\alpha'}$ (%)
Fe-10Cr-300°C-1dpa	7.66	1.18	0.66
Fe-10Cr-450°C-1dpa	1.08	1.00	0.072
Fe-16Cr-300°C-1dpa	27.1	1.25	3.15
Fe-13Cr-450°C-1dpa	12.6	1.08	0.85

The morphologies of α' precipitates in 1 dpa specimens varied with x_{Cr} and T_{irr}. The size was larger in 300°C than in 450°C irradiated samples. On the other hand, size increases with x_{Cr}, but less significantly. Therefore, it is suggested that $r_{\alpha'}$ was controlled more by the T_{irr} than by x_{Cr}.

Both the T_{irr} and x_{Cr} substantially affected the $N_{\alpha'}$. Specimens with higher x_{Cr} and T_{irr} exhibited higher $N_{\alpha'}$. Since $r_{\alpha'}$ were close to 1 nm for all conditions, the volume $f_{\alpha'}$ is essentially determined by the $N_{\alpha'}$. The $f_{\alpha'}$ of the four 1 dpa specimens is in accordance with the phase diagram [57][16].

3.2.2 Proximity histogram analysis

The proxigram analysis was performed on 1 dpa specimens. The α' precipitates were divided into several size groups, and a proxigram for each group was generated. Figure 3.88 is the proxigram of the selected size groups in 1 dpa Fe-10Cr specimen irradiated at 300 °C. The Cr concentration profiles of different size groups were coincident. The Cr concentration increased continuously toward the core of precipitates without forming a plateau.

The Cr concentrations at the core of precipitates increased with precipitate sizes as shown in Figure 3.88. In more detail, Figure 4 shows the core Cr concentration as a function

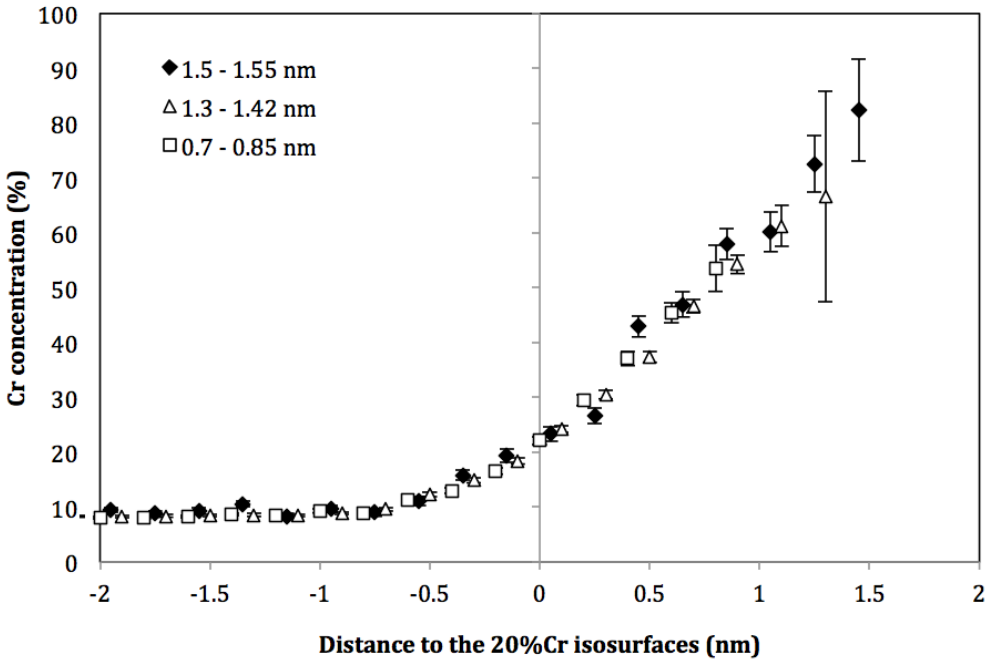

Figure 3.88: The proxigrams to the 20%Cr isosurfaces of α' precipitates in Fe-10Cr specimens irradiated at 300°C to 1 dpa. Three size groups are plotted: $r_{\alpha'}$ = 1.5 1.55 nm, 1.3 1.42 nm and 0.7 0.85 nm.

of precipitate size in 1 dpa Fe-10Cr specimens irradiated at 300 and 450°C. No significant difference was observed between the two temperatures. The core Cr concentration (55%) of precipitates with a size around 1.1 nm was coherent with earlier APT investigations on 0.6 dpa Fe-9Cr [97], implying that the effect of irradiation doses from 0.6 dpa to 1 dpa on the core Cr concentration was insignificant. The implication of the core Cr concentration dependence on the precipitate size is discussed in the discussion session.

3.2.3 Frequency distribution analysis

For specimens irradiated to a dose lower than 1 dpa, it is difficult to use isosurface to reveal α' precipitates. Instead, frequency distribution analysis was found useful to study the early stage of Cr segregations. The frequency distribution and the corresponding binomial distribution of Fe-Cr specimens are shown in Figure 3.90, Figure 3.91 and Figure 3.92. The μ-index derived from the frequency distribution is shown in Figure 3.93. As Figure 3.90 shows, the frequency distributions of the un-irradiated specimens are very close to the theoretical

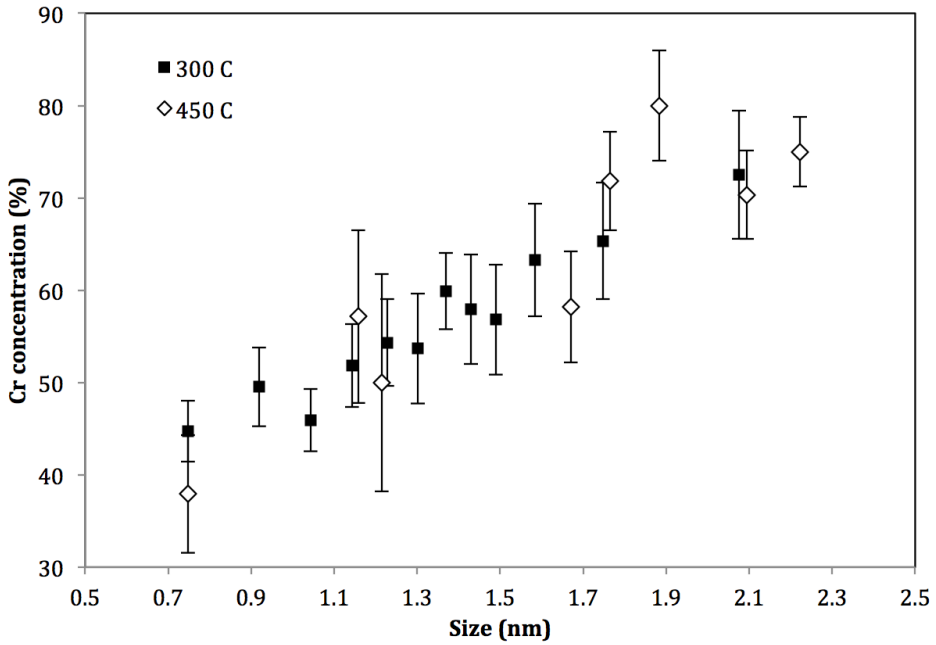

Figure 3.89: The core Cr concentration at the center of α' precipitates as a function of precipitate size in radius in 1 dpa Fe-10Cr specimens irradiated at 300 and 450°C

binomial distributions, indicating negligible α' phase in the as-received specimens.

Up to 0.1 dpa, the frequency distributions of irradiated Fe-10Cr poly-crystals are similar to as-received specimen. No evident segregations of Cr atoms were detected. At 1 dpa, however, considerable deviation, with frequencies moved toward two sides, was observed as shown in Figure 3.91. In addition, the deviation between the observed distribution and the binomial distribution was higher in 300°C than in 450°C irradiated samples.

For irradiated Fe-Cr single crystals (higher x_{Cr}), Cr segregation increased with irradiation dose. Some Cr segregations at lower doses of 0.01 and 0.1 dpa were detected, which was different from the polycrystalline Fe-10Cr specimens. This result indicated that the Cr segregations began earlier in Fe-Cr alloys with higher x_{Cr}. Because of the variations in x_{Cr}, it was more difficult to evaluate the Tirr effects on the Cr segregations in single-crystalline specimens. For instance, the 0.1 dpa Fe-10Cr-SC specimen irradiated at 300°C exhibited a particularly low Cr content (10.02%), which resulted in lower degree of Cr segregation.

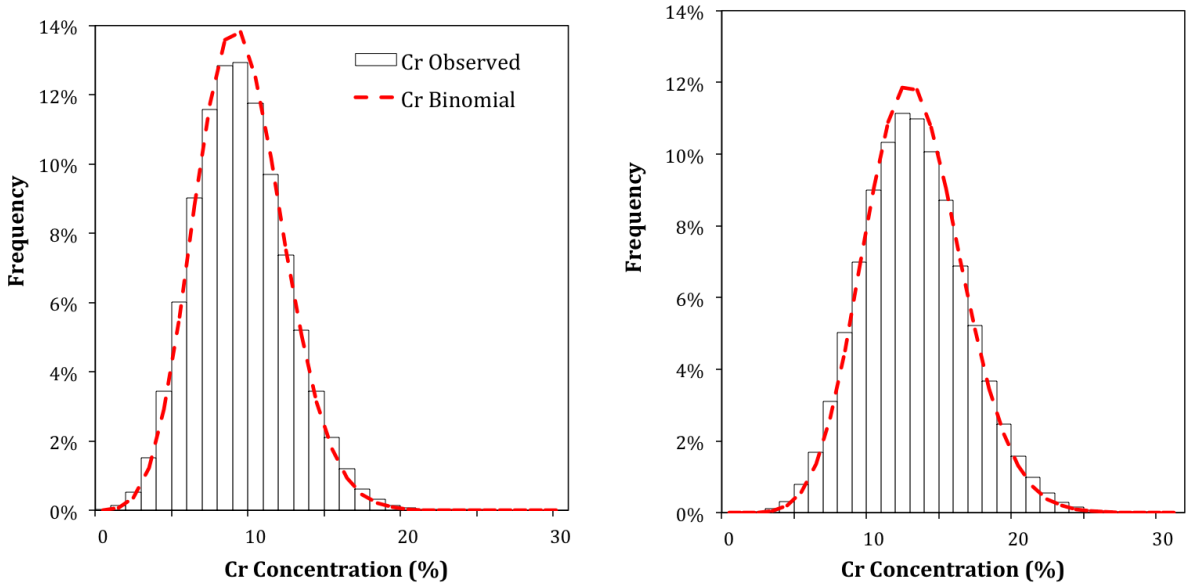

(a) Unirradiated Fe-10Cr Poly crystal

(b) UnirradiatedFe-14Cr Single Crystal

Figure 3.90: Frequency distribution of un-irradiated (a) poly-crystalline Fe-10Cr specimen and (a) Fe-14Cr single crystalline specimens.

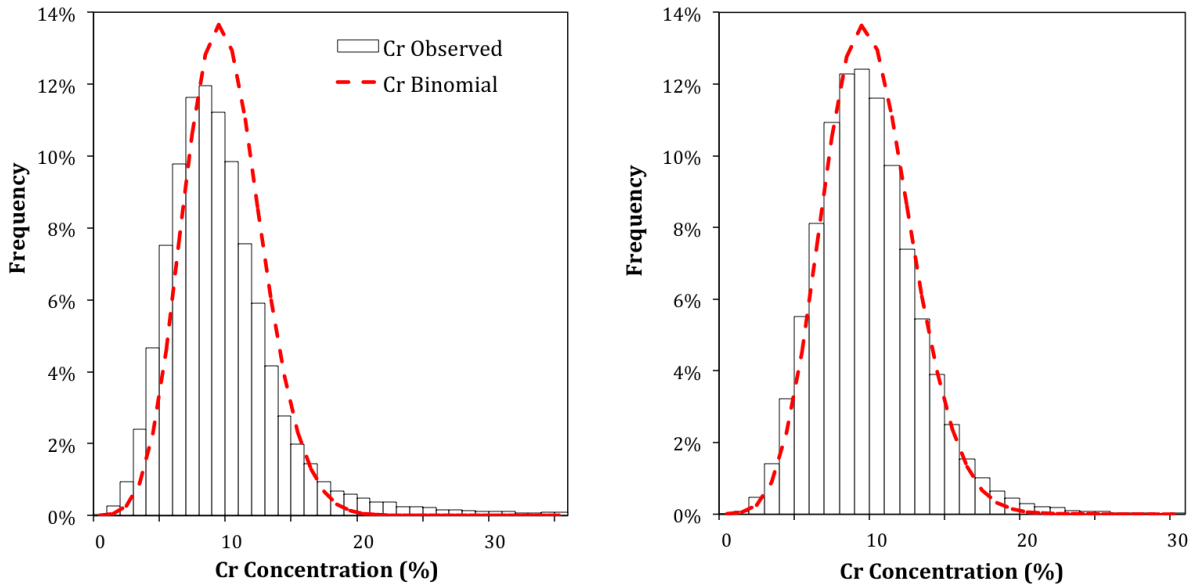

(a) Fe-10Cr 300°C 1 dpa

(b) Fe-10Cr 450°C 1 dpa

Figure 3.91: Frequency distribution of 1dpa Fe-10Cr poly-crystalline specimens irradiated at 300°C and 450°C.

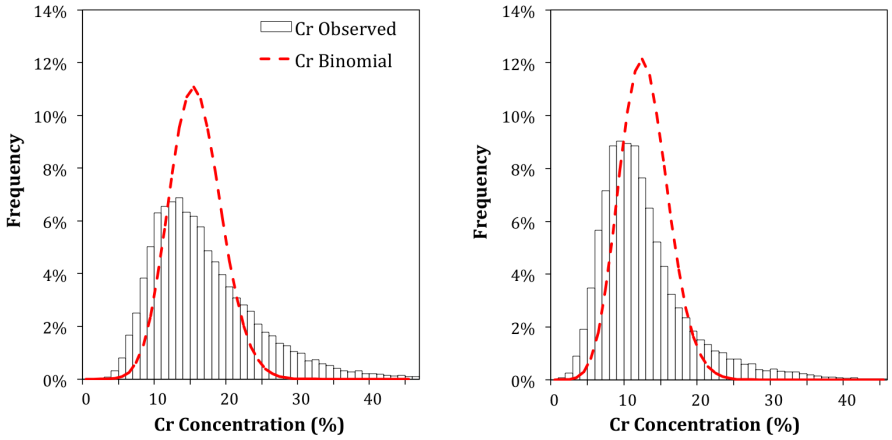

(a) Fe-16Cr 300°C 1 dpa

(b) Fe-13Cr 450°C 1 dpa

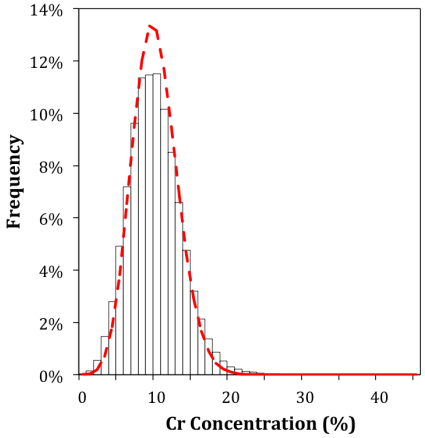

(c) Fe-10Cr 300°C 0.1 dpa

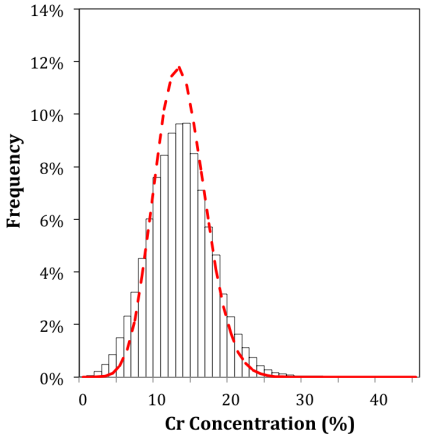

(d) Fe-14Cr 450°C 0.1 dpa

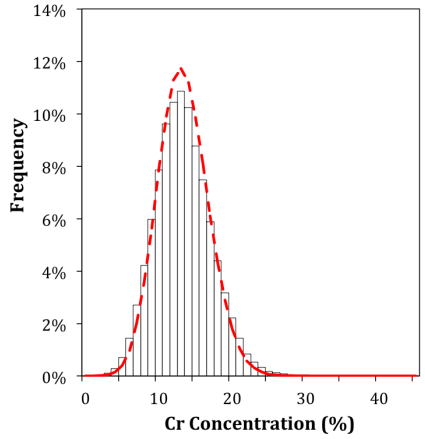

(e) Fe-14Cr 300°C 0.01 dpa

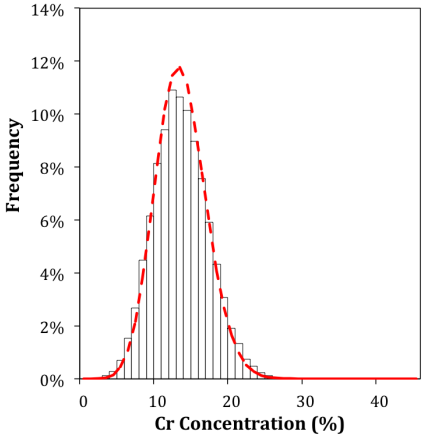

(f) Fe-14Cr 450°C 0.01 dpa

Figure 3.92: Frequency distribution of Fe-Cr single-crystalline specimens irradiated at 300°C and 450°C to doses of 0.01 dpa, 0.1 dpa and 1 dpa.

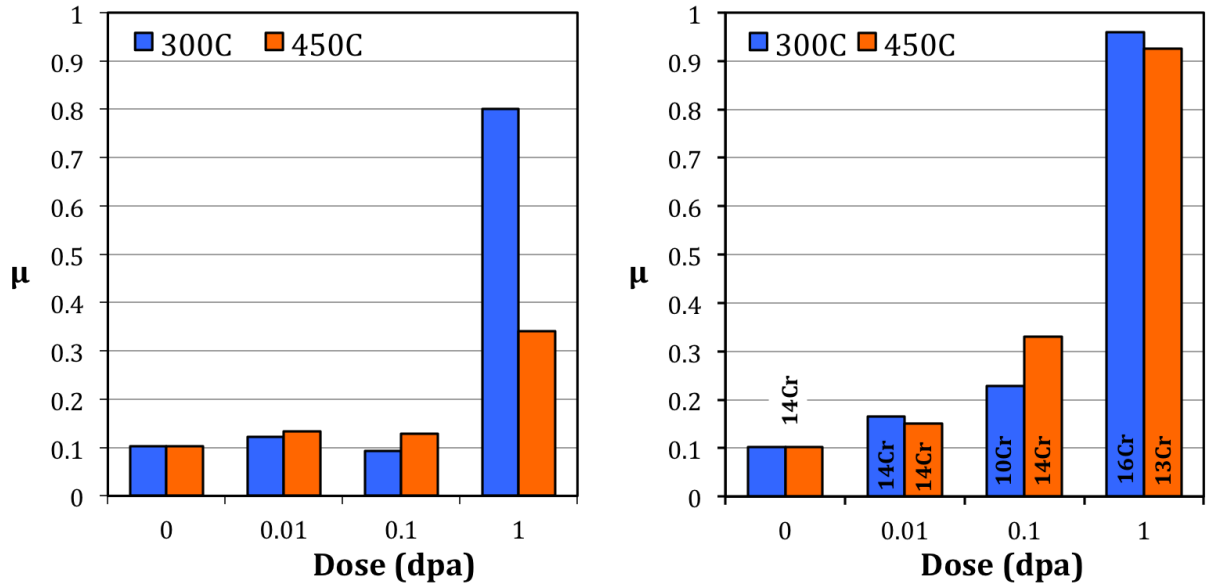

(a) Fe-10Cr Poly-Crystals

(b) Fe-Cr Single Crystals

Figure 3.93: The μ-index of un-irradiated and irradiated (a) poly-crystalline Fe-10Cr and (b) single-crystalline specimens, based on the frequency distribution analysis. The Cr contents of each single crystal Fe-Cr specimens are marked by their data bars.

3.3 Hardness Measurements

Two types of hardness testing (micro-hardness and nano-hardness) were performed. The micro-hardness results are presented in Chapter 3.3.1, and the nano-hardness are persented in Chapter 3.3.2. The data collected from the two methods were compared and discussed in Chapter 3.3.2.

3.3.1 Micro-hardness measurements

The micro-hardness was performed in the LAMBDA laboratory at ORNL using a Vicker's indenter with a 100 g load and 15 seconds dwell time. At least 7 indentations were performed for each specimen. Only a partial (6) of the whole conditions (21) were tested. After the hardness testing, the specimens were jet-polished for further TEM examinations.

Figure 3.94 and Table 3.8 shows the micro-hardness in Fe poly-crystals and Fe-Cr single crystals up to 0.1 dpa. To be noted, there is only one data point for the no-irradiation condition for each specimen category. They were duplicated in the plot and in the table

merely for the convenience to grouping them into 300°C and 450°C.

For Fe irradiated at 300°C, the hardness increased slightly with dose. On the other hand, the hardness decreased with dose in Fe irradiated at 450°C. Since there was no observable change in grain size (grain coarsening) after 450°C irradiation in Fe, the decrease in hardness was attributed to the irradiation-annealing that reduced the dislocation density. See Discussion for detailed analysis.

For Fe-Cr single crystals irradiated at 450°C, the hardness increased with dose. For 300°C, the trend is not straightforward. The hardness increased at 0.01 dpa but dropped at 0.1 dpa. More details are discussed in the next chapter combing the nano-hardness data.

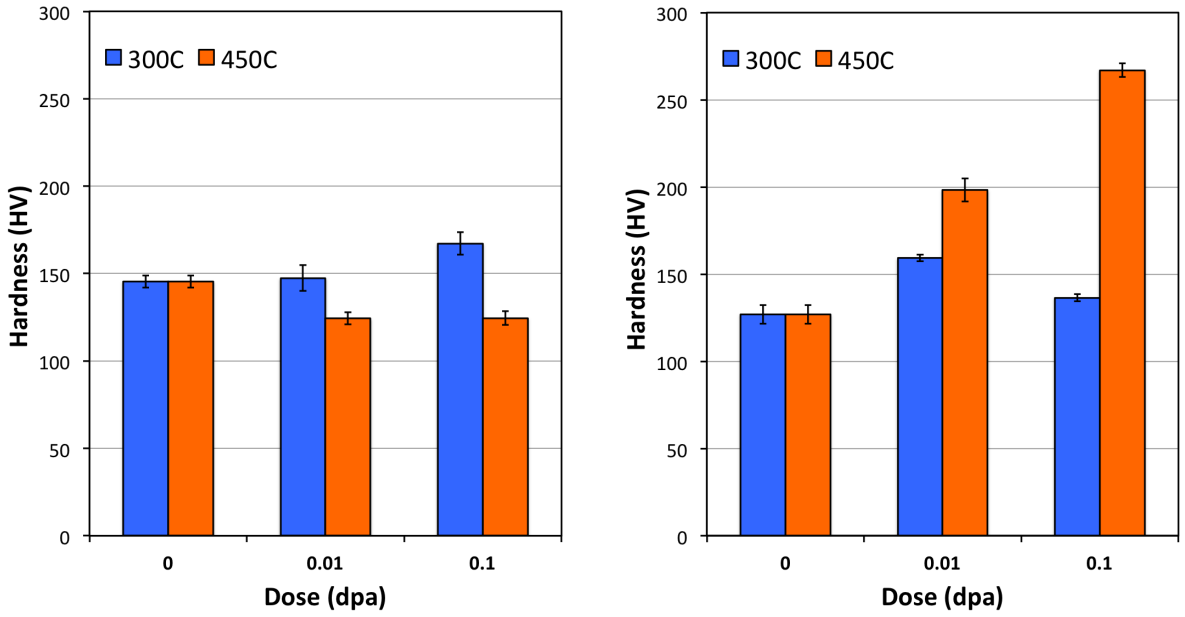

(a) Fe Poly-Crystals (b) Fe-Cr Single Crystals

Figure 3.94: The microhardness measurements

3.3.2 Nanoindentation testing

The nanohardness were performed in CAES with a Hysitron nanoindentor. A 5 μm fixed displacement are used for all of the tests with a 5-2-5 loading pattern (loading-holding-unloading, in seconds). At least 10 indentations were performed for each specimen. All of the specimens were tested. The same specimens tested with nanoindentation were examined

Table 3.8: The microhardness measurements

Specimen - T_{irr} (°C)	Hardness (HV) no irradiation	0.01 dpa	0.1 dpa
Fe - 300	145.43±3.51	147.37±7.40	167.2±6.38
Fe - 450	145.43±3.51	124.29±3.47	124.5±3.86
Fe-Cr Single Crystal - 300	127.00±5.41	159.19±1.89	136.44±2.09
Fe-Cr Single Crystals - 450	127.00±5.41	198.24±6.69	266.97±3.86

with APT except for the Fe specimens.

The results are shown in Figure 3.95 and in Table 3.9. The Figures 3.95(a)(c)(d) are plotted with the absolute hardness values, and Figures 3.95(b)(d)(f) shows the relative hardness increment compared to the initial values. Both the absolute and the relative values were shown in Table 3.9.

Comparing the micro-hardness and nano-hardness, it shows that the two measurements agree well to each other. For instance, the hardness decreased in Fe irradiated at 450°C up to 0.1 dpa in both measurements. Also, the strange hardness drop in 0.1 dpa Fe-Cr single crystal irradiated at 300°C were observed repeatedly. There is still some inconsistency between the micro-hardness and the nano-hardness data, but the discrepancy is fairly small. For example, micro-hardness measurement indicates hardening in Fe irradiated at 300°C up to 0.1 dpa, however nano-hardness measurement indicates softening. Nevertheless, the magnitude of change for both cases (hardening or softening) is low when compared to other conditions (ex. 1 dpa Fe-14Cr single crystal irradiated at 300°C).

Table 3.9: The nanohardness measurements

Specimen - T_{irr} (°C)	Hardness (GPa) & Relative Increment no irradiation	0.01 dpa	0.1 dpa	1 dpa
Fe - 300	2.69±0.29 -	2.49±0.23 -7.43%	2.57±0.19 -4.46%	2.88±0.06 +7.06%
Fe - 450	2.69±0.29 -	2.15±0.18 -20.07%	1.92±0.19 -28.62 %	3.12±0.21 +15.99%
Fe-10Cr - 300	1.78±0.08 -	1.88±0.08 +5.62%	1.77±0.04 -0.56%	3.48±0.06 +95.51%
Fe-10Cr - 450	1.78±0.08 -	2.23±0.08 +25.28%	3.13±0.15 +75.84%	3.05±0.24 +71.34%
Fe-Cr Single Crystal - 300	1.86±0.02 -	2.53±0.07 +93.13%	2.20±0.10 +67.94%	4.78±0.21 +264.89%
Fe-Cr Single Crystals - 450	1.86±0.02 -	2.70±0.17 +106.11%	3.89±0.17 +196.95%	4.03±0.15 +207.25%

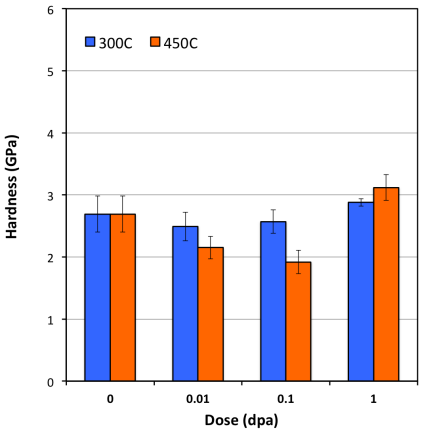

(a) Fe Poly-Crystals

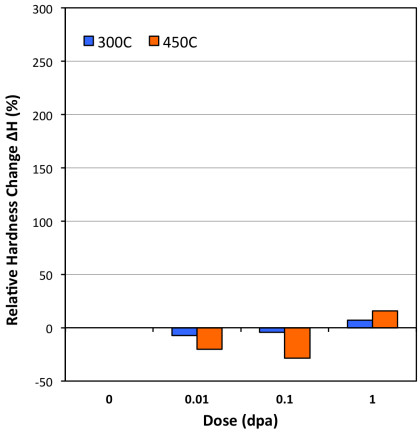

(b) Fe Poly-Crystals

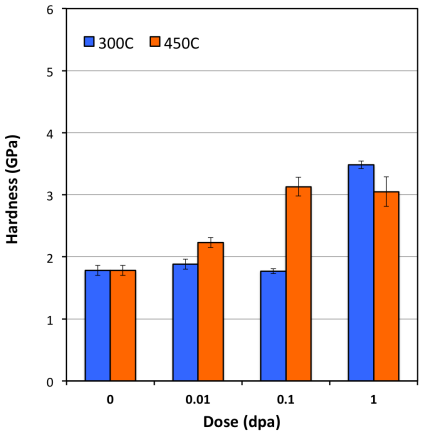

(c) Fe10Cr Poly-Crystals

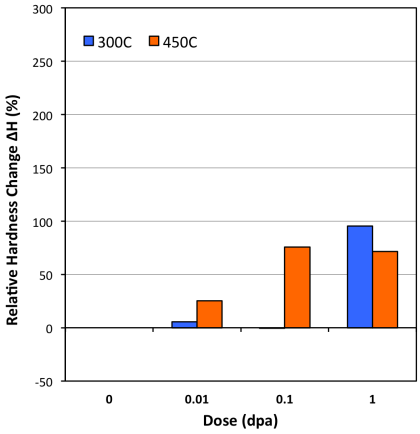

(d) Fe10Cr Poly-Crystals

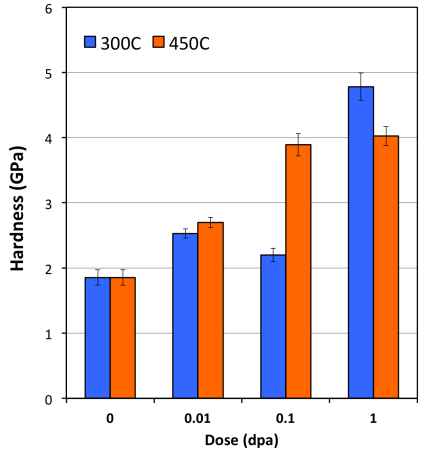

(e) Fe-Cr Single Crystals

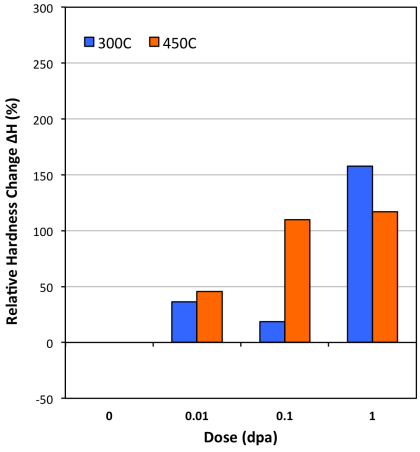

(f) Fe-Cr Single Crystals

Figure 3.95: The nanohardness measurements

The nano-hardness exhibits larger error (σ) than dose micro-hardness, which is reasonable considering nano-hardness uses a smaller indentation tip (smaller tip area) and shallower indentation depth. Smaller sampling volume of nanoindentation results in higher data fluctuation because it is more sensitive to the surface roughness, contamination and local inhomogeneity. This study confirms the traditional opinion that micro-hardness measurement is in general more reliable than nano-hardness measurement.

In Fe-Cr alloys, the hardness increased with dose at both 300°C and 450°C except for 0.1 dpa at 300°C, as mentioned in Chapter 3.3.1. It is interesting to observe that this suspicious hardness drop not only occured in Fe-Cr single crystal (10Cr for this specific sample) but also occured in Fe-10Cr poly-crystal. Several explanations have been considered:

- Lower Cr content than the rest of the Fe-Cr single crystals
- They were mistakingly switched with 0.01 dpa specimens
- They were mistakingly switched with 450°C specimens
- Their actual irradiation dose was deviating from the target dose
- Their actual irradiation temperature was deviating from the target temperature

Since the hardening is positively correlated to the Cr contents (which is apparently shown in Figure 3.95), the suppressed hardening in 300°C-0.1dpa Fe-Cr single crystal seems to correspond to its particularly-low Cr content (10Cr) compared to the rest of the Fe-Cr single crystals (13Cr-16Cr, see Table 2.2)). However, this could not explain why the similar suppression in hardening was repeated in the corresponding 300°C-0.1 dpa Fe-10Cr poly-crystal, as shown in Figure 3.95(c)(d). All of the Fe-10Cr poly-crystals have identical Cr content, therefore the simultaneous hardness drop in both 300°-0.1 dpa specimens could not be attributed to the Cr variation.

Human mistake that switched the 0.01 dpa specimens with 0.1 dpa specimens was considered. However, the radioactive dose rate (μR/hr at 30 cm) measurements show that the activity in 0.1 dpa Fe10Cr poly-crystal specimen was roughly 19 times higher than that in the 0.01 dpa Fe10Cr poly-crystal specimen. This indicates that 0.1 dpa specimen received

much more neutron dose than the 0.01 dpa specimen, and therefore excludes the possible switch between the two doses.

Another potential mistake is the switch between the *0.1 dpa-300°C* specimens and the *0.1 dpa-450°C* specimens. This is excluded, however, by examining the microstructure. The *0.1 dpa-450°C* Fe-Cr single crystal featured a high density of uniform ⟨100⟩ dislocation loops, which is a reasonable microstructure evolved from the *0.01 dpa-450°C* Fe-Cr single crystal specimen. Same situation occures in the Fe-10Cr poly-crystals. Switching between the *0.1 dpa-300°C* specimens and *0.1 dpa-450°C* specimens causes inconsistency in the microstructure evolution at both temperatures, and therefore rules out this possibility.

The last two candidates on the list arise from the uncertainty of the irradiation conditions. As will be discussed in more details in Chapter 4.1, the actual dose and the irradiation temperature of the this specific irradiation condition *0.1 dpa - 300°C* might deviate significantly from the target condition. It is challenging to justify because no reactor data, direct measurements or calculations, is available. The activity measurements, as mentioned earlier, implies that their actual irradiation dose should not be off too much. In addition, the dose control in ATR was considered more accurate over the irradiation temperature [98]. As a result, the deviation in irradiation temperature is the most likely explanation that cause the suspicious hardness drop for *0.1 dpa - 300°C* Fe-10Cr poly-crystal and Fe-Cr single crystal. However, evidence (ex. reactor measurements or calculations) is required to verify.

The above compared the micro-hardness and the nano-hardness. Besides, the questionable hardness data were discussed. The following is a list of observations of the hardness dependence on experimental parameters such as Cr concentration x_{Cr}, irradiation temperature T_{irr}. The mechanisms behind these observation will be discussed in Chapter 4.

- Initial hardness (no irradiation): Fe > Fe10Cr ∼ Fe14Cr. The solution hardening from Cr should result in an increase in yield strength, as shown by Matijasevic and Almazouzi [23]. The opposite trend observed in this study indicates that other hardening mechanisms also contributed to the initial hardness. These mechanisms are considered to be their dislocation density and the grain size.

- The hardening with increasing dose: Fe-Cr single-crystals > Fe-10Cr > Fe. This is

consistent with the current understanding about the 'snaky' Cr-content dependence of the irradiation-induced strengthening in Fe and Fe-Cr alloy: a minimum strengthening for pure Fe (0 %Cr) and a local minimum for 9 wt%Cr [22].

- For dose $\leq$ 0.1 dpa, the hardening in Fe-Cr alloys: 450°C > 300°C. Irradiation at lower irradiation temperature usually causes more hardening than that at higher temperature because it produces dislocation loops of much smaller size and higher density, leading to higher strengthening. The observation in this study is opposite where more hardening was observed actually at higher irradiation temperature of 450°C and not at 300°C. The microstructure observed with TEM described previously in this Chapter is in agreement with the hardness measurements. A higher density of dislocation loops was observed in 450°C specimens than in 300°C specimens. The mechanism that caused the microstructure will be discussed in more details in Chapter 4.

- For dose = 1 dpa, The hardening in Fe-Cr alloys: 300°C > 450°C. The TEM shows that the *1 dpa - 300°C* Fe-Cr exhibited a high density of dislocation loops. On the other hand, the density of dislocation loops in *1 dpa 450°C* Fe-Cr is much lower. In addition, the APT indicates that *1 dpa - 300°C* Fe-Cr contain more α' precipitates than *1 dpa - 450°C*. Therefore, higher density of dislocation loops and α' precipitates in *1 dpa - 300°C* specimens resulted in their higher hardness .

- Fe experienced softening when T_{irr} = 450°C to doses of 0.01 dpa and 0.1 dpa. At 1 dpa, the hardness rebounded and became greater than the initial value. The turning in hardness between 0.1 dpa and 1 dpa implies the existence of competitive mechanisms. For instance, (line) dislocation loss due to irradiation-enhanced annealing and a accumulation of irradiation-induced dislocation loops.

- When T_{irr} = 300°C, Fe experienced softening or hardening to begin with depending on weather micro-hardness or nano-hardness data is used. Considering that micro-hardness measurement is more accurate and more reliable than the nano-hardness measurement, the hardening is more likely than softening. Nevertheless, the overall hardness change was very tiny in Fe irradiated at 300°C even to the highest dose of 1

dpa.

CHAPTER 4

DISCUSSION

4.1 Uncertainties in Irradiation Conditions of the Specimens

Testing materials in a nuclear reactor is the most desirable since it simulate the irradiation environment in a way closest to the real conditions. However, these experiments are enormously expensive. In addition, the control of irradiation condition (i.e. dose, dose rate, temperature) is worse than other irradiation techniques such as ion irradiation [99]. This sections will discuss the uncertainties in the irradiation temperature and dose in this study.

The irradiation temperature (300°C and 450°C) and irradiation dose (0.01 dpa, 0.1 dpa and 1 dpa) were target values obtained through neutronics and thermal-hydraulics calculation prior to the experiments based on the 'planned' pattern of fuel loading and operation power. In general, the irradiation dose is better controlled than irradiation temperature [98]. In reality, the reactor operation might be modified from the original plan: the cycle length, the operation power, the materials (fuel and testing materials). All these changes will affect the neutron (dose) and temperature spectrum of the reactor, and make them deviate from the original calculations.

Deviation in irradiation temperature raises also when the reactor ramps up and down. During the period of increasing and decreasing the reactor power, the specimens experience an irradiation temperature lower than the target temperature. This issue is more serious for higher target irradiation temperature (i.e. 450°C for this study). Besides, this issue only affects specimens that stay in the reactor for complete cycles (1 dpa specimens. A-11 position of ATR, see Chapter 2.2). For the 0.01 and 0.1 dpa specimens (B-7 position of ATR), they were moved into and out of the reactor during the cycle, and do not experience this power change.

A core-follow calculation after the irradiation experiments using the real reactor parameters can provide more accurate dose and temperature history than the target values. In addition, silicon carbide temperature rod and melt wire was implemented in the capsule to indicate the irradiation temperature information. However, that information (calculations and device) are still not available at the time of this writing.

To qualitatively check the irradiation dose, the radioactivity levels (μR/hr) of the specimens were measured; the higher the irradiation dose they receive, the higher the radioactivity they should exhibit, provided that they were irradiated roughly at the same time (comparing to their decay half-life) and that they have a similar size. As a result, the radioactivity readings are qualitatively in agreement with the specimen target dose. For instance, the radioactivity at 30 cm for the disc Fe-10Cr polycrystals irradiated at 300°C to 0.01 and 0.1 dpa are 4 and 77 μR/hr, respectively. These measurements exclude the possibility of mistakingly switching specimens of different irradiation doses.

The correctness of the irradiation temperature was evaluated by comparing the observed microstructure in Fe with the data in literatures. Two phenomenons were used for the judgment. Firstly, the prevailing Burgers vectors of dislocation loops are $\frac{a}{2}\langle 111\rangle$ at RT-70°C and gradually become a$\langle 100\rangle$ as irradiation temperature increases. Above 300°C, a$\langle 100\rangle$ loops dominate [28][31][30][29]. The other phenomenon useful for judging is that the dislocation decoration, loop rafting and loop clustering occur in Fe at lower irradiation temperature (up to 300°C) and not at the higher [28][31][29]. For Fe-Cr alloys, no systematic data as a function of irradiation temperature is currently available in literatures. However, the Fe-Cr specimens were irradiated in the same capsule as the Fe and they should share the same irradiation temperature.

The Fe polycrystals irradiated at 300°C exhibit evident dislocation decorations at 0.1 and 1 dpa so their irradiation temperature should not exceed 300°C much [28], otherwise a uniformly-distributed loops would be observed. The $\mathbf{g}\cdot\mathbf{b}$ analysis performed in the 0.1 dpa specimen indicates that a$\langle 100\rangle$ loops dominate. Therefore, the irradiation temperature for this specimen is sufficiently high (much higher than 70°C [31]), otherwise $\frac{a}{2}\langle 111\rangle$ loops would dominate.

For 450°C experiments, the dislocation loops in 0.1 and 1 dpa specimens have Burgers

vectors of a⟨100⟩ with a distribution not associated with the grown-in dislocations. The absence of dislocation decoration indicates that the irradiation temperature is well above 300°C. However, the loop size (both average and maximum) in 1 dpa specimen is much smaller than that in the 0.1 dpa specimen, which is odd since larger loops are expected for higher dose. In addition, the slight heterogeneity of loop distribution was observed in the 1 dpa specimen (Figure 3.52(b)). These two observations imply that the irradiation temperature for 1 dpa specimen is lower than the 0.1 dpa specimen. In Fe-Cr alloys, the loop distribution is uniform in 0.01 dpa and 0.1 dpa specimens while 1 dpa specimen exhibit a heterogeneous distribution of dislocation decoration (Figure 3.70). This is consistent with the suggestion of the lower irradiation temperature in the 1 dpa specimens. The lower irradiation temperature in the 1 dpa specimen is possibly related to the transient period (power ramp-up and ramp-down) of the reactor.

4.2 Temperature and Cr Concentration Effects on the Evolution of Microstructure under Irradiation

4.2.1 On the dislocation decoration

The Effect of Irradiation Temperature

Dislocation decoration was observed in Fe irradiated at 300°C, but not at 450°C. The majority of dislocation loops in the *300°C-0.1 dpa* specimen are a⟨100⟩ loops (Chapter 3.1.5), which is consistent with other 300°C studies [30][24]. However, since the a⟨100⟩ loops are sessile, it is surprising that the decorating dislocation loops are a⟨100⟩ loops instead of $\frac{a}{2}\langle 111\rangle$ loops. Small $\frac{a}{2}\langle 111\rangle$ loops are glissile at as low as RT , and is believed to be easily trapped and to decorate the grown-in dislocations [100][101].

There are two mechanisms proposed concerning the formation of dislocation decoration in bcc Fe.

1. The formation of dislocation loops is promoted in the vicinity of the dislocations due to the strain field of dislocations, and the carbon Cottrell atmosphere that traps in-

terstitials and prevent interstitials from absorption by dislocations [102][28][29].

2. The dislocation loops are created randomly in the matrix (independent of the grown-in dislocations). The migrating $\frac{a}{2}\langle 111\rangle$ loops are trapped and accumulated at dislocations to form dislocation decoration [101][100][78][103].

Trinkaus et al. [100] theoretically exclude the possibility of preferential formation of dislocation loops due to the strain field of dislocations, however the carbon Cottrell atmosphere promoting loop formation at dislocations is still possible. As a result, this remains to be a debating area. An *in-situ* TEM experiment with ion irradiation that dynamically observes the decoration process may provide insight and evidence about this question. Such experiments have been performed by Dr. Yao and his colleagues in IVEM facility in Argonne National Laboratory. They observed that dislocation loops were randomly produced spatially under self ion irradiation, and later trapped by grown-in dislocations [104].

If the a$\langle 100\rangle$ dislocation loops were preferentially produced in the vicinity of the grown-in dislocations (first mechanism), the observation of a$\langle 100\rangle$ loops as decorating loops in *300°C-0.1 dpa* Fe specimen could be understood. However, it would then cause difficulty to explain the 450°C Fe results where no dislocation decoration presents. Firstly, the C and N Cottrell atmosphere exists as well at 450°C since strain field of dislocations exist also at high temperature, and dislocation decoration should equally occur at 450°C; however, it was not observed at 450°C. In addition, it is difficult to understand the extremely low loop density detected in the dislocation-free regions in the *300°C-1 dpa* Fe specimen (Figure 3.13). At least some a$\langle 100\rangle$ loops should be observed in these regions considering 1 dpa is not a very low dose, and also considering the fact that the corresponding *450°C-1 dpa* Fe specimen already contains considerable dislocation loops in the dislocation-free region. Therefore, the first mechanism is not favored according to the observations of this study.

On the other hand, if the dislocation loops were produced randomly in the specimen matrix (second mechanism), the loops must be $\frac{a}{2}\langle 111\rangle$ loops to begin with; otherwise, uniform a$\langle 100\rangle$ loops should have been observed because a$\langle 100\rangle$ loops are immobile and would remain right at where they were produced. Upon being produced, the mobile $\frac{a}{2}\langle 111\rangle$ loops can migrate freely until being trapped by the grown-in dislocations. In order to form the

microstructure observed in the *300°C-0.1 dpa* Fe specimen, i.e. a⟨100⟩ loops as decoration loops, a transformation of Burgers vector from $\frac{a}{2}\langle 111\rangle$ to a⟨100⟩ loops is required. This kind of transformation for loops smaller than 50 nm in Fe has been observed by Arakawa et al. [105]. The observations of this study thus favor the second mechanism provided the transformation of loop Burgers vector were involved.

At higher irradiation temperature of 450°C, the irradiation damage in Fe takes a form of uniform a⟨100⟩ dislocation loops (slightly heterogeneous for the 1 dpa specimen), and a absence of dislocation decoration. Based on the above discussion, it indicates that the dislocation loops were produced either directly as a⟨100⟩ loops, or firstly as $\frac{a}{2}\langle 111\rangle$ loops but quickly transformed to a⟨100⟩ before appreciable migration and interaction with other defects.

In summary, the effect of increasing irradiation temperature in Fe is to increase the stability of the Burgers vector of a⟨100⟩ relative to $\frac{a}{2}\langle 111\rangle$. When the $\frac{a}{2}\langle 111\rangle$ loops is stable or can survive a considerable period of time before they reach grown-in dislocations, the dislocation decoration occurs.

The Effect of Cr Addition

In general, the dislocation decoration in Fe-Cr alloys is less pronounced compared to Fe specimens. The effect of Cr is most striking when comparing the Fe and Fe-Cr specimens irradiated at 300°C to 1 dpa, as shown in Figure 4.1. The Fe specimen exhibits highly heterogeneous structure of dislocation decoration, whereas Fe-Cr specimen exhibits a homogeneous loop morphology. Therefore, it is evident that the addition of Cr decreased the mobility of $\frac{a}{2}\langle 111\rangle$ dislocation loops (consistent with *in-situ* TEM observation [48]), and prevent them from migrating to the grown-in dislocations, resulting a uniform distribution.

Although depressed, dislocation decoration can still occur in Fe-Cr alloys. For instance, the four Fe-Cr specimens of this study: *0.1 dpa-300°C* Fe-10Cr single crystal, *0.1 dpa-300°C* Fe-10Cr polycrystal (although limited), *1 dpa-450°C* Fe-13Cr single crystal and *1 dpa-450°C* Fe-10Cr polycrystal. Unlike Fe specimens where most dislocation loops are confined in the vicinity of grown-in dislocations, in Fe-Cr alloys many dislocation loops are not associated

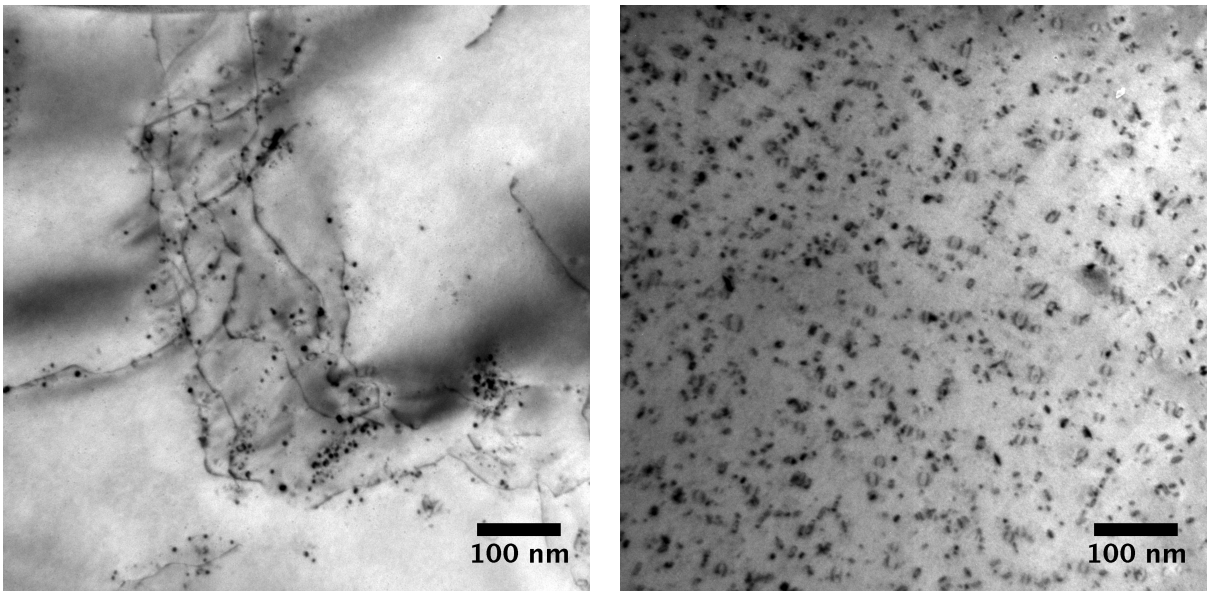

(a) 1 dpa - 300°C Fe

(b) 1 dpa - 300°C Fe-10Cr

Figure 4.1: A comparison of dislocation decoration in *1 dpa - 300°C* Fe polycrystalline specimen and *1 dpa - 300°C* Fe-10Cr polycrystalline specimen. Both micrographs were imaged under g = 110 kinematic condition.

with grown-in dislocations, as shown in Figure 4.2. In the Fe specimen (Figure 4.2(a)), dislocation loops are rarely observed in dislocation-free regions. In contrast, in the Fe-Cr specimen (Figure 4.2(b)), although dislocation lines are clearly decorated with small dislocation loops, a lot more dislocation loops were uniformly dispersed.

Finally, an odd point needs to be discussed. Since dislocation decoration was observed in Fe-Cr alloys at both 300°C and 450°C, it is surprising that it was observed only in the four specimens mentioned above, and not in all of the specimens. The answer seems to rely on the possible deviation of the irradiation conditions, particularly the irradiation temperature. For 300°C irradiation, that dislocation decoration occurs in 0.1 dpa Fe-Cr alloys and not occurs in 1 dpa Fe-Cr alloys implies that the mobility of $\frac{a}{2}\langle 111\rangle$ dislocation loops is higher in the 0.1 dpa Fe-Cr specimens than in 1 dpa Fe-Cr specimens. Thus, a higher irradiation temperature for the 0.1 dpa Fe-Cr specimens (than other 300°C Fe-Cr specimens) is suggested. This is consistent with Fe irradiated at 300°C where the 0.1 dpa specimen has larger dislocation loops than the 1 dpa specimen.

For 450°C irradiation, on the other hand, a lower irradiation temperature for 1 dpa Fe-Cr

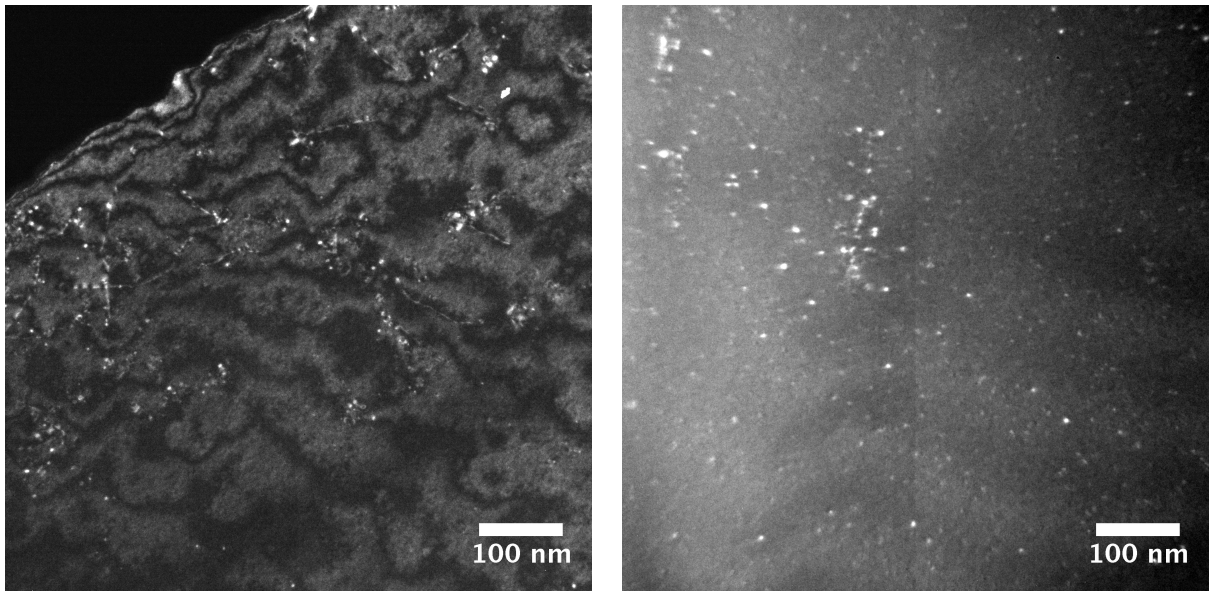

(a) 1 dpa - 300°CFe (b) 1 dpa - 450°C Fe-10Cr

Figure 4.2: A comparison dislocation decoration in *1 dpa - 300°C* Fe polycrystalline specimen and *1 dpa - 450°C* Fe-10Cr polycrystalline specimen. Both micrographs were imaged under g = 110 (g, 4.3g) DF.

specimens (than other Fe-Cr specimens) is suggested based on the observation that dislocation decoration occurs in 1 dpa specimens but not in 0.01 and 0.1 dpa specimens. The lower irradiation temperature for 1 dpa specimens resulted in a higher chance of producing/containing mobile $\frac{a}{2}\langle 111\rangle$ loops that can migrate to grown-in dislocations.

In summary, the addition of Cr greatly reduces the mobility of $\frac{a}{2}\langle 111\rangle$ loops. Dislocation decoration can occur in Fe-Cr alloys when sufficient $\frac{a}{2}\langle 111\rangle$ dislocation loops exist with sufficient mobility. To meet this condition, the irradiation temperature must be high enough so $\frac{a}{2}\langle 111\rangle$ dislocation loops are mobile, but not too high so the immobile $a\langle 100\rangle$ dislocation loops would not take over and become predominant. This temperature window seems to fall between 300°C and 450°C.

4.2.2 On the burgers vector of dislocation loops

The ratio of dislocation loops with Burgers vector $\mathbf{b} = a\langle 100\rangle$ and $\frac{a}{2}\langle 111\rangle$ are affected both by the irradiation temperature and the Cr concentration. Increasing irradiation temperature

increases the stability of the a⟨100⟩ loops against the $\frac{a}{2}\langle 111\rangle$loops. On the other hand, increasing Cr concentration in Fe equalizes the fraction between the two Burgers vectors. Detailed literature review about the loop Burgers vector dependence on the irradiation temperature and Cr concentration can be found in Chapter 1.3.1. Here, the Burgers vector analysis in this study is discussed and compared with literatures.

Table 4.1 summarizes the Burgers vector analysis. Only a portion of the specimens was analyzed due to a combination of limited time, the magnetic nature of the specimen (hard to perform necessary tilting in TEM) and the undesired specimen quality (especially in Fe). The Fe specimens irradiated at 300°C exhibit a microstructure of dislocation decoration, therefore $\frac{a}{2}\langle 111\rangle$ loops are considered as the primary loops (at least before they being trapped by grown-in dislocations). Increasing the irradiation temperature from 300°C to 450°C results in an increase of the ratio of a⟨100⟩ loops in Fe as well as in Fe-Cr alloys, which is consistent with other studies in literatures.

Table 4.1: Summary of Burgers Vector Analysis ($\langle 100\rangle$:$\frac{a}{2}\langle 111\rangle$)

Specimen	Temperature	0.01 dpa	0.1 dpa	1 dpa
Fe	300°C	n.d.	Majority a⟨100⟩	n.d.
Fe	450°C	n.d.	All a⟨100⟩	All ⟨100⟩
Fe-10Cr poly	300°C	n.d.	n.d.	65%: 35%
Fe-10Cr poly	450°C	85%:15%	95%:5%	n.d.
Fe-Cr single	300°C	n.d.	n.d.	84% :16%
Fe-Cr single	450°C	n.d.	Majority a⟨100⟩	n.d.

n.d. Not Determined.

On the other hand, the addition of Cr in Fe increases the appearance of the Burgers vectors of $\frac{a}{2}\langle 111\rangle$. For instance, whereas dislocation loops observed in Fe specimens irradiated at 450°C are exclusively a⟨100⟩ loops, some $\frac{a}{2}\langle 111\rangle$ loops were found in the Fe-10Cr polycrystalline specimens irradiated at the same irradiation temperature. Therefore, the result of this study supports the opinion that the addition of Cr increases the fraction of $\frac{a}{2}\langle 111\rangle$ loops [22][23]. However, as the data is limited, this study dose not exclude the possibility of the Cr addition equalizing the two Burgers vectors instead of simply increasing the $\frac{a}{2}\langle 111\rangle$ loops [53][48]. Especially, the dislocation loops decorating the grown-in dislocations in the

300°C-1 dpa Fe specimen are likely $\frac{a}{2}\langle 111\rangle$ loops, although rigorous $\mathbf{g}\cdot\mathbf{b}$ analysis had not yet performed. If that is true, then the higher ratio of a$\langle 100\rangle$ loops in the *300°C-1 dpa* Fe-Cr specimens would be an evidence of Cr equalizing the $\frac{a}{2}\langle 111\rangle$ and a$\langle 100\rangle$ loops, and not simply increasing the $\frac{a}{2}\langle 111\rangle$ loops.

4.2.3 On the evolution of dislocation loops: size and density

Irradiation Temperature Effect

The density and size of dislocation loops in irradiated Fe are plotted in Figure 4.3 along with the literature data. The grey, white and orange backgrond color is used to roughly divide the irradiation temperature into three groups: reactor ambient (60-80C), ∼300°C and higher temperatures >400°C. In general, the loop density decreases and the loop size increases with increasing irradiation temperature.

The 300°C data of this study is fitting fairly well in the map, consistent with literature data. The density increases monotonically with increasing dose. For size, the dependence is relatively flat. The lower loop size of 1 dpa specimen implies that their actual irradiation temperature is lower than that of the 0.1 dpa specimen.

The loop size (density) in 450°C specimens are consistently larger (smaller) than that in the 300°C specimens. However, their dependence on dose is not monotonic. The 1 dpa specimen exhibits a smaller loop size and a higher loop density compared to 0.1 dpa, making it actually closer to the ∼300°C zone of the map. Similar to the observation in 300°C, the loop size in the *450°C-1 dpa* specimen is smaller than the corresponding 0.1 dpa specimen. The size drop in the 450°C, however, is more significant than 300°C. As discussed previously in Chapter 4.1, this observation of size drop for 1 dpa (drop-in) specimen is likely due to irradiation during the reactor transient period when the actual irradiation temperature was lower then the target temperature.

The density and size measurements in Fe-Cr alloys are plotted in Figure 4.4 and 4.5. Unlike Fe, there is no literature data with similar conditions (ex. irradiation temperature, Cr concentration and dose) to compare with. Clearly, the two Fe-Cr alloy systems (Fe-10Cr

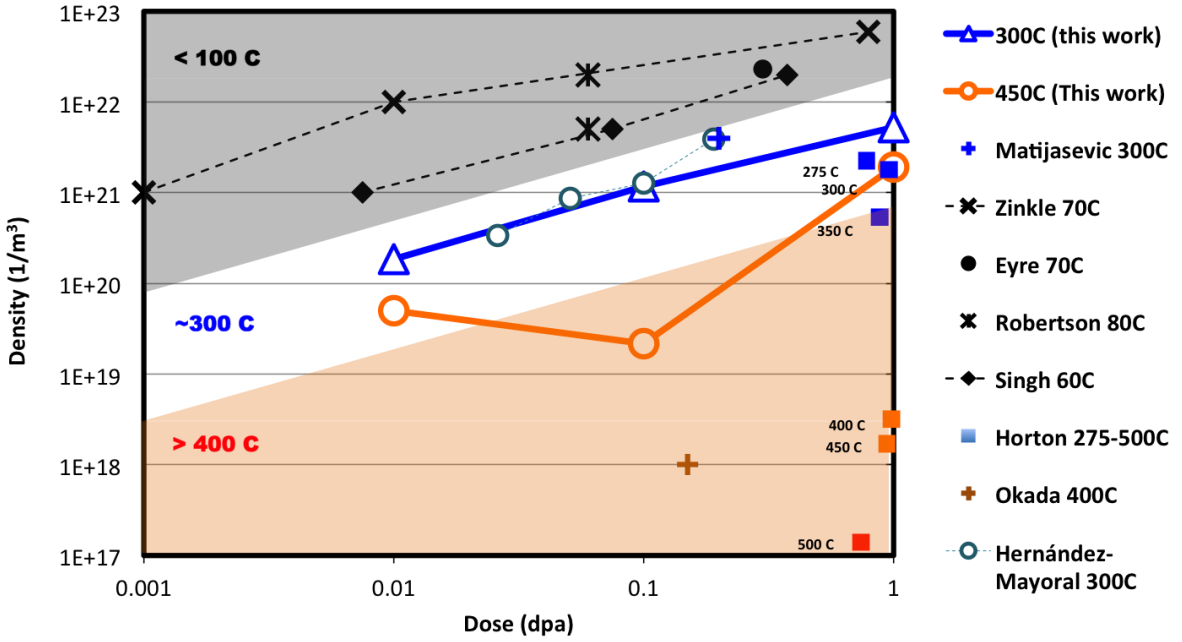

(a) Loop Density

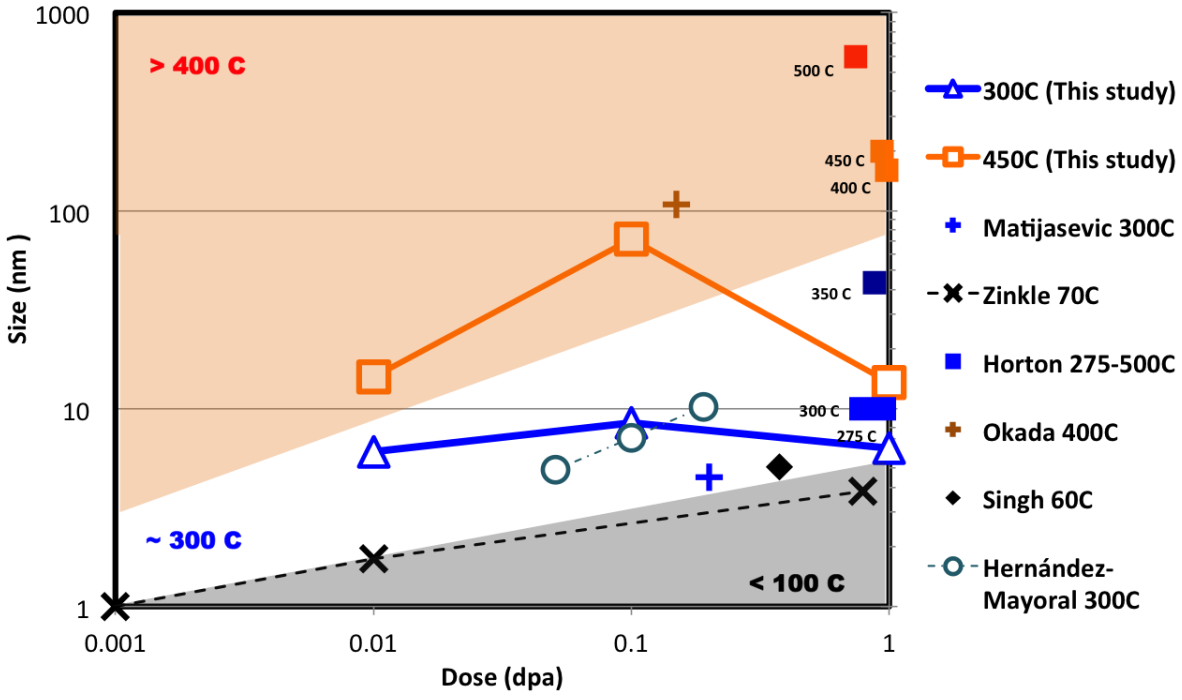

(b) Loop Size

Figure 4.3: The summary of loop density and size measurements in irradiated Fe from this study and from literatures [36][31][17][75][29][26][24][32]. The background colors of orange, white and gray is to guide the eyes.

polycrystals and Fe-Cr single crystals) behave highly similarly. For lower doses of 0.01 dpa and 0.1 dpa, the loop density are higher at 450°C than 300°C (see TEM images in Figure 4.6 for visual comparison) while a crossover appears roughly at 0.4 dpa and the loop density in 300°C specimen become higher than 450°C specimen at 1 dpa. This dependence of loop density on irradiation temperature in Fe-Cr alloys is very different from the Fe metals; they are opposite at 0.01 dpa and 0.1 dpa.

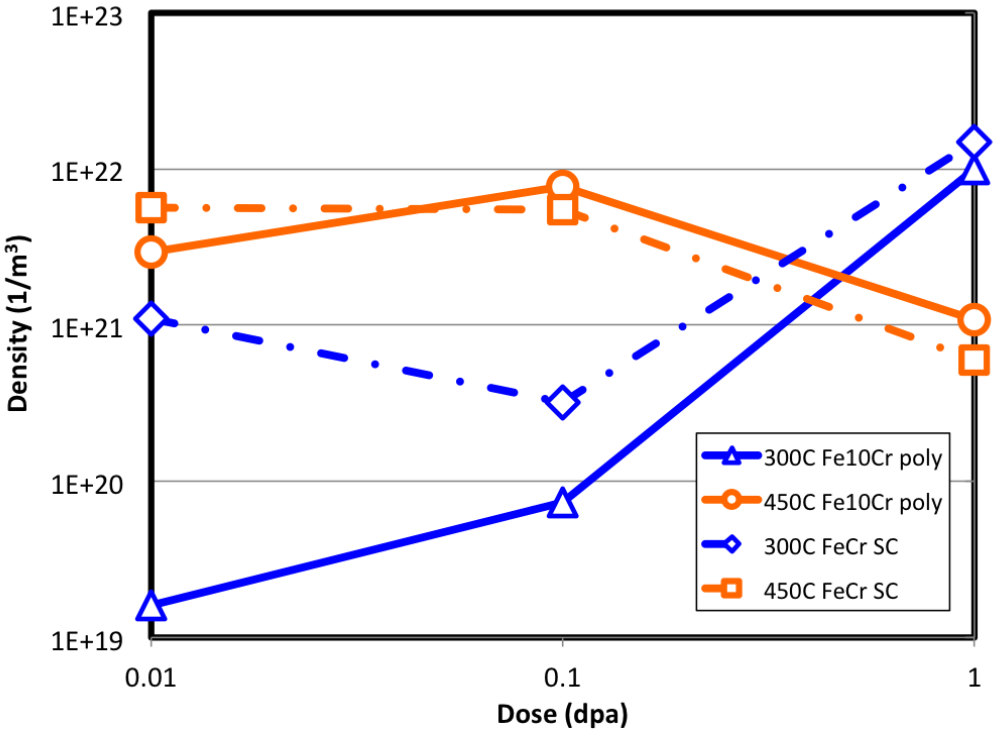

Figure 4.4: The summary of density measurements on Fe-Cr alloys.

This result is confusing because the conventional opinion is that lower irradiation temperature produces a higher density of dislocation loops. More confusingly, the 1 dpa result seems to turn over and return to a microstructure normally expected; the *1 dpa-300° C* Fe-Cr specimens exhibits much denser dislocation loops than the *1 dpa - 450° C* Fe-Cr specimens. To understand this observation, the Cr effect on the formation of dislocation loops needs to be discussed.

Similar observations have been reported previously in several low-dose studies. Matijasevic et al. [36] examined Fe and Fe-15Cr irradiated at 300°C to 0.2 dpa. They found a high

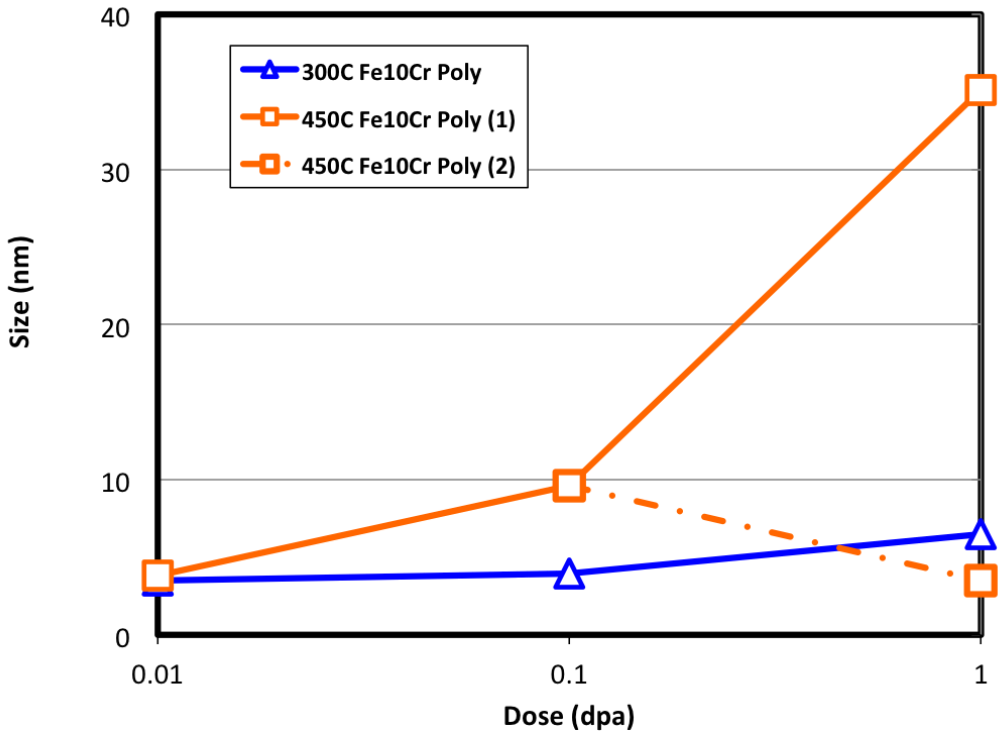

(a) Fe-10Cr Poly-crystals

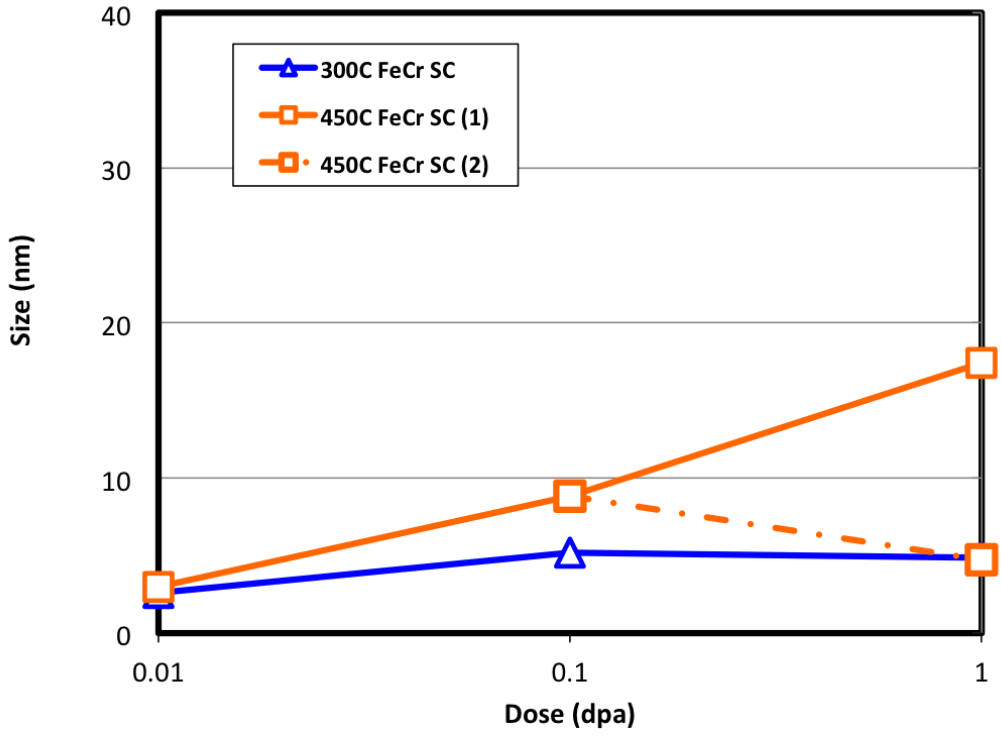

(b) Fe-Cr Single crystals

Figure 4.5: The summary of size measurements on Fe-Cr alloys. For 450°C: (1) the large loops associated with dislocations and (2) the uniformly distributed small loops.

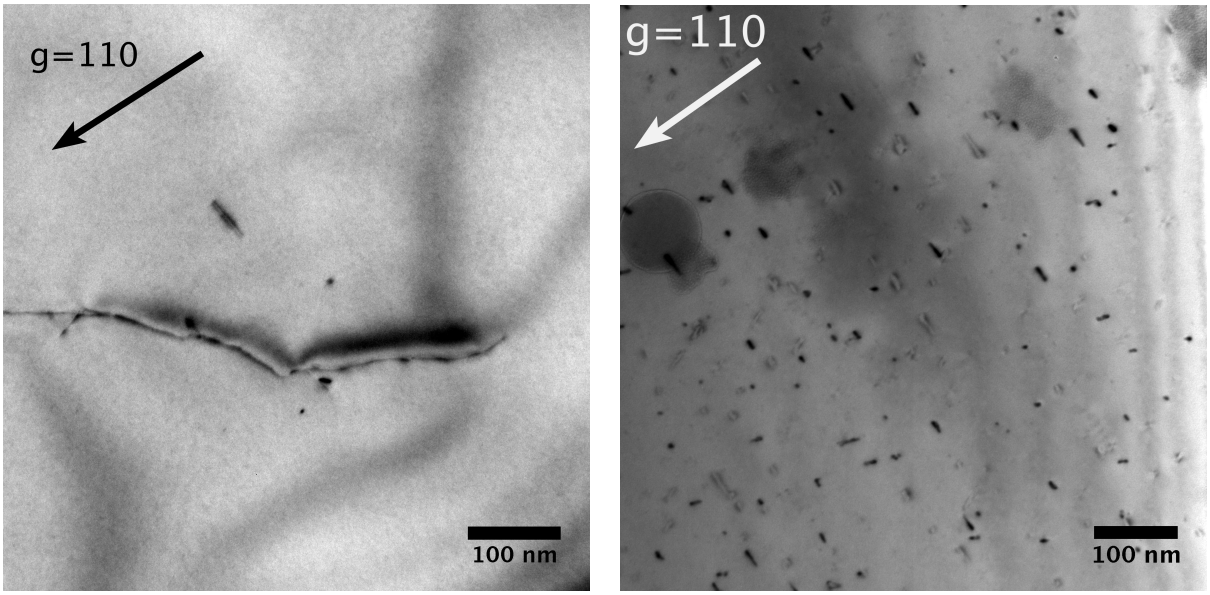

(a) 300°C 0.1 dpa Fe-10Cr (b) 450°C 0.1 dpa Fe-10Cr

Figure 4.6: A comparison of TEM micrographs showing the irradiation temperature effects in Fe-10Cr polycrystals irradiated to 0.1 dpa. Both micrographs were imaged under g = 110 kinematic conditions.

density of uniform dislocation loops in Fe, whereas no visible loops were observed in Fe-15Cr. Interstitial impurities (C, N) seems to have the same effects as Cr. Robertson et al. [29] compared 0.06 dpa high-purity Fe and low-purity Fe (with more C and N) irradiated at reactor ambient temperature, and found that no visible damage can be observed in low-purity Fe whereas high-purity Fe already developed a highly-heterogeneous distribution of dislocation loops (dislocation decoration). Both studies concluded that the dislocation loops should exist in those 'seemingly clean' specimens (irradiated Fe-15Cr and low-purity Fe) but the loops were too small to be resolved by TEM.

A list of possible explanations leading to the low loop density observed in the *300°C - 0.01 and 0.1 dpa* specimens is presented and discussed below.

- With the addition of Cr, the mobility of dislocation loops (particularly $\frac{a}{2}\langle 111\rangle$ loops) is greatly reduced [48], which leads to higher recombination of point defects, resulting in lower loop formation [36].

  Comparing the data between *1 dpa-300°*C Fe and Fe-Cr of this study, the loop density is higher in Fe-Cr while their sizes are similar. It indicates that the irradiation damage

accumulated in Fe-Cr is more than that in Fe. Therefore, the mechanism of higher defect recombination with the Cr addition is not supported by the data of this study.

- The $\frac{a}{2}\langle 111\rangle$ loops are more stable at 300°C than at 450°C [41][44]. Provided more $\frac{a}{2}\langle 111\rangle$ loops were produced at 300°C, then more $\frac{a}{2}\langle 111\rangle$ loops could migrate to the sinks and disappear afterward. On the other hand, at 450°C more loops were produced as immobile a$\langle 100\rangle$ loops. The a$\langle 100\rangle$ loops would not migrate to the sinks. Therefore the defect accumulation is suggested to be faster at 450°C [43].

  Since the mobility of $\frac{a}{2}\langle 111\rangle$ loops is significantly reduced by Cr [48], it is questionable if the $\frac{a}{2}\langle 111\rangle$ loops can still effectively migrate to the sinks. Besides, heterogeneous loop morphology (dislocation decoration, loop rafting etc.) should be observed if $\frac{a}{2}\langle 111\rangle$ loops are produced and are still sufficiently mobile. However, dislocation loop morphology observed in the *300°C-1 dpa* Fe-Cr specimens is 'uniform small dislocation loops', not heterogeneous structure. Therefore, this mechanism of mobile dislocation loops migrating and annihilated to the sinks is not favored, either.

- Based on the above argument, the addition of Cr in Fe did not enhance the rate of defect recombination or the rate of loop lost to the sinks. The true microstructure of the *0.01-300°C* and *0.1 dpa-300°C* Fe-Cr specimens is thought to be a high density of very small dislocation loops (smaller than the TEM resolution). The measured loop density in the 300°C 0.01 and 0.1 dpa Fe-Cr specimens might be under-estimated.

The temperature effects of the loop size in Fe-Cr alloys are shown in Figure 4.5. For both polycrystalline Fe-10Cr and single crystal Fe-Cr, the average size of the dislocation loops is larger at 450°C than at 300°C. The *450°C-1 dpa* cases are more complicated because those specimens exhibit large dislocation loops as well small as ones. The small dislocation loops appeared both uniformly (Figure 3.65) and heterogeneously decorating dislocations (Figure 3.70). The small dislocation loops were thought to be produced at a lower-than-target irradiation temperature possibly during the reactor transient period, as discussed previously in Chapter 4.1. The average size of these small loops is plotted with dotted lines and the large loops with solid lines. For both Fe and Fe-Cr alloys, the increasing loop size with

increasing irradiation temperature indicates the loop growth rate increases with increasing irradiation temperature, which is consistent with experiments and rate theory calculation on austenitic stainless steels [106][107].

Cr Concentration Effect

The size and density of irradiation-induced dislocation loops in Fe metal and Fe-Cr alloys as a function of Cr concentration are shown in Figure 4.7 and 4.8. In general, the loop size (both the average and the maximum) decreased with increasing Cr concentration, especially from Fe metal to Fe-Cr alloys. This correlation between the loop size and the Cr content is in agreement with previous studies [23][22][35]. A few exceptions, however, were observed:

- In Figure 4.7(a), whereas the average size consistently decreases with increasing Cr, the maximum loop size is larger in Fe-14Cr single crystal specimen than in the Fe-10Cr polycrystal specimen. This is thought to be due to the insufficient statistics in the Fe-10Cr polycrystal specimen (with extremely low loop density) that falsely report the true maximum loop size.

- In Figure 4.7(c), the two Fe-10Cr polycrystal and Fe-Cr single crystal have a close Cr concentration, respectively 9.65% and 10.0%. Both the average and the maximum loop size is larger in the single crystal specimens. Since dislocation decoration was much more frequently observed in the single crystal specimen than in the poly-crystal specimen, perhaps due to higher dislocation density, the larger loop size in the single crystal specimen is likely caused by the enhanced loop coalescence at the vicinity of line dislocations.

- In Figure 4.7(f), both the average and maximum loop size is smaller in Fe than in Fe-Cr, which is the only one among the total six cases. The reduced size in Fe compared to Fe-Cr alloys might be related to its smaller grain size and higher initial dislocation density. The smaller grain size is known to delay the loop development by strong sink effects of grain the boundary [108]. However, it is not clear why the loop size is still larger in Fe for the other five cases.

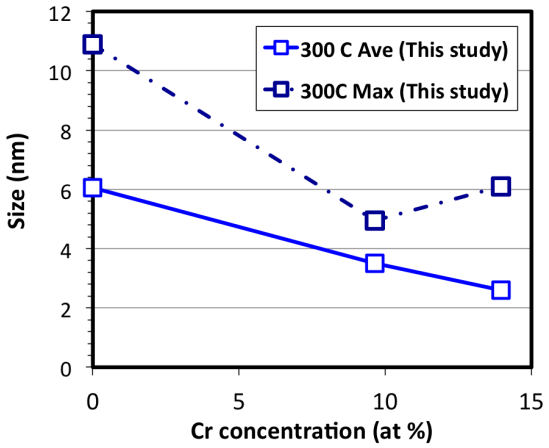

(a) 300C-0.01 dpa

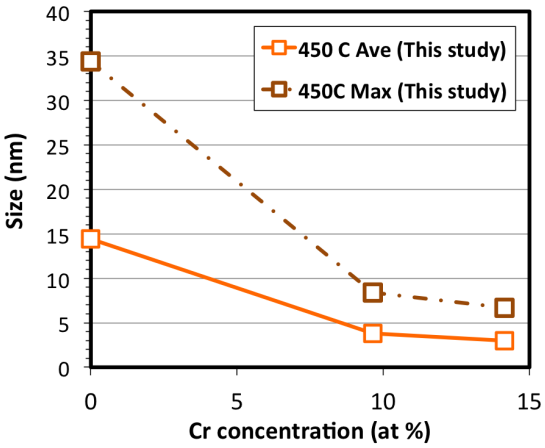

(b) 450C-0.01 dpa

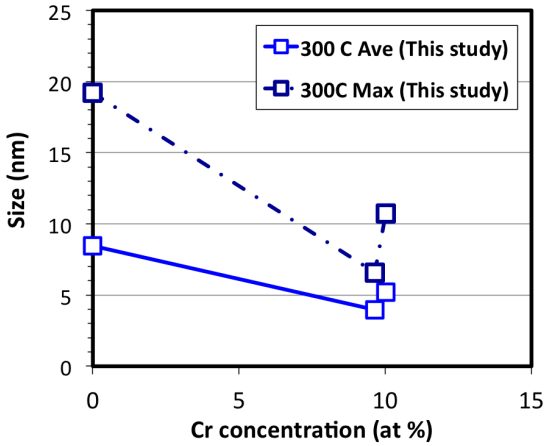

(c) 300C-0.1 dpa

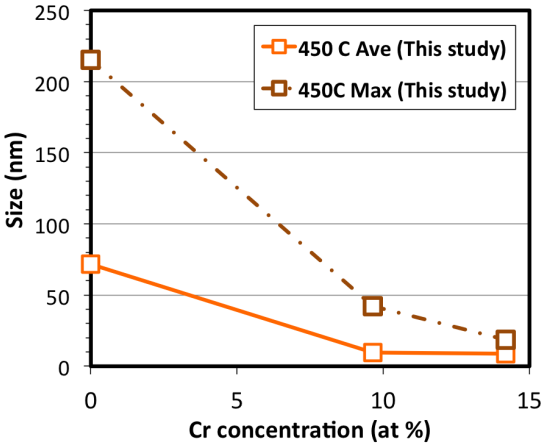

(d) 450C-0.1 dpa

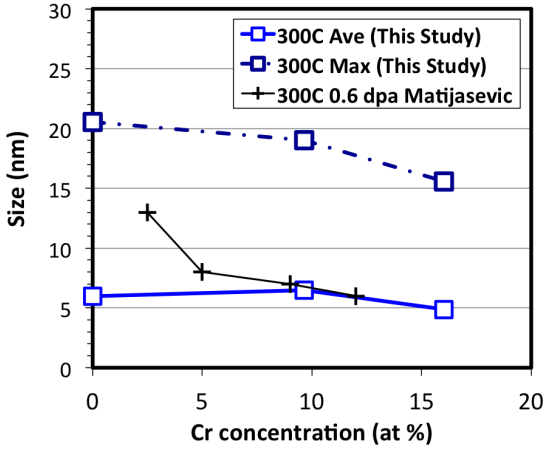

(e) 300C-1 dpa

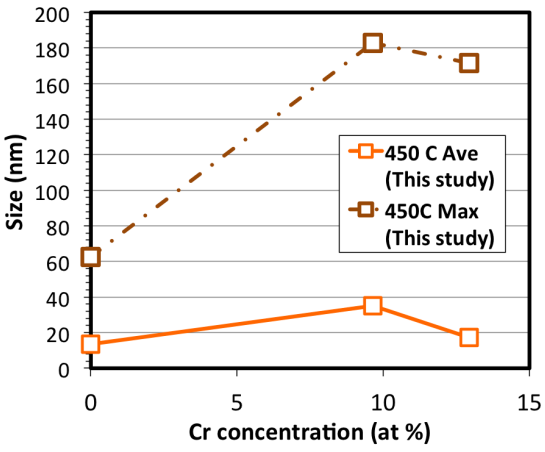

(f) 450C-1 dpa

Figure 4.7: A summary of average (Ave) and maximum (Max) observed loop size as a function of Cr contents for each irradiation condition. The literature data used for comparison is from Matijasevic and Almazouzi [23].

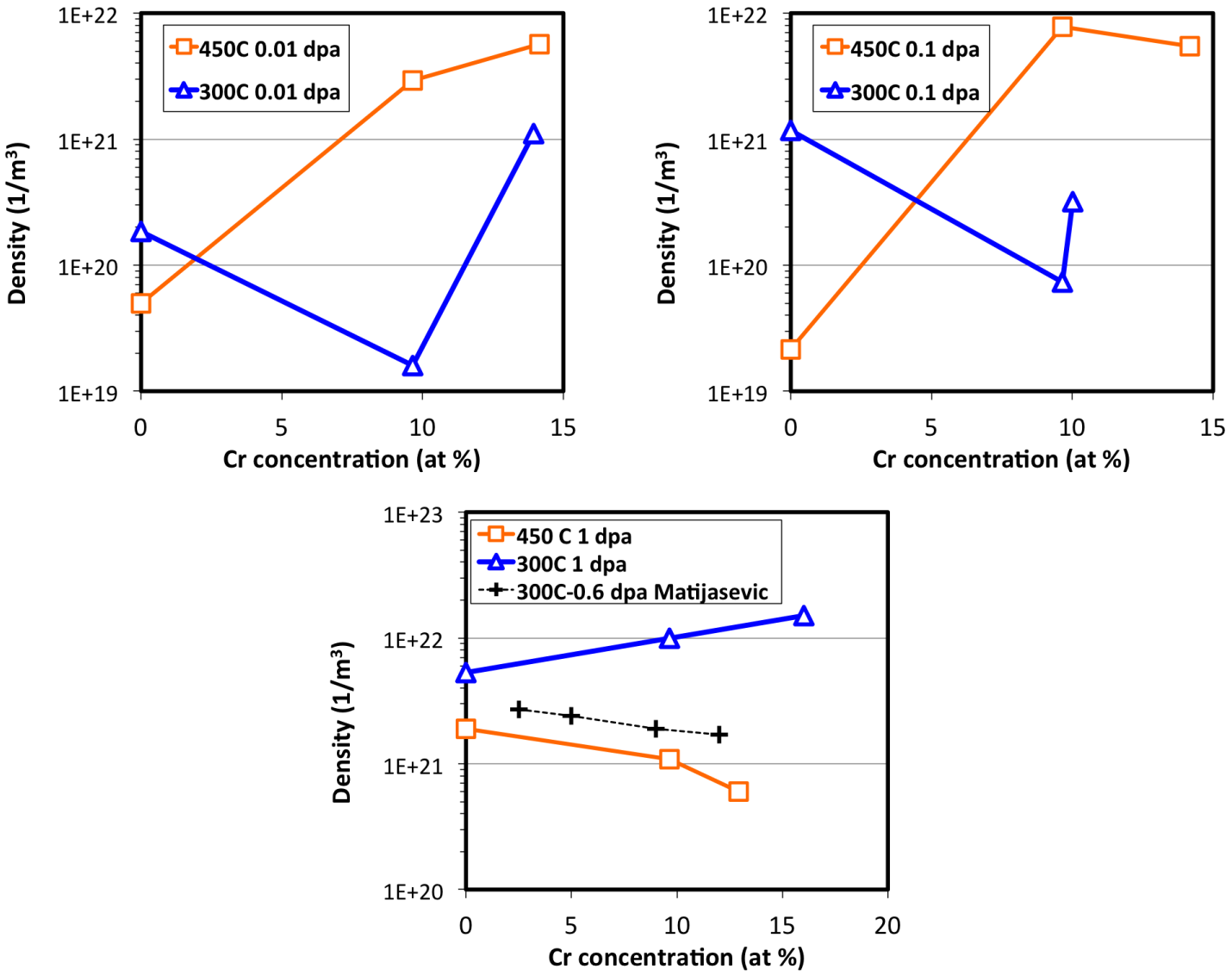

Figure 4.8: A summary of the loop density as a function of Cr concentration for each irradiation condition. The literature data is obtained from Matijasevic and Almazouzi [23].

As mentioned in the literature review, the dislocation loop density increases sharply with the addition of 1-2% Cr into the Fe metals [22][35][21]. However, the effect of further increase in Cr contents on the loop density is not conclusive where positive [35], negative [23][22] and mixed [34] effects have all been reported previously. In addition to neutron irradiation results, self-ion irradiation experiments show no significant difference in loop density between Fe-5Cr, Fe-8Cr and Fe-11Cr [48].

In this study, the effect of Cr on the loop density is complicated, as is shown in Figure 4.8. It is difficult to draw conclusions about the effect of Cr on the dislocation density. For instance, the loop density in Fe in this work, is not always lower than the Fe-Cr alloys under the same irradiation conditions, which is against most other studies. Also, increasing Cr from the polycrystalline Fe-10Cr specimens to the single-crystalline specimens (10-16%Cr) could either increase and decrease the loop densities. The reasons for this scattering data is given below:

- The dose of this study is fairly low, particularly the 0.01 and 0.1 dpa. The small loop size in the Fe-Cr alloys might result in an under-estimate on the density of dislocation loops, as is suggested in [36][29].

- In addition to the Cr concentration, the grain size and initial dislocation density vary significantly from specimen to specimen. Fe specimens have the smallest grain size and largest grown-in dislocation density. The effect of grain boundary and dislocations as the sinks for point defects in Fe would be much higher than in Fe-Cr alloys. Even within one category, differences were recognized. For instance, the grown-in dislocation density is particularly higher in *300°C-0.1 dpa* Fe-10Cr single crystal specimen than the rest of Fe-Cr single crystal specimens. As a result, the plot in Figure 4.8 is not simply a function of Cr concentration but is also affected by grain size and the initial dislocation densities, which make it difficult to interpret the single-parameter-effect of Cr in the dislocation density.

4.2.4 On the α' precipitation

Effects of Irradiation Dose

Precipitation kinetics of the α' phase is much faster under irradiation than under thermal aging conditions alone due to irradiation-enhanced diffusivity [109][56]. Figure 4.9 shows a compilation of experimental data showing the evolution of $f_{\alpha'}$ for Fe-Cr alloys with Cr contents x_{Cr} = 9-10% irradiated at Tirr = 300-325°C. The dashed line is the fα' for Fe-Cr with xCr = 9.65% at 300°C predicted by the phase diagram using lever rule [16]. Except for one data point from [109], fα' remains below the saturation limit as it evolves with irradiation. The threshold dose required to form observable α' precipitates is estimated to be between 0.1 to 0.6 dpa. Beyond the threshold dose, the $f_{\alpha'}$ increases with dose and approaches the saturation limit. On the other hand, the corresponding mean precipitate size $\bar{r_{\alpha'}}$ (not shown) is within 1.0-1.2 nm, and there is no evident trend of $\bar{r_{\alpha'}}$ with dose. Therefore, for this specific condition, it is still in the nucleation regime. For other x_{Cr} or Tirr, it may enter growth regime at a lower dose. For instance, larger α' precipitates with radius $\bar{r_{\alpha'}}$ = 2-5 nm were observed in Fe-Cr with x_{Cr} ~12% irradiated at 400°C to a dose of ~7 dpa [110][22]. However, a systematic investigation over a range of dose is currently not available because the irradiation data for those x_{Cr} and T_{irr} is limited.

Effects of Cr Concentration on the Irradiation-Enhanced α' Precipitation

The α' precipitation in Fe-Cr alloys is significantly dependent on x_{Cr}. Under equivalent irradiation condition, Fe-Cr alloys with higher x_{Cr} have larger $\bar{r\alpha'}$, higher precipitate density $N_{\alpha'}$, higher α' volume fraction $f_{\alpha'}$, and lower threshold dose for observable precipitation.

As shown in Table 3.7, $\bar{r_{\alpha'}}$ increases slightly with x_{Cr} at both 300°C and 450°C. This is consistent with the Monte Carlo modeling on thermally-aged bcc Fe-Cr [113][57]. Since the Cr diffusivity does not increase with x_{Cr} [60], the growth rate of precipitates is not the cause. Instead, the onset dose of nucleation accounts for this phenomenon. The precipitates in specimens with higher x_{Cr} nucleate α' precipitates earlier and they have more time to grow. This is supported by the frequency analyses in this study, and by modeling [57].

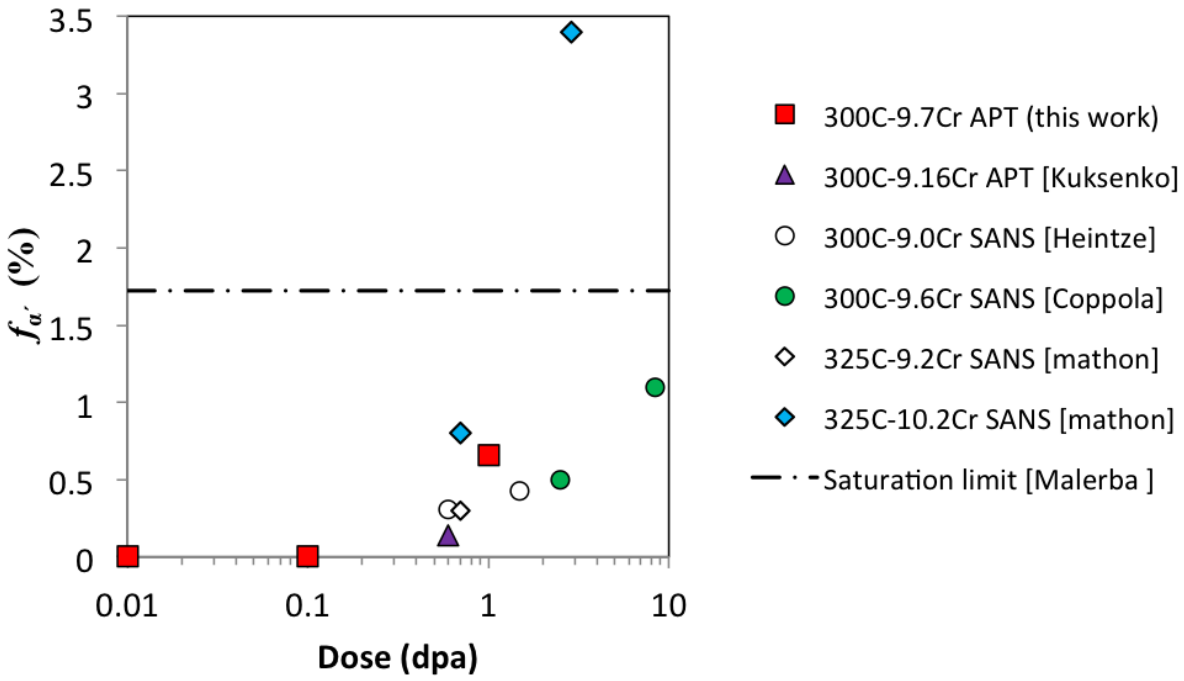

Figure 4.9: ′ volume fraction deduced from APT and SANS for Fe-Cr model alloys and commercial RAFM steels irradiated to doses of 0.6-8.4 dpa with Cr concentration x_{Cr}=9-10% and irradiation temperature Tirr = 300-325°C. The dashed line is the saturation limit calculated for Fe-Cr alloys with xC=9.65% at 300°C. The literature data are taken from [97][111][112][109]

.

Nevertheless, the $r_{\alpha'}^{-}$ is relatively insensitive to x_{Cr}, consistent with other experiments and modeling [91][97][109][113][57].

On the other hand, $N_{\alpha'}$ increases significantly with x_{Cr}. This can be understood using the Gibbs homogeneous nucleation theory, expressed in Eq 4.1 [114].

$$\dot{N}_p = x_{Cr}\left(e^{-\frac{\Delta G^*}{RT}}\right) \tag{4.1}$$

$\dot{N}_p$ is the nucleation rate, ΔG^* is the activation energy for α-α' phase transformation, R is gas constant, and T is absolute temperature. ΔG^* decreases with x_{Cr} because of the increasing driving force of phase transformation with x_{cr}. Since both x_{Cr} and the exponential terms increase with x_{Cr}, $\dot{N}_p$ increases with x_{Cr}. The observation of this study that $N_{\alpha'}$, and not ($r_{\alpha'}^{-}$, varies strongly with x_{Cr} is in accordance with the modeling result in [57].

To study the x_{Cr} effects on $f_{\alpha'}$, a compilation of experimental data is shown in Figure 4.10 for Fe-Cr ferritic alloys irradiated at about 300°C to a dose around 1 dpa. The dashed line is the α' volume fraction predicted by the phase diagram in Ref [16] using lever rule at 300°C. No α' precipitation was observed below the threshold x_{Cr} of 8.1%, which is consistent with the prediction from the phase diagram. Beyond the threshold, $f_{\alpha'}$ increases with x_{Cr}. As discussed above, this is primarily due to the higher nucleation rate $\dot{N}_{\alpha'}$ in the specimens with higher x_{Cr}.

Irradiation temperature effects on the irradiation-enhanced α' precipitation

As shown in Figure 3.86 and in Table 3.7, $r_{\alpha'}^{-}$, $N_{\alpha'}$ and $f_{\alpha'}$ of α' precipitate in Fe-Cr specimens decrease with T_{irr}. This is in agreement with the prediction from the phase diagram in [16] that f decreases with T_{irr}. The observation of lower $N_{\alpha'}$ with higher Tirr might be attributed to a decreasing nucleation rate $\dot{N}_{\alpha'}$with increasing T_{irr}. In terms of Gibbs homogeneous nucleation theory in Equation 4.1 [110], T_{irr} has effects on both the ΔG* and the RT terms. When Tirr increases, the RT terms result in an increase in $\dot{N}_{\alpha'}$. On the other hand, increasing T_{irr} results in a reducuction in the driving force for precipitation, leading to an increase in ΔG*, and therefore, and a decrease in $\dot{N}_{\alpha'}$. In this case, the effect of increasing T_{irr} on the ΔG* term is inferred to be more significant than on RT term.

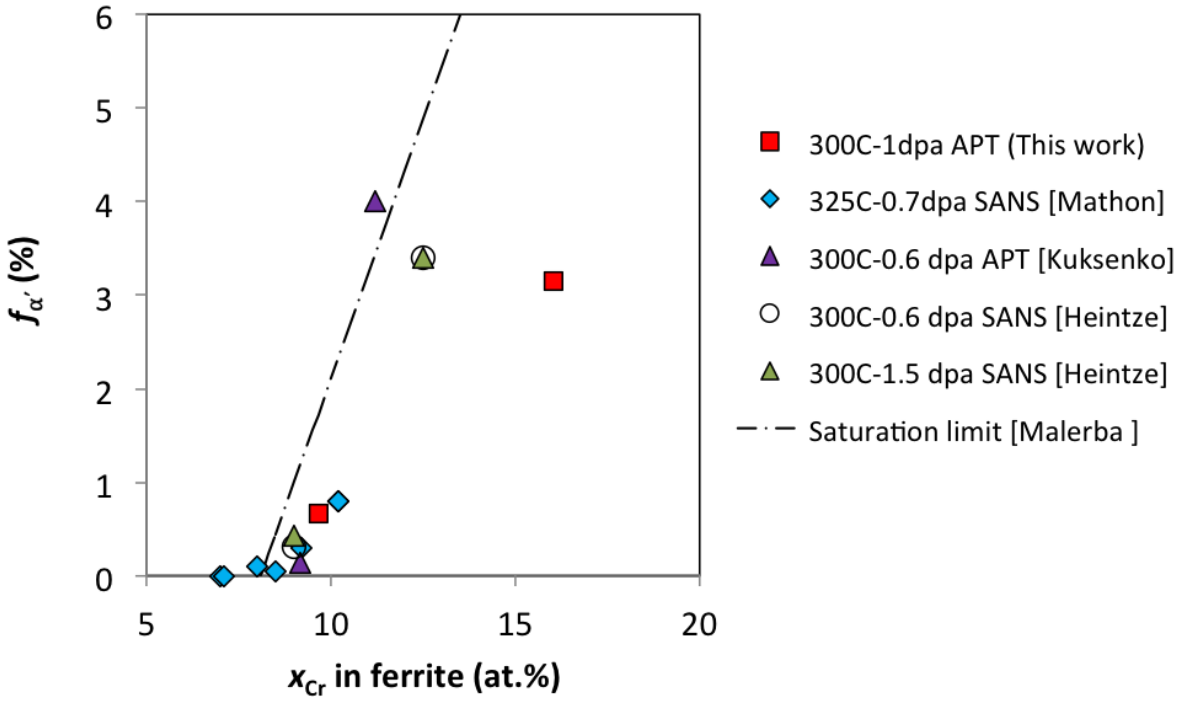

Figure 4.10: α' volume fraction $f_{\alpha'}$ deduced from APT and SANS on Fe-Cr model alloys and commercial RAFM steels with Cr concentration x_{Cr} of 7-16 at.% with a irradiation temperature and a dose close to 300°C and 1 dpa, respectively. The dashed line is the saturation limit calculated for Fe-Cr alloys at 300°C. The literature data obtained from [109][97][111].

The size $r_{\alpha'}^{-}$ decrease with T_{irr}. Compared to x_{Cr}, the effect of T_{irr} on $r_{\alpha'}^{-}$ is more significant. The Cr diffusivity is not applicable to interpret this temperature dependence because increasing T_{irr} should enhance Cr diffusivity and the precipitate growth rate, provided diffusion-controlled mechanism. Therefore, there must be other mechanism controlling the growth of α' precipitate. Perhaps, the smaller $r_{\alpha'}^{-}$ with T_{irr} is due to the smaller $N_{\alpha'}$ that come with a delayed onset for precipitation growth. These questions remain unclear at this point.

The Core Cr Concentration Dependence on the Size of α' Precipitates

As Figure 3.89 shows, the majority of precipitates in this study had a core Cr concentration considerably below the equilibrium concentration predicted by the phase diagram (>90%). Several hypotheses have been proposed to explain this APT observation, such as the non-classical nucleation, the modified phase diagram and APT artifacts. With phase field calculations, Li et al. [115] showed that the critical nuclei of α' precipitates are non-classical where the Cr concentration in the nuclei is smaller than thermaldynamic equilibrium value. The deficit of Cr in nuclei decreases with 1) decreasing overall Cr content, 2) increasing aging temperature and 3) increasing nuclei size (during growth). However, this study does not favor the non-classical nucleation explanation because of the low nominal Cr contents [116][91]. In addition, the dependence on 1) Cr content and 2) temperature described in Ref. [115] were not observed in this study, although the 3) size effects seems to be captured in Figure 3.89. The irradiation-induced point defects (super-saturated) has been suggested to change the phase diagram, resulting in a higher Fe solubility in Cr [91][56]. However, this can not explain the observed correlation between the core Cr concentration and precipitate sizes.

The blurring of the APT data at the interface could cause a deficit of precipitate component (Cr for this study) in very small clusters [90]. As the size of the precipitate increased, the blurring effects at the interface became less significant and therefore the core Cr concentration would approach the equilibrium value. This hypothesis is more in agreement with the concentration-size correlation. Finally, another plausible explanation from the work of

Svetukhin et al. showed that the precipitate composition is determined by the interface surface energy in the Fe-Cr binary system, resulting in increasing Cr content of α' precipitates with increasing precipitate size [117]. To justify these hypotheses, further studies combining experiments, atom probe simulation and thermodynamic calculations are required.

4.2.5 On the voids formation

A comparison of voids formation in the 1 dpa Fe polycrystalline specimens irradiated respectively at 300°C and 450°C was shown in Figure 4.11. The cavity evidently exists in both specimens while the size is much larger in the 450°C specimen than in the 300°C specimen. On the other hand, no voids can be evidently found in the Fe-Cr alloys. Therefore, this study confirms the well-established understanding about that minor alloying addition of substitutional (and interstitutional) impurities in Fe based alloys (actually both all pure metal and complex alloys in bcc and fcc) improves the swelling resistance under irradiation [72].

These cavities could be voids (cluster of voids) or bubbles (clusters of vacancy plus helium). The Advanced Test Reactor is a thermal reactor, and it is known that the steels under a thermal neutron spectrum have a higher transmutants (mostly helium) production compared to fast neutron spectrum. Therefore, some suggest that the observed cavities here is due to helium and not simply due to the clustering of irradiation-induced vacancies because it is irradiated under a thermal neutron spectrum. However, the primary source of helium is boron and nickel interacting with thermal neutrons. The Fe used in this study is model with no detectable boron and with low nickel contents (<0.05 at ppm), so such phenomenon should not have occurred. In other words, the cavities observed in Figure 4.11 are believed to be pure vacancy clusters.

The above argument is also supported by comparing literature data. Several studies are considered: proton irradiation by Okuniewski [93] and neutron irradiation by Horton et al., Zinkle and Singh, and Hernández-Mayoral and Gómez-Briceño [28][31][32]. The Fe specimens used in those thermal reactor irradiations were not ultra-high purity. They contained considerable boron and nickel (ex. 3 ppm B and 2 ppm Ni in [31]), and helium production

is expected in those studies. The comparison is plotted in Figure 4.11. Clearly, the void size is much smaller in this study (higher purity Fe) and in proton ion irradiation (no transmutation reaction), compared to other thermal reactor irradiations (Fe with some B and Ni). The void size in [31] is small, however, due to the much lower irradiation temperature.

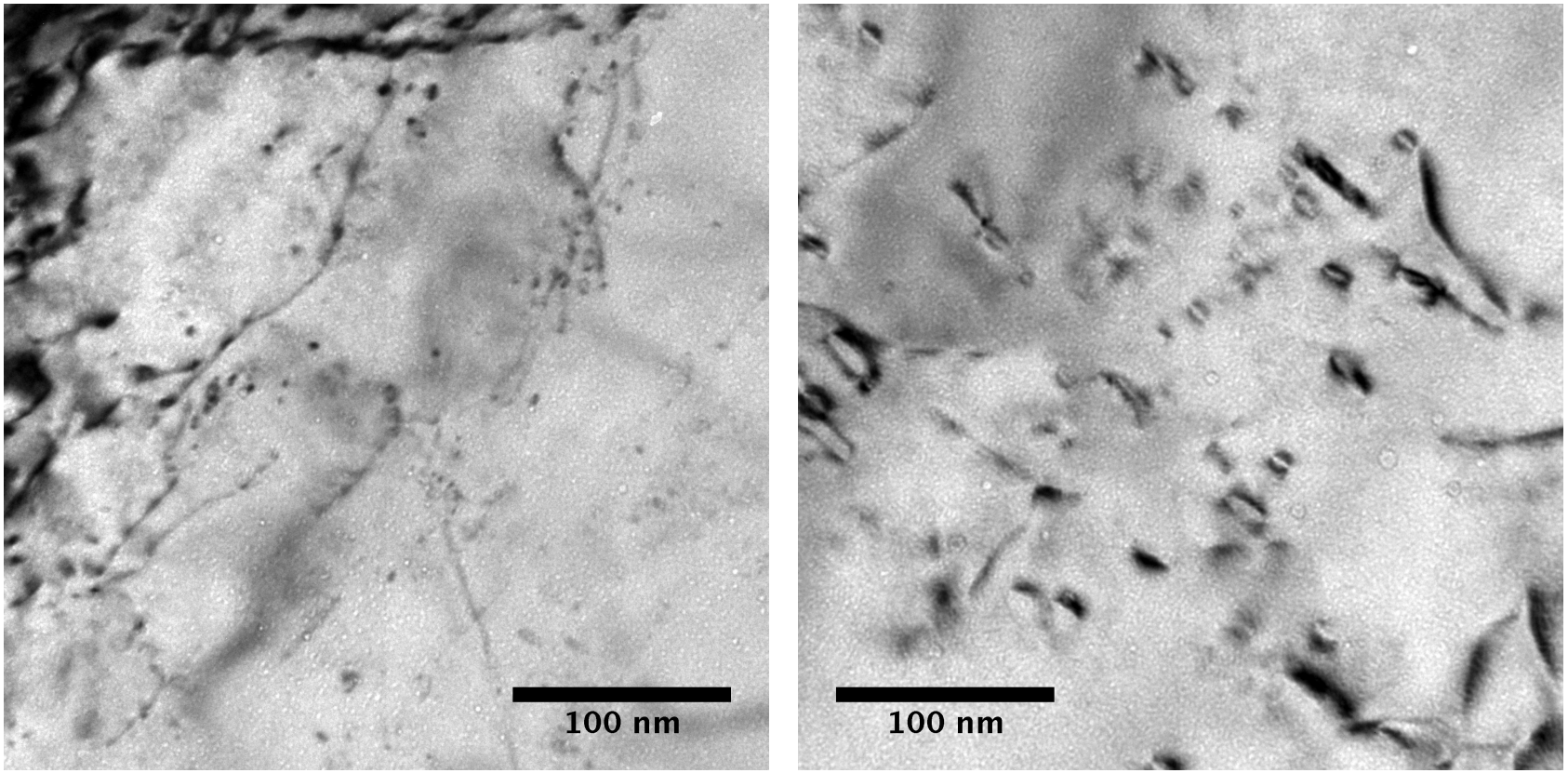

(a) 300°C

(b) 450°C

Figure 4.11: The voids observed in Fe polycrystalline specimens irradiated at 300°C and 450°C. The voids were imaged under under-focus condition.

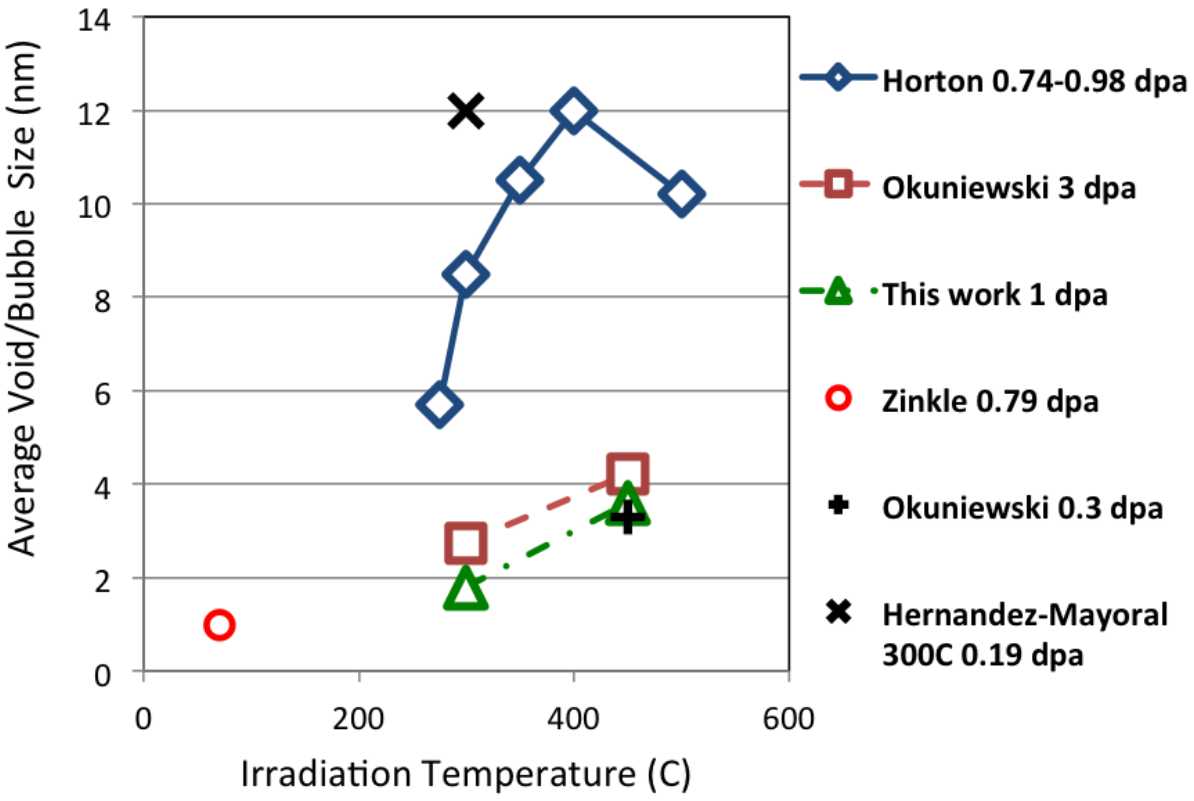

Figure 4.12: Summary of TEM void observation in neutron irradiated Fe in this work and in [28][31][32] and proton irradiated Fe [93].

Since the cavities are vacancy clusters without the involvement of helium, the observation of voids in both 1 dpa specimens is simply a result of the migration and clustering of irradiation-induced vacancies. This is reasonable since the irradiation temperature of 300°C and 450°C are both well above the temperature at which vacancies become mobile (the stage III temperature in Fe is roughly -30°C [76][118]). Increasing the irradiation temperature from 300°C to 450°C enhances the diffusivity of vacancies and therefore larger voids were observed.

When Cr is added, the irradiation-induced void formation in Fe is greatly reduced [22][35]. The absence of voids in Fe-Cr alloys observed in this study is thus in line with other studies. While the Cr strongly decreases the mobility of interstitials and small interstitial clusters (especially $\frac{a}{2}\langle 111\rangle$ loops), DFT result shows that Cr has no effect on the migration energy of vacancies [60]. Gelles et al. suggested that the suppression of swelling in Fe-Cr Ferritic steels is associated with the formation of α' phases [74]. Although suitable for this study

where both 1dpa Fe-Cr specimens exhibited α' precipitates, this hypothesis can not explain the fact that the suppression of swelling also occurs in the Fe-Cr alloys with low Cr contents (with Cr content <9% [57]).

Some researchers proposed that the reduced mobility of interstitial defects (both point defects and clusters) by the Cr atoms leads to enhanced mutual annihilation and thus suppressed swelling [36][119][72]. In the modeling work by Terentyev et al. [119], the reduce in diffusivity of interstitial loops in Fe-Cr has a Cr dependence similar to the swelling suppression. Enhanced mutual combination between interstitial defects and vacancies were surmised. This suggestion, however, is not based on a solid foundation since no detailed mechanisms about how slowed-down interstitial dislocation loops could enhance its recombination interaction with vacancies. More importantly, in this study, the density of dislocation loops observed in the *1 dpa-300°C* Fe-Cr alloys is fairly high and it dose not show any superior recombination than the *1 dpa-300°C* Fe specimen.

Little and Stow [72] proposed that a Cr would be enriched around the periphery of voids because vacancy would preferentially exchange with Cr atoms. The 'Cr shell' around the voids was suggested to deter the voids from accepting additional vacancies [120] because of the strain field. This is a plausible explanation. However it could not be proved in this study.

4.3 Microstructure and the Mechanical Property

In general, the irradiation behavior (both microstructure and mechanical property) between Fe metal and Fe-Cr alloy is quite different. Meanwhile, Fe-10Cr polycrystal and Fe-Cr (10-16Cr) single crystal are pretty close. At both 300°C and 450°C, hardness increased more in Fe-Cr alloys than in Fe metals.

The simple Orowan model is used to compare the microstructure and the mechanical property. This model is based on a periodic array obstacles. The Orowan formula is given by the following equation:

$$\Delta\sigma_y = \alpha_{dis}\mu b\sqrt{\rho_{dis}} + M\alpha_{loop}\mu b\sqrt{N_{loop}d_{loop}} + M\alpha_{\alpha'}\mu b\sqrt{N_{\alpha_{\alpha'}}d_{\alpha_{\alpha'}}} + \Delta\sigma^{Others} \quad (4.2)$$

where M is the Taylor factor, here M = 3.06 [23][121], μ is the shear modulus, here μ = 83 GPa [22][23], and b is the burgers vector, here b = 0.248 nm. The α_{dis}, α_{loop} and $\alpha_{\alpha'}$ are barrier strength constants for network dislocations, dislocation loops and α' precipitates. Here, α_{dis} = 0.64 [22], α_{loop} = 0.4 [121] and $\alpha_{\alpha'}$ = 0.048 [121]. The last term $\Delta\sigma^{Others}$ is introduced to include other hardening mechanisms not covered by the first three terms. These possible mechanisms include, but not limited to, invisible defect clusters [23], ratio of a$\langle 100\rangle$-to-$\frac{a}{2}\langle 111\rangle$ loops [23], voids [22] and degree of Cr segregation to dislocation loops [25]. This term, however, was not considered in this study because sophisticated quantitative model describing these effects are not currently available. For voids, accurate density was not obtained in this study.

The results of calculated increase in yield strength due to the observed defects (dislocations, loops and α' precipitates) are plotted in Figure 4.13 to Figure 4.15. According to Busby et al. [122], the change in micro-hardness is correlated to the change to yield strength with a constant factor. In addition, the nano-indentation and the microhardness can be related through the Nix and Gao model [123]. Therefore, the measured hardness can be directly compared with the calculated yield strength increase, as plotted in the bottom panel of the Figures.

In general, the trend of calculated hardening as a function of dose is qualitatively consistent with the measured hardening, indicating that the hardening of the irradiated materials can be attributed to the observed defect microstructure. Dislocation loops are the primary hardening contributor for all cases. The α' precipitates do not play role until 1 dpa. Increasing the Cr contents increased the amount of hardening from α' precipitates, but seemed not to affect the part from dislocation loops. For instance, the $\sigma_{y-defect}$ from dislocation loops for 1 dpa Fe-10Cr polycrystal and Fe-Cr single crystal are almost the same.

In addition to the qualitative agreement, reasonable quantitative comparability between the calculated and the measured mechanical property is obtained. Only in the 300°C Fe

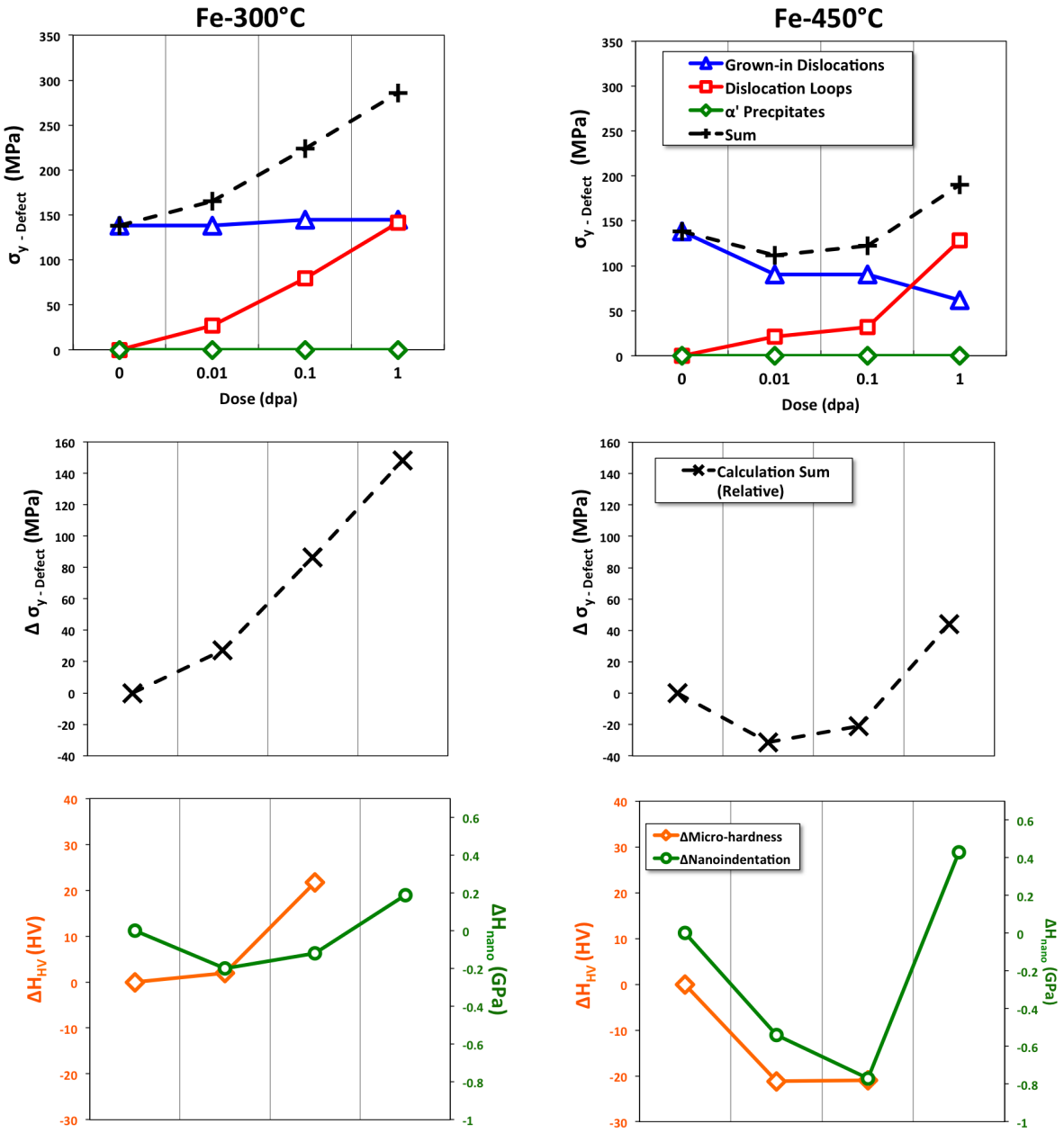

Figure 4.13: A summary of the (Top and Middle Panel) increase in yield strength due to defects estimated from equation and (Bottom Panel) the measured increase in hardness in archive and irradiated Fe polycrystalline specimens.

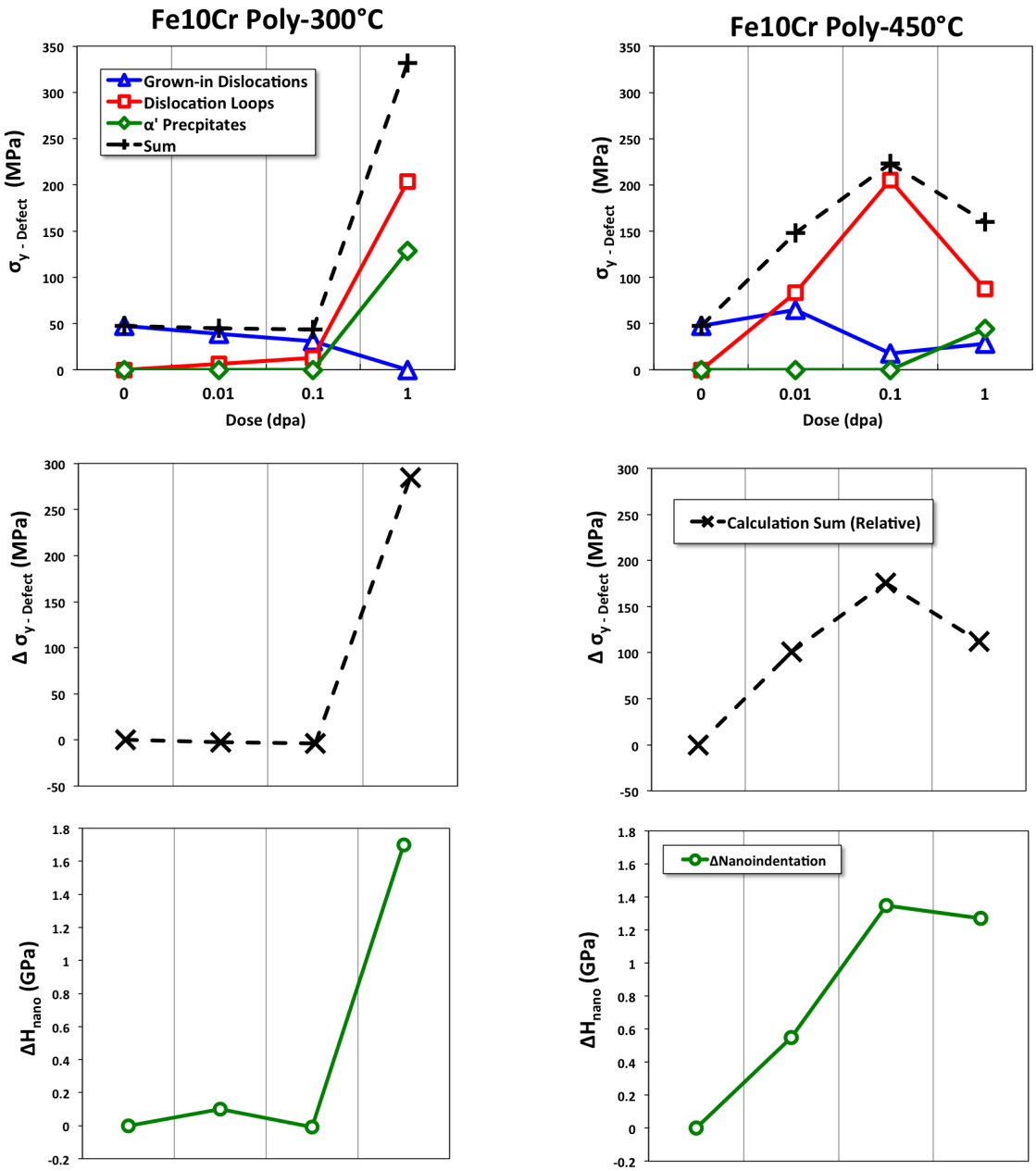

Figure 4.14: A summary of the (Top and Middle Panel) increase in yield strength due to defects estimated from equation and (Bottom Panel) the measured increase in hardness in archive and irradiated Fe-10Cr polycrystalline specimens.

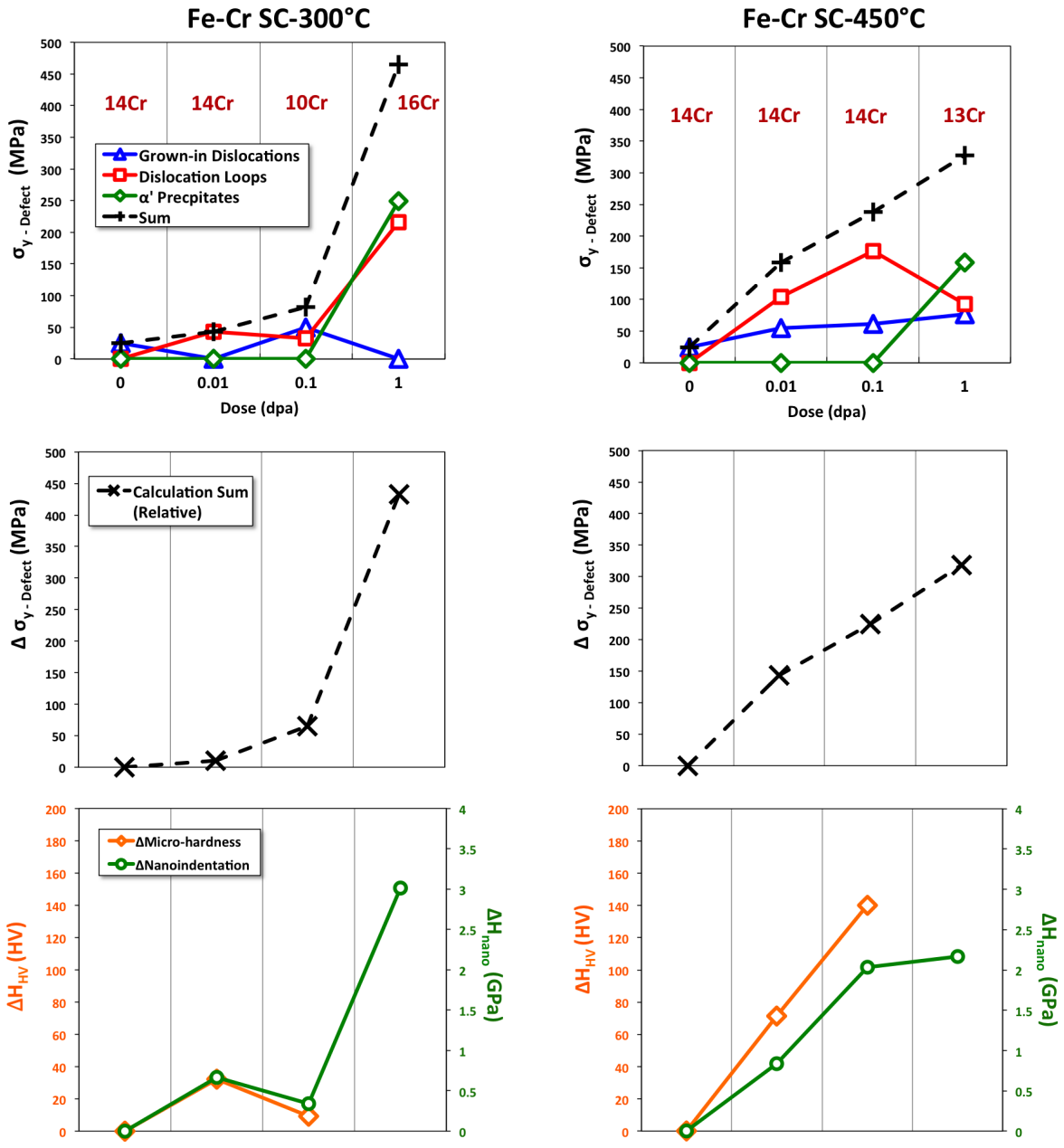

Figure 4.15: A summary of the (Top and Middle Panel) increase in yield strength due to defects estimated from equation and (Bottom Panel) the measured increase in hardness in archive and irradiated Fe-Cr single crystalline (SC) specimens.

specimens (the left side of Figure 4.13), the calculation significantly overestimates. The Orowan model assumes a uniform distribution of obstacles. However, The 300°C-irradiated Fe specimens exhibit a heterogeneous loop distribution (dislocation decoration) and therefore the Orowan model would break down for this case. The rest of the specimens exhibit a relatively uniform loop distribution, leading to a quantitative consistency between calculation and the measurement.

In the following sections, several observation on the evolution of hardening and the corresponding microstructure are discussed.

4.3.1 In Fe polycrystalline specimens

The Irradiation Softening in Fe Poly-crystals Irradiated at 450°C

As shown in Figure 3.94(a), irradiation at 450°C resulted in evident softening in Fe up to 0.1 dpa. At 1 dpa, the hardness rebounded again. Two possible explanations of the softening were considered: irradiation-enhanced grain growth and irradiation-enhanced annealing (reduing dislocation density). For the first one, although 450°C is well below the $\frac{1}{3}T_m$ of ferritic steels , the grain size in archive and irradiated Fe polycrystalline specimens were examined with EBSD to confirm if there was any grain growth. As shown in Figure 4.16, the four Fe specimens (of increasing irradiation dose) have similar microstructures of small sub-grains of a few micro-meters in size.

Some 'noisy regions' are recognized in all of the images. Some occupy a wide area as a patch, and some reside along the grain boundary. They were originally black in color because their orientation could not be determined, but afterward designated a color in the noise reduction process. These noise were considered to be surface oxides resulted from insufficient polishing. The area marked with a letter 'A' in Figure 4.16(b) is an imprint of the indentation test where the grains were greatly deformed and no longer produced well-defined Kikuchi patterns for orientation determination.

Quantitative analysis about the grain size had been attempted, but no useful results were produced. This was mostly due to the tiny orientation difference between sub-grains that

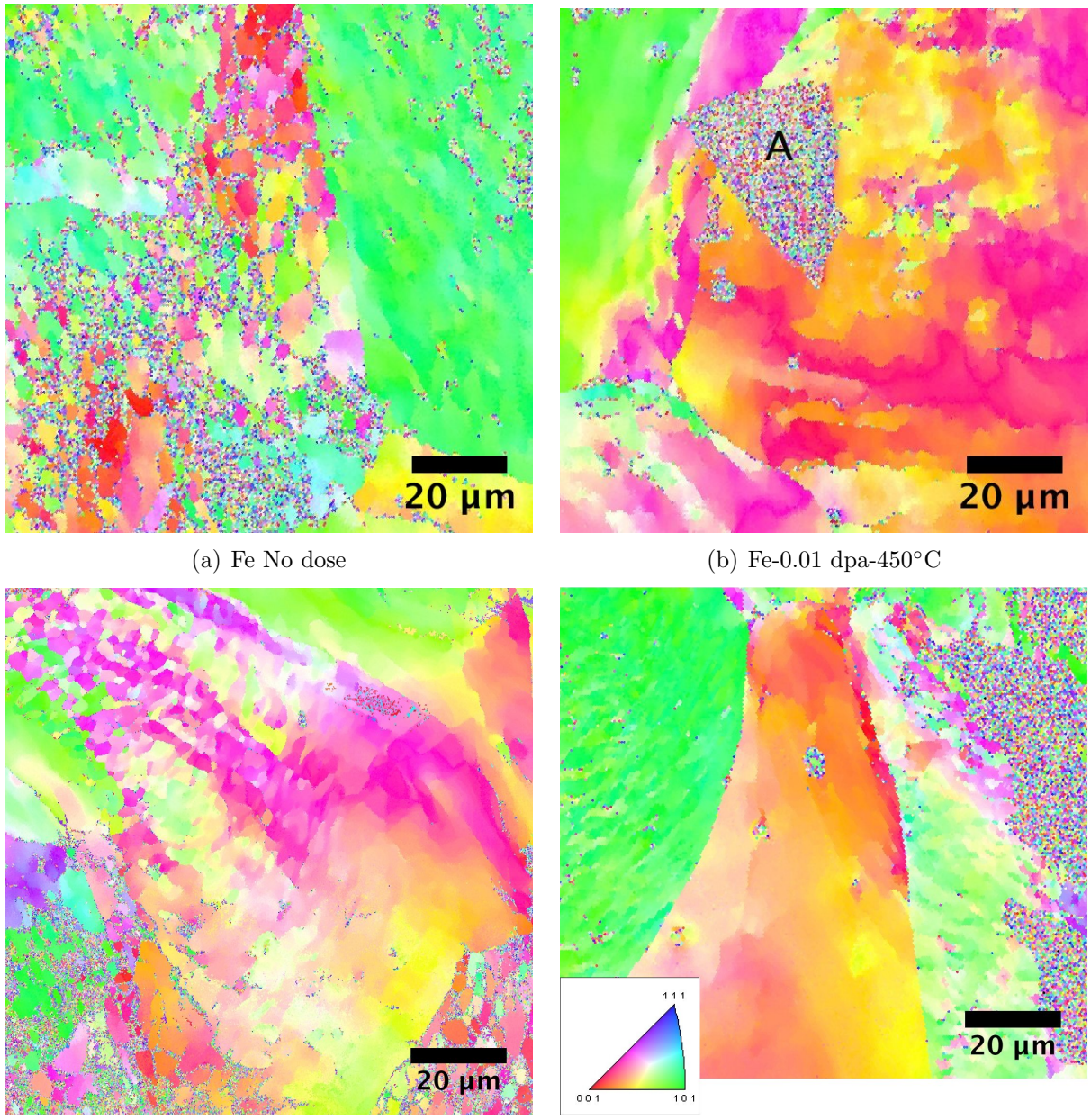

(a) Fe No dose

(b) Fe-0.01 dpa-450°C

(c) Fe-0.1 dpa-450°C

(d) Fe-1 dpa-450°C

Figure 4.16: EBSD images of Fe polycrystalline specimens. The inset in (d) shows the color keys of the crystal orientations.

made it difficult to decide the grain size in the software. In addition, the surface oxides caused degradation on the image quality, which also hindered the software from estimating the grain size. Nevertheless, just by qualitatively observing the images, it seems that irradiation at 450°C did not result in grain growth in Fe poly-crystals.

Another plausible explanation about the softening in Fe is the enhanced recovery (annealing) by irradiations that (1) reduced the dislocation density in the regions enclosed by dislocation cell walls, and (2) rearranged the dislocations in cell walls or low-angle grain boundaries (LAGBs) into ordered array. The first explanation was verified by examining the evolution of dislocation density with irradiation dose in Fe irradiated at 450°C. The dislocation density measurements were carefully conducted to avoid the LAGBs and clear cell walls. That is, the reported densities correspond to the regions inside the LAGBs or dislocation cell walls, and not include grain boundaries or cell walls themselves. The dislocation density dropped monotonically from $1.1\times10^{14}\frac{1}{m^2}$ (no irradiation) to $2.2\times10^{13}\frac{1}{m^2}$ (1 dpa), consistent with the recovery process that reduces dislocation densities.

On the other hand, it is not clear if ordering of dislocations in cell walls or LAGBs had occurred in this study. Figure 4.17 shows the low-angle grain boundaries in Fe irradiated at 300°C to 0.01 dpa (considered to be close to the structure without irradiation) and Fe irradiated at 450°C. There is no significant difference between no irradiation (4.17(a)(b)) and 0.01 dpa (4.17(c)). It should be noted that this is only a preliminary result. More data (more LAGB images) and more systematic comparisons (consistent foil depths, crystal orientations, diffraction conditions etc.) need to be performed in order to obtain comprehensive conclusions.

For 0.1 dpa and 1 dpa, no LAGBs similar to the ones in Figure (a)(b)(c) were observed. Figure 4.17(d) shows a region with relative high dislocation density in the 0.1 dpa specimen. Figure 4.17(e) shows the microstructure in the 1 dpa specimen where only dislocation segments can be observed. This disappearance seems to indicate a dissolve of LAGBs or cell walls in Fe irradiated at 450°C to relatively high dose. However, since only a few grains were examined in each specimen, no strong conclusion can be made about this point due to insufficient statistics.

The correlation between the grown-in dislocations, the dislocation loops and the measured

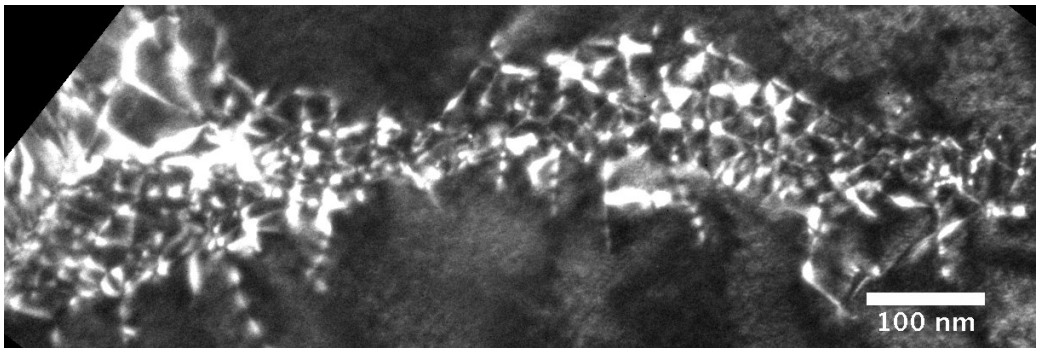

(a) Fe-300°C-0.01dpa case 1

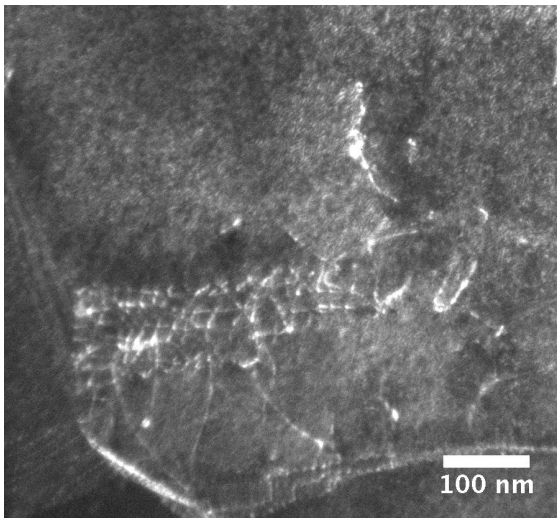

(b) Fe-300°C-0.01dpa case 2

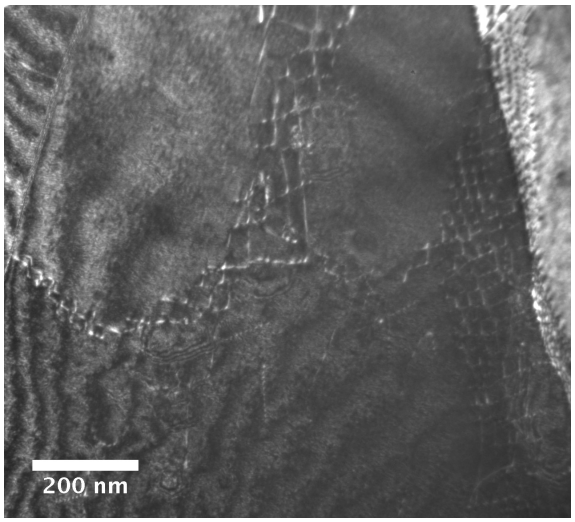

(c) Fe-450°C-0.01 dpa

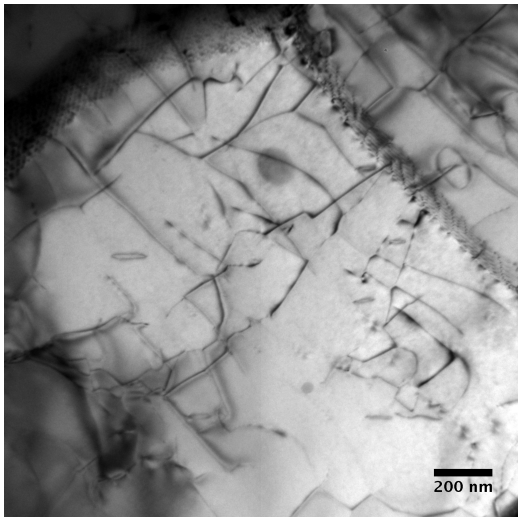

(d) Fe-450°C-1 dpa

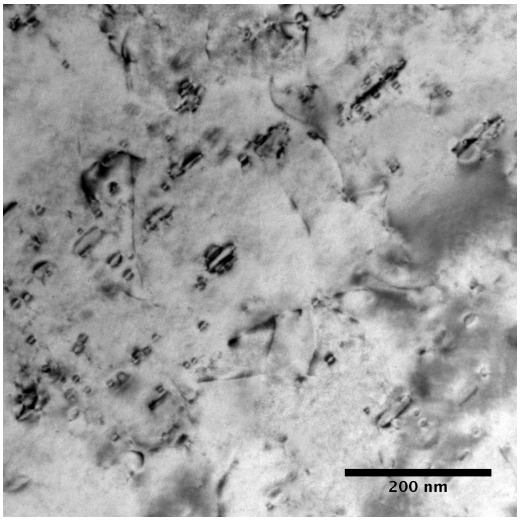

(e) Fe-450°C-1 dpa

Figure 4.17: Low-angle grain boundaries in irradiated Fe specimens. No clear low-angle grain boundaries were found in Fe irradiated at 450°C to (d)0.1 dpa and (e)1 dpa possibly due to insufficient examination areas.

hardness is shown in Figure 4.13. It shows that the decrease in the grown-in dislocations as a result of irradiation-annealing is the major cause for the softening in Fe from no dose to 0.1 dpa. While the dislocation loops increased in the mean time, their effect is too low to compensate the decline in hardness. At 1 dpa, the density of line dislocations continued to drop, but the positive contribution from the dislocation loops increased sharply, surpassing the line dislocations and resulting a rebound in the hardness.

Softening-hardening Ambiguity in Fe irradiated at 300°C

As mentioned in Chapter 3.3.2, the microhardness shows hardening but the nanoindentation shows softening, in Fe polycrystalline specimens irradiated at 300°C from no dose up to 0.1 dpa. It was suggested earlier that the hardening is more plausible over the softening because the microhardness measurements are considered more reliable than the nanoindentation.

This suggestion is further confirmed by examining the microstructure data. In Figure 4.13, the calculated change in yield strength $\sigma_{y-defect}$ is monotonically increasing with dose and there is no sign of annealing or softening. Therefore, it is likely that the nano-hardness measurement on the archive Fe specimen is inaccurate due to surface roughness, oxidation or contamination. The nano-hardness of the archive Fe might have been over-estimated by $\sim$0.2 GPa, if the microhardness is accurate.

4.3.2 In Fe-Cr alloys

The low hardening in Fe-Cr irradiated at 300°C to 0.01 and 0.1 dpa

For both Fe-10Cr polycrystals and Fe-Cr single crystals, the irradiation-induced hardening is little at 0.01 and 0.1 dpa. At 1 dpa, the hardness increases sharply. The low hardness increment for 0.01 and 0.1 dpa is corresponding to a very low (visible) density of dislocation loops and the absence of α' precipitates. The boost in hardness for 1 dpa is clearly due to a high density of dislocation loops and α' precipitates combined. The hardness measurements and the microstructure are, hence, consistent.

As discussed in Chapter 4.2.3, a significant amount of tiny and invisible (in TEM) dislo-

cation loops are speculated in those seemingly low-loop-density Fe-Cr specimens (0.01 and 0.1 dpa at 300°C). The low hardness indicates that, if the speculated tiny loops do exist, their contribution to hardening are limited because of their small size. As shown in MD simulation, small loops (<1 nm) can easily be absorbed by gliding dislocations. In addition, their ability as obstacles decreases with decreasing loop size [124]. Figure 4.18 shows that loops with a size smaller than 1 nm have extremely low hardening effect.

Besides, this close match between the TEM observation and the hardness measurements implies that the information of dislocation loops 'with a size above TEM resolution' is adequate to estimate the mechanical property, regardless of the lack in the knowledge for those tiny invisible loops.

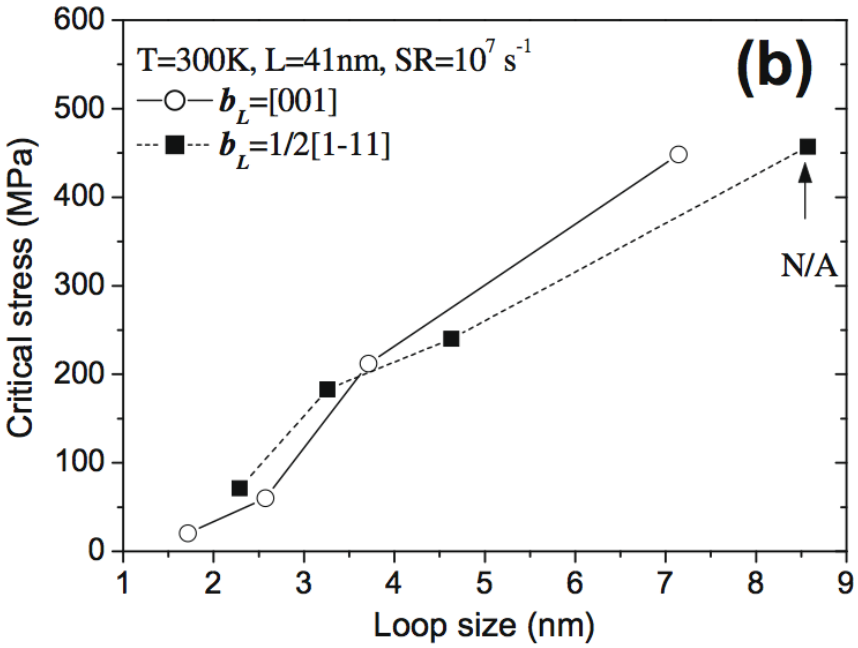

Figure 4.18: The MD calculation showing the critical stress of an edge dislocation passing a periodic row of dislocation loops as a function of loop size for both Burgers vector $\mathbf{b} = a\langle 100\rangle$ and $\frac{a}{2}\langle 111\rangle$ [124].

CHAPTER 5

CONCLUSION

Ferritic-Martensitic steels are considered as lead candidate structural materials for the use in next generation fission reactors and in fusion reactors. One of the challenge in this class of material is to understand the low-temperature irradiation-induced embrittlement. Ferritic-Martensitic steels exhibit a so called 'snaky' dependence of embrittlement [25] on the Cr concentration. The ΔDBTT increases sharply with the an addition of 1-2% Cr in Fe. With more Cr, it decreases to a local minimum around 9 wt% Cr and increases again. On the other hand, the complication about the irradiation temperature effect involves the change of prevailing loop Burgers vector from $\frac{a}{2}\langle 111\rangle$ to a$\langle 100\rangle$ with increasing irradiation temperatures [44][41].

The degradation in mechanical property is related to the irradiation-induced defect clusters that act as obstacles when dislocation glides. These obstacles include dislocation loops, α' precipitates and voids. Dislocation loops and α' precipitates are more important in hardening than small voids [22]. To understand the effect of Cr concentration and the irradiation temperature on the microstructure evolution under irradiation, bcc model Fe and Fe-Cr (10-16 at%Cr) alloys irradiated at 300 and 450°C to 0.01, 0.1 and 1 dpa were examined with TEM, APT and SEM/EBSD. Quantitative information of the grown-in dislocations, dislocation loops, α' precipitates and voids was gathered. In additon, the degradation in mechanical property of the irradiated materials was evaluated by measuring their hardness.

Some highlights of this study are concluded as follows:

1. Voids were observed in 1 dpa Fe at both 300°C and 450°C, but not in lower doses. The void size is larger at 450°C than at 300°C, indicating higher diffusivity of vacancy with increasing temperature. On the other hand, no evident voids can be found in Fe-Cr alloys of all irradiation conditions.

2. The addition of Cr in Fe results in reduced mobility of small $\frac{a}{2}\langle 111\rangle$ loops, leading to less loop coalescence and smaller loop size. The dependence of loop density on the Cr concentration is not obvious in this study.

3. In Fe, higher irradiation temperature results in lower loop density and higher loop size. In Fe-Cr alloys, lower irradiation temperature also results in smaller loop size. In particular, it is suggested that a significant amount of dislocation loops in 0.01 and 0.1 dpa Fe-Cr alloys irradiated at 300°C have a size below TEM resolution.

4. The stability of loop Burgers vector $\mathbf{b} = \mathrm{a}\langle 100\rangle$ and $\mathbf{b} = \frac{a}{2}\langle 111\rangle$ is dependent on both irradiation temperature and Cr concentration. Increasing the irradiation temperature increases the relative stability of $\mathrm{a}\langle 100\rangle$ over $\frac{a}{2}\langle 111\rangle$. On the other hand, the addition of Cr seems to equalize the presence of the two Burgers vectors.

5. Dislocation decoration was observed in both Fe and Fe-Cr. Weather or not a dislocation decoration structure could develop depends on the availability of mobile $\frac{a}{2}\langle 111\rangle$ loops. In Fe, irradiation at 450°C produced mostly immobile $\mathrm{a}\langle 100\rangle$ loops, and no dislocation decoration occurred. In Fe-Cr, the mobility of $\frac{a}{2}\langle 111\rangle$ loops were reduced and, therefore, the dislocation decoration was in general suppressed. However, dislocation decoration can still occur if the irradiation temperature is raised to increase the mobility of $\frac{a}{2}\langle 111\rangle$ loops, while in the mean time keeping the irradiation temperature low enough so $\mathrm{a}\langle 100\rangle$ are not becoming overwhelming. According the results of this study, this temperature range seems to locate between 300°C and 450°C.

6. Evident α' precipitates were observed in the 1 dpa Fe-Cr specimens of both 300°C and 450°C. The volume fraction of the α' phase increases with decreasing irradiation temperature and increasing Cr concentration, which is consistent with phase diagram prediction. In addition, the irradiation temperature and Cr concentration significantly affect the density, but no the size, of the α' precipitates.

7. The increase in hardness with dose ranks as: Fe-Cr single crystals >Fe-10Cr poly-crystals >Fe poly-crystals. For Fe-Cr alloys irradiated at 450°C, the hardening seems

to saturate at 1 dpa . For Fe-Cr irradiated at 300°C, there is no no sign of saturation at 1 dpa.

8. The microstructure and the measured mechanical property were compared by using Orowan model. The hardening predicted by microstructure is generally in agreement with the measured hardness. The hardening of irradiated Fe and Fe-Cr model alloys can be attributed to the changes in the grown-in dislocations, dislocation loops and α' precipitates. Dislocation loops begin to affect the hardness in the lowest dose of 0.01 dpa. The α' precipitates start to contribute considerable hardening until 1 dpa.

9. Irradiation annealing was observed in Fe irradiated at 450°C up to 0.1 dpa. The initial density of the grown-in dislocations in Fe specimens is fairly high (order of 10^{14} $\frac{1}{m^2}$). As the dose increases, the density of grown-in dislocations decreases faster than what dislocation loops can compensate for, resulting a reduce in the overall effect of hardening from dislocations (i.e. softening).

REFERENCES

[1] U. DoE, "A technology roadmap for generation iv nuclear energy systems," in *Nuclear Energy Research Advisory Committee and the Generation IV International Forum*, 2002.

[2] R. Nanstad, "Encyclopedia of materials science and engineering, ed. mb bever," 1986.

[3] S. J. Zinkle and J. T. Busby, "Structural materials for fission & fusion energy," *Materials Today*, vol. 12, no. 11, pp. 12–19, 2009.

[4] R. Klueh and D. Harries, *High Chromium Ferritic and Martensitic Steels for Nuclear Applications*. American Society for Testing and Materials, West Conshohocken, PA, 2001.

[5] R. Klueh and A. Nelson, "Ferritic/martensitic steels for next-generation reactors," *Journal of Nuclear Materials*, vol. 371, no. 1, pp. 37–52, 2007.

[6] D. Blasl, H. Tsunakawa, K. Miyahara, and N. Igata, "Void swelling and microstructure evolution of a dual phase (ferritic and austenitic) stainless steel," *J. Nucl. Mater.*, vol. 133-134, no. we, pp. 517–520, 1985.

[7] D. Gelles, "Microstructural examination of commercial ferritic alloys at 200 dpa," *J. Nucl. Mater.*, vol. 233-237, pp. 293–298, 1996.

[8] R. G. Faulkner and K. Anderko, "High temperature ductility of irradiated ferritic and austenitic steels," *J. Nucl. Mater.*, vol. 113, pp. 168–171, 1983.

[9] F. H. Huang, "Comparison of fracture behavior for low-swelling ferritic and austenitic alloys irradiated in the fast flux test facility (fftf) to 180 dpa," *Engineering Fracture Mechanics*, vol. 43, pp. 733–748, 1992.

[10] M. L. Grossbeck, L. T. Gibson, and S. Jitsukawa, "Irradiation creep in austenitic and ferritic steels irradiated in a tailored neutron spectrum to induce fusion reactor levels of helium," *J. Nucl. Mater.*, vol. 233-237, pp. 148–151, 1996.

[11] Jung, "Radiation effects in structural materials of spallation targets," *Journal of nuclear materials*, vol. 301, pp. 15–22, 2002.

[12] T. Lechtenberg, "Irradiation effects in ferritic steels," *J. Nucl. Mater.*, vol. 133-134, pp. 149–155, 1985.

[13] A. Koyama, A. Hishinuma, D. S. Gelles, R. L. Klueh, W. Dietz, and K. Ehrlich, "Low - activation ferritic and martensitic steels for fusion application," *J. Nucl. Mater.*, vol. 233-237A, pp. 138–147, 1996.

[14] R. Klueh and E. Bloom, "The development of ferritic steels for fast induced-radioactivity decay for fusion reactor applications," *Nuclear engineering and design. Fusion*, vol. 2, no. 3, pp. 383–389, 1985.

[15] R. W. Conn, E. E. Bloom, J. Davis, R. E. Gold, R. Little, K. R. Schultz, D. L. Smith, and F. Wiffen, "Lower activation materials and magnetic fusion reactors," 1984.

[16] L. Malerba, A. Caro, and J. Wallenius, "Multiscale modelling of radiation damage and phase transformations: The challenge of fecr alloys," *Journal of Nuclear Materials*, vol. 382, no. 2, pp. 112–125, 2008.

[17] B. Singh, A. Horsewell, and P. Toft, "Effects of neutron irradiation on microstructure and mechanical properties of pure iron," *Journal of nuclear materials*, vol. 271, pp. 97–101, 1999.

[18] M. Eldrup, B. Singh, S. Zinkle, T. Byun, and K. Farrell, "Dose dependence of defect accumulation in neutron irradiated copper and iron," *Journal of nuclear materials*, vol. 307, pp. 912–917, 2002.

[19] K. Verheyen, M. Jardin, and A. Almazouzi, "Coincidence doppler broadening spectroscopy in fe, fec and fecu after neutron irradiation," *Journal of nuclear materials*, vol. 351, no. 1, pp. 209–215, 2006.

[20] K. Suganuma, H. Kayano, and S. Yajima, "Mechanical properties changes of fe-cr alloys by fast neutron irradiation," *Journal of Nuclear Materials*, vol. 105, no. 1, pp. 23–35, 1982.

[21] A. Okada, N. Kawaguchi, M. Hamilton, K. Hamada, T. Yoshiie, I. Ishida, and E. Hirota, "Mechanical property change in neutron irradiated fe-cr and fe-mn alloys, and their defect structures," *Journal of nuclear materials*, vol. 212, pp. 382–387, 1994.

[22] S. Porollo, A. Dvoriashin, A. Vorobyev, and Y. V. Konobeev, "The microstructure and tensile properties of fecr alloys after neutron irradiation at 400 c to 5.57.1 dpa," *Journal of nuclear materials*, vol. 256, no. 2, pp. 247–253, 1998.

[23] M. Matijasevic and A. Almazouzi, "Effect of cr on the mechanical properties and microstructure of fecr model alloys after n-irradiation," *Journal of Nuclear Materials*, vol. 377, no. 1, pp. 147–154, 2008.

[24] A. Okada, T. Yasujima, T. Yoshiie, I. Ishida, and M. Kiritani, "Mechanical property changes and microstructures of iron irradiated with fission and fusion neutrons," *Journal of nuclear materials*, vol. 179, pp. 1083–1087, 1991.

[25] D. Terentyev, G. Bonny, C. Domain, G. Monnet, and L. Malerba, "Mechanisms of radiation strengthening in fe-cr alloys as revealed by atomistic studies," *Journal of Nuclear Materials*, vol. 442, no. 1, pp. 470–485, 2013.

[26] B. Eyre and A. Bartlett, "An electron microscope study of neutron irradiation damage in alpha-iron," *Philosophical Magazine*, vol. 12, no. 116, pp. 261–272, 1965.

[27] J. Bryner, "A study of neutron irradiation damage in iron by electron-transmission microscopy," *Acta Metallurgica*, vol. 14, no. 3, pp. 323–336, 1966.

[28] L. Horton, J. Bentley, and K. Farrell, "A tem study of neutron-irradiated iron," *Journal of Nuclear Materials*, vol. 108, pp. 222–233, 1982.

[29] I. Robertson, M. Jenkins, and E. C.A., "Low-dose neutron-irradiation damage in α-iron," *Journal of Nuclear Materials*, vol. 108&109, p. 209, 1982.

[30] A. Nicol, M. Jenkins, and M. Kirk, "Matrix damage in iron," in *Materials Research Society Symposium Proceedings*, vol. 650. Cambridge Univ Press, 2001, pp. R1. 3–R1. 3.

[31] S. J. Zinkle and B. N. Singh, "Microstructure of neutron-irradiated iron before and after tensile deformation," *Journal of nuclear materials*, vol. 351, no. 1, pp. 269–284, 2006.

[32] M. Hernandez-Mayoral and D. Gomez-Briceno, "Transmission electron microscopy study on neutron irradiated pure iron and rpv model alloys," *Journal of Nuclear Materials*, vol. 399, no. 23, pp. 146–153, Apr. 2010.

[33] D. Gelles, "Microstructural examination of neutron-irradiated simple ferritic alloys," *Journal of Nuclear Materials*, vol. 108, pp. 515–526, 1982.

[34] Y. Katoh, A. Kohyama, and D. S. Gelles, "Swelling and dislocation evolution in simple ferritic alloys irradiated to high fluence in fftf/mota," *Journal of nuclear materials*, vol. 225, pp. 154–162, 1995.

[35] Y. V. Konobeev, A. Dvoriashin, S. Porollo, and F. A. Garner, "Swelling and microstructure of pure fe and fe-cr alloys after neutron irradiation to $\sim$26dpa at 400°c," *Journal of nuclear materials*, vol. 355, no. 1, pp. 124–130, 2006.

[36] M. Matijasevic, W. Van Renterghem, and A. Almazouzi, "Characterization of irradiated single crystals of fe and fe15cr," *Acta Materialia*, vol. 57, no. 5, pp. 1577–1585, 2009.

[37] B. Eyre, "Direct observations of neutron irradiation damage in -iron," *Philosophical Magazine*, vol. 7, no. 84, pp. 2107–2113, 1962.

[38] T. Matsui, S. Muto, and T. Tanabe, "Tem study on deuterium-irradiation-induced defects in tungsten and molybdenum," *Journal of nuclear materials*, vol. 283, pp. 1139–1143, 2000.

[39] P. Rice and S. Zinkle, "Temperature dependence of the radiation damage microstructure in v4cr4ti neutron irradiated to low dose," *Journal of nuclear materials*, vol. 258, pp. 1414–1419, 1998.

[40] J. Hirth and J. Lothe, "Theory of dislocations, 1982," *John Willey and Sons, NewYork*.

[41] S. L. Dudarev, R. Bullough, and P. M. Derlet, "Effect of the α-γ phase transition on the stability of dislocation loops in bcc iron," *Phys. Rev. Lett.*, vol. 100, p. 135503, Apr 2008.

[42] J. Marian, B. D. Wirth, and J. M. Perlado, "Mechanism of formation and growth of 100 interstitial loops in ferritic materials," *Phys. Rev. Lett.*, vol. 88, p. 255507, Jun 2002.

[43] H. Xu, R. E. Stoller, Y. N. Osetsky, and D. Terentyev, "Solving the puzzle of $\langle 100 \rangle$interstitial loop formation in bcc iron," *Physical review letters*, vol. 110, no. 26, p. 265503, 2013.

[44] Z. Yao, M. Jenkins, M. Hernandez-Mayoral, and M. Kirk, "The temperature dependence of heavy-ion damage in iron: A microstructural transition at elevated temperatures," *Philosophical Magazine*, vol. 90, no. 35-36, pp. 4623–4634, 2010.

[45] M. Jenkins, Z. Yao, M. Hernndez-Mayoral, and M. Kirk, "Dynamic observations of heavy-ion damage in fe and fecr alloys," *Journal of Nuclear Materials*, vol. 389, no. 2, pp. 197–202, May 2009.

[46] L. Mansur, "Theory and experimental background on dimensional changes in irradiated alloys," *Journal of Nuclear Materials*, vol. 216, pp. 97–123, 1994.

[47] K. Arakawa, K. Ono, M. Isshiki, K. Mimura, M. Uchikoshi, and H. Mori, "Observation of the one-dimensional diffusion of nanometer-sized dislocation loops," *Science*, vol. 318, no. 5852, pp. 956–959, 2007.

[48] Z. Yao, M. Hernandez-Mayoral, M. Jenkins, and M. Kirk, "Heavy-ion irradiations of fe and fe-cr model alloys part 1: Damage evolution in thin-foils at lower doses," *Philosophical Magazine*, vol. 88, no. 21, pp. 2851–2880, 2008.

[49] M. Hernandez-Mayoral, Z. Yao, M. Jenkins, and M. Kirk, "Heavy-ion irradiations of fe and fe-cr model alloys part 2: Damage evolution in thin-foils at higher doses," *Philosophical Magazine*, vol. 88, no. 21, pp. 2881–2897, 2008.

[50] I. Robertson, Ph.D. dissertation, Oxford University UK, 1982.

[51] K. Arakawa, M. Hatanaka, H. Mori, and K. Ono, "Effects of chromium on the one-dimensional motion of interstitial-type dislocation loops in iron," *Journal of nuclear materials*, vol. 329, pp. 1194–1198, 2004.

[52] C. Tomchik, "In situ transmission electron microscopy ion irradiations of model iron-chromium alloys," M.S. thesis, University of Illinois at Urbana-Champaign, 2011.

[53] S. Xu, Z. Yao, and M. Jenkins, "Tem characterisation of heavy-ion irradiation damage in fecr alloys," *Journal of Nuclear Materials*, vol. 386, pp. 161–164, 2009.

[54] A. Almazouzi, T. Diaz de la Rubia, B. Singh, and M. Victoria, "Basic aspects of differences in irradiation effects between fcc, bcc and hcp metals and alloys," *Journal of nuclear materials*, vol. 276, no. 1, pp. 295–296, 2000.

[55] M. Pohl, O. Storz, and T. Glogowski, "Effect of intermetallic precipitations on the properties of duplex stainless steel," *Materials Characterization*, vol. 58, no. 1, pp. 65–71, Jan. 2007.

[56] M. Miller, R. Stoller, and K. Russell, "Effect of neutron-irradiation on the spinodal decomposition of fe-32%cr model alloys," *J. Nucl. Mater.*, vol. 230, no. 3, pp. 219–225, June 1996.

[57] G. Bonny, D. Terentyev, and L. Malerba, "On the α-α-$'$ miscibility gap of fe-cr alloys," *Scripta Materialia*, vol. 59, no. 11, pp. 1193–1196, Dec. 2008.

[58] W. Xiong, M. Selleby, Q. Chen, J. Odqvist, and Y. Du, "Phase equilibria and thermodynamic properties in the fe-cr systems," *Critical reviews in solid state and materials sciences*, vol. 35, no. 2, pp. 125–152, 2010.

[59] I. Mirebeau and G. Parette, "Neutron study of the short range order inversion in $fe_{1-x}cr_x$," *Phys. Rev. B*, vol. 82, no. 10, p. 104203, Sep. 2010.

[60] P. Olsson, I. A. Abrikosov, L. Vitos, and J. Wallenius, "Ab initio formation energies of fecr alloys," *Journal of Nuclear Materials*, vol. 321, no. 1, pp. 84–90, 2003.

[61] P. Olsson, I. Abrikosov, and J. Wallenius, "Electronic origin of the anomalous stability of fe-rich bcc fe-cr alloys," *Physical Review B*, vol. 73, no. 10, p. 104416, 2006.

[62] P. Olsson, C. Domain, and J. Wallenius, "Ab initio study of cr interactions with point defects in bcc fe," *Physical Review B*, vol. 75, no. 1, p. 014110, 2007.

[63] W. Xiong, M. Selleby, Q. Chen, J. Odqvist, and Y. Du, "Phase equilibria and thermodynamic properties in the fe-cr system," *Crit. Rev. Solid State Mater. Sci.*, vol. 35, p. 125, 2010.

[64] T. Hamaoka, A. Nomoto, K. Nishida, K. Dohi, and N. Soneda, "Effects of aging temperature on g-phase precipitation and ferrite-phase decomposition in duplex stainless steel," *Philosophical Magazine*, vol. 92, no. 34, pp. 4354–4375, 2012.

[65] M. Miller and J. Bentley, "Apfim and aem investigation of cf8 and cf8m primary coolant pipe steels," *Mater. Sci. Technol.*, vol. 6, pp. 285–292, 1990.

[66] H. Chung and T. Leax, "Embrittlement of laboratory and reactor aged cf3,cf8, and cf8m duplex stainless steels," *Mater. Sci. Technol.*, vol. 6, pp. 249–262, 1990.

[67] P. Auger, F. Danoix, A. Menand, S. Bonnet, J. Bourgoin, and M. Guttmann, "Atom probe and transmission electron microscopy study of aging of cast duplex stainless steels," *Materials Science and Technology*, vol. 6, pp. 301–313, 1990.

[68] F. Danoix and P. Auger, "Atom probe studies of the fe-cr system and stainless steels aged at intermediate temperature: A review," *Materials Characterization*, vol. 44, no. 12, pp. 177–201, Jan. 2000.

[69] M. Miller, J. Hyde, M. Hetherington, A. Cerezo, G. Smith, and C. Elliott, "Spinodal decomposition in fe-cr alloys: Experimental study at the atomic levels and comparison with computer models - part i. introduction and methodology," *Acta Metall. Mater.*, vol. 43, pp. 3385–3401, 1995.

[70] M. Miller, in *Proc. 2nd Int. Conf. Solid-solid phase transformations 87*, G. Lorimer, Ed. Cambridge: Institute of Metals, London, 1987, p. 89.

[71] F. Garner, M. Toloczko, and B. Sencer, "Comparison of swelling and irradiation creep behavior of fcc-austenitic and bcc-ferritic/martensitic alloys at high neutron exposure," *Journal of Nuclear Materials*, vol. 276, no. 13, pp. 123–142, Jan. 2000.

[72] E. Little and D. Stow, "Void-swelling in irons and ferritic steels: Ii. an experimental survey of materials irradiated in a fast reactor," *Journal of Nuclear Materials*, vol. 87, no. 1, pp. 25–39, 1979.

[73] D. Gelles, "Void swelling in binary fecr alloys at 200 dpa," *Journal of Nuclear Materials*, vol. 225, no. 0, pp. 163–174, Aug. 1995.

[74] D. Gelles, "Effects of irradiation on ferritic alloys and implications for fusion reactor applications," *Journal of Nuclear Materials*, vol. 149, no. 2, pp. 192–199, July 1987.

[75] L. Horton, J. Bentley, and W. Jesser, "The microstructure of triple-beam ion irradiated fe and fe-cr alloys," *Journal of Nuclear Materials*, vol. 104, no. 0, pp. 1085–1089, 1981.

[76] C.-C. Fu, J. Dalla Torre, F. Willaime, J.-L. Bocquet, and A. Barbu, "Multiscale modelling of defect kinetics in irradiated iron," *Nature materials*, vol. 4, no. 1, pp. 68–74, 2004.

[77] B. Singh and J. Evans, "Significant differences in defect accumulation behaviour between fcc and bcc crystals under cascade damage conditions," *Journal of Nuclear Materials*, vol. 226, no. 3, pp. 277–285, Nov. 1995.

[78] M. Victoria, N. Baluc, C. Bailat, Y. Dai, M. Luppo, R. Schaublin, and B. Singh, "The microstructure and associated tensile properties of irradiated fcc and bcc metals," *Journal of nuclear materials*, vol. 276, no. 1, pp. 114–122, 2000.

[79] T. Allen et al., *ATR NSUF 2012 Annual Report*, 2012. [Online]. Available: https://atrnsuf.inl.gov/documents/ATRNSUFAnnualReport2012.pdf

[80] D. B. Williams and C. B. Carter, *The Transmission Electron Microscope*. Springer, 1996.

[81] F. Maury, M. Biget, P. Vajda, A. Lucasson, and P. Lucasson, "Anisotropy of defect creation in electron-irradiated iron crystals," *Physical Review B*, vol. 14, no. 12, p. 5303, 1976.

[82] M. Jenkins, "Characterisation of radiation-damage microstructures by tem," *Journal of nuclear materials*, vol. 216, pp. 124–156, 1994.

[83] P. B. Hirsch, A. Howie, R. Nicholson, D. Pashley, and M. J. Whelan, *Electron microscopy of thin crystals*. Butterworths London, 1965, vol. 320.

[84] J. Bailey and P. Hirsch, "The dislocation distribution, flow stress, and stored energy in cold-worked polycrystalline silver," *Philosophical Magazine*, vol. 5, no. 53, pp. 485–497, 1960.

[85] C. Smith and L. Guttman, "One and two dimensional sections of three dimensional structures," *Journal of Metals*, vol. 4, no. 2, p. 150, 1952.

[86] R. Ham, "The determination of dislocation densities in thin films," *Philosophical Magazine*, vol. 6, no. 69, pp. 1183–1184, 1961.

[87] M. K. Miller and R. Forbes, "Atom probe tomography," *Materials Characterization*, vol. 60, no. 6, pp. 461–469, 2009.

[88] M. P. Moody, L. T. Stephenson, A. V. Ceguerra, and S. P. Ringer, "Quantitative binomial distribution analyses of nanoscale likesolute atom clustering and segregation in atom probe tomography data," *Microscopy research and technique*, vol. 71, no. 7, pp. 542–550, 2008.

[89] M. Miller, *Atom Probe Tomography: Analysis at the Aomiic Level*. Springer, New York, 2000.

[90] O. C. Hellman, J. A. Vandenbroucke, J. Rusing, D. Isheim, and D. N. Seidman, "Analysis of three-dimensional atom-probe data by the proximity histogram," *Microscopy and Microanalysis*, vol. 6, no. 05, pp. 437–444, 2000.

[91] V. Kuksenko, C. Pareige, C. Genevois, F. Cuvilly, M. Roussel, and P. Pareige, "Effect of neutron-irradiation on the microstructure of a fe12at.alloy," *Journal of Nuclear Materials*, vol. 415, no. 1, pp. 61–66, 2011.

[92] B. Gault, M. P. Moody, J. M. Cairney, and S. P. Ringer, *Atom probe microscopy*. Springer, 2012, vol. 160.

[93] M. A. Okuniewski, "Irradiation-induced microstructure evolution and mechanical preperties in iron with and without helium," Ph.D. dissertation, University of Illinois at Urbana-Champaign, 2008.

[94] F. Schulz and H. Hanemann, "Die bestimmung der mikroharte von metallen," *Zeitschrift Fur Metallkunde*, vol. 33, pp. 124–133, 1941.

[95] D. L. Holt, "Dislocation cell formation in metals," *Journal of Applied Physics*, vol. 41, no. 8, pp. 3197–3201, 1970.

[96] S. P. Fitzgerald and Z. Yao, "Shape of prismatic dislocation loops in anisotropic -fe," *Philosophical Magazine Letters*, vol. 89, no. 9, pp. 581–588, 2009.

[97] V. Kuksenko, C. Pareige, and P. Pareige, "Cr precipitation in neutron irradiated industrial purity fe-cr model alloys," *Journal of Nuclear Materials*, vol. 432, no. 1, pp. 160–165, 2013.

[98] J. Gan and D. Ogden, "Private communication."

[99] P. Hosemann, "Studying radiation damage in structural materials by using ion accelerators," *Reviews of Accelerator Science and Technology*, vol. 4, no. 01, pp. 161–182, 2011.

[100] H. Trinkaus, B. Singh, and A. Foreman, "Mechanisms for decoration of dislocations by small dislocation loops under cascade damage conditions," *Journal of nuclear materials*, vol. 249, no. 2, pp. 91–102, 1997.

[101] B. Singh, A. Foreman, and H. Trinkaus, "Radiation hardening revisited: role of intracascade clustering," *Journal of nuclear materials*, vol. 249, no. 2, pp. 103–115, 1997.

[102] L. Hulett Jr, T. Baldwin, J. Crump III, and F. Young Jr, "Effect of neutron irradiation on copper crystals at high temperatures," *Journal of Applied Physics*, vol. 39, no. 8, pp. 3945–3954, 1968.

[103] M. Wen, N. M. Ghoniem, and B. N. Singh, "Dislocation decoration and raft formation in irradiated materials," *Philosophical Magazine*, vol. 85, no. 22, pp. 2561–2580, 2005.

[104] Z. Yao, "Private communication."

[105] K. Arakawa, M. Hatanaka, E. Kuramoto, K. Ono, and H. Mori, "Changes in the burgers vector of perfect dislocation loops without contact with the external dislocations," *Phys. Rev. Lett.*, vol. 96, p. 125506, Mar 2006.

[106] S. Zinkle, P. Maziasz, and R. Stoller, "Dose dependence of the microstructural evolution in neutron-irradiated austenitic stainless steel," *Journal of Nuclear materials*, vol. 206, no. 2, pp. 266–286, 1993.

[107] R. E. Stoller and G. R. Odette, "A composite model of microstructural evolution in austenitic stainless steel under fast neutron irradiation," in *Radiation-Induced Changes in Microstructure, 13th International Symposium, ASTM STP*, vol. 955, 1987, pp. 371–392.

[108] G. Vetterick, C. Barr, M. Taheri, J. Baldwin, A. Misra, K. Hattar, M. Kirk, and R. Unocic, "In-situ tem observation of the grain size effect on radiation induced defect distribution in iron," *Microscopy and Microanalysis*, vol. 18, pp. 1350–1351, 2012.

[109] M. Mathon, Y. De Carlan, G. Geoffroy, X. Averty, A. Alamo, and C. De Novion, "A sans investigation of the irradiation-enhanced α-α' phases separation in 7-12 cr martensitic steels," *Journal of nuclear materials*, vol. 312, no. 2, pp. 236–248, 2003.

[110] Z. Jiao, V. Shankar, and G. S. Was, "Phase stability in proton and heavy ion irradiated ferritic-martensitic alloys," *Journal of Nuclear Materials*, vol. 419, no. 1, pp. 52–62, 2011.

[111] C. Heintze, F. Bergner, A. Ulbricht, and H. Eckerlebe, "The microstructure of neutron-irradiated fe-cr alloys: A small-angle neutron scattering study," *Journal of Nuclear Materials*, vol. 409, no. 2, pp. 106–111, 2011.

[112] R. Coppola, R. Lindau, R. May, A. Moslang, and M. Valli, "Investigation of microstructural evolution under neutron irradiation in eurofer97 steel by means of small-angle neutron scattering," *Journal of Nuclear Materials*, vol. 386, pp. 195–198, 2009.

[113] M. Y. Lavrentiev, R. Drautz, D. Nguyen-Manh, T. Klaver, and S. Dudarev, "Monte carlo study of thermodynamic properties and clustering in the bcc fe-cr system," *Physical Review B*, vol. 75, no. 1, p. 014208, 2007.

[114] J. Gibbs, *Trans. Conn. Acad. Arts Sci*, vol. 3, 102, 1878.

[115] Y. Li, S. Hu, L. Zhang, and X. Sun, "Non-classical nuclei and growth kinetics of cr precipitates in fecr alloys during ageing," *Modelling and Simulation in Materials Science and Engineering*, vol. 22, no. 2, p. 025002, 2014.

[116] S. Novy, P. Pareige, and C. Pareige, "Atomic scale analysis and phase separation understanding in a thermally aged fe20at.*Journal of nuclear materials*, vol. 384, no. 2, pp. 96–102, 2009.

[117] V. Svetukhin, P. L'vov, E. Gaganidze, M. Tikhonchev, and C. Dethloff, "Kinetics and thermodynamics of cr nanocluster formation in fe-cr systems," *Journal of Nuclear Materials*, vol. 415, no. 2, pp. 205–209, 2011.

[118] S. Takaki, J. Fuss, H. Kuglers, U. Dedek, and H. Schultz, "The resistivity recovery of high purity and carbon doped iron following low temperature electron irradiation," *Radiation effects*, vol. 79, no. 1-4, pp. 87–122, 1983.

[119] D. Terentyev, P. Olsson, L. Malerba, and A. Barashev, "Characterization of dislocation loops and chromium-rich precipitates in ferritic ironchromium alloys as means of void swelling suppression," *Journal of Nuclear Materials*, vol. 362, no. 23, pp. 167–173, May 2007.

[120] Y. Zhang, "Private communication."

[121] F. Bergner, C. Pareige, M. Hernandez-Mayoral, L. Malerba, and C. Heintze, "Application of a three-feature dispersed-barrier hardening model to neutron-irradiated fe-cr model alloys," *Journal of Nuclear Materials*, vol. 448, no. 1, pp. 96–102, 2014.

[122] J. Busby, M. Hash, and G. Was, "The relationship between hardness and yield stress in irradiated austenitic and ferritic steels," *J. Nucl. Mater.*, vol. 336, pp. 267–278, 2005.

[123] W. D. Nix and H. Gao, "Indentation size effects in crystalline materials: a law for strain gradient plasticity," *Journal of the Mechanics and Physics of Solids*, vol. 46, no. 3, pp. 411–425, 1998.

[124] D. Terentyev, Y. Osetsky, and D. Bacon, "Competing processes in reactions between an edge dislocation and dislocation loops in a body-centred cubic metal," *Scripta Materialia*, vol. 62, no. 9, pp. 697–700, May 2010.